Development of Low Dimensional Nanostructured Materials for Green Energy Harvesting

By

Yuanxing Fang

A Thesis Submitted for the Degree of Doctor of Philosophy

School of Life Sciences

University of Sussex

April 2016

Acknowledgements

First of all, I would like to express my sincere gratitude to my main supervisor, Dr Qiao Chen for his invaluable support and guidance whilst completing my research. I would also like to thank my co-supervisor, Prof. Wendy Brown for her support and helpful advice during my study at Sussex.

I would like to thank Prof. Bin Hu at Huazhong University of Science and Technology, and Dr Xuenong Bo at Queen Mary University of London, for supporting my research as external collaborators.

I would like to express my special thanks to the members of nano group at University of Sussex, Dr Wei Cheat Lee, Dr Jasbir Bedi, Giacomo Canciani, Dr Brnyia Alwhshe, Thomas Draper, Dr Rantej Kler, Dr Ali Shahroozi and Dr Zainab Abdullah. I would also like to acknowledge the MChem students for their assistance in my group during their MChem projects.

Last but not least, I would especially like to thank my entire family, my wife and my closest friends for their love, fun, support and continued encouragement.

University of Sussex

Yuanxing Fang

Doctor of Philosophy

Development of Low Dimensional Nanostructured Materials for Green Energy Harvesting

Abstract

The decreasing availability of fossil fuels and their negative environmental impacts requires urgent need of developing renewable energy. The main objective of this research was to develop low-dimensional nanomaterials for harvesting solar and mechanical energy with high conversion efficiency. In particular, photoelectrochemical water splitting and photovoltaic cell applications driven by sunlight were investigated in this project. A highly efficient triboelectric nanogenerator was investigated for harvesting mechanical energy. The device was further integrated with an organic solar cell for harvesting both mechanical energy and solar energy.

My research work started with the synthesis of nanostructured materials. Electrospinning, as well as electrospray, was developed to synthesise nanofibres and hollow hemispheres. The influences of processing parameters to the morphologies and structures of the nanomaterials were systematically investigated. An electrophoretic deposition method was also developed to form good-quality nanostructured metal oxide thin films, which were applied in photoelectrochemical water splitting. The metal oxide hollow hemisphere thin films were also applied in dye-sensitised solar cells.

A transparent and flexible triboelectric nanogenerator was developed in order to harvest mechanical energy. The contact electrodes were created using metal nanowire percolation networks embedded in a polymer matrix. The correlation between the

energy conversion performances and optical property of the triboelectric electrodes were comprehensively studied as a function of the areal fraction of the metal nanowires.

A flexible hybrid cell, integrating the solar cell with the triboelectric device, was designed by constructing an organic solar cell under a single-electrode triboelectric nanogenerator. The hybrid cell could convert both solar and mechanical energies into electricity independently and simultaneously. Such devices are potentially able to supply electricity day and night. Nanomaterials offer novel approaches for enhancing the efficiency of harvesting solar and mechanical energy in a hybrid device.

Table of Contents

List of Abbreviations

0D	Zero-dimensional
1D	One-dimensional
2D	Two-dimensional
3D	Three-dimensional
AF	Areal fraction
AF_{BOT}	Areal fraction in bottom electrode
AF_{TOP}	Areal fraction in top electrode
AFM	Atomic force microscope
AgNW	Silver nanowire
AM	Air mass factor
ATR	Attenuated total reflectance
BHJ	Bulky heterojunction
CB	Conduction band
CBD	Chemical bath deposition
CIGS	Copper/indium/gallium/selenide
CIS	Cadmium/indium/selenide
DMF	Dimethylformamide
DSSC	Dye sensitised solar cell
E_{bg}.	Band gap energy
EG	Ethylene glycol
EPD	Electrophoretic deposition
EQE	External quantum efficiency
FEP	Fluorinated ethylene propylene
FF	Fill factor

FTIR	Fourier transform infrared spectrometer
FTO	Fluorine-doped tin oxide
FWHM	Full width of half maximum
HHSs	Hollow hemispheres
HMT	Hexamethylenetetramine
HOMO	Highest occupied molecular orbital
HPPS	Hydrolysis precipitation phase separation
$IC_{60}BA$	1',1",4',4"-Tetrahydro-di[1,4methanonaphthaleno[1,2:2',3',56,60:2",3"][5,6]fullerene-C60,C60 derivative or Indene-C60 bisdduct
ITO	Indium tin oxide
J_{sc}	Short circuit current
kWh	Kilowatt hour
LCAO-MO	Linear combination of atomic orbital
LCCT	Ligand-centred charge transfer
LED	Light-emitting diode
LSM	Sr-doped LaMnO3
MDMO-PPV	Poly(2-methoxy-5-(3,7, dimentyloctyloxy)-1,4-phenylenevinylene
MLCT	Metal-to-ligand charge transfer
η	Photoenergy conversion percentage
NHE	Normal hydrogen electrode
Ni-CSZ	Platinum (Pt)-coated-nickel (Ni) -calcium oxide (CaO)-stablised zirconium dioxide (ZrO_2)

NM	Nitromethane
OSC	Organic solar cell
P3HT:$IC_{60}BA$	Poly(3-hexylthiophene) : indene-C60 bis-adduct
PCBM	Phenyl-C61-butyric acid methyl ester
PDMS	Polydimethylsiloxane
PEC	Photoelectrochemical
PEDOT:PSS	Poly(3,4-ethylenedioxythiophene): Poly(styrenesulfonate)
PEG	Polyenethylene glycol
PEI	Polyethylenimine
PI	Polyimide
PLA	Polyactic acid
PMII	1-methyl-3-n-propylimidazolium iodide
PMMA	Poly (methyl methacrylate)
Power XRD	X-ray powder diffractometer
PPy	Polypyrrole
PVA	Polyvinyl alcohol
PVDF	Polyvinyldene fluoride
PVP	Polyvinyl pyrrolidone
R_s	Sheet resistance
SOFC	Solid oxide fuel cell
STENG	Single-electrode triboelectric nanogenerator
STM	Scanning tuning microscope
TBP	4-tert-butylpyridine
TCO	Transparent conductive oxides

TENG	Triboelectric nanogenerator
T-TENG	Transparent TENG
TIRFM	Total internal reflection fluorescence microscope
TTIP	Titanium isopropoxide
tWh	Terawatt hour
u_e	Electrophoretic mobility
UV	Ultraviolet
VB	Valence band
V_{oc}	Open circuit voltage
VS	Vapour solid
W	Watt
YSZ	Yttria stabilized zirconia
λ	Light wavelength
Φ	Photon flux

List of Figures

List of Tables

List of Publications

1. Y. Fang, J. Tong, Q. Zhong, Q. Chen. J. Zhou, Q. Lou*, Y. Zhou*, Z.L. Wang. B. Hu*. Nano Energy, 2015, 16, 301-309.
2. Y. Fang, W. C. Lee, G. E. Canciani, T. C. Draper, Z. F .Al-Bawi, J. S. Bedi, C. C. Perry, Q. Chen*. Material Science and Engineering B, 2015, 202, 39-45
3. W. C. Lee, Y. Fang*, J. F. C. Turner, J. S. Bedi, C. C. Perry, H. He, R. Qian, Q. Chen*. Sensor and Actuators B: Chemical, 2016, 273, 724-732.
4. W. C. Lee, Y. Fang, R. Kler, G. E. Canciani, T. C. Draper, Z. F. Al-Bawi, S. M. Alfadul, C. C. Perry, Q. Chen*. Materials Chemistry and Physics, 2015, 149-150, 12-16.
5. H. Xia, Q. Chen, Y. Fang, D. Liu, D. Zhong, H. Wu, Y. Xia, Y. Yan, W. Tang, X. Sun*. Brain Research, 2014, 1565, 18-27.
6. J. S. Bedi, D. W. Lester, Y. Fang, J. F. C .Turner, J. Zhou, S. M. Alfadul, C. C. Perry, Q. Chen*. Journal of Polymer Engineering, 2012, 33(5), 453-461.

Chapter 1 Introduction

1.1 Meeting the energy challenges

Energy is a vital commodity to make modern life possible.[1] It is essential for agricultural, industrial and domestic activities in human society. Currently, the majority energy sources are still based on fossil fuels. The historical global fossil fuels consumption since 1965 is presented in Figure 1.1a.[2] A rapid increase of energy consumption is observed with a growing rate of 200 million tonnes of oil equivalent annually.

Major fossil fuels are in the forms of oil, coal and natural gas, as seen in Figure 1.1b.[2] However, the limited availability of fossil fuels, as well as their negative environmental impact, raises a realistic alarm for future energy security. The US Central Intelligence Agency predicted that the reserve oil would be completely run out by the year 2052 even without any consideration of the growing population and aspirations.[3] Moreover, some critical environmental damages associated with fossil fuels were also observed. The increased emission of atmospheric particulate matter and greenhouse gases is directly linked to the increasing combustion of fossil fuels. The particulate pollution also poses a serious threat to the public health.[4] The greenhouse gases were considered as the most significant factor causing global warming with a temperature increase over 1.02 ℃ in 2015.[5, 6] Such rapid, persistent temperature rising is shown in Figure 1.1c,[5, 6] which is directly correlated with the CO_2 emission as seen in Figure 1.1d.[7] Therefore, finding alternative reliable energy sources with less environmental impact is critical for slowing down of global warming, and is necessary for the sustainability of future living environment. Nuclear power is the one considered as the alternative energy source due to its extremely high energy density. By 2013, 437

operational nuclear power reactors were running in 31 countries, provide about 13% electricity around the world.[8] However, the high cost of constructing and maintaining a nuclear plant and the challenge of safely handling the high-risk radiation and nuclear waste limit the development of the nuclear power stations.

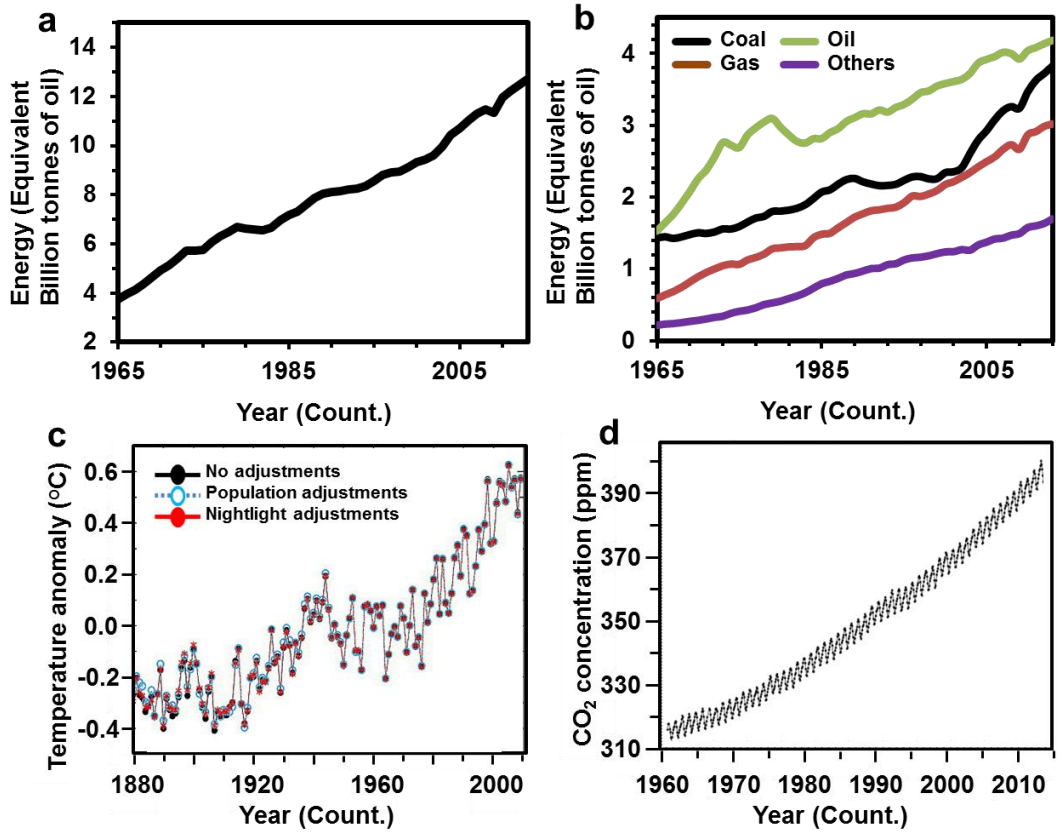

Figure 1.1 The historical energy consumption, temperature change and the CO_2 emission around the world. (a) The total energy consumption.[2] (b) The consumption of fossil fuels.[2] (c) The global temperature change,[5, 6] and (d) CO_2 emissions.[7]

Green energy can be replenished constantly from natural processes. It can be used as long-term energy supply with minimised negative impacts on global environment. Variety of renewable energy sources exist around us, such as solar power, wind power, hydroelectricity and biomass energy. The quantity of the available renewable energy, in

principle, is sufficient to replace fossil fuels. Currently, total global electricity consumption is about 2.5×10^{13} kWh, within which, 11% is from nuclear power.[9] For replacing this energy with solar energy, assuming the solar-electricity conversion efficiency is 100% with 8 hours solar illumination, it requires a solar panel area of 3.6×10^{12} m^2, or 3.6 million km^2. This area corresponds to 1/3 of the Sahara desert area. With current achievable conversion efficiency of 16%, an area of twice that of the Sahara desert will be required for the global energy supply. The European Union plans to reach a target of 27% of energy consumption from renewable energy by 2030.[10] However, the costs of current renewable technologies are still too high to compete with conventional energy sources, and the energy conversion efficiency of harvesting solar energy is still too low. Such challenges can only be overcome by developing new materials and new energy devices.

1.2 Review of renewable energy technologies

Numerous approaches can be used to harvest renewable energy. Some of them have already been successfully commercialised with some government incentive subsidies. Such technologies were reviewed and compared to establish the bench mark of current renewable technologies. Commercialised technologies are currently targeting the harvesting of different renewable energies, including biofuels, mechanical and solar energy.

1.2.1 The use of biomass energy

Biomass is the organic matter derived from plants, animals or wastes. High energy-density plants, like corn, have been mass planted in order to obtain ethanol as fuel. In such cases, the biomass is generated by harvesting solar energy through natural photosynthesis processes. The ethanol can be stored as an energy source and used in

internal combustion engines or chemical fuel cells to generate electricity. Biomass is a truly renewable energy, as it only uses sunlight as the energy source. It reduces the carbon footprint by utilising the CO_2 in the atmosphere. However, as the rate of the photosynthesis process is normally slow and less energy efficient,[11] large areas of farm land are required in order to generate sufficient biomass energy, which could dramatically affect global food supply.

Alternatively, biomass energy can also be generated by recycling residual energy in waste through an anaerobic digestion process.[12] In the process, natural gas (methane) is evolved through the breaking down of biodegradable material by micro-organisms, and used as fuel in the energy grid, although the quantity of such fuel is very limited.

1.2.2 Harvesting mechanical energy

Mechanical energy is the sum of potential and kinetic energy. Wind energy and hydropower are the most important environmental mechanical energy. Currently, they contribute a significant portion to the global energy supply. Wind is the movement of atmospheric air masses, induced by the variation of atmospheric pressure and temperature. Hydropower is the mechanical energy of water moving, which is caused by gravity. Conventional electrical generators can be easily adapted to convert this kind of mechanical energy into electricity with high efficiency. Although a large amount of wind energy is available, it is highly dependent on the atmospheric conditions, and cannot be managed by human effort. Therefore, the electrical energy output through harvesting wind energy is not reliable, unless a large bank of batteries is used as buffer for the energy storage and regulator. This strategy will significantly increase the cost of the project. Meanwhile, the noise pollution caused from each wind turbine in the area of a 350 m radius is larger than 45 decibel (dB), which cannot be tolerated by most living animals.[13]

Hydroelectricity provides one sixth of the annual electrical output around the world, forming the largest part of the renewable energy supplies.[2] In comparison with the wind energy, the output of hydroelectricity is flexible, because the constructed reservoir is capable of storing the water and regulates the electricity. The economic issue has less concerns, because of a good reliability of the water source for hydropower. However, the environmental and ecological impacts associated with hydroelectricity are still crucial. An installation of the hydroelectric power system involves rearranging the aqua resource, which could damage the surrounding fragile eco-system.

1.2.3 Current solar energy harvesting technologies

Solar radiation is primarily caused by the nuclear fusion at the core of the Sun. The solar energy transmits to the Earth in the form of electromagnetic waves (sunlight). Enormous solar energy is constantly bathing the Earth. When the Sun is overhead, about 865 W of solar energy can reach a 1 m^2 of the Earth surface.[14] The total solar energy radiated on the Earth is about 8000 times in respect to the current global energy consumption.[13] Therefore, using solar energy to replace fossil fuels is realistic with minimised impacts on global environment.

Generally, two ways were mainly used to harvest solar energy: solar thermal energy and photovoltaics/solar cells. In general, solar energy is thermally collected within three routes: active solar heating, passive solar heating and solar thermal engines.[15] The rooftop solar water-heating panel is a typical example to harvest active solar heating, about 35 km^2 of heating panel has already been installed in Europe to supply hot water by 2010. In the UK, such systems could provide over 1100 kilowatt hour (kWh) annually, which would contribute 40% of hot water for households.[16] The passive solar heating is normally embedded in the buildings, which are designed to

absorb and store solar thermal energy that can be released at night. Such designs could reduce the household energy consumption. The solar thermal engine is a complex setup. It employs parabolic mirrors to concentrate the light radiation, which produces extremely high temperature to heat the water. The formed steam is then used to drive turbines for generating electricity. However, the efficiency is very low, to my knowledge, the maximum conversion efficiency is only around 15%.[15] Meanwhile large land area is required to accommodate the mirrors, and limits the land use for agriculture purposes.

Using solar cells to harvest solar energy directly into electrical power is an ideal approach. Monocrystalline silicon (Si) based solar cells are the most efficient commercialised solar panels. The photoconversion efficiencies of the Si solar cells are between 12 % and 16%, depending on the quality of the Si crystal. The major problem is the high cost to manufacture and its environmental impact during the production, which sets the current unit price over 24 pence/kWh. Development of new materials with lower cost and less environmentally hazardous could significantly reduce the cost and improve the competitiveness against conventional energy sources.

1.2.4 Improving the renewable energy harvesting

Among the renewable energy harvesting technologies, the hydroelectric plant is the most effective approach. Therefore, it is widely constructed around the world for local energy supply. For instance, the Three Gorges Dam in China is capable of generating 98.8 terawatt hour (TWh) annually.[17] However, using hydroelectric is still more expensive than non-renewable sources, while solar energy is the most expensive form of renewable energies. Therefore, in order to offer long term, commercially viable energy solution, it is essential to improve the technologies for harvesting mechanical and solar energies.

Over the past two decades, nanomaterials were widely developed for renewable energy harvesting devices with improved performances. Nanotechnology opens new opportunities to create new materials with new nanostructures and properties. Nanostructured materials present surface areas significantly larger than that of bulk materials. Materials with nanometre dimension may also have significant effects on the optoelectronic properties. For instance, when the size of the material is sufficiently small, the quantum confinement effect could limit the electron mean free path.[18] This phenomenon could sufficiently reduce the electron collision, reducing energy loss in transportation, but could also increase the charge recombination probability. On the optical side, periodic nanostructures of semiconductor materials can also manipulate their light reflection and refraction with effects like optical confinement[19] and photonic localisation.[20] These unique properties of nanomaterials benefit its applications in solar energy harvesting. The details of the benefits and the fundamental principle of energy harvesting and conversion will be discussed in the following sections (1.3 and 1.4).

1.3 Applications for harvesting solar energy

In this research, photovoltaics and photoelectrochemical water splitting were developed for harvesting solar energy. In order to improve the photoconversion efficiency, it is essential to understand the physics and chemistry of the semiconductor nanomaterials, as well as the working mechanism of these applications.

1.3.1 Fundamentals of the semiconductors

A semiconductor generally has fairly low electrical conductivity compared to typical metals, with band gap energy less than 4 eV. As a solid material, the physical and chemical properties of a semiconductor are determined by the distribution of the electrons in the continuum of electronic states, defined as the band structure. Here, the

fundamental of the band structure for a solid material will be discussed, using a linear combination of atomic orbitals (LCAO-MOs) as a one-dimensional model.

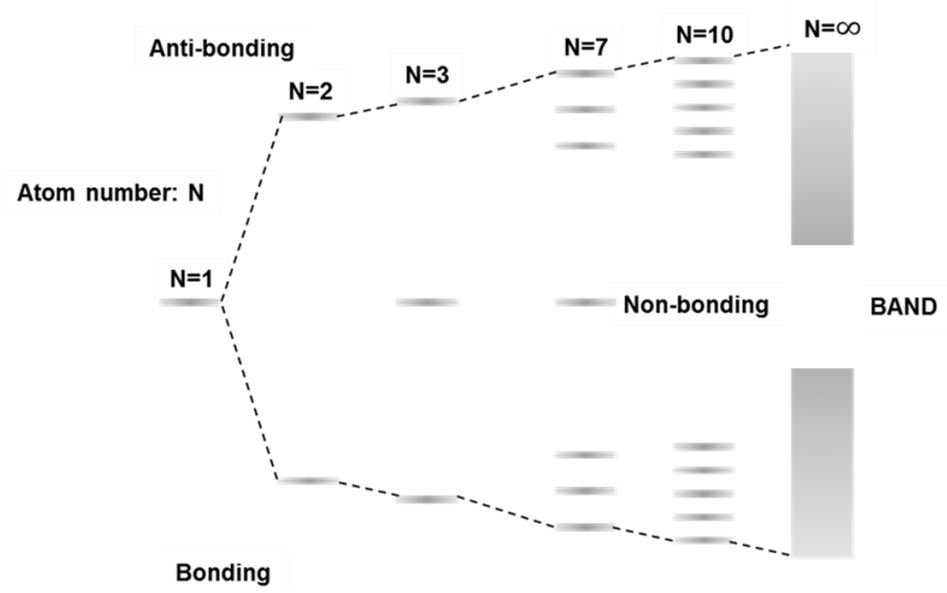

Figure 1.2 The overlap of s orbitals gives rise to an s band. Atoms are arranged in a line, forming bonding and anti-bonding orbitals with separated electronic band structures.

This model is based on a single, infinitely long chain of atoms bonded together. As shown in Figure 1.2, the LCAO-MO theory can be used to construct the electronic states of a linear chain of atoms. For a diatomic system (N=2), the *s* orbitals from both atoms will form a bonding and an anti-bonding orbital, separated in energy space. The separation energy corresponds to the energy requirement for an electronic transition from the ground state to the first excited state. With increasing number of atoms in the chain, a continuum band structure will be formed as many electronic states with a small energy difference are spread in a band. With a similar principle, *p* orbitals can also form their band structure. As the energy of the *p* orbital is normally higher than the *s* orbital, the bands formed from the *p* orbital are higher than the *s* orbital bands. However, in

some cases, the *p* bonding band might overlap with the *s* antibonding bands, depending on the degree of atomic orbital interaction and the nuclear charge.

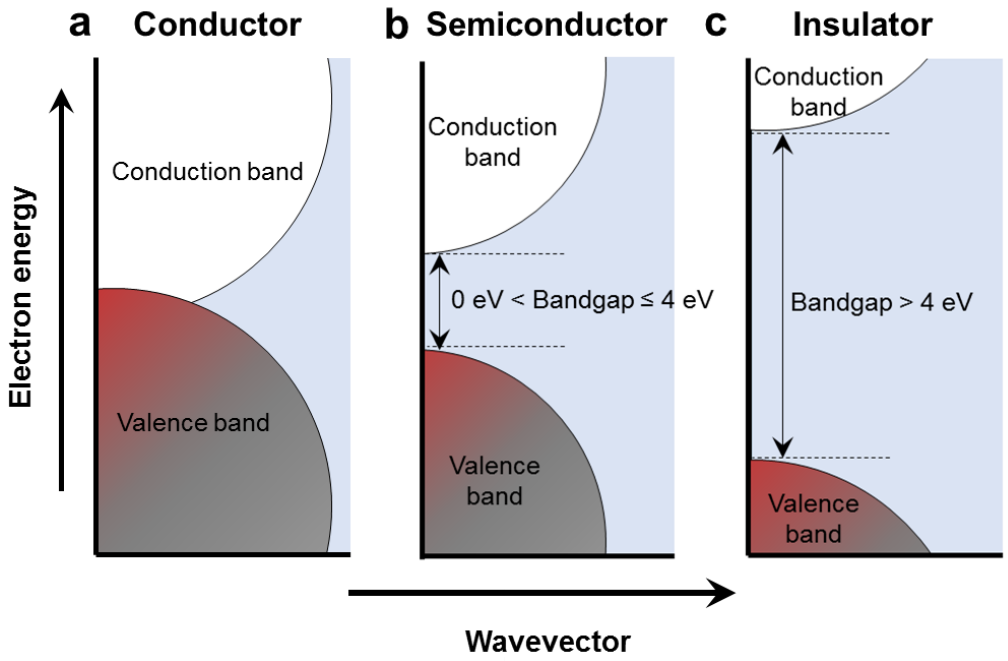

Figure 1.3 Schematic diagram of the band gaps of solid-state material, (a) conductor, (b) semiconductor and (c) insulator. The VB is filled with valence electrons and the CB is empty.

The electronic properties of a solid material can be deduced from its band structure. The electrons fill the lowest band of electronic states and leave the upper level empty. The filled band is defined as the valence band (VB) while the empty band is defined as the conduction band (CB). This is because that the VB is filled with valence electrons, which are responsible for the bonding between atoms within the solid. Any electrons in the conduction band are surrounded by empty states, which allow them to move freely, contributing to the conductivity of the materials. The energy difference between the minimum of the CB and maximum of the VB is defined as the bandgap,

E_{bg}. Figure 1.3 shows schematic diagrams of three typical band gaps of solid materials. The band gap structure of a conductor is shown in Figure 1.3a, where the VB and the CB are overlapped with the effective E_{bg} = 0 eV. It costs little energy for an electron to be excited to the CB to be mobile. The band gap structure of the semiconductor is shown in Figure 1.3b. The electrons stay in the fully occupied VB. The energy gap between the VB and the CB exists, but ≤ 4.0 eV, which allows most of the electrons to be excited by absorbing energy equal or large than 4.0 eV. Consequently, when electrons are promoted to the CB, positively charged 'holes' (charge-carriers) are left in the VB. Both excited electrons and holes are mobile to give conductivity. Due to the thermal excitation, the conductivity of a semiconductor increases when the temperature increases, since more electrons can be excited at a higher temperature. When the band gap is too large (>4.0 eV), shown in Figure 1.3c, the electrons in the VB are almost impossible to excite to reach the CB under normal conditions, therefore, the material is classified as an electrical insulator.

Semiconductors can be classified as *p*- or *n*-type, depending on the position of the Fermi level and the polarity of the majority charge carriers. For a *p*-type semiconductor, the Fermi level is close to the maximum of the VB and the majority of charge carriers are holes. For an *n*-type semiconductor, the Fermi level is close to the minimum of the CB and majority of the charge carriers are electrons. A *p*-type semiconductor can be created if an intrinsic group IV semiconductor, such as silicon (Si) is doped with a boron (B) atom. As shown in Figure 1.4a, the acceptor impurities create holes due to the lack of electrons in the B atom. This doping moves the intrinsic Fermi level downwards closer to the VB maximum. On the other hand, if dopants carry extra electrons, an *n*-type semiconductor can be formed by doping. As shown in Figure 1.4b, when an antimony (Sb) atom is doped into Si, the Sb is able to contribute an additional free

electron. This doping could shift the Fermi level up towards the CB. The created electrons near the Fermi level can be excited to the CB with less energy.

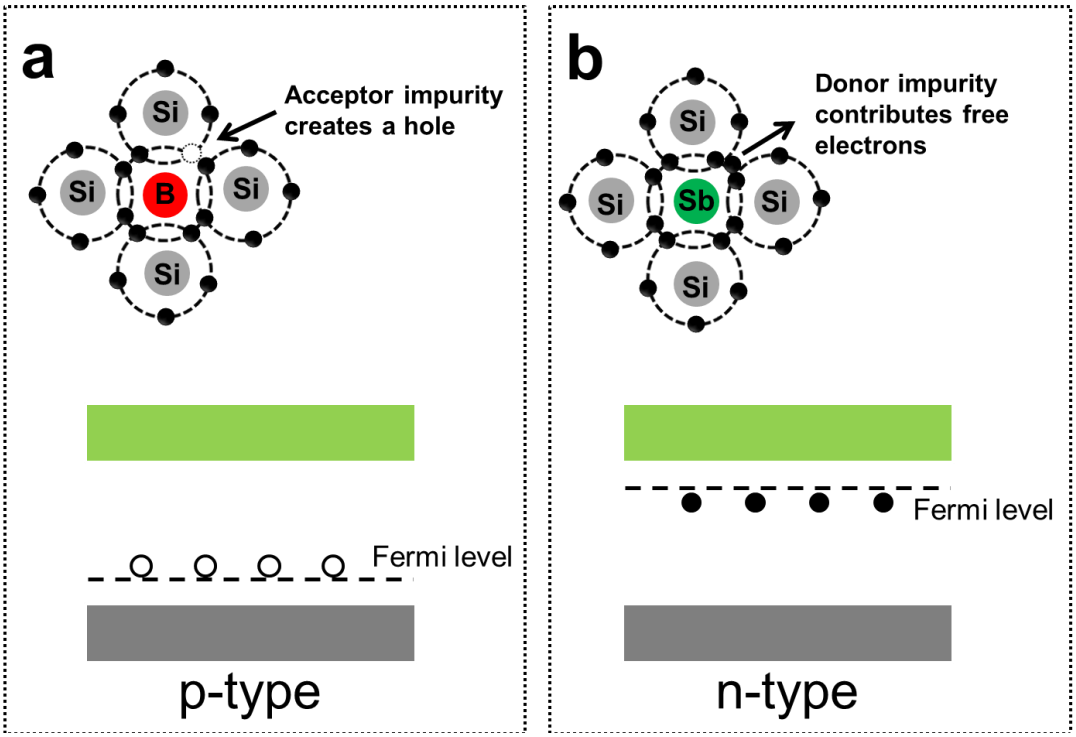

Figure 1.4 The electronic structures and band gap of (a) a *p*-type and (b) an n-type doped Si semiconductor. The Si is doped with either a boron atom as an acceptor to create a hole or an antimony atom as a donor to contribute a free electron.

An important example of doped *p*-type semiconductor is indium-doped tin oxide (ITO). Extra holes are created near the Fermi level by the dopants (indium atoms), which allow the excited electrons from VB. ITO was developed as the most important optical transparent oxide conductor. With a careful control of the concentration of the dopants, it is possible to create enough 'holes' to carry charges with low sheet resistance (<10 Ω/sq) and optical transparency (>90%).[21] A broad range of applications were developed based on the conductivity of ITO, such as optoelectronics and solar cells.[22]

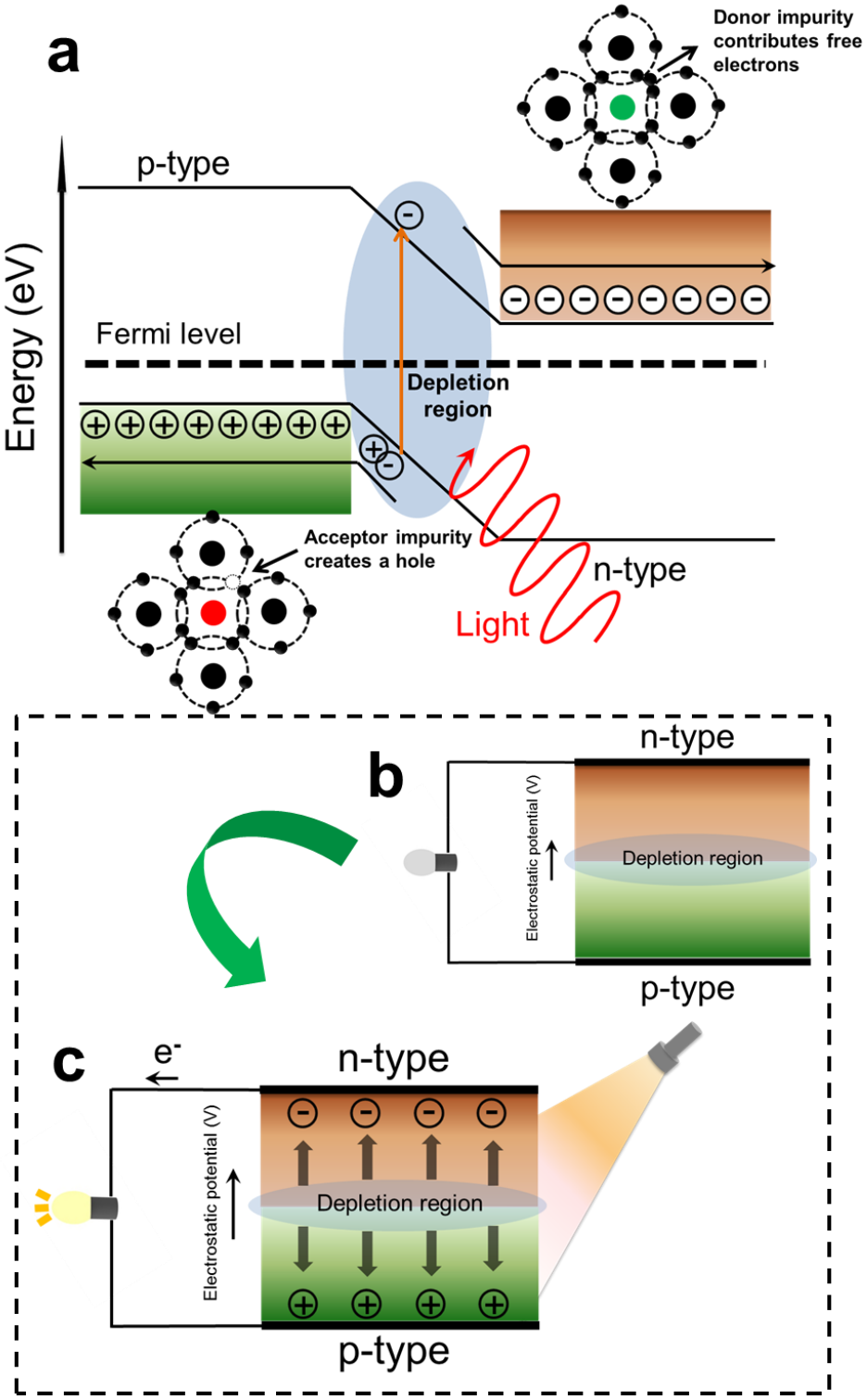

Figure 1.5 (a) The formation of a *p-n* junction, and the flow of electrons and holes in the depletion region under the light irradiation. (b) The formation of the depletion region, and (c) the working mechanism of *p-n* junction solar cells.

A *p*-*n* junction can be formed at the interface between *p*- and *n*-type semiconductors. As displayed in Figure 1.5a, due to the alignment of the Fermi level, the bands have to be bent at the interfaces. The valence electrons in the *n*-type semiconductor will diffuse across the junction to the *p*-type semiconductor, and thus eliminate the holes. This will create a region at the interface, in which the mobile charge carriers are depleted, and this region is illustrated in Figure 1.5a, defined as the depletion region. In the meantime, an electrostatic field is formed across the depletion zone, since the *n*-type is slightly positively charged, while the *p*-type is slightly negatively charged. Applying a positive voltage on the *n*-type semiconductor (reverse bias) could widen the depletion region, which will restrict the current flow from the *n*-type to *p*-type semiconductor. If a positive voltage is applied on the *p*-type semiconductor (forward bias), the depletion layer will be narrowed, which allows current flow. When light irradiates at the *p*-*n* junction, both *p*- and *n*-type semiconductors are excited to form excitons, which are pairs of electron and hole in an excited state. When the excitons diffuse into the depletion region, they will be separated to form electrons and holes due to the electrostatic field. The electrons will travel to the CB of the *n*-type semiconductor, while the holes will travel to the VB of the *p*-type semiconductor, shown in Figure 1.5a. This mechanism is essential to develop thin film solar cells, as illustrated in Figure 1.5b and 1.5c. The voltage difference between the CB of the *n*-type semiconductor and the VB of the *p*-type semiconductor determines the maximum output voltage (open circuit voltage) of the *p*-*n* junction solar cell, while the output current is determined by the effective *p*-*n* junction interface area and light absorption efficiency.

1.3.2 First and second generation solar cells

First and second generation solar cells were based on the principle of the *p*-*n*

junction. First generation solar cells mainly used monocrystalline Si as basis, which were doped to form *p*- and *n*-type semiconductors. Because Si mineral is one of the most abundant natural sources available on the Earth, Si-based solar cells are still dominant in the photovoltaic market. Although monocrystalline Si solar cells give a high photoconversion efficiency so far, they are very expensive to manufacture.[23] The requirement of high quality crystallinity restricts the application of first generation solar cells to the fields of military, satellite and spacecraft.

Second generation solar cells are based on thin-film technologies to produce polycrystalline semiconductors. A lot of materials were developed for this type of solar cell, such as polycrystalline Si, cadmium/indium/selenide (CIS) and copper/indium/gallium/selenide (CIGS). Thin film solar cells can be fabricated with the low cost chemical/physical vapour deposition (CVD/PVD) and spray pyrolysis techniques with a capability of mass production. Such fabrication techniques are simpler and more efficient than that for first generation solar cells. Second generation solar cells also present excellent photoconversion efficiencies. For instance, a CdTe thin film solar cell achieved the maximum efficiency of 21.7%.[24] Unfortunately, the manufacture of the raw materials (precursors) had a significant impact on the environment with large energy consumption, and some devices suffered from limited stability.[24]

To overcome those problems, dye sensitised solar cells (DSSCs)[25] and organic solar cells (OSCs)[26] were emerged as third generation solar cells. Low-cost metal oxides were used for DSSCs, and inexpensive organic semiconductors were the main materials for OSCs. Also, PEC water splitting systems were developed to convert solar energy to a green chemical energy in the form of H_2.[27]

1.3.3 The dye sensitised solar cell

The DSSC was originally co-invented in 1988 by Brain O`Regan and Michael

Gratzel.[28] It is an ‘artificial photosynthesis’ structure by sandwiching electrolyte solution and a dye-sensitised metal oxide thin film between two conducting glasses. DSSCs present many advantages with respect to the first and the second generation solar cells. They can be fabricated using the conventional printing and spraying technology. The cells can be semi-transparent, which allows them to be used as a coloured glass, as well as to generate electricity. More importantly, the key components of the cell, metal oxide thin film and sensitising dyes, can be optimised individually. Nanostructured metal oxides can be used to maximise surface area, while the electronic structure of the dye determines the wavelength of the absorbed light. Currently, developing and improving this type of solar cell still attracts a lot of attention.

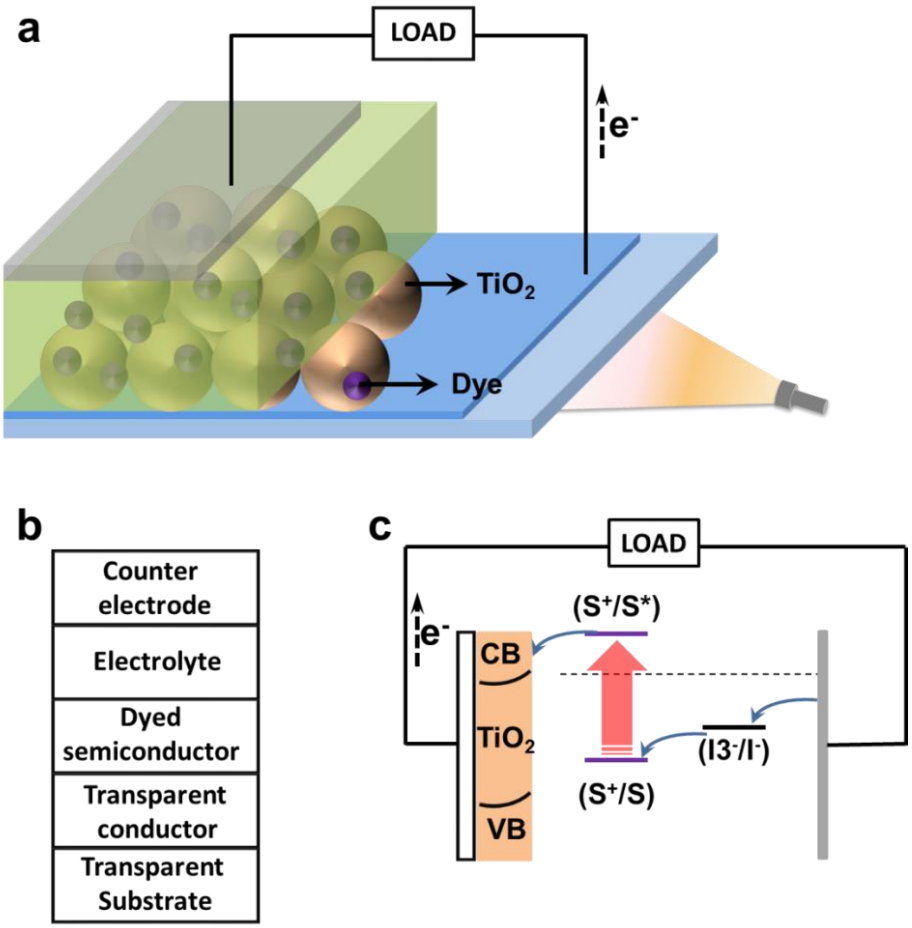

Figure 1.6 A design and working mechanism of a DSSC. (a) A typical structure of the DSSC. (b) The schematic illustration of the DSSC. (c) The band gap of the functional layers, and the electron migration in the DSSC.

The working mechanism of a DSSC is shown in Figure 1.6. Generally, a nanostructured titanium dioxide (TiO_2) thin film was used as the base of a DSSC, shown in Figure 1.6a and 1.6b. The TiO_2 film is dyed with an inorganic/organic complex (ruthenium dye (Ru) is used as an example here), which has the suitable electronic states to absorb visible light for electron migration to the TiO_2, as shown in Figure 1.6c. Here, (S^+/S^*) and (S^+/S) is the excited-state and ground-state oxidation potential of Ru dye. In this case, when the DSSC is illuminated, the electron in the occupied states of the dye will be excited first into unoccupied states, which will inject

into the CB of the TiO_2 subsequently, since the energy level of the CB in the TiO_2 is lower than the unoccupied states of dye. The electron continues to move toward the lower potential counter electrode through an external circuit, forming electric current. Between the photoanode and the counter cathode, the electrolyte solution acts as 'vehicle' to transfer charges through the solvent by ions. Iodine/iodide (I_3^-/I^-) ions were usually used as the electrolyte. The oxidised dye acquires electrons from the I^- in solution, and the I_3^- obtained the electrons from the injection of the cathode.

The dye sensitiser is one of the critical components in a DSSC to determine the photoconversion efficiency. The light absorption of a DSSC is directly influenced by the properties of the sensitiser. A few chemical structures of the dyes are shown in Figure 1.7. The most popular dye is the Ru inorganic complex. This dye is stable, and offers a high photoconversion efficiency.[29] Recently, many metal-free dyes were also developed as sensitisers for DSSCs,[30] such as C219, WS9 and RK1. In the search for a good organic dye for DSSC, a donor moiety and an acceptor moiety should be connected by a π-conjugated structure, which allows an efficient electron migration. The donor moiety usually has a strong light absorption in the visible region. The acceptor moiety is capable of strongly binding with the semiconductor base, which allows the excited electrons to inject into the base metal oxide. From the example of the C219 dye, the donor group of 3,4-ethylenedioxythiophene (EDOT) gives a broad spectral response.[31] The dithienosilole (DTS) structure acts as an efficient π-conjugated linker connected with a carboxylic group, acting as an anchor to bind to the metal oxide. When the DSSC was sensitised using C219, a remarkable photoconversion (10.2%) performance was achieved.[31] When the WS9 dye was used to sensitise a DSSC, a high photocurrent was obtained (18 mA/cm^2)[32] due to an improved binding between the dye and the semiconductor film with respect to the Ru dye. When the RK1 dye was tested,

the cell showed a fairly long working life without any measurable degradation after 2200 hours of the light soaking.[33] This result offers the potential to commercialise DSSCs for a long-term energy supply. Furthermore, because the noble metal is eliminated, the cost of the dyes was significantly reduced.

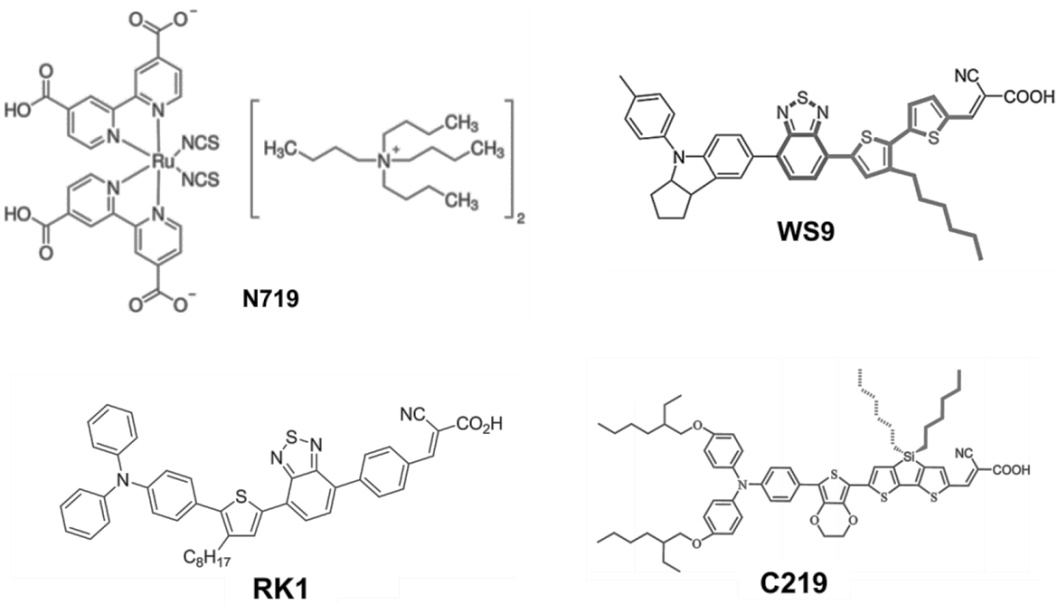

Figure 1.7 The chemical structures of Ru based and three metal-free dyes for DSSCs. N719 is a general ruthenium dye, WS9, RK1 and C219 are organic dyes.

The structure of the semiconductor film is also important for solar cells. Over the past two decades, varieties of the nanostructured materials were synthesised. The structures mainly include nanoparticles, nanowires, nanotubes and particle aggregates. Nanoparticles have an advantage of providing a large surface area for dye absorption, which subsequently increases the light absorption. However, this kind of thin film has a high interfacial charge recombination rate, which occurs between the photogenerated electrons and the oxidised species in the electrolyte. Poor electrical connectivity between nanoparticles increases the internal resistance and restricts the electrons travelling to through the internal structures. To overcome such problems, one-

dimensional (1D) nanostructures were used for DSSCs, such as vertically aligned nanorod and nanotube array structures. They are able to provide direct pathways for electron transport from the interfacial reaction centres to the electrode.[28] However, in comparison with the 0D nanomaterials, the density of the interfacial reaction centres are decreased, since the overall surface area is reduced. Metal oxides aggregates were also developed for DSSCs, and are typically assembled with nanoparticles to form submicron-size spheres. Employing such an aggregated structure of TiO_2, a breakthrough of the DSSC photoconversion efficiency (around 12%) was made.[4] This is because the aggregates could provide a large surface area (112 m^2/g). More importantly, it also presented an efficient electron pathway due to the formation of the single-crystal-like anatase framework,[4] which significantly reduced the charge recombination rate.

1.3.4 The organic solar cell

The concept of an organic solar cell (OSC) was first realised by the observation of the photovoltaic effect from organic materials.[34] In 1986, the first OSC was created using donor-acceptor heterojunctions, based on *p*- and *n*-type organic semiconductors.[35] Following that, the photoconversion efficiency of OSCs was significantly improved by an introduction of a inter-mixing of a donor-acceptor structure in a single layer, which is defined as the bulk heterojunction (BHJ) active layer.[36] For an ideal BHJ system, nanostructured materials should be used in order to improve the charge generation. Also, the BHJ domains should sufficiently overlapped to allow percolation of exciton charge carriers to the electrodes.

To date, OSCs still attract a lot of attention,[37] because some advantages can be observed with respect to inorganic solar cells. They can be manufactured by a cost-effective roll-to-roll method to coat organic films on a flexible electrode. Since the organic film is generally very thin (a few tens of nanometres), the overall thickness of

an OSC can be easily controlled by adjusting the thickness of the electrode. The flexibility of OSCs extends their potential applications to integrate with modern wearable electronics. OSCs also show excellent photoconversion efficiencies, the maximum recorded is about 11.5% in 2015,[38] which is similar to the best DSSC.

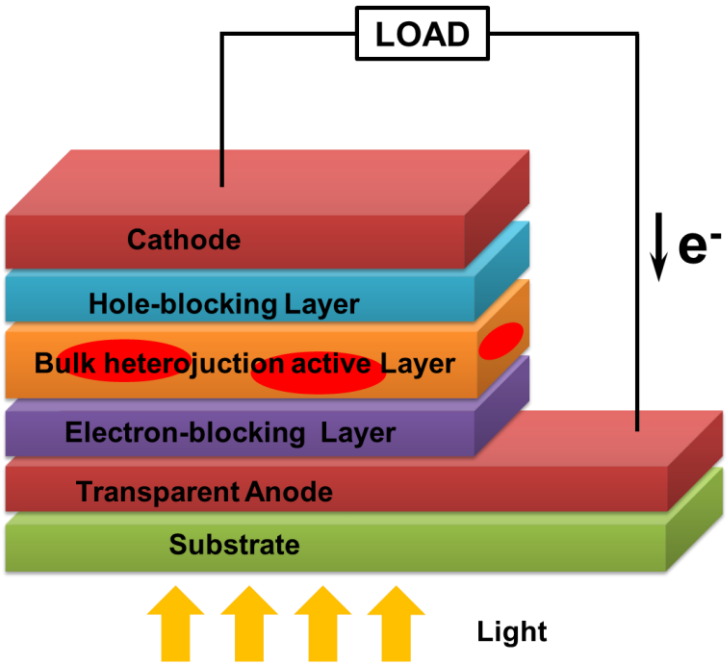

Figure 1.8 Schematic illustrations of organic solar cell components. BHJ layer is functional to absorb light. The hole-blocking and electron blocking layer could dissociate the excitons to form free electrons and holes, respectively. The substrate should be carefully designed to ensure the flexibility and transparency of OSCs. It is usually transparent plastic.

A typical structure of an OSC is shown in Figure 1.8. The working mechanism is similar to a *p*-*n* junction solar cell. Light is absorbed by the BHJ active layer. In an OSC, when light irradiates the BJH layer, excitons are formed. The excitons are preferentially formed in OSCs, due to strong Coulomb forces between the excited electrons and holes.[39] Therefore, both the electron-blocking layer and the hole-blocking

layer are used to dissociate the excitons to form free electrons and holes, respectively. Then, an electrical potential is formed between the cathode and anode to generate electrical current. In order to take the advantage of the flexibility of organic thin film, transparent plastic films were normally used as the flexible substrates for flexible OSC solar cells.[38]

In OSCs, the BHJ active layer is the most important composite, determining efficiencies of the light absorption and energy conversion. Morphology of the BHJ layer is significantly affected by the solvent. Li et al. [40] proposed a temperature controlled annealing method to improve the morphology of the film. By controlling the polymer solidifying rate, the polymer chains are able to self-organise into domains. The process resulted in a well-arranged BHJ layer with an enhanced photoconversion efficiency.[40] Controlling the ratio of the donor and acceptor materials in the BHJ layer is also important to determine the morphology. Van Duren et al. investigated the nanoscale morphology of the (poly[2-methoxy-5-(3',7'-dimethyloctyloxy)-1,4-phenylenevinylene]):phenyl-C61-butyric acid methyl ester (MDMO-PPV:PCBM) as a function of the blend ratio.[41] When the concentrations of the PCBM were in the range of from 50% to 60%, a fairly homogenous film was observed by atomic force microscopy (AFM). If the PCBM was increased to between 60 and 67.5%, a phase separation was observed. The phase separation leads to enhance electron transport and reduce bimolecular charge recombination, resulting in an increased photoconversion efficiency.

In order to improve the mechanical stability and flexibility of the device, conductive carbon materials and metal nanowires were developed as alternative transparent conductive materials for the solar cell electrodes. Traditionally, transparent conductive oxides (TCO), such as ITO, were used as electrodes, due to its high conductivity and transparency. However, metal oxides are brittle, which restricts the

flexible applications of OSCs. The conductive carbon materials, including carbon nanotube, carbon nanofibre and graphene, have been investigated as flexible electrode materials, although large resistance exists at junctions of this kind of materials. Welding or bonding of the carbon junctions remains a challenge. In comparison to the carbon conductor, metal nanowire percolation networks present a similar optical transparency and flexibility. Moreover, they show excellent electrical conductivity, since the junctions of the metal nanowires can be easily welded by thermal annealing. The development of these flexible conductors offers an opportunity to fabricate a truly flexible energy harvesting device.

1.3.5 Photoelectrochemical water splitting

Photoelectrochemical (PEC) water splitting was first demonstrated by Fujishima and Honda in 1972.[27] They used bulk TiO_2 as a photoanode to split water to form H_2 by absorbing solar energy. The simple chemical form of H_2 is a zero carbon emission green fuel, since water is the only product after combustion of H_2. Moreover, H_2 has a very high energy density (around 120 MJ/kg), about 3 times of petrol (44 MJ/kg).[42] Although, H_2 risks ignition in air, so there are safety challenges for its use, storage and transport. Overall, photogenerated H_2 is still considered as a potential replacement of the fossil fuels.

In principle, the setup of the PEC system is similar to DSSC. The anode and cathode in the PEC system are separated, and they directly contact with the aqueous electrolyte, such a setup avoids a complicated fabricating process. In the PEC water splitting, an electron in the VB of a photoelectrode is excited to the CB by solar energy, leaving a hole in the VB. The separated electron and hole move to the cathode and the anode to react with water, evolving hydrogen and oxygen gas, respectively. The major difference between PEC water splitting and solar cells is the choice of electrolyte. For

solar cells, a reversible redox couple of I_3^-/I^- in an organic solvent (*e.g.* acetonitrile) is used as electrolyte. The reversible redox couple helps to reduce the internal potential drop, and the non-aqueous solvent is used to avoid the evolving of the gases (H_2 and O_2). For PEC water splitting, the electrolyte is simplified to an aqueous solution of salts, which reduces the internal ionic resistance.

The capability of semiconductor materials to split water using solar energy is determined by the E_{bg} and the band-edge positions. The molar Gibbs free energy change (ΔG) to decompose H_2O to H_2 and O_2 under standard condition is 237.2 kJ/mol, which corresponds to a potential (E) of -1.23 V, according to the Nernst equation, as follows:

$$\Delta G = -vFE \qquad \text{(Equation 1.1)}$$

where F is Faraday's constant, v is the stoichiometric coefficient of the electrons in the half reactions into which the cell reaction can be divided. This photolysis process can be considered as a one-step-four-electron water splitting route, as follows from equations 1.2 to 1.4:[30]

$$2H_2O \rightarrow 2H_2 + 2O_2 \qquad \text{(Equation 1.2)}$$

H_2 gas is evolved from the photocathode following Equation 1.3:

$$4e^- + 4H^+ \leftrightarrows 2H_2\ (0\ V) \qquad \text{(Equation 1.3)}$$

O_2 gas is evolved from the photoanode following Equation 1.4:

$$2H_2O \leftrightarrows 4H^+ + O_2 + 4e^- \ (-1.23\,V) \qquad \text{(Equation 1.4)}$$

Nevertheless, the mechanism of the redox photoreaction involves the formation of H_2O_2 as an intermediate, through a two-step-two-electron route. Energy of 1.78 V is required to oxidise H_2O to H_2O_2, shown in Equation 1.6. The full redox reaction is described in the following from equation 1.5 to 1.7:[43]

$$2H_2O \rightarrow H_2O_2 + H_2 \qquad \text{(Equation 1.5)}$$

H_2 gas is evolved from the cathode following Equation 1.6:

$$2e^- + 2H^+ \leftrightarrows H_2\ (0\,V) \qquad \text{(Equation 1.6)}$$

H_2O_2 is formed at the photoanode following Equation 1.7:

$$2H_2O \leftrightarrows 2H^+ + H_2O_2 + 2e^- \ (-1.78\,V) \qquad \text{(Equation 1.7)}$$

Then the H_2O_2 is decomposed to evolve O_2 gas as shown in Equation 1.8:

$$H_2O_2 \rightarrow H_2O + \frac{1}{2}O_2 \qquad \text{(Equation 1.8)}$$

Thermodynamically, energy of 1.23 V is required to split water, as the one-step-four-electrode route stated. However, kinetically, energy of 1.78 V is needed as the two-step-two-electron route, when the intermediate of H_2O_2 is formed. Therefore, the minimal width of the band gap is required around 1.78 V for a successful PEC water

splitting with good efficiency. In general, a total energy of 2 V is required to overcome the overpotential (around 0.77 V), mainly due to the loss of the energy in the water splitting process, such as the internal resistance and gas bubble formation. More importantly, a few factors have to be considered in the process of PEC water splitting. The decomposition of H_2O_2 is exothermic but fairly slow, which may limit the reaction rate, and the strongly oxidising property of H_2O_2 is likely to oxidise the photocatalysts.[43]

The band edges of a semiconductor also determine the ability of the PEC water splitting. Figure 1.9 shows the band-edge positions versus the normal hydrogen electrode (NHE) for several common *p*- and *n*-type metal oxide semiconductors. Theoretically, in a dual photoelectrode system, a photocathode requires the edge of the CB higher than the potential to reduce H_2O to H_2, and a photoanode requires the VB edge lower than the potential to oxidise H_2O to O_2 at least. In a single photoelectrode system, the CB should be higher than the reduction potential, while the VB should be less than the oxidation potential for splitting water.

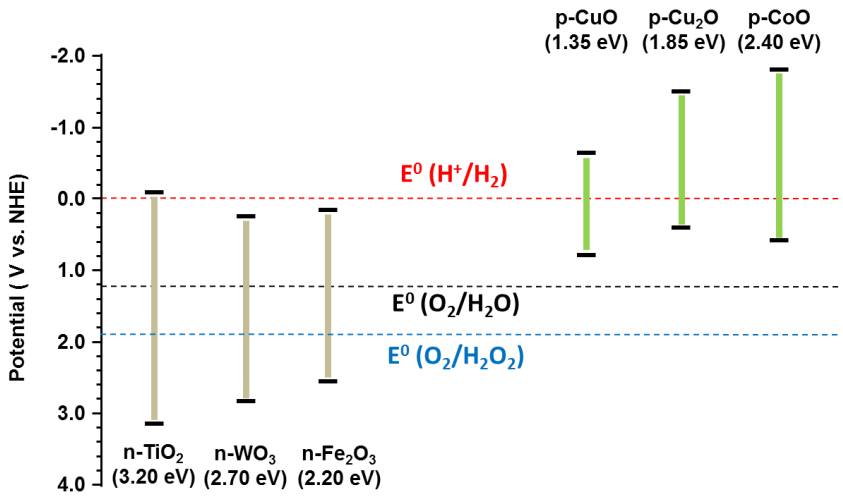

Figure 1.9 The CB (upper bar) and VB (lower bar) position vs NHE of common metal oxide semiconductors used in PEC system, [44-46] including *n*-TiO_2, *n*-WO_3, *n*-Fe_2O_3, *p*-CuO, *p*-Cu_2O and *p*-CoO.

The single-photoanode system is the focus of this research. In this system, TiO_2 is still one of the most suitable materials for PEC water splitting. The band edges of TiO_2 are sufficient for PEC water splitting as shown in Figure 1.9. Acting as an *n*-type semiconductor, the CB level of TiO_2 is suitable to reduce the hydrogen, but the VB of TiO_2 is far too positive for water splitting (more than 1 eV is wasted for this purpose). Also, the large band gap of TiO_2 means that electrons can only be excited by absorbing ultraviolet (UV) light, which is only about 10% of solar emission.[47]

Semiconductors with narrow band gap widths were also considered for water splitting,[30] such as Fe_2O_3[48] and WO_3[49] as photoanode, as well as CuO[50] and Cu_2O[51] as photocathode. The band gaps are shown in Figure 1.9. Because the width of the band gap is relatively narrow, they can be excited by visible light.[52] However, their CB and VB edges are not simultaneously suitable for a single photoelectrode system. Therefore, both *p*- and *n*-type semiconductors should be used in the PEC water splitting, as a double-photoelectrode system.

Also, the band gap of a metal oxide can be modified by a doping method. Non-metallic elements (e.g. C, N and S), alkaline earth and transition metals have been widely investigated as dopants in TiO_2.[53, 54] The dopant is able to create impurity energy levels in the band gap or narrow the width of the band gap, thus shifting the photo-response of the TiO_2 towards the visible spectrum.[55] However, introduction of too much dopant usually leads enhanced concentrations of crystal defects and charge traps, which could increase the charge recombination probability.

Electron-hole recombination is an inevitable process during PEC water splitting. Excited electrons and holes are naturally bound as excitons, which have limited life. The recombination could result a loss of the energy as fluorescence emission or lattice thermal energy. Carefully engineered nanostructures could control the electronic structure of semiconductor materials, and improve the photoactivities by reducing the charge recombination probability. The nanomaterials have large surface area, which provides a large amount of reaction centres to facilitate the redox reactions. More importantly, for a thin film photoelectrode, there are two necessary requirements. Firstly, the photocatalyst film must be thick enough to maximise the light absorption; secondly, a necessary electronic band structure of the electrode is required to ensure that the excited charge carriers are energetic enough for the redox reactions. However, an increase of the film thickness normally increases the probability of charge recombination. When a nanostructured electrode is used, the light absorption can still increase with the increase of the film thickness. However, as the electrolyte is in contact with the nanostructured material, the required travelling distance of the minority carriers is effectively reduced. Hence the light absorption and carrier diffusion can be independently controlled.[56] For instance, Mohamed et al. prepared TiO_2 nanotubes with ultrathin wall thicknesses (3-5 nm) for a PEC water splitting, and presented an improved

photoconversion efficiency with respect to the nanotube with thick wall (few tens of nanometres). Since this wall thickness was thinner than the hole diffusion length of TiO_2 (10 nm), the holes can easily travel to the surface of the nanotube with a reduced charge recombination probability.[57] Lin et al.[58] studied the electro-optical and photocatalytic properties of ultra-fine TiO_2 nanoparticles (17-29 nm). They reported that when the particle size decreased from 29 to 17 nm, the band gap decreased from 3.239 to 3.173 eV. This is due to the presence of crystal defects; this phenomenon is contradictory to the prediction of quantum confinement effects. Subsequently, when the particle size further decreased from 17 to 3.8 nm, the band gap increased from 3.173 to 3.289 eV. In their work, the extended optical absorption spectrum enhanced photoconversion efficiency.

1.3.6 Comparisons of DSSC, OSC and PEC water splitting

In comparison with the PEC water splitting technology, currently, solar cells still are the main devices to harvest solar energy. The historical data for the photoconversion efficiencies of solar cells from different modules are shown in Figure 1.10. DSSC and OSC are two of the most important solar cells to investigate. The contents of DSSC involve inorganic metal oxide, organic dye and liquid electrolyte. OSC is fabricated using all solid organic materials. Fundamentally, a DSSC requires a liquid redox mediator to facilitate semiconductors for light absorption, while an OSC uses organic semiconductors to form *p*-*n* junctions to harvest light. A major drawback of DSSC is the use of liquid electrolyte; such liquid electrolytes are likely to leak. In comparison with OSCs, because the use of brittle inorganic semiconductor, the DSSCs are relatively rigid, while all solid OSCs can be truly flexible. Although OSC requires a vacuum environment for manufacture, it is still printable for a large-area fabrication. So the production of OSCs is considered more efficient than that of DSSC. However, the

materials for DSSC are relatively cost-effective. To date, in Figure 1.10, the highest photoconversion efficiency of DSSC and OSC are 14.1% and 11.1%, respectively.[59]

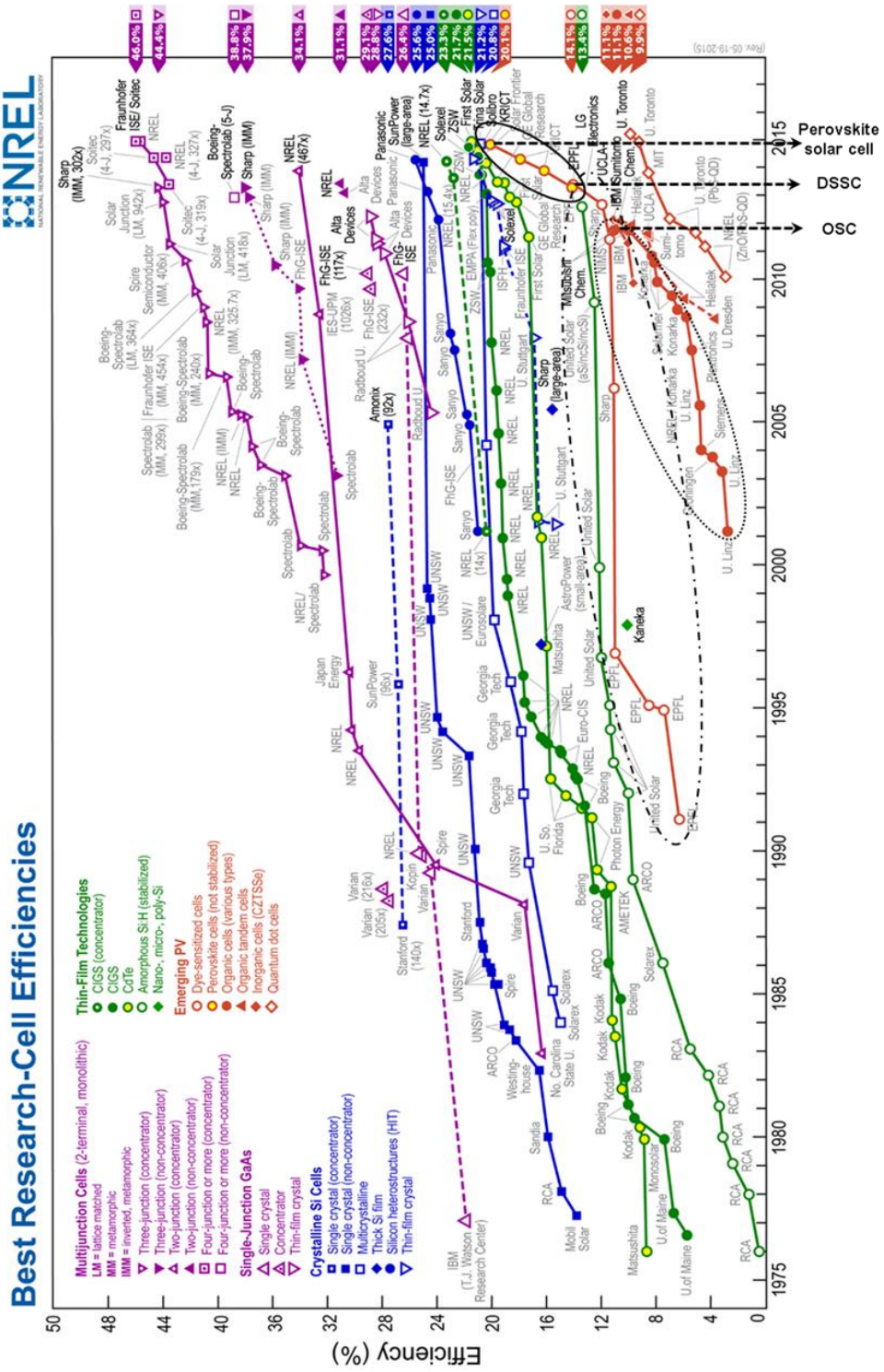

Figure 1.10 The achieved records of the conversion efficiency of the photovoltaic cells since 1975,[59] the efficiencies of perovskite solar cell, DSSC and OSC are marked.

Recently, perovskite materials made a breakthrough as a third generation solar cells, and such cells presented a photoconversion efficiency approaching 20%.[60] Taking advantages of the perovskite materials, it not only got rid of the liquid electrolyte, but also further deceased material costs. Using this material, the price of the solar cell is expected to decrease dramatically. However, the stability of this solar cell remains as the main challenge for commercialisation.

On the other hand, H_2 synthesis from the PEC water splitting also has advantages, since H_2 can be stored and used when sunlight is not available. However, the conversion efficiency is too low. A recent report presented that the best efficiency of a tandem cell is around 7%,[61] while the single cell generally has an efficiency as low as 2%.[30] This is mainly due to the difficulty of finding a semiconductor with suitable band gaps for PEC water splitting, as well as a good chemical stability. Therefore, PEC water splitting has yet to be commercialised, and still attracts a lot of attention to investigate and improve.

1.4 Applications of harvesting mechanical energy

Modern technologies to harvest natural mechanical energy are mainly based on four effects: the electromagnetic, electrostatic, piezoelectric and triboelectric effects. The electromagnetic effect has been used to harvest mechanical energy, and generate electricity following the well-known Faraday's law, which is discovered in 1831.[62] Electromotive force could interact with a magnetic field to generate electricity. It is very convenient to harvest kinetic energy, such as hybrid cars and wind farms.[63, 64] The generators have high conversion efficiencies, and the generated power can be easily integrated to an existing electric power system. However, the availability of concentrated kinetic energy is very limited. The constructional and operational costs for such devices are also relatively high. Electrostatic and piezoelectric devices are

designed to harvest other forms of mechanical energy. High conversion efficiencies can also be achieved from these devices. The electrostatic devices harvest energy from relative movement between two charged electrodes,[65] while the piezoelectric devices harvest energy in a pressure changing process.[66] Recent developed triboelectric devices are designed to harvest mechanical energy, and convert it to a charge separation between two surfaces with different dielectric constants and surface chemical potentials. Although only the triboelectric device was studied this research, summaries of the mechanisms of electrostatic devices and piezoelectric devices will also be discussed in the following section (1.4.1). The detail of triboelectric device will be discussed in section 1.4.2.

1.4.1 Electrostatic and piezoelectric effects to harvest mechanical energy

The electrostatic effect was first discovered by British scientist John Canton in 1753.[67] Usually, the electrostatic generator has two electrodes, which are separated by an insulating dielectric material. A DC voltage is applied between the electrodes to generate static charges on the electrodes. Any external repetitive mechanical movement will create a relative oscillation movement between the electrodes, which causes oscillations of the electrical potential. This phenomenon creates an AC voltage over the applied DC bias. Two simple working mechanisms are shown in Figure 1.11. The electrodes can be moved either vertically (Figure 1.11a) or horizontally (Figure 1.11b) by external mechanical movements to change the electrostatic field.

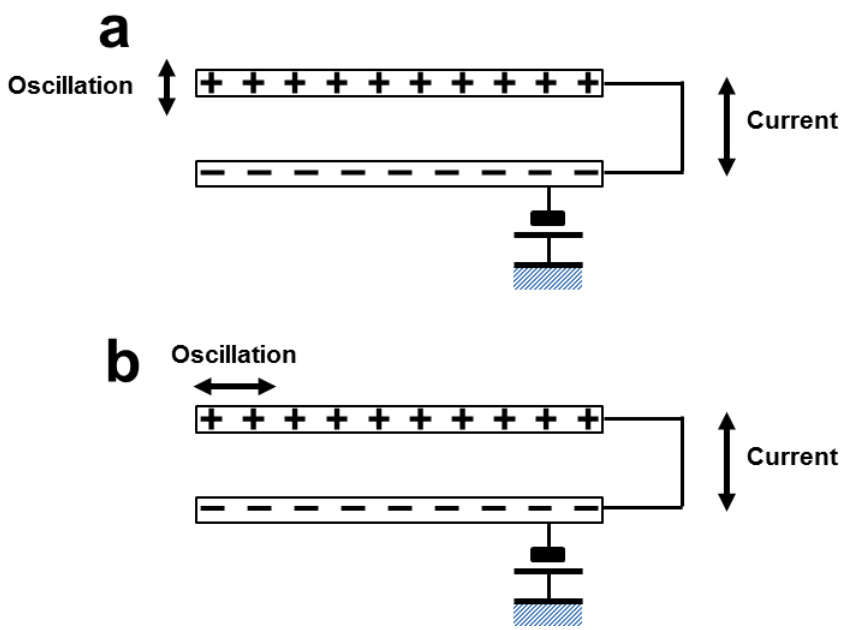

Figure 1.11 Two working mechanisms of the electrostatic generator. (a) The gap-change and (b) the overlapping-area-change system.

Piezoelectricity was first discovered in 1880 by French physicists Jacques and Pierre Curie.[68] The applications based on piezoelectricity were widely developed. It was used as the core component of scanning probe microscopies and quartz crystal microbalances.[69] For a piezoelectric material, when a pressure is applied, it generates an electrical pulse and vice versa. A piezoelectric device generally has the advantages of high-power density, low weight and cost-effective manufacture.

A piezoelectric material is a type of polarised dielectric material. It exhibits a polarised crystal structure due to a systematic separation of positive and negative charged ions along a specific crystal orientation. By applying a pressure along that crystal direction, a distortion of the dipole is induced, which results in a rebalance of the charges within the crystal.

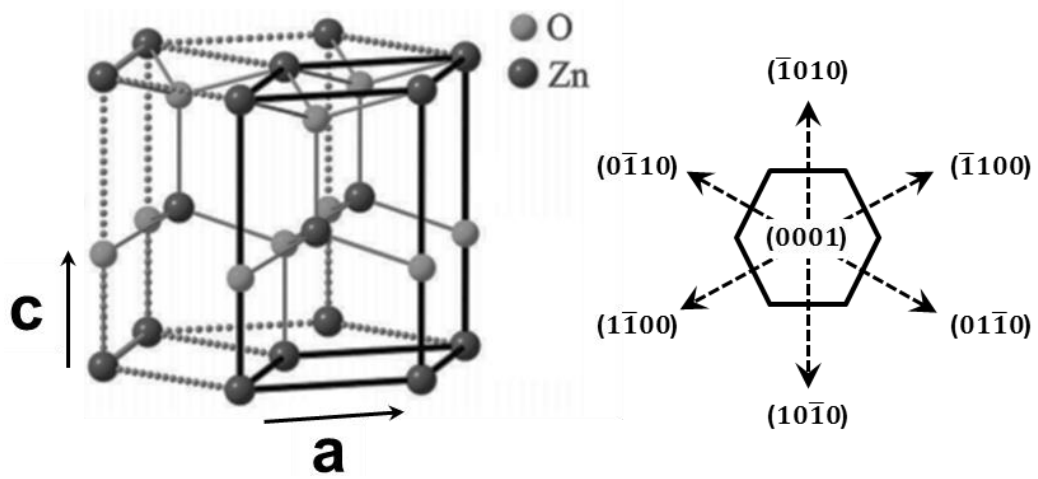

Figure 1.12 The cystal structure of wurtzite ZnO as a typical piezoelectric material.[70]

Wurtizite ZnO is a typical piezoelectric material. It has a hexagonal structure (space group $P6_3mc$) with lattice parameters a = b = 3.250 Å and c = 5.207 Å (*JCPDS # 36-1451*), as shown in Figure 1.12. The crystal is formed with alternating positively charged Zn layers and negatively charged oxygen layers with a non-centrosymmetric structure. This leads to a polarised (0001) crystal plane with the dipole moment perpendicular to it. The dipole density, defined as the dipole moment in a unit of volume, will change upon the application of an external mechanical stress, which generates electricity. Conversely, the electrons will move in opposite direction, when the external mechanical force is released after rearrangement of the dipole moment. Hence, with a pulsed pressure, AC voltage and current will be generated. Piezoelectricity can be observed in a lot of materials, such as ceramics (SiO_2, $AlPO_4$ and $PbTiO_3$), as well as some organic materials (silk, wood and DNA).

Recently, nanostructured piezoelectric materials were widely explored, since the seminal demonstration by Wang et al.[71] They found that a piezoelectric nanogenerator based on vertical ZnO nanorods is able to harvest mechanical energy effectively with small-scaled mechanical energy sources. The applications include harvesting energy

from body movements,[72] muscle stretching[73] and acoustic waves.[74] This opened potential to use piezoelectric devices in portable self-powered electronics and wearable electronics.

1.4.2 Triboelectric devices

A triboelectric nanogenerator (TENG) was recently developed based on nanomaterials. The triboelectric effect can be traced back to ancient Greek times, although its mechanism is still being studied and debated.[75, 76] A general view of the mechanism is related to the dielectric constant and the surface chemical potentials of materials.[77] When they contact each other, some weak charge transfers between the atoms on the two surfaces, caused surface molecular polarisation and pulsing of electricity. Dielectric mismatch leads to trapping potential at the interfaces. The capability for energy storage is inversely proportional to the dielectric constant (ε), and proportional to the electrode thickness of the triboelectric device. Also, the large ε of the electrode leads to solvation of the charge by dipole relaxation. Therefore, a good triboelectric material requires materials with high surface potential, large thickness and a low ε of the electrode.

The known triboelectric materials are listed in Figure 1.13. They are classified in two categories based on their tendency to gain or lose electrons in a triboelectric process.[78] Since the material that has a strong triboelectric effect is usually less conductive, the triboelectric effect is also believed to relate to the dielectric constant of the material. Typically, a high dielectric constant means the material is able to capture charges, and retain them for an extended period, which also could enhance the output of a TENG.

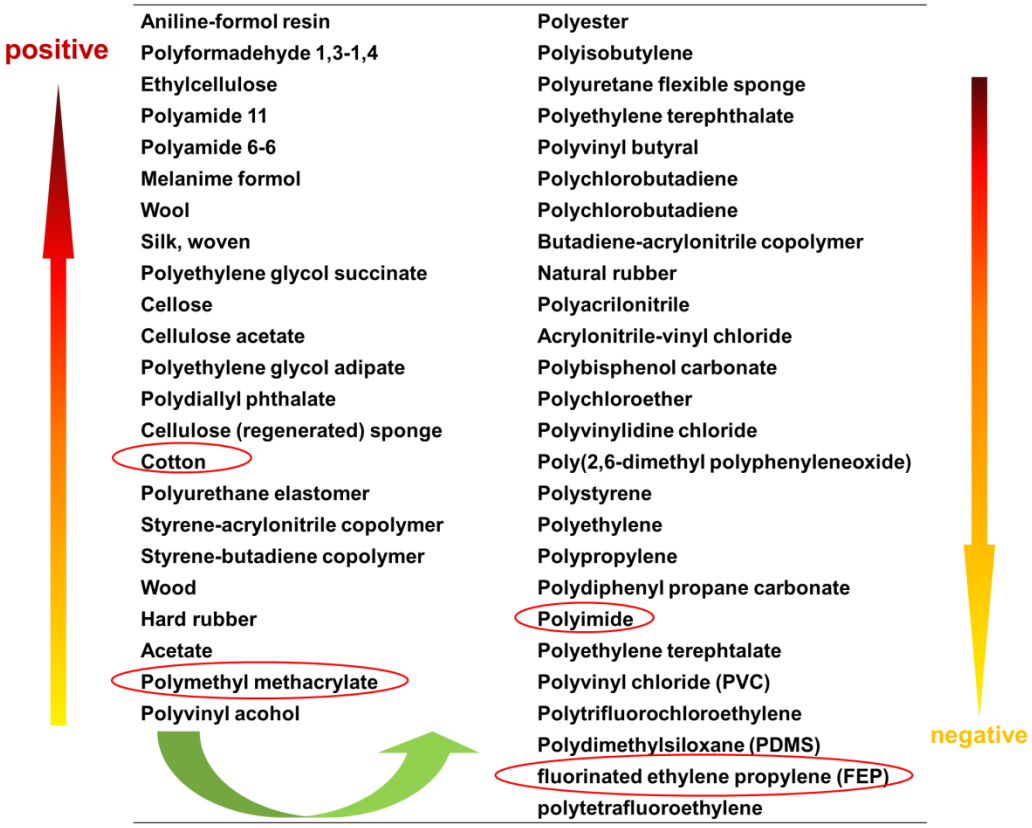

Figure 1.13 The triboelectric series of the materials according to their tendency to gain (negative) or lose electrons (positive) in contact charging and frictional charging process.[78] The highlighted materials were studied in this project.

There are two mechanical movement modes, which are used for the contact-separation in a TENG, illustrated in Figure 1.14. Figure 1.14a shows the operation of TENG by vertical contact separation, driven by compression and expansion. The surfaces of the two triboelectric electrodes are initially separated, the mechanical energy that presses them to contact generates a net charge flow between the electrodes. The device will expand to break the contact, which results in charge flow in the opposite direction. In the other design, a lateral sliding motion is applied, as shown in Figure 1.14b. In this design, the mechanical energy that pushes and pulls the triboelectric electrodes creates a shear movement, which oscillates the effective contacting surface

area. This will generate electrical pulses with polarity, determined by the direction of the shear movement. In this works, the vertical contact-separation mode was experimentally investigated in Chapter 7.

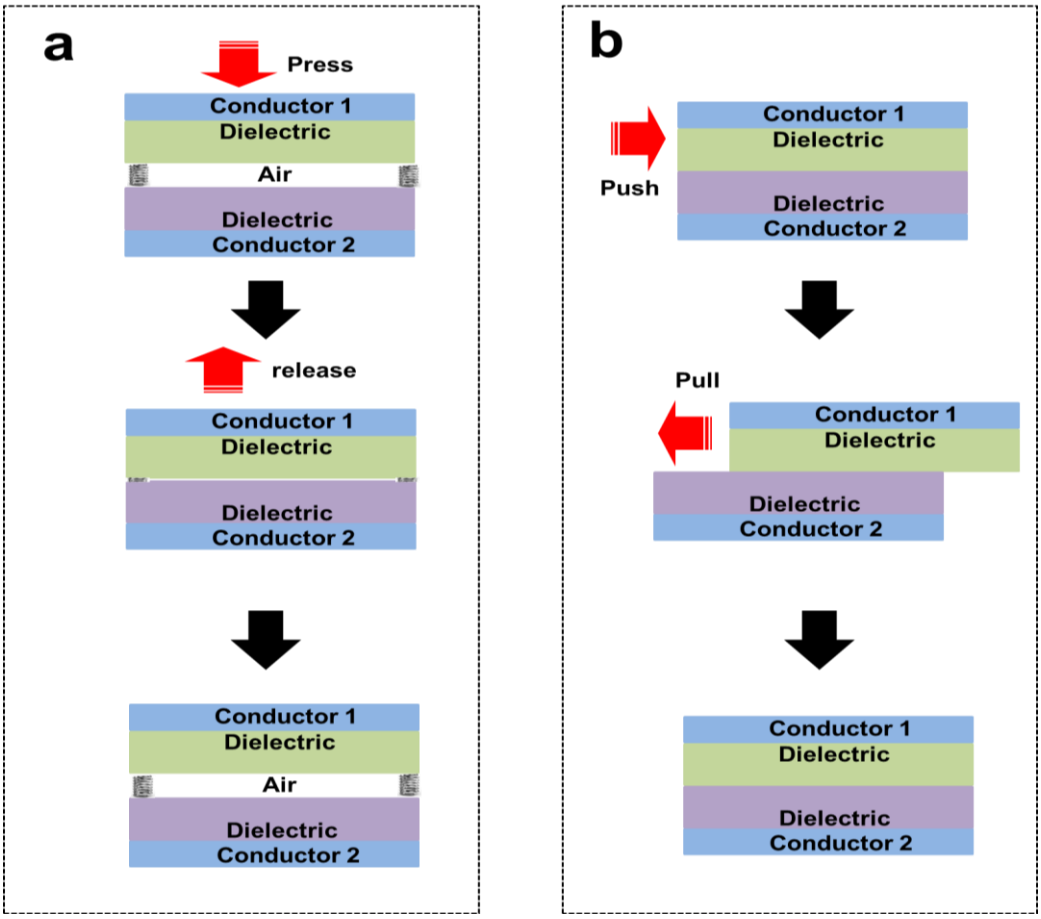

Figure 1.14 Two working mechanisms of the triboelectric generator. (a) The vertical contact-separation and (b) the lateral sliding mode.

The TENG are flexible, mechanical stable, robust and potentially transparent, since they are based on dielectric polymer materials. Moreover, the polymer materials are relatively easy to process into thin films. It is also easy to integrate with nanostructure to achieve additional functionalities.

Since the successive mechanical deformation is the energy source for a TENG, the mechanical robustness and the flexibility of the components is critical for the stability

and durability of the TENG. However, most of the transparent electronic devices have been constructed using indium tin oxide (ITO) as the conductor, which is a brittle ceramic material. Therefore, the ITO based transparent conductive electrode could result in a short working life and unreliable output of the transparent triboelectric nanogenerators (T-TENGs). More importantly, since the flexibility of the device is restricted, it is incompatible with wearable and epidermic electronics.[79]

In order to improve the toughness and flexibility, alternative materials were developed as the transparent electrodes in T-TENG, such as carbon based conductive materials[80] and metal nanowires.[81] Among them, the electrode based on one dimensional (1D) metal nanowires exhibited many advantages. Metal nanowires can be synthesised in solution processes in a large quantity. By thermal welding, their electrical resistance can be effectively reduced while their mechanical strength can be improved significantly.[82] This type of electrode also exhibits excellent light transmittance through a broad range of wavelength, in addition to an outstanding flexibility with a small bending radius (at least 1 mm).[83] In such a flexible T-TENG system, the efficiency of a triboelectric device will increase if the density of AgNWs increases, but its optical transparency will be reduced. The fine balance between the conductivity and optical transparency will be further discussed in Chapter 7. By using this type of the electrode, a transparent TENG (T-TENG) were integrated with an OSC as a hybrid device for harvesting both mechanical and solar energies, in Chapter 8.

In comparison of these technologies to harvest mechanical energy, the electromagnetic generator is well developed and very efficient. However, the rigidness of the device makes it difficult to integrate with modern wearable and portable electronics. Meanwhile, nanostructured piezoelectric nanogenerators present the potential to integrate with wearable electronics. But the metal oxide based

nanogenerators (piezoelectric devices) are normally mechanically fragile. When repeated mechanical stress is applied, the lifetime of the device is very limited. On the other hand, triboelectric devices show good durability, since they mainly use polymer components. Also, since a lot of polymers are biocompatible, this kind of triboelectric device can be easy to apply with human organs, such as heart and epithelial tissue.[84] Therefore, triboelectric devices are more convenient than piezoelectric devices for many modern applications.

1.5 Purpose and structure of the research

The goal of this research is to develop low-dimensional nanomaterials with high conversion efficiencies for harvesting solar and mechanical energy. Several approaches were developed in this work. A PEC water splitting method was used to store solar energy in the form of H_2. Solar cells were developed to convert solar energy directly into electric power. Triboelectric devices were constructed to harvest mechanical energy. In the final part of the thesis, by integrating an OSC with a TENG, a flexible hybrid cell was fabricated. It is capable of harvesting both solar and mechanical energies simultaneously.

The thesis has 9 chapters. Chapter 1 will briefly introduce the fundamentals of energy harvesting and conversion. Chapter 2 discusses the synthesis methods for generating nanomaterials, including electrospinning for nanofibres chemical bath deposition of nanorods, polyol synthesis of metal nanowires, as well as the electrophoretic deposition (EPD) of nanostructured thin film.

Chapter 3 outlines the analytical methods used in this research. A standard light source is described first. The principle and operation of analytical instruments for characterising nanomaterials will also be discussed, including scanning electron microscopy (SEM), ultraviolet-visible (UV/Vis) spectroscopy, powder X-ray diffraction

(XRD) and atomic force microscopy (AFM). Setups for the measurements of PEC water splitting and solar cells will be presented together, as well as the setup to characterise triboelectric devices.

Chapter 4 systemically studies a pump-free electrospinning system to create nanofibres. The critical parameters for controlling the morphology of the nanomaterials will be investigated. Following that, in Chapter 5, an EPD deposition of WO_3 nanofibre thin films is discussed. The thicknesses of the thin films will be controlled through the EPD parameters (concentration, current and deposition time). The thin film structure will be optimised for the photoconversion efficiency of PEC water splitting. In Chapter 6, electrospray method is used to synthesise TiO_2 hollow hemispheres (HHSs). The applications of the HHSs in PEC water splitting and DSSC will be demonstrated, as such structure reveals an enhanced photoconversion efficiency in comparison with a P25 thin film.

Chapter 7 focuses on the fundamental study of transparent triboelectric devices to harvest mechanical energy. Metal nanowires were synthesised using a polyol method, and were applied for flexible transparent electrodes. The influences of the area fraction of the metal nanowires on the output performance and transparency of the TENG is comprehensively studied. Following that, in Chapter 8, a unique hybrid device, which involves an OSC and a TENG to integrate together, will be demonstrated to harvest both solar and mechanical energy individually or simultaneously.

The thesis is concluded by summarising the work in Chapter 9, together with some outlook on future research directions. Different approaches for improving the energy conversion and harvesting are presented with emphasis on the developing novel structured materials.

Chapter 2 Methods for synthesising low dimensional nanostructured materials

2.1 Abstract

This chapter described several synthesis methods to develop nanostructured materials. The principles and applications of electrospinning/electrospray technique were discussed. Wet chemistry synthesis methods, including chemical bath deposition (CBD) method and polyol synthesis, to produce metal oxide nanorods and metal nanowires were reviewed. Electrophoretic deposition (EPD) to fabricate porous thin film from electrospun nanofibres was also discussed, and the related applications were also reviewed.

2.2 Introduction to synthesis of nanomaterials

Nanomaterials are usually classified by the dimensions. Zero-dimensional (0D) nanostructured materials have a structure with all three dimensions less than the Bohr exciton radius, which is determined by the effective mass of the electron and the dielectric constant of the material. One-dimensional (1D) nanomaterials have a structure of two dimensions in nanoscale, such as nanotubes, nanofibres and nanorods. Thin films are classified as two-dimensional (2D) nanomaterials. In such cases, the scale of the third dimension is normally over μm in length. Broad ranges of synthesis methods were developed to control the morphologies and structure of the nanomaterials. Many such methods rely on either chemical or physical properties of the material optimisation for specific growth kinetics in a certain dimension.

Physical processes are very important to control the morphology of nanomaterials. Two novel methods are mainly studied since they are related to this research: ball milling[85] and vapour-solid (VS) methods.[86] Ball milling method uses mechanical force

to grind a bulk structure into nanostructure. Therefore, this method can be widely applied for ceramics and metals, but it is relatively difficult to obtain homogeneous nanomaterials.

VS method is derived from the conventional chemical or physical vapour deposition method, which vaporises the precursors, and allows them to form solid nanomaterials through either chemical reactions or physical condensations. It offers a better control of the morphology and structure, since both of the temperature and concentration can be precisely controlled. Using appropriate temperature, many solids can be evaporated to deposit on a substrate to form novel nanostructures, driven by their own differentiation in crystallisation kinetics. For example, core/shell heterogeneous nanospheres were successfully developed through VS method.[87, 88] By using zinc acetate as Zn precursor, 1D ZnO nanorods can be readily deposited on different substrates by holding at 550 ℃ for 20 mins.[89] The growth direction of the ZnO nanorod crystals can be further controlled with the initial seed of nanoparticles on the substrate.[90] Recently, VS method was also applied to synthesise a monolayer graphene film by depositing carbon vapour on a Cu foil.[91]

Nanodevices can be fabricated using conventional methods, such as doctor-blade, spin coating and hot-pressing methods. Doctor-blade uses a blade to disperse a liquid material homogeneously to a thin film. Spinning coating method uses a rotating substrate to disperse a liquid material into a film. Hot-pressing usually applies for solid material, i.e. solid materials are pressed at high temperature to form a thin film. They are all frequently used to fabricate semiconductor nanomaterials for photoelectrochemical (PEC) applications. However, the films formed from these methods are weakly bonded with poor mechanical stability. Therefore, an EPD method is adapted to deposit nanofibre film as PEC device, demonstrated in this thesis (Chapter

5). In a comparison with the above-mentioned methods, the EPD method offers a better control of the film thickness. The formed film is mechanically strong with an excellent electrical contact to a substrate, which is essential for an efficient PEC device.

2.3 Electrospinning and electrospraying

2.3.1 Fundamentals of electrospinning/electrospraying

Electrospinning and electrospraying are versatile methods for creating nanofibres and nanoparticles, respectively. In a typical setup as shown in Figure 2.1a, a polymer solution with certain viscosity is used as the carrier solution, and a high voltage is applied to the nozzle, which delivers the polymer solutions with static charges. The polymer solution will be stretched and dried during its deposition process onto the counter electrode. If the polymer solution has sufficient viscosity (large amount of entanglement), nanofibres will be formed, classified as electrospinning. On the other hand, with low viscosity, the polymer solution will break into droplets in the electrical field, classified as electrospraying. The realisation of electrospinning/electrospraying phenomenon can be traced back to the 16th century, when William Gilbert observed the behaviour of electrosprayed water.[92] Such method has been explored as a simple and versatile method to synthesise nanomaterials since 1930s, at Karpov Institute in the former Soviet Union .[93]

To date, many polymers, ceramics and metal nanomaterials were successfully synthesised through electrospinning method. Poly(methyl methacrylate) (PMMA) nanoring, poly(vinyl alcohol) (PVA) nanospheres and poly(lactic acid) (PLA) nanofibres were reported.[94] For creating metal and metal oxide nanomaterials using electrospinning/electrospraying method, appropriate metal precursors (either soluble or as suspension) were added to the polymer solution. In such case, in order to achieve pure nanomaterials, a post process is necessary to remove the polymer content. Using

electrospinning method, more than 40 ceramic fibres were fabricated, including ZnO,[95] WO_3[96] and TiO_2[97] nanofibres, as well as doped metal oxide nanofibres[98]. The method was also successfully used to synthesise complex nanotubes by using a co-axial double nozzle to deliver core-shell structured nanofibres. Once the core material is removed, the tubular structure is formed.[99]

Electrospraying method has identical setup as electrospinning, but it produces 0D nanomaterials instead of a continuous fibrous structure, such as mesoporous nanoparticle,[100] hollow hemisphere[101] and rice-grain shaped structure.[102] More interestingly, a twin-head setup of the electrospray was used to create Janus particles, a type of nanoparticle whose surfaces have at least two physical properties, so two or more different types of chemistry can happen on a single particle. This special property makes Janus particles useful for many novel applications. For instance, anisotropic probes for optical traps and E-paper display technology.[103]

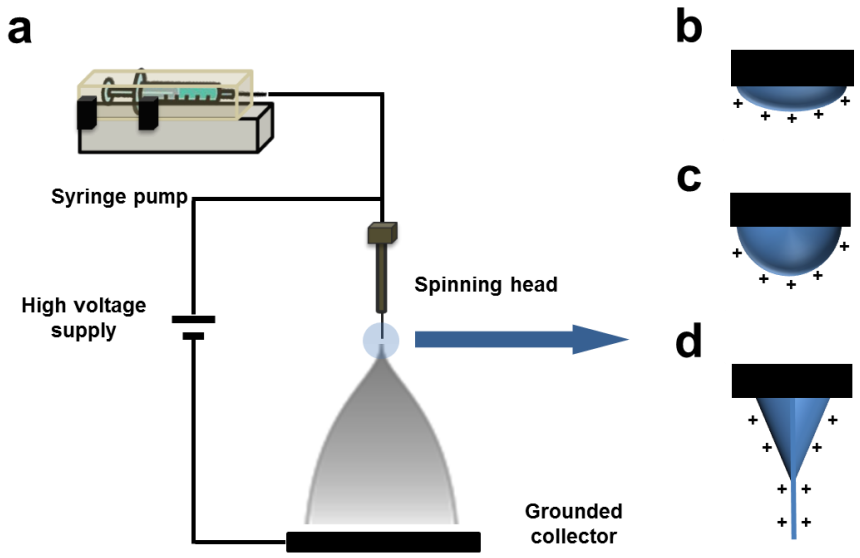

Figure 2.1 (a) A schematic diagram of the electrospinning setup. (b), (c) and (d) The electrostatic induction of the Taylor cone to produce nanofibres.

Figure 2.1a depicts a typical setup for electrospinning/electrospray. There are three critical components to fulfil the process: the high voltage supply, the capillary-sized spinneret and the metal collector. In the electrospinning process, a high voltage is applied between the spinneret and the metal collector to create an electrostatic field, extruding a viscous solution of the precursor sol-gel with the syringe pump. The electrostatic repulsion between the charged polymer droplets counteracts the surface tension of the liquid, as shown in Figure 2.1b. Following that, as presented in Figure 2.1c, the electrostatic force stretches the liquid into droplets. At a critical point, a stream of the liquid erupts from the end of the drop, forms a jet of fibres flowing away from the liquid drop as in Figure 2.1d. In the meantime, the solvent in the flowing fibres is evaporated to leave solid nanofibres. However, if the viscosity of the solution is too low to compensate the surface tension, the jet of fibres breaks down to form small droplets instead of a fibrous structure.

Two types of parameters are significant in controlling the morphology and structure of electrospun nanomaterials. One is the setup parameters, including the electrostatic field strength, the distance between the spinneret and the collector, the spinneret nozzle size, the rotational speed of the collector, the structure of the collector, and the solution injection rate. For example, two grounded parallel metal strips with 1 cm gap was reported to collect aligned polymer nanofibres.[104] In such case, the charged fibres jump between the metal strips alternately without enough time for twisting and rotating (spinning instability). In this work (Chapter 4), a pump-free method was developed with a comprehensively study of the setup parameters, in order to develop a reliable technique for a high throughput mass production of nanofibres at industrial scale.

The other is the solution parameters, including the solution composition and the

concentration, are also important to determine the morphology and the structure of the nanomaterials. For instance, the concentration of the inorganic precursor in the polymer solution could reduce the viscosity of the polymer solution significantly, leading to the formation of small particles instead of the fibrous structure.[105] A polymer solution contains metal ions could result in thinner nanofibres, as this could increase the density of the static charges that carried by the solution jet. The increased density of the static charges generates high elongation forces to extract the polymer droplets.[106] Multiplying electrospinning needles, such as a hollow tube with multiple spinnerets, have also been designed to increase the production rate of the nanofibres.[107]

2.3.2 Applications of electrospun/electrosprayed nanomaterials

Electrospinning/electrospray is a versatile, convenient and cost-effective method to produce nanomaterials. The applications of the nanomaterials created by such methods have been widely studied. A non-woven filtration film can be fabricated using electrospun nanofibres. The efficiency of the filtration can be improved by using the appropriate polymer material with a control of the density and dimeter of the non-woven media.[65] Bio-engineering is another one of the major applications using electrospun fibres. Biocompatible electrospun nanofibres can be fabricated as a scaffold to provide an optimal template for cells to seed, migrate and grow.[106] Direct spraying of biodegradable polymer loaded with antibiotics and drugs can form a breathable fibrous wound dressing mat with a controlled release of the drugs. Such dressing encourages the formation of skin, and could eliminate the formation of scar tissue.[108] In addition, electrospun nanomaterials are also commonly used for cosmetics, such as care mask, skin healing and skin cleansing.[109]

Since the composition of electrospun metal oxide nanofibres can be freely controlled, a broad range of electronic applications was also investigated using

electrospun nanostructured materials, including solar cell, fuel cell, mechanical energy harvesting device and PEC water splitting. Onozuka et al. reported the applications of electrospun metal oxide nanofibres with larger pores for dye-sensitised solar cell (DSSC).[110] Although the improved penetration of the electrolyte into the semiconductor film could enhance the photoconversion efficiency of DSSC, the major problem is the poor adhesion of the long, rigid fibres to the substrate. A high calcination temperature may further induce stresses between the fibres. A later developed solvent vapour method allowed a relaxation of the TiO_2 nanofibres, thus the stability of the film for PEC applications was substantially enhanced.[107] In this method, the solvent vapour was used to soften the rigid morphology of the as-electrospun nanofibres. Furthermore, a hybrid structure of TiO_2/SiO_2 nanofibrous mat was synthesised with TiO_2 nanoparticles using the electrospinning method. With such material, the assembled DSSC achieved an enhanced photoconversion efficiency of 6.67%.[107]

The electrospun fibres can also be applied for organic solar cells (OSC). The photoconversion efficiency of an OSC is determined by the structure of the bulk heterojunction (BHJ). However, the structure is usually highly folded, and presents a discontinuous topology of the donor-acceptor interface, which restricts the photoconversion efficiency. Replacing the disordered phase with ordered fibres potentially increases the photoconversion efficiency. However, most of the conjugated semiconductor polymers are difficult to electrospin, due to the limitation of the choice of effective solvent. Electrospun polypyrrole (PPy) was demonstrated by mixing PPy with poly (ethylene oxide) (PEO). PPy is an attractive electronic material due to its unique electrical, optical and photoelectric properties.[111] The produced nanofibres show excellent electrical conductivity, and can be potentially used as the BHJ layer in an organic solar cell.[111] Inorganic electrospun materials can also be blended into the

organic BHJ film to increase the photoconversion efficiency. The inorganic composition in OSC increases the donor-acceptor interface area, which could enhance the dissociation efficiency of the excitons.[112]

Piezoelectric materials, such as poly(vinyldene fluoride) (PVDF), can also be downsized into 1D nanoscale using the electrospinning method.[113] The large surface of the nanofibres is significant to the performance of the piezoelectric device.[60] Such performance can be further improved by adding carbon nanotube into the piezoelectric nanofibres.[114] The near-field electrospinning method was specifically developed for producing aligned fibrous patterns. In this near-field system, the electrode-to-collector distance is small (ca. 500 μm). When a bias voltage of 600 V is applied, the position of the electrospun nanofibre can be easily controlled. Such control could enhance the efficiency of piezoelectric devices.[115]

Electrospun inorganic nanofibres also have been applied for energy storage. Battery applications using inorganic electrospun nanofibres are widely developed. For instance, as cathode materials, electrospun $LiCoO_2$ nanofibres presented a high initial charge and discharge capacity of 216 and 182 milliampere hour per gram (mAh/g), respectively.[116] Here, the unit (mAh/g) is used to describe the energy storage weight density, it is equivalent to the charge transferred by a steady electrical current flowing for one hour with one gram of the cathode material. Creation of porous nanofibres also offers the potential for hydrogen storage. Electrospun carbon nanofibres have shown a high hydrogen storage capacity.[117]

Electrospinning has become an essential technology to generate 0D and 1D nanomaterials, and such materials are widely used into energy related applications. However, one of the drawbacks is that, when the diameter of the 1D nanofibre or 0D nanoparticle is below 50 nm, the homogeneity of the nanomaterial is difficult to control.

In the long-term development, the electrospun nanomaterial is expected to decrease the diameter of nanofibre with preserved morphology and structure. On the other hand, single crystalline nanomaterials are fairly difficult to synthesise through electrospinning method; it usually requires very restricted conditions. As an example, electrospun single crystal α-Al_2O_3 nanofibres were created through calcination of the as-prepared fibres at 1300 $^{\circ}$C under Ar atmosphere.[118]

2.4 Wet chemistry method for synthesis of nanomaterials

Wet chemistry methods are generally used to synthesise inorganic nanomaterials in liquid. In comparison with the electrospinning method, wet chemistry is performed under mild conditions with an improved control of the chemical reaction. A number of wet chemistry methods have been demonstrated for synthesis of nanomaterials with uniform sizes, and with smooth and defect-free crystal faces.[119] Wet chemistry methods are widely expanded with specific-reaction conditions, including chemical bath deposition,[120] hydrothermal synthesis,[121] metal-organic vapour-phase deposition,[122] vapour-liquid-solid deposition,[123] and polyol synthesis.[124] The chemical bath deposition and polyol synthesis methods were used to synthesise inorganic nanomaterials in this thesis.

2.4.1 Chemical bath deposition for the synthesis of metal oxide nanomaterials

Chemical bath deposition (CBD) is an important method to synthesise nanomaterials. Bruckman first adapted this method to synthesise lead sulfide (PbS) thin film.[125] Following that, numerous good-quality semiconductor films were synthesised using this method, such as cadmium sulfate (CdS), cadmium selenide (CdSe), zinc sulfate (ZnS) and zinc selenide (ZnSe) films.[126] High quality films were widely applied into solar energy related work with a promised efficiency for the electron collection and

transport.

High quality ZnO nanorod and nanowire can be synthesised using CBD method. It was firstly developed by Vayssieres in 2003.[127] The applications of ZnO nanorods were widely developed, including piezoelectric devices,[71] PEC applications,[55] solar cells[128] and superhydrophobic devices.[129] In this CBD process, zinc nitrate hexahydrate, zinc acetate or zinc chloride precursor is normally used as the zinc precursor. Hexamethylenetetramine (HMT) or ethylenediamine was used as the hydroxide anion source. The mechanism is proposed as the following sequence of chemical reactions:[130]

$$(CH_2)_6N_4 + 6H_2O \rightleftharpoons 4NH_3 + 6HCHO \quad \text{(Equation 2.1)}$$

$$NH_3 + H_2O \rightleftharpoons NH_3 \cdot H_2O \quad \text{(Equation 2.2)}$$

$$NH_3 \cdot H_2O \rightleftharpoons NH_4^+ + OH^- \quad \text{(Equation 2.3)}$$

$$Zn^{2+} + 2OH^- \rightleftharpoons Zn(OH)_2 \quad \text{(Equation 2.4)}$$

$$Zn(OH)_2 \rightleftharpoons ZnO + H_2O \quad \text{(Equation 2.5)}$$

In this growth process, the substrate should be pre-seeded by deposition of ZnO nucleation sites on the substrate, and then the substrate is immersed into the precursor solution for growth of nanorods. The HMT in the solution is thermally decomposed to form NH_4^+ and OH^- as illustrated from equation 2.1 to 2.3, and the *pH* of the solution increases. Meanwhile, the Zn^{2+} will be hydrolysed to form $Zn(OH)_2$, as seen from Equation 2.4. Then, $Zn(OH)_2$ will be deposited on the ZnO nucleation sites on the substrate, as shown in Equation 2.5. The ZnO nanorod is formed by further decomposition of the $Zn(OH)_2$. The balance of the precipitation rate and the growth rate determines the morphology and structure of the ZnO.

The morphology and structure of ZnO nanostructures can be controlled by the

experimental parameters, including the concentration of the zinc precursor, the hydroxide anion precursor, the duration of the reaction and the surfactant. Xu et al. reported the effect of the growth temperature, the concentration of the zinc precursor, and the reaction duration on the morphology of ZnO nanostructured using seedless CBD method.[130] The results revealed that a longer reaction time and a higher concentration of the Zn precursor caused the formation of longer and larger ZnO rods.[130] Meanwhile, a higher reaction temperature caused a change in the nanorod from hexagonal to tapered-like structure.[130] The growth of ZnO nanorods can also be controlled by the pre-seeding process, the alignment and diameter of ZnO nanorods can be optimised by control of the crystalline form and size of the seeding ZnO.[131]

The CBD method can be further controlled by combining a strong vibrational energy, typically generated in an ultrasonic bath. This method is named as the sonochemical CBD method. The precursors in such CBD method are similar to those used in the traditional CBD. However, the precursor solution is placed in an ultrasonochemical apparatus. The ultrasonication releases a large amount of energy by the collapsing of microbubbles, causing increased temperature and pressure. The generated energy could facilitate the growth of the ZnO. The sonochemical method allows further control of the size, shape and morphology of the ZnO nanostructure, including nanorod, nanoflowers, nanocups and nanodics.

CBD method presents many advantages, compared with the other synthesis methods. The reaction is operated in mild conditions (<100°C and normal pressure). It offers the potential for large area deposition on a variety of substrates. It is a cost-effective and environmentally friendly technique, requiring no complicated chemical synthesis strategy or hazardous components.

2.4.2 The polyol method for the synthesis of metal nanowires

The polyol method was first described by Fievet et al. to synthesise nanomaterials in alcohols in 1989.[132] Chemically, this method is based on the family of ethylene glycol (EG) compounds. To date, the polyol method is generally used to prepare high-quality nanomaterials. There are several advantages to synthesise inorganic nanomaterials with polyols. The reaction is carried out in a water-comparable liquid, which can dissolve numerous kinds of inorganic precursors. The high boiling point (up to 320°C) of EG compounds can facilitate the formation of high quality crystalline material without the need of an autoclave. The fast reduction reaction allows near-instantaneous synthesis of nanomaterials. A wide range of compounds of the EG family, from low molecularweight EG to high molecular weight poly(ethylene glycol) (PEG), is available for different kinds of reaction.

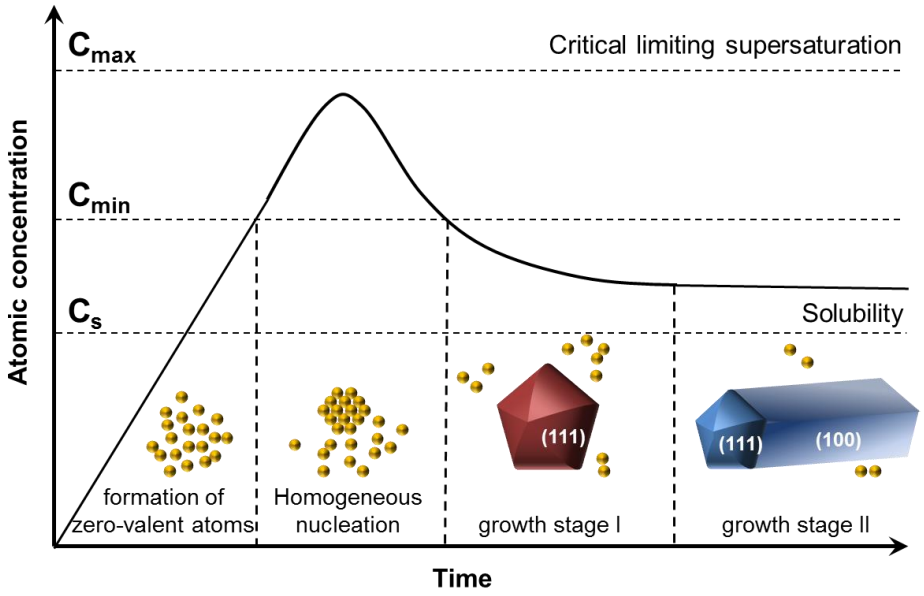

Figure 2.2 The growth mechanism of the silver nanowires in four stages: (1) Formation of the zero-valent atoms, (2) Homogeneous nucleation, (3) Growth stage I and (4) Growth stage II. C_s is the supersaturation point of the atom concentration. C_{min} and C_{max} are the minimum and maximum concentration for atom nucleation, respectively.[133]

The polyol method was widely applied to synthesise noble metal nanoparticles. In the reaction, the metal cation is firstly coordinated with the polyol solution, and reduced to form elemental metals. Patrice et al. reported a comprehensive study to deduce the reducibility of metals ions in different polyol solutions.[134]

The polyol method is especially important to synthesise free-standing noble metal nanowires. In this work, the polyol method was used to synthesise silver nanowires (AgNWs) for transparent and conductive electrode in Chapter 7 and 8. Metal nanowires are considered as the source for next generation transparent conductor, to substitute indium tin oxide (ITO). The growth mechanism of the silver nanowire (AgNW) is illustrated in Figure 2.2. The precursor of $AgNO_3$ is initially reduced to form zero-valent silver atoms by polyol following Equation 2.6 and Equation 2.7.[133]

$$2OHCH_2CH_2OH \xrightarrow{Heating} 2CH_2CHO + H_2 \qquad \text{(Equation 2.6)}$$

$$2CH_2CHO + 2Ag^+ \xrightarrow{Heating} Ag^\circ + 2H^+ + CH_2COCOCH_3 \qquad \text{(Equation 2.7)}$$

As the concentration of the zero-valent Ag atoms steadily increases, they start to aggregate into a small Ag nucleus via a homogeneous nucleation. After the initiation of the nucleation, the rate of reduction of the atomic concentration slows down due to the formation of the large multiply twinned Ag seed under generally controlled conditions, as presented in the growth stage I in Figure 2.2. This kind of seed is polycrystalline nuclei, which can be considered 5 to 20 f.c.c. tetrahedra joined by twin boundaries to give decahedral[135] or icosahedral[136] forms. The morphology of the nuclei can be controlled by the processing parameters, such as the reaction temperature and the polyol solution.[135, 136] In the growth stage II, an anisotropic growth of decahedral Ag seeds is thermodynamically induced to form AgNW. In this process, larger particles are more

stable than small particles, since the small particles have a high solubility, which drives the ions to deposit on the large particles. A polymer-capping agent is usually used to stabilise the side faces and to control the nanorod morphology. In this work (Chapter 7 and 8), poly(vinyl pyrrolidone) (PVP) is used for this purpose.[137]

Recently, polyol methods were also used to synthesise metal oxide nanomaterials through high temperature hydrolysis. A high boiling point of the polyol solvent allows a wide range of reacting temperatures, which is essential to control the morphology, structure and crystallinity of the metal oxide nanomaterials. More importantly, the formation of the metal oxide nanomaterials can be controlled by the concentration of water in the polyol solvent. Water can be added either as a starting material or separately during the polyol reaction. Generally, large particles can be formed, when a large concentration of water is used initially. The particle size can be significantly reduced with water injected separately into the hot polyol solvent during the reaction.[138]

ZnO and CoO nanoparticles were synthesised using the polyol method by Fievet et al. in 1994.[139] Recently, Feng et al. synthesised TiO_2 mesoporous nanospheres through the polyol method for application in Li batteries. They presented a comparable performance with the materials synthesised from other methods, but the reaction rate is accelerated.[140] Su et al. reported that WO_3 nanoparticles synthesised by the polyol method can be used for a NO_2 gas sensor. The large surface area of the WO_3 nanoparticles offered an improved sensitivity.[141] Itoh et al. reported a synthesis of large grain Al_2O_3 nanoparticles with the polyol method.[142] To date, a broad range of metal oxide nanomaterials were successfully produced using polyol method, including MnO_x nanowires,[143] V_2O_x nanoplates,[144] Fe_2O_3 polyhedral crystals[145] and Cu_2O hollow spheres.[146]

Furthermore, synthesis of complex ternary and multi-component metal oxides is

also possible with the polyol method. For instance, nanostructured $CuWO_4$ was obtained using the polyol synthesis with control of the reaction temperature and the polyol solution composition.[147] The $CuWO_4$ presented a pure phase with high crystallinity. Generally, it is difficult to avoid by-products, such as Cu(0), Cu_2O, CuO or WO_3,[147] if conventional hydrothermal or CBD methods were used. This is due to the lack of fine control of the growth process in these method to reach the restricted reaction conditions.[147] The high quality crystallized pure nanomaterials offer the potential for many applications, including catalysis, photocatalysis, sensors, magnetic oxides, DSSCs and high-power batteries.[148] For instance, the polyol synthesised $In_2(MoO_4)_3$:Eu nanoparticles showed highly efficient fluorescence,[149] and β-$SnWO_3$ presented excellent photocatalytic performance.[150]

2.5 Electrophoretic deposition

2.5.1 Fundamentals of electrophoretic deposition

Although the polyol method is versatile and effective to create complex nanomaterials, the products are normally suspended in the solution. In order to create electronic devices, such particulate nanomaterials must be deposited on to solid substrates. Conventionally, either spin-coating or spray-coating methods are used to create nanofilms. Although spin-coating can create high quality thin films, it is difficult to create a thick film. Spray-coating is very effective for creating thick films but control of the thickness is difficult. In this work, an EPD method has been used to deposit metal oxide thin film with an improved control of the morphology and the thickness of the films. The EPD phenomenon was firstly observed by Ruess in 1808. However, the practical use of this technique was much later in 1933.[151] An EPD process uses a suspension of nanoparticles in liquid with substrates. The particles, surrounded by the solvent molecules, normally have surface charges. The charged particles are driven by

an applied voltage towards the conductive substrate to form thin films. In comparison with other physical methods, EPD presents many advantages. It is highly versatile, and can be applied to different materials. In a comparison, a spin-coating process requires to add some polymers in the precursor solution in order to have a required viscosity. Thus a high temperature calcination becomes inevitable for the spin-coated thin films to remove the residual polymer. In an EPD process, since only the suspended material is in the organic solvent, the post calcination is not required. It is cost-effective for very simple apparatus with little restriction on the shape and size of the substrates. Particularly for nanomaterials, it offers a good control of the thickness, structure and morphology of the films.

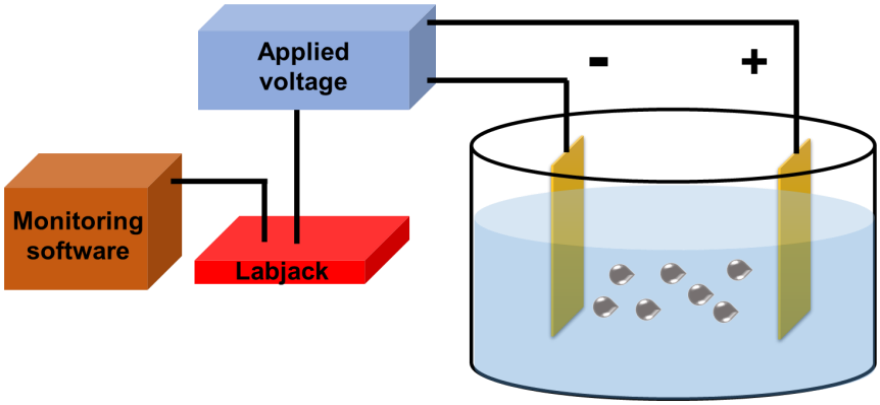

Figure 2.3 The setup and control system of electrophoretic deposition unit, the Labjack system is a data logger to record the applied and voltage and current between the electrodes.

The setup and control system for an EPD is shown in Figure 2.3. The power supply can be operated as a constant voltage or current source for EPD experiments, which is monitored through USB data logger (Labjack) linked with a computer. When the suspended particles are positively charged, the deposition occurs on the cathode; this

is called cathodic EPD as shown in Figure 2.4a. When the negatively charged particles are deposited on positive electrode, this is defined as anodic EPD, as seen from Figure 2.4b.

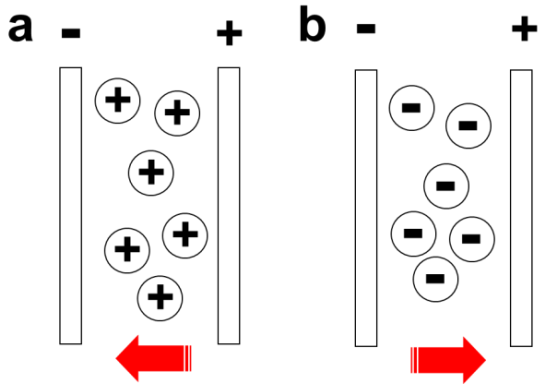

Figure 2.4 Schematic illustration of the EPD. (a) Cathodic and (b) anodic EPD process.

In this process, both the intrinsic physical and chemical properties of the suspension and the experimental conditions determine the morphology and structure of the deposited film. The suspension related parameters include the size, the zeta-potential and the conductivity of the suspended nanoparticles, and the dielectric constant and the viscosity of the solution. The particle size is obviously significant to affect the depositing process. It is important that the particles are capable of remaining completely dispersed and stable for homogeneous deposition. If the average size of the particles is too large, the particles usually precipitate quickly depending on the viscosity of the solution. The conductivity of the particle is also critical to determine the quality of the deposited film. Ferrari and Moreno showed that a higher conductivity of the suspension could lead a lower motion of the particles.[152] Conversely, when the suspension is too resistive, the particles are charged electronically, losing the stability of the particles.[152] The experimental conditions include the applied voltage, the deposition time, and the distance between two electrodes. The processing parameters of the EPD will be comprehensively studied in Chapter 5, in order to control the formation of the WO_3

nanofibrous thin film.

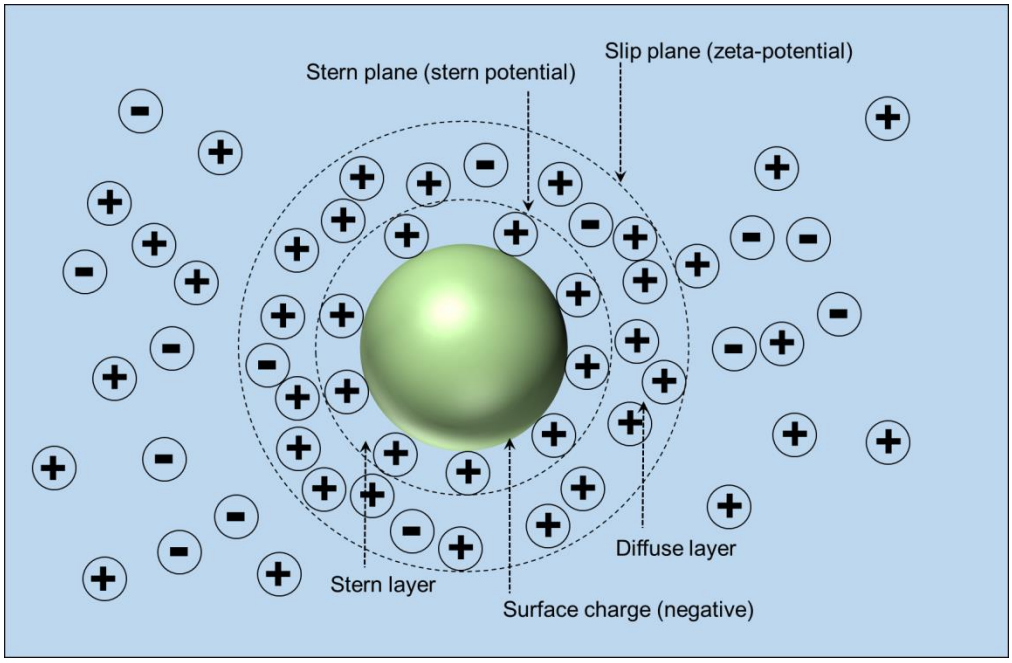

Figure 2.5 Schematic illustration of a double layer of a solid particle. The first layer (Stern layer) comprises ions adsorbed onto the particle due to chemical interactions. Second layer (diffuse layer) comprises ions attracted to the surface charge via Coulomb force.

Zeta-potential of the particles is a key factor in the EPD process. It is formed when the particles are suspended in a polar solution. When a solid particle is suspended in the dispersion medium, it preferentially adsorbs ions to form charged due to a double layer. The double layer is illustrated in Figure 2.5. The inner region is called Stern layer, in which, the particle has the solvent ions strongly bound with it. The outer region is defined as diffusion layer, it has a relatively low firmly association between ions and particles. The boundary between the diffusion layer and the dispersion medium is defined as the slip plane. Within the Stern layer, it shows a linear drop in potential until the Stern plane, then exponential decay (by a factor of 1/e) in the diffuse layer. The

difference of the electrical potential between the dispersion medium and the slipping layer of the suspended particles is defined as zeta-potential. In EPD process, the zeta-potential determines three significant factors. Firstly, it determines the intensity of the repulsive interaction between particles, stabilising the suspension in the solution. Secondly, it determines the migration velocity of the particles. Thirdly, it determines the density of the deposition. The zeta-potential can be controlled by adding charging agents to the suspensions, such as acid, base and specifically adsorbed ions. For instance, Chen et al. reported that the deposition rate of Al_2O_3 powder became maximal at *pH* value of 2.2 in ethanol, due to the largest zeta-potential of Al_2O_3 being observed at this *pH* value.[153]

In an EPD process, as a suspension is used for the deposition, the solubility of the particles in the dispersion medium is not a necessary concern. Therefore, a rich variety of liquid organic media can be considered for this purpose. The dielectric constant of the organic medium determines the incidence of the deposition. When the dielectric constant is too low, the deposition can fail. Since the insufficient dissociative power or a low adsorptive charging of the particles could limit the movements of the particles. In contrast, if the dielectric constant is too high, the high ionic concentration in the liquid reduces the size of the double layer region, affecting the electrophoretic mobility. The dielectric constants of the common solvents for EPD are shown in Table 2.1.[151]

Table 2.1 The dielectric constants of common solvents for EPD.[151] Ethanol and acetylacetone are considered as good solvents for EPD.

Solvent	Relative dielectric constant
Methanol	32.63
Ethanol	24.55
n-Propanol	20.33
Iso-propanol	19.92
n-Butanol	17.51
Ethylene glycol	37.7
Acetone	20.7
Acetylacetone	25.7

2.5.2 Applications of the electrophoretic deposited nanomaterials

EPD is an efficient and reliable method to assemble materials into a thin film with a controllable structure. Assembling nanomaterials is usually based on the creation of the free-standing nanomaterials, which are then fused into densely packed thin film structure. The applications of such materials are highly affected by the size and shape of the individual nanomaterial, and the geometrical arrangements of the produced structure. For instance, a hot-pressing method was used to fuse electrospun metal oxide nanofibres into a thin film for PEC water splitting, but the nanofibrous structure is difficult to preserve with such processes.[110]

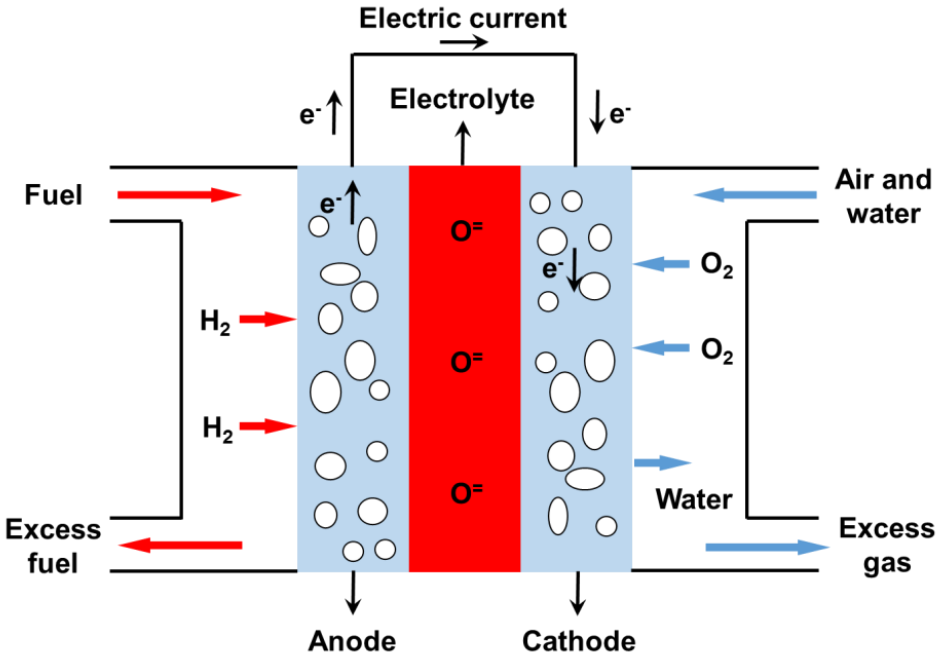

Figure 2.6 Schematic illustration of basic working mechanism for an SOFC fuel cell. Air is carried to the cathode with the dissociation of O_2 gas to O_2 anions, which migrate over to oxidise the fuel (H_2) to generate electric energy.

The depositing rate of a EPD method is fast, and the thickness of film can be controlled with the concentration of the suspension, and the depositing time.[72] Because the double layer system of colloidal suspensions can form from many materials, so the concept of EPD can be conducted with a wide range of the nanomaterials, such as polymers,[154] biomaterials,[155] ceramics[156, 157] and metals.[158] Subsequently, a lot of applications were developed based on this method. Kumancheva et al. prepared a highly ordered PMMA monolayer film using the EPD method.[159] In a comparison with the self-assembly method, the quality of the prepared PMMA film is quite similar, but the deposition rate of EPD is much faster.[159]

The EPD method has shown special advantages to fabricate thin films for solid oxide fuel cells (SOFCs).[160] Generally, a SOFC cell comprises a solid electrolyte film between the oxidiser electrode (cathode) and the fuel electrode (anode), as shown in

Figure 2.6. A porous or permeable structure is required for the electrodes, in order to maximise the oxidation reaction by supplying oxidiser at the cathode and fuel at the anode. Meanwhile, the electrolyte layer must be dense enough to avoid any leakage of gases across the layer. Conventionally, chemical vapour deposition, pulsed laser sputtering deposition, molecular beam epitaxy and combustion chemical vapour deposition methods were used to produce SOFCs. However, these deposition methods require expensive equipment with sophisticated processes, which lead a high manufacturing cost for commercialisation. Conversely, using the EPD method to fabricate thin films from colloids provides improved efficiency with a cost-effective route to make SOFC electrodes. A careful control of the parameters can easily generate a porous electrode film and dense electrolyte film in a one-pot reaction.

Ishihara et al. used EPD to fabricate SOFCs.[161] In their studies, the cermet anode was made of platinum-coated-nickel-CaO-stabilised ZrO_2 (Ni-YSZ), the cathode was formed with porous Sr-doped $LaMnO_3$ (LSM), and ZrO_2 was used as electrolyte. Porous electrodes and non-porous electrolyte were achieved, such control results in a high performance of the SOFC.[161]

2.6 Conclusions

The synthesis methods used in my research work were reviewed, including electrospinning/electrospray technique, solution-phase method, and EPD method. The mechanisms of electrospinning/electrospray method to create nanofibres and the nanoparticles were studied. For wet-chemistry synthesis, two methods were reviewed, the CBD method was used to synthesise ZnO nanorods, and the polyol method was applied for the formation of metal nanowires and metal oxide nanoparticles. The mechanism of the EPD method to fabricate nanostructured thin films is also reviewed. The related applications were also discussed, including applications in DSSC, for

transparent and flexible electrodes and for SOFC electrodes.

Chapter 3 Characterisation of nanomaterials and their applications

3.1 Abstract

This chapter described the instruments to analyse the nanomaterials, and the characterisations of the related applications. The details of the simulated solar source were presented for photoelectrochemical (PEC) water splitting, dye-sensitised solar cells (DSSCs), and organic solar cells (OSCs). The principles of the instruments were summarised, involving scanning electron microscopy (SEM), X-ray powder diffraction (powder XRD), ultraviolet/visible (UV/Vis) spectroscopy and atomic force microscopy (AFM). The energy harvesting applications were further explained, including PEC, DSSC, OSC and triboelectric nanogenerator (TENG).

3.2 Instrumental characterisations

3.2.1 Solar simulator

A standard light source is important for reliable measurements of the solar energy related applications. When light is shining from the Sun to the surface of the Earth, the atmosphere of the earth affects light radiation by both absorption and scattering. If the thickness of the atmosphere normal to the surface of the earth is l_0, the optical path length of the solar radiation through the atmosphere (l) at incident angle (a) is defined as Equation 3.1.

$$l = l_0 / \cos a \qquad \text{(Equation 3.1)}$$

The ratio l/l_0 is defined as the air mass factor (AM), the light intensity is decreased with increasing path length of the radiation. The light irradiance outside of the

atmosphere is defined as AM 0. The perpendicular incidence of the light on the surface of the earth is denoted as AM 1. For moderate weather, the average incidence light air mass is normally specific as AM 1.5G, corresponding to the incident angle of 48.2 , with respect to the surface normal. The AM 1.5G is defined as 1 sun, given a mean intensity of the irradiation of 100 mW/cm^2.

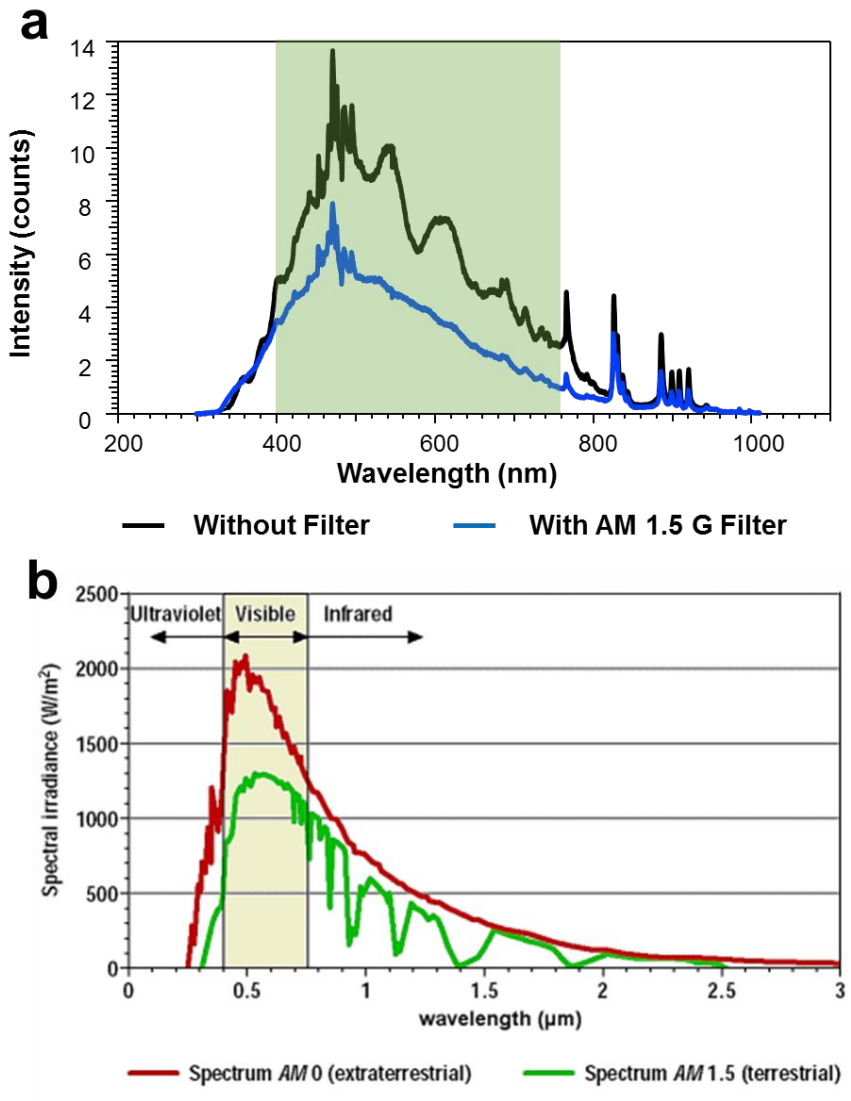

Figure 3.1 (a) light spectrum from 300 W arc xenon lamp with and without AM 1.5G filter and (b) natural solar radiation spectrum from AM 0 and AM 1.5G. (Figure 3.1b is adapted from reference[162])

In my research for the applications of PEC water splitting and solar cells, a 300 W xenon arc lamp was used to simulate the solar radiation. The light source was calibrated as standard 1 sun power radiation, using the International Electrochemical Commission (standard #60904-1). The light has a top-hat intensity profile on the samples. The output of the light power is 100 mW/cm^2 with an AM 1.5G filter at temperature of 25 $^{\circ}$C. Figure 3.1a shows the light spectrum from the xenon lamp with and without AM 1.5G filtration. Figure 3.1b presents the light spectrum from natural AM 0 and AM 1.5G.[162] After the AM 1.5G filtration, if the xenon is calibrated at 100 mW/cm^2, the spectrum of the light source is quite close to the natural AM 1.5G, especially in the UV spectral range. But the natural AM 1.5G light has a stronger intensity in the visible spectrum than that from the xenon lamp. The UV light filter (GG395, Schott) and visible light filter (UG11, Schott) are also used to further measure the photoconversion efficiency within the visible and UV spectrum of the AM 1.5G light.

3.2.2 Scanning electron microscope

The modern scanning electron microscope (SEM) was developed by Sir Charles W. Oatley with his students at Cambridge University from 1948 to 1961.[163] It is one of the key instruments to study the morphologies and to characterise the chemical compositions of nanostructured materials. A photograph of the SEM is shown in Figure 3.2a, and the corresponding schematic views of the critical components are presented in Figure 3.2b. The SEM in the University of Sussex (Chapter 4, 5 and 6) is a JSM 820M, which is manufactured by Jeol, and the one in the collaborative university (Chapter 7 and 8) is NanoSEM 450, manufactured by FEI Nova. The samples in my research are generally prepared by adhering them onto conductive carbon tapes, while samples with high resistance, such as semiconductors and polymers, require sputter coating of thin metal layer to eliminate sample charging effects.

In an SEM, a high energy electron beam is generated from the electron gun, and is accelerated by a high voltage. The beam is focused through a system, which involves condenser lenses and probe lens, to reach the sample. Scanning coils are used to scan over the sample by deflecting the beam horizontally and vertically. The signals provided by secondary and back-scattered electrodes are collected for the morphological information, and projected as image on a computer.

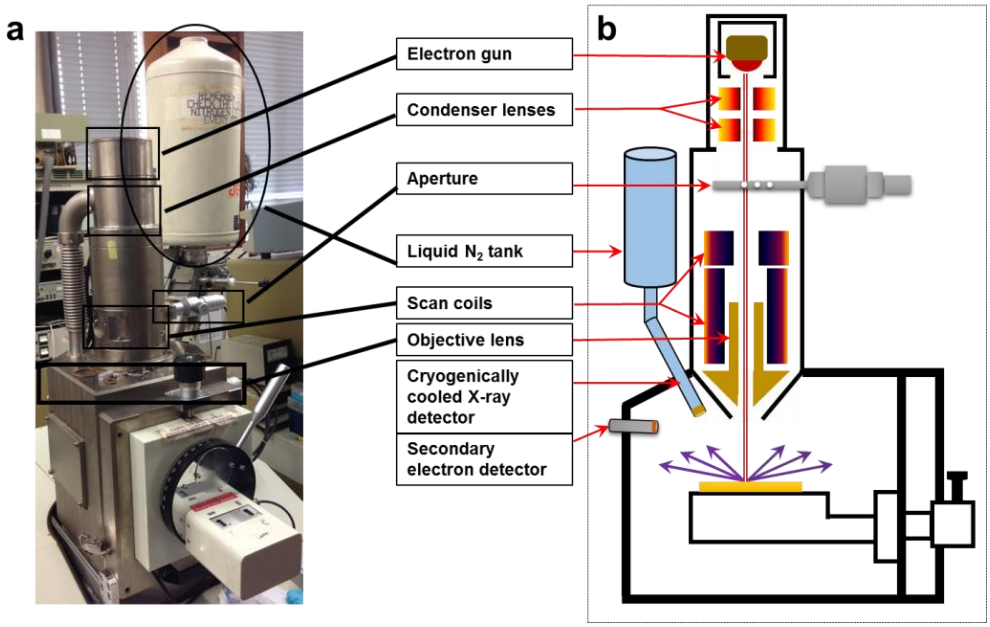

Figure 3.2 (a) A photograph of the SEM, and (b) the corresponding schematic diagram. The illustrated components include electron gun, condenser lenses, aperture, liquid N_2 tank, scan coils, objective lens, cryogenically cooled X-ray detector and secondary electron detector.

In SEM, the inelastic secondary electrons are used to provide topological information of samples. As the primary electron beam interacts with the sample, the core level electrons of the sample are ionised, which leaves a hole in the core level. An electron in an upper level will relax and fill the hole. In this process, energy,

corresponding to the difference in binding energy, is released into the system, either as an X-ray photon, or by ionising another electron (secondary electron) at the upper level. The secondary electrons normally have a low kinetic energy in the range of 100~500 eV, therefore have small mean free path with sampling depth and profile. This is essential for high resolution imaging. In addition to the secondary electrons, the back-scattered elastic electrons are also collected to show the surface morphology with an enhanced contrast determined by the nuclear scattering behaviour related to the atomic weight. However, the elastic electrons normally have high kinetic energy up to 30 keV, in order to reduce space charge dispersion. The back scattered electrons with such high energy have large mean free path, resulting in deeper and larger sampling profile with reduced image resolution.

In addition to the secondary electron and back scattering electron detection, SEM is also able to identify elements by collecting the X-ray emission signal from the electron scattering process. The energy of the emitted X-ray corresponds to the binding energy difference of the particular atom, which can be used to identify the elemental composition. The fluorescent intensity is proportional to the quantities of the elements in the sample. In my work, the information provided from the secondary electron and X-ray florescence are combined to characterise the nanomaterials.

3.2.3 X-ray diffraction

XRD is a technique to identify the crystal structures of nanostructured materials. The periodic atomic arrangements of the crystal interact with incident X-rays to produce a constructive interference of the diffracted beam, which can be detected, to present the diffraction patterns in monitoring software. The spacing in the sets of the crystal planes can be characterised by specifying the diffraction angle, the geometry of the X-ray diffractometer is shown in Figure 3.3, where the detector follows the diffraction angle

for collecting the scattered X-rays. When the wavelength (λ) of the X-ray is fixed, the relationship between the spacing among planes in the crystal lattice and the angle between the incident beam and scattering planes is defined by Bragg equation, as shown in Equation 3.2,[164]

$$n\lambda = 2d_{hkl}\, sin\, \theta_{hkl} \qquad \text{(Equation 3.2)}$$

where d_{hkl} is the spacing between the plane in the atomic lattice, θ_{hkl} is the angle between the incident X-ray beam and the scattering planes, and *h*, *k*, *l* are the Miller indices of the crystal plane.

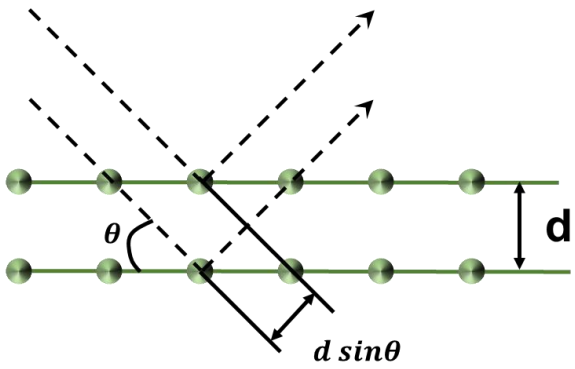

Figure 3.3 X-ray diffraction follows the Bragg's law when an X-ray passes through the crystal lattice.

Two modes are usually used in powder XRD. One mode is $\theta/2\theta$ scan, in which, the sample is rotated relative to the X-ray incidence by θ, the detector is rotated by 2θ. In the other mode, the detection angle is rotated to collect the crystal information, while the incident angle is fixed. The standard $\theta/2\theta$ scan is commonly applied for most powder samples. When incident angle is fixed and only the detection angle moves, a very thin film sample can be analysed, since the X-ray beam can be fixed at a small

incidence angle, which samples a shallow depth of the material. For identifying polymorphs, such as TiO_2 anatase and rutile, the unit cell vectors (*a b* and *c*) and the symmetry of the crystals are determined quantitatively. Table 3.1 lists the Miller indices, *d* spacing, diffraction angles 2θ and relative diffraction intensities of low index crystal planes of anatase and rutile.[165] This data was used as the standard to identify the TiO_2 nanostructured materials in this work.

Table 3.1 The XRD patterns of the anatase and rutile.[165]

Anatase

h	***k***	***l***	***D***	***2 θ***	***I***
1	0	1	3.5163	25.308	100.0
1	0	3	2.4307	36.950	6.5
0	0	4	2.3786	37.790	20.3
1	1	2	2.3322	38.571	7.4
2	0	0	1.8921	48.046	28.2
1	0	5	1.7001	53.884	18.1
2	1	1	1.6662	55.071	17.8
2	1	3	1.4931	62.115	3.1
2	0	4	1.4808	62.690	13.9
1	1	6	1.3642	68.754	6.2
2	2	0	1.3379	70.302	6.8
2	1	5	1.2646	75.051	10.5
3	0	1	1.2505	76.049	9.8

Rutile

h	k	l	D	2θ	I
1	1	0	3.2477	27.440	100.0
1	0	1	2.4875	36.078	46.0
2	0	0	2.2965	39.196	7.1
1	1	1	2.1873	41.239	18.0
2	1	0	2.0541	44.049	6.5
2	1	1	1.6874	54.323	56.0
2	2	0	1.6239	56.634	16.5
0	0	2	1.4795	62.750	7.8
0	0	2	1.4795	62.750	7.8
3	1	0	1.4524	64.057	8.1
3	0	1	1.3598	69.001	19.6
1	1	2	1.3464	69.792	9.8
3	1	1	1.3038	72.534	2.2
2	1	2	1.2005	79.827	1.1

In addition, line widths in diffraction peaks are also important to indicate the crystal grain size and the density of defects. The peak width is inversely proportional to the average crystal size of the sample. The crystal domain of the nanostructures can be quantitatively determined using Scherrer's equation:[166]

$$D = (K\lambda)/(\beta \cos\theta) \qquad \text{(Equation 3.3)}$$

where D is the diameter of crystal; K is the shape factor (Scherrer constant), which varies from 0.62 to 2.08, and commonly used either as 0.94 or 0.89. The value of 0.94 is

used for the assumptions of full width half maximum of spherical crystals with cubic symmetry, and 0.89 is used for the assumption of integral breadth of spherical crystal with cubic symmetry.[167] θ is the Bragg angle of the diffraction peak (in degrees); λ is the wavelength of the X-ray source (Cu target, λ = 1.541 Å in this work); and β is the linewidth of the diffraction peak, which is defined as:

$$\beta = \sqrt{\beta_M^2 - \beta_I^2} \qquad \text{(Equation 3.4)}$$

where β_M is the linewidth and β_1 is the instrumental broadening, which is determined by the linewidth (FWHM) from standard crystallised particles of size (larger than 200 nm).

3.2.4 Ultraviolet/visible spectrometer

UV/Vis spectrometer is an instrument to study the optical absorption within the typical wavelength ranges from 200 to 1100 nm. The UV-Vis in Chapter 7 and 8 is UV2550, manufactured by Shimadzu. The result of UV-Vis is commonly expressed as either absorbance (*A*) or transmittance (*T*). The method quantitatively determines the optical properties of the solution usually following Beer-Lambert law, which is shown in Equation 3.5:[168]

$$A = log_{10}(I_0/I) = \varepsilon cL \qquad \text{(Equation 3.5)}$$

where I_0 and I are the incident and transmitted light intensities, respectively, referring to the results from the reference and the sample. The constant ε is the molar absorptivity or extinction coefficient of a sample, and L is the optical path length. The extinction coefficient can be calculated from the absorption by the solution with known concentration, c. The transmittance can be calculated using Equation 3.6:

$$T = 10^{-A} \quad \text{(Equation 3.6)}$$

In this research, UV-Vis spectrometer was used to determine the optical properties of the solid samples; it is significant to the optical characteristics of transparent triboelectric devices and semi-transparent OSCs. The optical properties of the semiconductors are useful to study the band gap, which can be calculated through Equation 3.7,[169] describing the Tauc relationship:

$$(\alpha h\nu)^n = A_0(h\nu - E_{bg}) \quad \text{(Equation 3.7)}$$

where A_0 is a constant that depends on the electron-hole mobility of the material, h denotes Planck`s constant, *v* is the frequency of the incident photon, so the term of $h\nu$ is light intensity. *n* can either be ½ or 2, when the semiconductor is indirect or direct band gap, respectively. E_{bg} is the optical band gap energy, and α is the measured absorption coefficient, which is obtained from Equation 3.8,

$$\alpha = 1/d \ln(1/T) \quad \text{(Equation 3.8)}$$

where d is the thickness of the sample film, and *T* is the optical transmittance. A typical Tauc plot is shown in Figure 3.4. However, when a non-transparent substrate is used or a semiconductor film is too thick, the optical properties of the solid film have to be measured through reflected light from the semiconductor film. An integrating sphere can be used for this purpose. The band gap is calculated using Equation 3.9:

$$E_g = h * c/\lambda \qquad \text{(Equation 3.9)}$$

where c is the speed of light, and λ is cutting off wavelength.

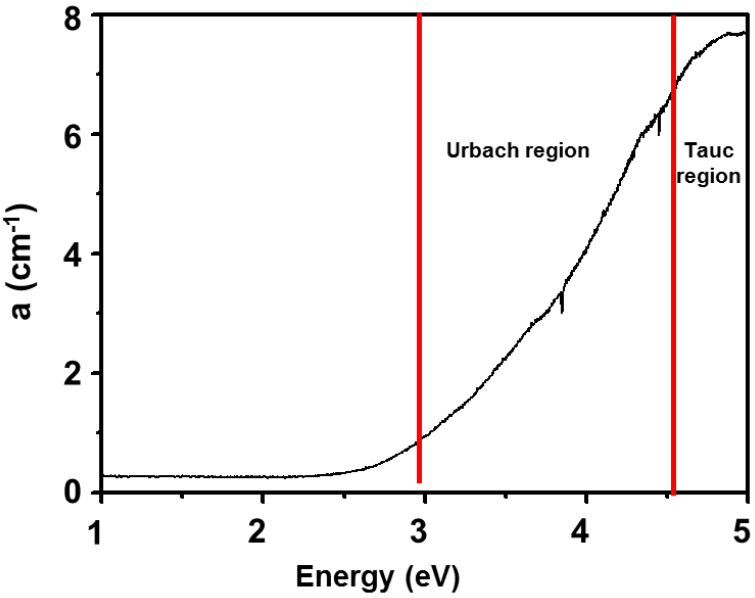

Figure 3.4 A typical example of the Tauc plot, showing the Tauc region and the Urbach region.

In addition, the crystal defects or dopant ions in the semiconductor crystal lattice can be investigated using the band tailing in the band gap plot, which results in an exponential tail at the edge of the optical absorption. The tail is defined as the Urbach tail, which corresponds to the width of the localised state available in the optical band gap that affects the optical band gap structure and optical transitions, the Urbach region is also shown in Figure 3.4. In the exponential edge region, Urbach rule is expressed as Equation 3.10:[170]

$$a = a_o \exp(h\nu/E_u) \qquad \text{(Equation 3.10)}$$

a_o is a absorption constant of a defect free single crystal and E_u is the Urbach energy which characterises the slope of the exponential edge. The Urbach plot and the following relation were used to calculate the E_u of the samples:

$$E_u = [d(\ln a)/d\,(hv)]^{-1} \qquad \text{(Equation 3.11)}$$

E_u can be determined from the inverse of the slope of $\ln a$ as a function of hv. The value of E_u indicates the crystal quality of the semiconductors. A large value of $E_u$implies a high structural disorder, and a large quantity of defects in the film.[171] Experimentally, the crystal quality can be conventionally improved through an annealing process.

3.2.5 Atomic force microscope

AFM is one type of scanning probe microscope (SPM).[172] The first AFM was demonstrated at 1986 by Binnig. *et. al.* at IBM.[173] In my work, the AFM in Chapter 7 and 8 is SPI 4000, manufactured by Seiko. The working mechanism of AFM is shown in Figure 3.5a, a sharp tip is mounted on a micro-fabricated cantilever, which is made of silicon or silicon nitride. The measurements are performed with an optical tracking system: when a tip is scanning over the sample, a laser is focused on the back of the cantilever, which is normally coated with Al to improve the reflection. The cantilever scans through the surface of the sample while maintaining a certain level of the light deflection. Alternatively, the cantilever is mechanically oscillated to reduce the direct contact with a sample. The phase and amplitude of the oscillation will be affected by the atomic interaction between the tip and the sample surface, they are monitored by the deflected laser beam. With a fixed resonant frequency, the cantilever tip height is controlled by a piezoelectric tube to achieve the set values for the phase shift and the

oscillation amplitude. Topographic information of the sample can be collected by plotting the cantilever height in z direction, while scanning in x, y directions over the sample.

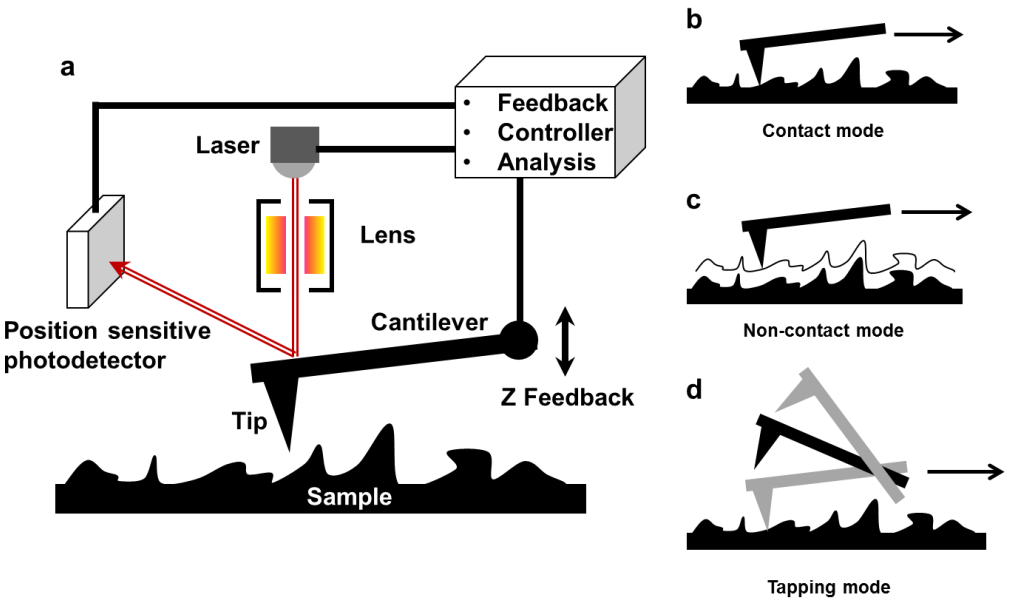

Figure 3.5 (a) the schematic diagram of an AFM with three operation modes: (b) contact mode, (c) non-contact mode and (d) tapping mode.

AFM can be operated in three modes, according to the control of the tip: contact mode, non-contact mode and tapping mode. In the contact mode, as shown in Figure 3.5b, a tip statically touches a sample surface, and the variation of the cantilever deflection directly converts into topographic data. In this mode, a sample is scanned with frictional and adhesive forces. Thus, the morphologies of the sample can be easily damaged. Therefore, this mode is only suitable for samples with extremely smooth surfaces. The non-contact mode is illustrated in Figure 3.5c, minimises the damage of a sample by avoiding a direct contact. When an AFM works under this mode, the points for the variations of the deflections are reduced to the minimal value. Although, this

mode is better in preserving the morphologies of samples, it usually gives low resolution topographic images. The most reliable operation of AFMs is the tapping mode, as shown in Figure 3.5d. The detail of this operation mode is discussed above, it has a small interaction with samples. The signals collected from the phase shifts and variations with oscillating amplitudes are normally clean with low background noise. This working mode can result in a high resolution topographic image, and also avoids the damage of the sample surface. However, the time to scan over a sample is longer than the other two modes, therefore the samples for the tapping mode are required to be stable.

In my research, AFM was operated in the tapping mode to determine the morphology of the silver nanowire transparent electrode in Chapter 7 and 8. Especially, when applying them for OSCs, since the functional layers of OSC are fragile and very thin (few tens of nanometres).

3.3 Application characterisations

3.3.1 Photoelectrochemical water splitting

PEC water splitting is demonstrated to harness the solar energy and convert into H_2. The standard three-electrode configuration in Figure 3.6 was used to characterise the performance. A platinum electrode was used as the counter electrode and a KCl saturated Ag/AgCl electrode was used as a reference electrode. 1 M KOH solution (*pH* 13.6), was used as the electrolyte for TiO_2 photoanodes (Chapter 6), which was changed to 0.5 M H_2SO_4 (*pH* 0) for WO_3 photoanodes (Chapter 5). This is because the efficiency of the energy extraction is optimised for WO_3 by varying the electrochemical potential of the redox system,[174] since the CB of WO_3 is not sufficiently negative to reduce water as seen in Figure 1.9. Although the standard redox potentials are fixed by the desired chemistry (water oxidation and reduction), the relative potentials for reducing and

oxidising water can be shifted with a change of the *pH* of the solution. Equation 3.12 and 3.13 show the redox potentials for the water splitting as *pH* dependent via the Nernst equation.[175]

$$E^o(O_2/H_2O) = 1.23\,V - 0.059\,V \times pH\ (vs\ NHE) \qquad \text{(Equation 3.12)}$$

$$E^o(H^+/H_2) = 0\,V - 0.059\,V \times pH\ (vs\ NHE) \qquad \text{(Equation 3.13)}$$

In PEC water splitting system, when the concentration of protons is increased (*pH* decrease), the redox potentials, $E^0(H^+/H_2)$ and $E^0(O_2/H_2O)$, are also decreased. So as example for a WO_3 photoanode, the down shift of $E^0(H^+/H_2)$ $E^0(O_2/H_2O)$ moving close or even below the CB of WO_3, giving an increased PEC efficiency. Meanwhile, the decreased $E^0(O_2/H_2O)$ has no significant effective to the PEC efficiency, since the VB is already lower than the $E^0(O_2/H_2O)$ initially. The PEC applications were investigated with a standard 1 sun illumination (AM 1.5G). UV and visible light were also measured for the WO_3 sample in Chapter 5 using visible and UV optical filters. The illumination area on the photoanode is kept at 1 cm^2.

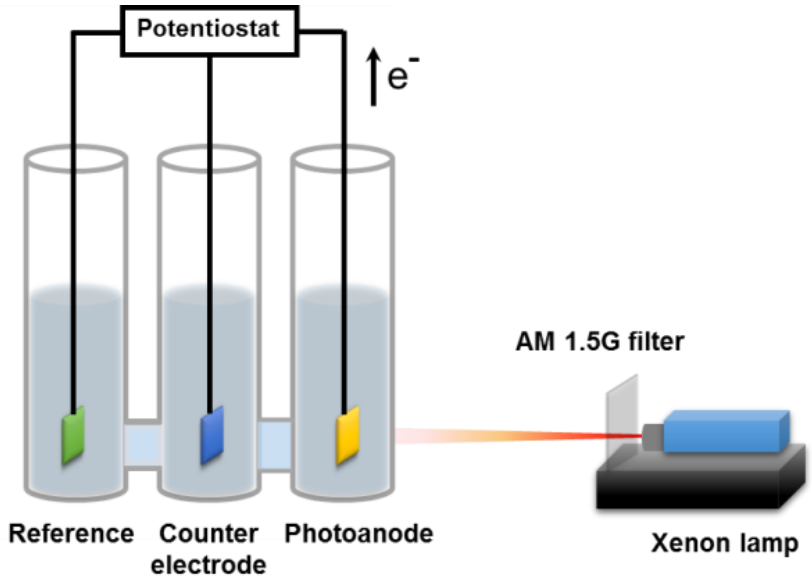

Figure 3.6 A schematic diagram of three-electrode configuration to measure the photoconversion efficiency of the PEC water splitting. A photoanode (metal oxide semiconductors), a counter electrode (Pt foil) and a reference electrode (KCl saturated Ag/AgCl) are immersed in the electrolyte without any membrane among them.

As most of my photoanodes are based on *n*-type semiconductors, H_2 is evolved at the cathode, which is a counter Pt electrode, where O_2 is evolved. Photoanode, counter electrode and reference electrode are immersed in the electrolyte without any membrane. Since a reasonable concentrated ionic solution (normally 1M) is used as electrolyte, such electrolyte has limited influences to the measurements of the cell. A potentiostat was used to monitor the behaviour of the photocurrent density versus the applied voltage. The PEC water splitting efficiency can be calculated from the data of the photocurrent density versus the applied voltage using Equation 3.14: [45]

$$\eta_1(\%) = J_p\left(E^0_{rev} - E_{app}\right)/P_{in} \times 100\% \qquad \text{(Equation 3.14)}$$

where η_1 is the photoconversion efficiency of the photoanode, J_p is the photocurrent

density (mA/cm^2), E^0_{rev} = 1.23V, E_{app} = E_{meas} - E_{oc} where E_{meas} is the working electrode potential (versus Ag/AgCl) and E_{oc} is the working electrode potential (versus Ag/AgCl) under the open circuit condition (J_p = 0 mA/cm^2) whilst illuminated, and P_{in} is the incident light power intensity. As illustrated in Figure 3.7, the cross point of the measurements, with and without light irradiations, is defined as open circuit voltage. Then the short circuit current can be identified at the potential about 1.23 V above the open circuit voltage. The photocurrent at this potential represents the short circuit current.

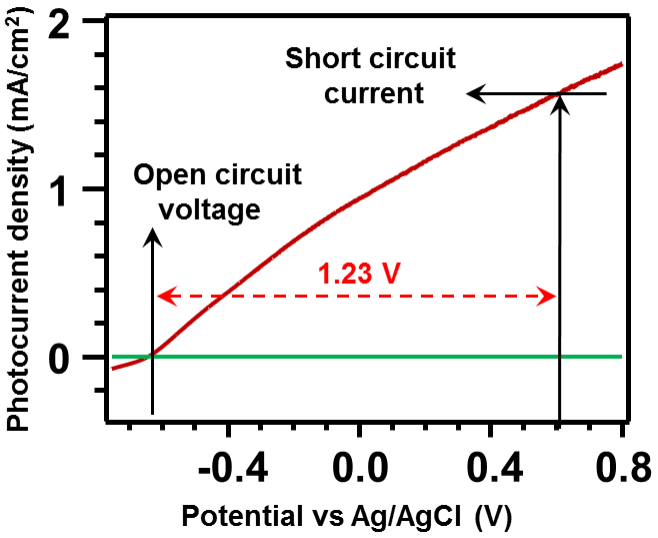

Figure 3.7 A typical *I-V* curve of a PEC water splitting measurements. The green curve is a measurement without light irradiation. Under irradiation, the open circuit voltage and short circuit current are indicated.

3.3.2 Measurement of the dye-sensitised solar cells and organic solar cells

In my research of DSSCs, TiO_2 nanostructured films were dyed with the inorganic Ru complex as photoanodes, a Pt foil was used as a counter electrode, and liquid I_2/I_3^- is

used as electrolyte. An OSC is fabricated by spin-coating organic thin films, a bulk heterojunction (BHJ) structured poly(3-hexylthiophene):indene-C60 bis-adduct (P3HT:ICBA) film was used as an active layer. The details of the components to fabricate DSSC and OSC are presented in Chapter 6 and chapter 8, respectively. Both DSSC and OSC require good packages to seal the cells. For DSSC, the liquid electrolyte is fairly easy to evaporate under AM 1.5G irradiation, such evaporation easily affects the performance of the DSSC. For OSC, the active organic layer is highly sensitive and degradable by contacting with moisture. In my research, both of the cells were sealed with UV curing epoxy resin (Solarez).

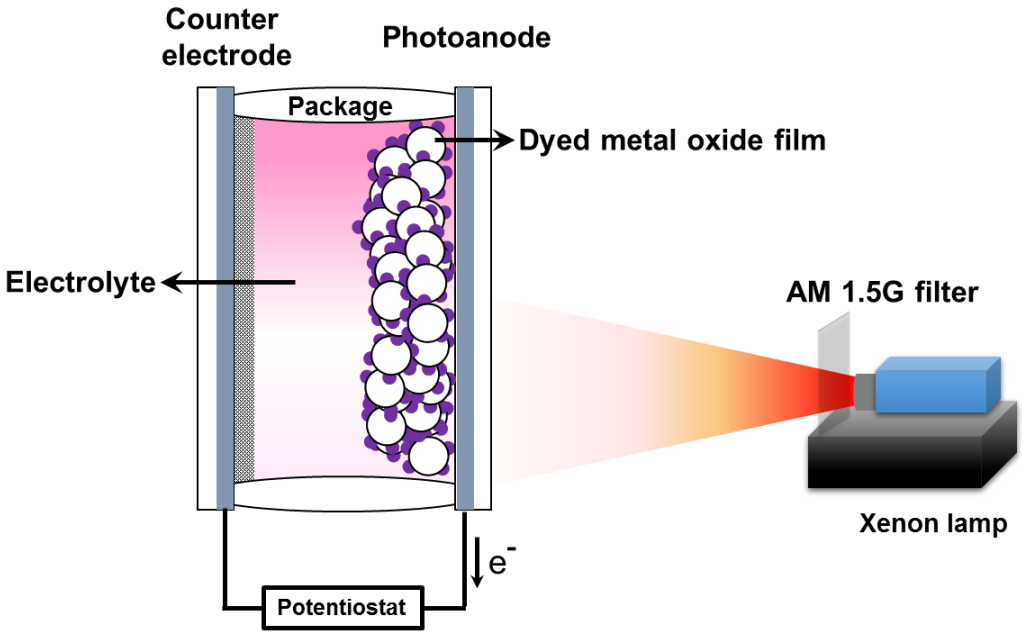

Figure 3.8 A typical setup to measure the photoconversion efficiency of the DSSC, which is constructed by packaging electrolyte between a photoanode and cathode. Under the AM 1.5G irradiation, the output performance can be measured using a potentiostat.

A typical photoconversion efficiency measurement of a solar cell is shown in

Figure 3.8. This system was used to characterise the performances of the DSSCs and the OSCs in my research. The setup of solar cell is slightly different to that of PEC water splitting. For solar cells, a potentiostat was connected with the photoanode and cathode to monitor the behaviour of the photocurrent density versus the applied voltage. The energy conversion efficiency (η_2) is defined as by the ratio of the maximum generated electric power (P_{max}) and the incident light power (P_{in}), following Equation 3.15:[176]

$$\eta_2 = P_{max}/P_{in} = V_{OC} \cdot J_{SC} \cdot FF/P_{in} \qquad \text{(Equation 3.15)}$$

where V_{oc} is the open circuit voltage, obtained when the current is zero, J_{sc} is the short circuit current that obtained when the voltage is zero, and *FF* is the fill factor. *FF* can be used to calculate the electrochemical efficiency of solar cell through Equation 3.16:[177]

$$FF = I_m \cdot V_m/V_{OC} \cdot J_{SC} \qquad \text{(Equation 3.16)}$$

where I_m and V_m correspond to the current and voltage that are capable of generating the maximum electric power, respectively. A typical current-voltage curve is shown in Figure 3.9, illustrating the parameters abovementioned to calculate photoconversion efficiency of solar cells.

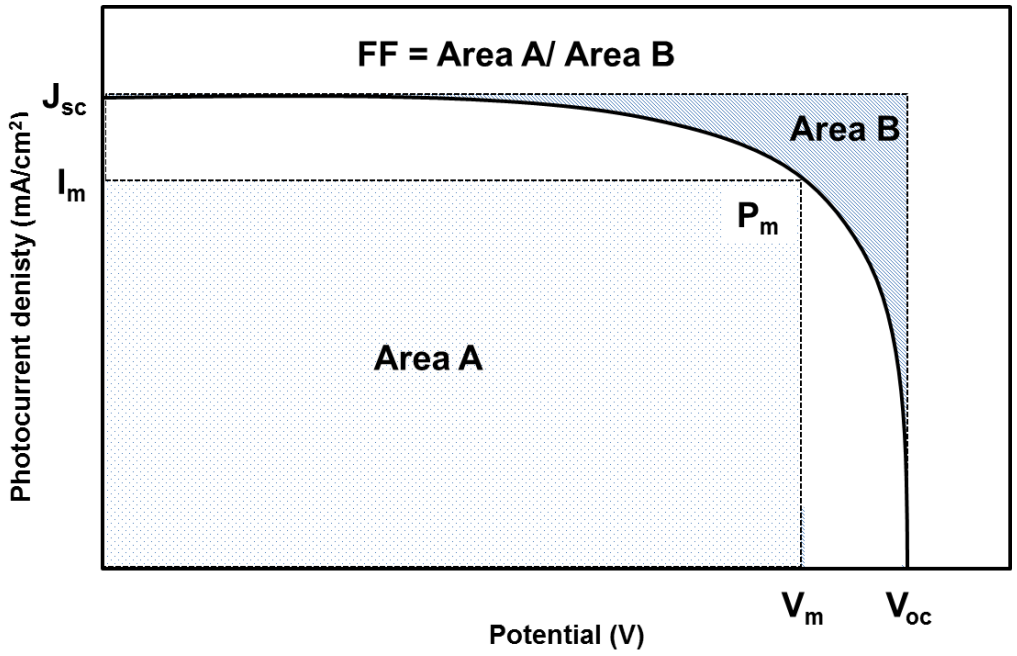

Figure 3.9 A typical *I-V* curve of a DSSC measurement, illustrating the fill factor (*FF*), short circuit (J_{sc}) density, open circuit voltage (V_{oc}), maximum power output (P_m), photocurrent at maximum power (I_m) and voltage at maximum power (V_m).

The efficiency of a solar cell is mainly determined by the light absorption of the active layer. The spectral response ($S(\lambda)$) of a solar cell is given as Equation 3.17:[178]

$$S(\lambda) = J_{SC}(\lambda)/\Phi\ (\lambda) \qquad \text{(Equation 3.17)}$$

where $\Phi(\lambda)$ and $J_{SC}(\lambda)$ are the photon flux and short circuit current at the wavelength of λ, respectively. This response can be directly related to the external quantum efficiency $(EQE)(\%)$, shown in Equation 3.18:[179]

$$EQE(\%) = (hc \cdot J_{SC})/(q \cdot S(\lambda)) \qquad \text{(Equation 3.18)}$$

where *h* is Plank`s constant, *c* is speed of light and *q* is elementary charge.

3.3.3 Triboelectric generator measurements

Triboelectric devices were fabricated to harvest mechanical energy. A general working mechanism is illustrated in Section 1.4.2. A setup is shown in Figure 3.10, two separated electrodes are stacked parallel as a general TENG. A resonator (JZK, Sinocera) drives a TENG to work (compression and separation) at a certain frequency (ranging from 0 to 10 Hz) controlled by a signal generator (YE 1311-d, Sinocera). Here the resonator is used to simulate an input of mechanical energy. A output current of TENGs were measured by a low noise current preamplifier (Keithley 6514), while the output voltage was measured by a low-noise voltage preamplifier (Stanford Research SR560). The output signal was recorded by a computer with homemade software.

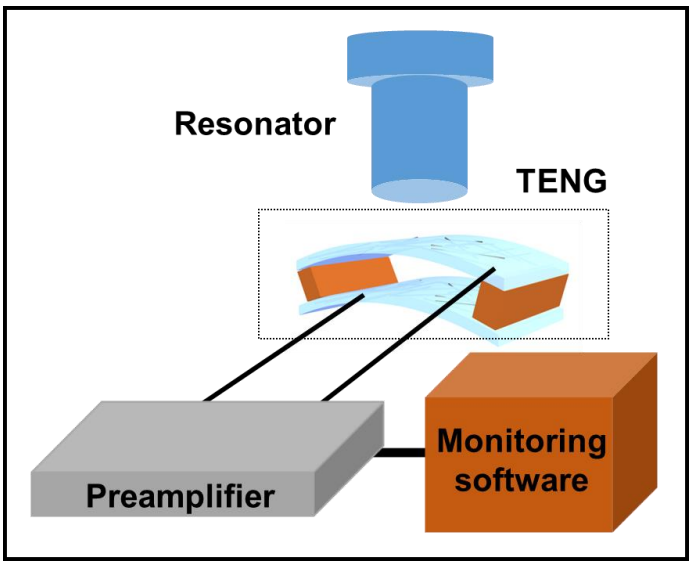

Figure 3.10 The schematic diagram of the setup for stimulating TENG to harvest mechanical energy. The resonator is an electronic device to simulate the input mechanical energy to trig the TENG, and the output performance is collected a monitoring software through a preamplifier.

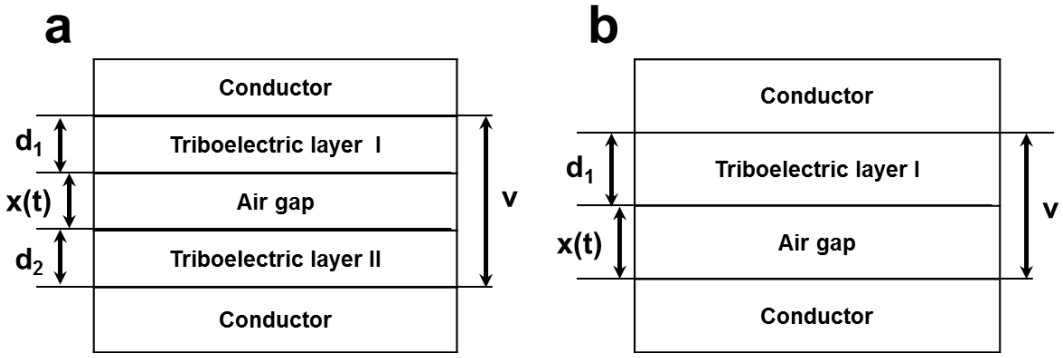

Figure 3.11 A schematic diagrams of (a) dielectric-to-dielectric-mode TENG and (b) conductor-to-dielectric-mode TENG.

Two typical structural modes of the TENGs were reported: the dielectric-to-dielectric-mode and the conductor-to-dielectric-mode, the corresponding schematic diagrams are illustrated in Figure 3.11a and 3.11b, respectively. In a dielectric-to-dielectric-mode, when contact surface area is *S*, the electric field strength at each region is given by the following equations.[180] The inside surface of triboelectric I layer (Figure 3.11a) is shown in Equation 3.19:

$$E_1 = -Q/S\varepsilon_0\varepsilon_1 \qquad \text{(Equation 3.19)}$$

where Q is the amount of the transferred charge in between the inner layers, ε and ε_0 are the dielectric constants of the triboelectric I layer and the air space, respectively. The inside surface of triboelectric II layer (Figure 3.11a) is shown in Equation 3.20:

$$E_2 = -Q/S\varepsilon_0\varepsilon_2 \qquad \text{(Equation 3.20)}$$

ε_2 is the dielectric constant of the triboelectric II layer. Inside dielectric of the air gap (Figure 3.11a) is followed Equation 3.21:

$$E_{air} = (-\frac{Q}{S} + \sigma\ (t))/\varepsilon_0 \qquad \text{(Equation 3.21)}$$

σ is the real-time surface static charge, which is equally distributed on the inner triboelectric surface after contact. The voltage between the two electrodes is given by Equation 3.22:

$$V = E_1 d + E_2 d + E_{air} X \qquad \text{(Equation 3.22)}$$

d is the thickness of the triboelectric layer and the *X* is the real-time distance between the electrodes. The *V-Q-X* relationship can be obtained by substituting Equation 3.19, 3.20 and 3.21 into Equation 3.22, which gives to Equation 3.23:[180]

$$V = -\frac{Q}{\varepsilon_0 S_c}\left(\frac{d}{\varepsilon_1} + \frac{d}{\varepsilon_2} + X(t)\right) + \frac{\sigma X(t)}{\varepsilon_0} \qquad \text{(Equation 3.23)}$$

For the conductor-to-dielectric-mode, as shown in Figure 3.10b, the conductor on the bottom acts as both the active layer and electrode. Therefore, the active layers are the triboelectric layer I and the air gap, as shown in Figure 3.11b, the *V-Q-X* relationship for this mode is given by Equation 3.24:[180]

$$V = E_1 d + E_{air} X = -\frac{Q}{\varepsilon_0 S_c}\left(\frac{d}{\varepsilon_1} + X(t)\right) + \frac{\sigma X(t)}{\varepsilon_0} \qquad \text{(Equation 3.24)}$$

A corresponding schematic diagram of Equation 3.23 and Equation 3.24 are shown in Figure 3.12, the output voltage as a function of the time is oscillating and

superimposed on a direct current (DC) offset voltage.

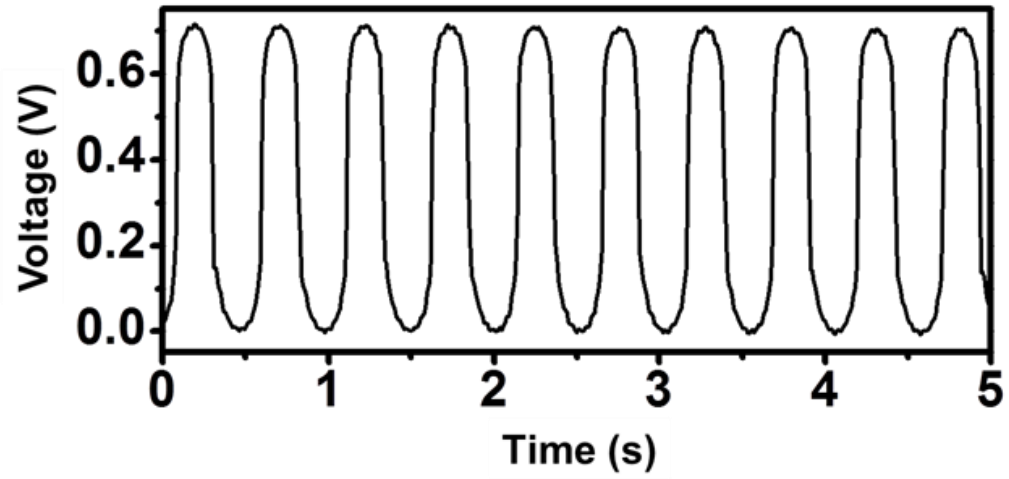

Figure 3.12 The representative of the output voltage from a TENG as a function of time, corresponding to Equation 3.23.

In my research, both modes of the TENG were investigated. A transparent TENG (T-TENG) was achieved using conductor-to-dielectric-mode. In this triboelectric device, the silver nanowire percolation networks act as the conductor and the triboelectric active layer (Chapter 7). A transparent single electrode TENG was also developed using dielectric-to-dielectric-mode, which is further integrated with an OSC (Chapter 8).

Chapter 4 Synthesis of nanofibres in a pump-free electrospinning process

4.1 Abstract

Electrospinning method, as a cost-effective and versatile method, was initially investigated to synthesise nanofibres. A unique pump-free approach was adapted to the conventional electrospinning process. The effects of processing parameters, including solution concentration, viscosity, nozzle diameter, voltage bias and nozzle-collector distance, on the morphology and diameters of the poly (methyl methacrylate) (PMMA) fibres has been systematically studied. The pump-free method minimised the interference of flow rate on the morphology of the nanofibres. Through concentration-dependent viscosity measurements, the critical entanglement concentration, c_e = 3.3 wt%, has been identified for PMMA in dimethylformamide (DMF). Prolate spheroid-shaped droplets or beads with fibres were formed, when the concentration of the solution was less than c_e. By further reduction of solution viscosity and vapour pressure of the solvent, hollow hemispheric structure could form, which will be discussed in Chapter 6. In this chapter, good quality, bead-free fibres were formed with polymer concentration above c_e. Significantly, a quantitative analysis revealed a linear dependence between the solution viscosity and the fibre diameter. Fibres with diameter less than 200 nm were achieved by using nozzles with small inner diameters (0.1 mm). Increasing the nozzle diameter significantly increased the fibre diameter and its distribution, when the flow of the solution was not limited by the nozzle diameter. With increasing voltage bias, the diameter of the electrospun fibres also increased with a broader distribution as a result of splaying and splitting. On the other hand, when the electrical field was reduced by increasing the distance between the nozzle and collector,

the overall fibre diameter was reduced.

4.2 Introduction

Recently, one-dimensional (1D) nanofibres have become the focus for immediate applications due to their good mechanical strength, while maintaining high surface area to volume ratio. A substantial amount of research is being carried out in order to explore the prospective application areas for nanofibres, which include ion conductive nanofibrous membranes for high performance batteries,[181] piezoelectric fibres,[106] filtration,[182] tissue engineering scaffolds,[183] solar cells[184] and photocatalysts.[185]

This work has been focused on controlling and understanding the formation and morphologies of electrospun fibres. Correlating the electrospun fibre diameter to the process parameters and polymer solution rheology is a challenging task, since many parameters are correlated to each other. Many inconsistent experimental results have been reported. For example, Katti et al.[186] reported that larger nozzle diameter resulted in larger fibre diameter, while Macossay et al.[187] reported that the nozzle diameter has no influence on the fibre diameter. Although, it is generally agreed that larger bias voltage creates larger diameter fibres, Katti et al.[186] reported that an increase in voltage caused a decrease in nanofibre diameter initially, and further increase of the voltage caused the fluctuation of the nanofibre diameter. More controversially, measurements taken by Gu et al.[188] showed no correlation between fibre diameter and bias voltage. Such contradictory results suggest a significant interference between processing parameters. Most of those reported results are obtained with a flow controlled electrospinning process, in which the effects of the nozzle diameter and voltage bias could be severely affected by the solution pumping rate.

To avoid such complications, in my study, I used a glass capillary without solution feed control, thus ensuring that the results of the electrospinning are dominated

by the strength of electrical field, nozzle diameters and solution viscosity. To my knowledge, such pump-free study of the processing parameter effects is still very limited. It was the objective of this study to systematically investigate the effects of these parameters on the diameter of polymer fibres avoiding the effect of flow control. Based on this study, the conditions were identified to create polymer fibres with diameter at true nanometre scale.

4.3 Experimental

The solutions used in the electrospinning experiments were prepared using PMMA with an average molecular weight of 996,000 g/mol, determined by gel permeation chromatography performed by the supplier (Sigma-Aldrich). PMMA was dissolved in DMF forming solutions in the concentration ranging from 1 to 10 wt%.

The viscosity of the solutions at different concentrations were measured at room temperature using an Ostwald viscometer (PSL tube viscometer, BS/U type) with a capillary diameter of 4 mm. Glycerol was used to calibrate the viscometer. To determine the reproducibility and the consistency of the viscosity readings, the viscosity measurements were repeated twice. The facility for electrospinning consists of a glass pipette with a controlled orifice diameter varying from 0.1 to 1.2 mm. The pipette orifice diameter was measured using optical microscopy and calibrated with the scanning electron microscopy (SEM). The fibres were collected on a sheet of grounded aluminium foil, which was spaced away from the end of the pipette at distances ranging from 10 to 20 cm. The pipette was mounted horizontally to reduce the effect of gravity on the flow rate. A wire, connected to a high voltage DC supply (maximum 50 kV), was directly inserted into the pipette to supply the positive bias. However, gravity is still able to influence the flow rate, particularly with large spinneret diameter. In this research, spinneret diameter is controlled to be less than 1.2 mm, and with sufficient

viscosity, the liquid flow driven by gravity at horizontal configuration is neglectable. All experiments were carried out at room temperature, stabilised at 22 ℃ with a relative humidity of 35%.

The diameter and morphology of the collected polymer fibres were studied by SEM. For each electrospun sample, the diameters of 100 fibres were measured in at least 20 different fields and were then averaged. The error bars of the fibre diameter plots correspond to the full width of half maximum (FWHM) of the diameter distribution.

In order to understand the influence of processing parameters individually and to determine their sensitivity towards the morphology of the electrospun polymer fibres, only one parameter at a time was varied, while all the other physical parameters were kept constant. Thus, the results of this work offer some reliable and systematic experimental information, which can be used for further theoretical modelling.

4.4 Results and discussion

4.4.1 Viscosity measurements

For a linear polymer like PMMA, the solution viscosity reflects the entanglement of the polymer molecules. Such intermolecular interactions form one of the most critical parameters influencing the morphology of the electrospun polymer fibre. At very low concentrations and therefore viscosities, hollow hemispheres, rings and other morphologies are formed instead of fibres.[101, 189] The metal oxide hemispheric structure was further investigated to enhance the light absorption for photoelectrochemical (PEC) water splitting in Chapter 6.

The measured specific viscosity as a function of PMMA concentration is shown in Figure 4.1a and 4.1b. An almost linear dependence of the viscosity on the PMMA concentration can be found at very low concentration, which gives an intrinsic viscosity

of 145.4 cm^3/g, followed by a nonlinear increase of the viscosity, shown in Figure 4.1a. The intrinsic viscosity describes the physical property of the polymer chain. Such viscosity value is obtained by extrapolating the curve to zero of the solution concentration. This measured intrinsic viscosity of PMMA in DMF is in excellent agreement with the predicted value of 150.3 cm^3/g, using the polymer molecular weight of 996,000 g/mol, and parameters from Dobkowski.[190]

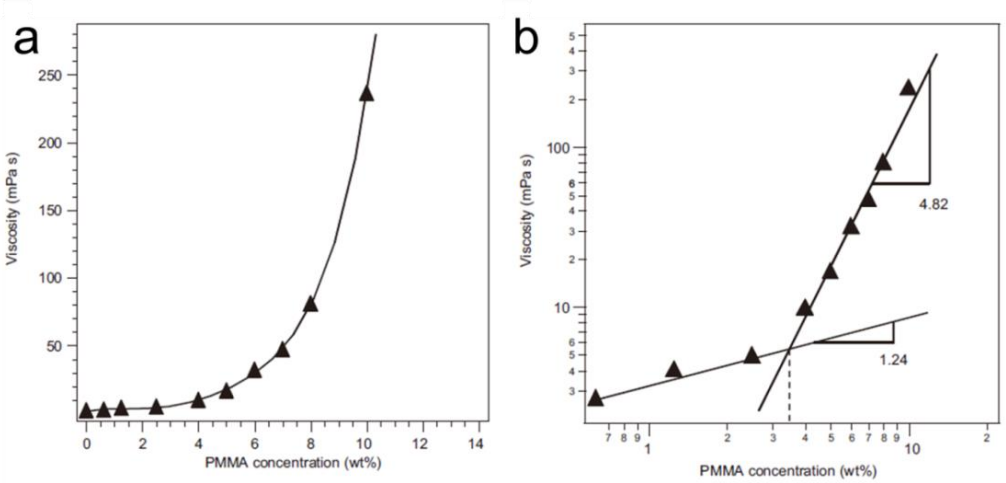

Figure 4.1 (a) Dependence of solution viscosity as a function of PMMA concentration in DMF. (b) Plotted on a logarithmic scale with two exponents indicated at different concentrations.

The logarithmic scale plot, shown in Figure 4.1b, reveals two different power law dependences in different concentration regions. The intersection of the two concentration dependencies of these regimes yields the critical entanglement concentration, c_e. The measured value for these solutions is 3.3 wt%. As c_e represents the point, above which, a significant 3D entanglement dominates the observed viscosity, this concentration is highly important in the electrospinning process. Since significant inter-chain interactions are essential to balance the surface tension and the viscosity of

the solution, with a $c<c_e$, the viscosity will be unable to compensate the surface tension, resulting in droplets rather than fibres.

The quantitative analysis of two power law behaviour of the viscosity reveals an exponent of 1.24 for the semi-dilute untangled regime and an exponent of 4.82 for the semi-dilute entangled regime. For low concentration solutions, McKee et al.[191] have identified an exponent of 1.25, while for high concentration solutions, Colby et al.[192] predicted an exponent of 4.5, and measured experimentally a value of 4.8. My measurements are in good agreement with these values. An exponent value of 4.82 corresponds to significant closely packed polymer chains, if the Huggins equation is obeyed in this system. Gupta et al.[193] reported exponents of 0.65 and 5.3 for the two concentration regimes. Essentially, the Huggins equation relates the decreased viscosity of a dilute polymer solution to the concentration of the polymer solution:[194]

$$\frac{n_i}{c} = [n_a] + k_H[n_a]^2 c \qquad \text{(Equation 4.1)}$$

where n_i and c are the relative viscosity increment and the concentration in the polymer solution, respectively; $[n_a]$ is the intrinsic viscosity of the solution; and k_H is the Huggins coefficient, which depends on the thermodynamic quality of the solvent, ranging from 0.3 (for a good solvent) to 0.5 (for a poor solvent).

4.4.2 Effect of polymer concentration

The elongated flow of PMMA solutions resists the break-up of the viscoelastic jet, which leads to the formation of long fibres. The morphology and diameter of such spun fibres depends upon the factors that affect the viscosity of solution, such as the polymer concentration and the molecular weight of polymer. Since the molecular weight of PMMA was fixed in this study, the viscosity of solution is solely determined by the

concentration of the PMMA.

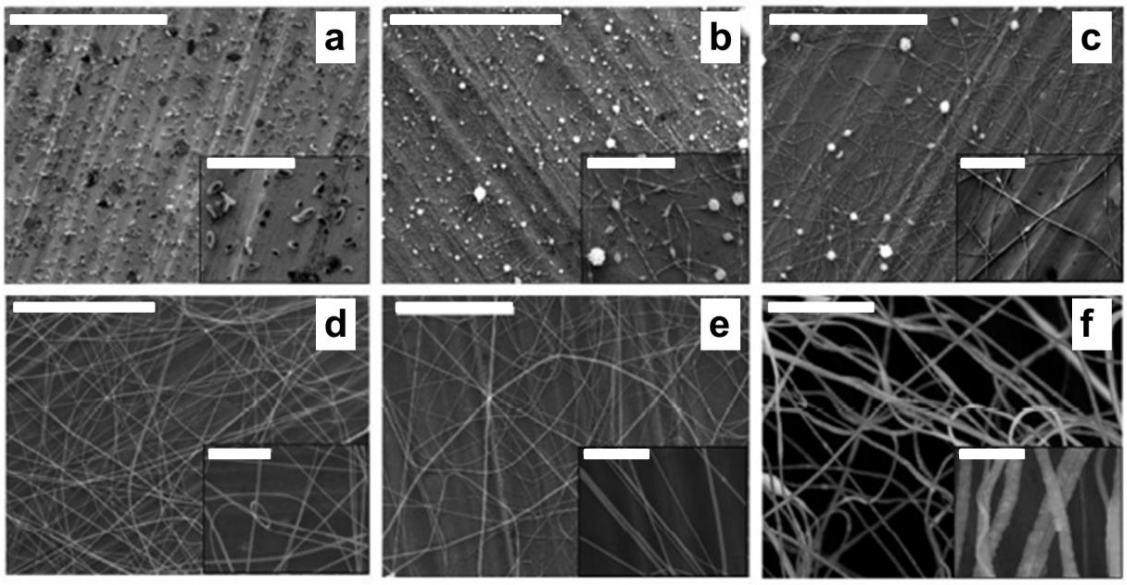

Figure 4.2 SEM images of PMMA electrospun from solution with different concentrations. (a) 1 wt%, (b) 2 wt%, (c) 4 wt%, (d) 6 wt%, (e) 8 wt% and (f) 10 wt%. The scale bar of the main image corresponds to 50 μm. The inserts show a magnified SEM image with scale bar corresponding to 10 μm.

The concentration-dependent morphologies of electrospun PMMA solutions were observed by SEM (Figure 4.2) with all other parameters being fixed: the pipette diameter was 0.4 mm, the distance between end of the nozzle and the collector was 20 cm with a bias of 20 kV. At a concentration of 1 wt%, which is substantially lower than c_e = 3.3 wt%, only polymer droplets were observed (Figure 4.2a). The droplets were in the prolate spheroid-type shape with a range of dimensions between 890 nm and 300 nm. Such an elongated shape is a direct result of the stretching in the electrical field during the spinning process. Most of the droplets had dimples in the middle, which was due to the evaporation of the solvent. Due to this evaporation mechanism, different solvents were further studied to synthesise hollow hemispheres in Chapter 6.

At a polymer concentration of 2 wt% (Figure 4.2b), beaded fibres were formed. The residual beads between the fibres were in a similar prolate spheroid shape as observed at 1 wt% solution in Figure. 4.2a. Larger droplets (different from beads) were also formed due to the high flow rate at low viscosity. The average diameter of the fibre was about 88 nm in the bead free sections. The formation of polymer droplets and beaded fibres is controlled by the balance of the viscosity and the surface tension. For solution with a low viscosity and a high surface tension, the spinning solution breaks down into droplets, while for solutions with a high viscosity and a low surface tension, fibres can be formed. In this case, the surface tension was balanced by the viscosity when the concentration increased from 1 to 2 wt%. Therefore, both beads and fibres were formed. The measured viscosity was about 4.5 mPa s.

When the concentration was slightly larger (i.e. 4 wt%) than the c_e (3.3 wt%), the interactions between polymer chains were improved. The measured viscosity was increased to 9.9 mPa s. The percentage of beads was reduced dramatically, while the diameter of the fibres also increased to 182 nm, shown in Figure 4.2c. At 6 wt%, shown in Figure 4.2d, uniform fibre structure was found with far fewer beads, with an average fibre diameter increasing to 294 nm. However, further increasing the polymer concentration to 8 wt% does not increase the fibre diameter significantly, although the viscosity increases to 81 mPa s. As the concentration increases to 10 wt%, the viscosity of the solution increases to 236 mPa s. Not only does the average diameter increase to over 900 nm, but also the diameter distribution becomes much wider in comparison to the fibres spun from 4 to 8 wt% solution, which is possibly due to the fibre splaying and splitting, shown in the SEM image in Figure 4.2f.

Wnek et al.[195] have reported a semi-empirical analysis to explain the polymer entanglements for the limit of concentration in fibre formation. Chain entanglements in

a melt are essentially the physical interlocking of polymer chains, and affect the morphology and structure of the electrospun product. In the polymer solution, the chain overlap determines the entanglement number, which is increased by increasing the molecular weight or the chain length of the polymer. Accordingly for moderately concentrated or concentrated solutions, the entanglement number n_e can be determined using Equation 4.2:[195]

$$n_e = M_W/(M_e)_{soln} = (\emptyset_P M_w)/M_e \qquad \text{(Equation 4.2)}$$

where M_W is the molecular weight of the polymer; $(M_e)_{soln}$ and M_e are the entanglement molecular weight in the solution and the melt, respectively; and $\emptyset_P$ is the polymer volume fraction. In this experiment, M_e = 12500 g/mol,[196] and M_W = 996,000 g/mol. When the concentration of the PMMA in the DMF is c_e, and $\emptyset_P = c_e \times \rho_{DMF} \div \rho_{PMMA}$, where ρ_{DMF} and ρ_{PMMA} are the density of the DMF and PMMA, which are 0.944 and 1.13 g/cm^3, respectively. Hence the $\emptyset_P$ can be obtained as 2.75%. The n_e can then be calculated through Equation 4.2, giving a value of 2.19. Since $(M_e)_{soln}$ is the value of the entanglement molecular weight in a solvent, it also could be influenced by the quality of the solvent.

Comparing with experimental results, Wnek et al.[195] reported that with entanglement number, n_e, between 2 and 3.5, a mix of fibres and beads was formed, while for n_e larger than 3.5, good quality, bead-free fibres were formed. These entanglement numbers correspond to the limit of the concentration of 3.1 wt% and 5.4 wt% for the PMMA solution in DMF. The viscosity measurements indicate a critical entanglement concentration of 3.3 wt%. The observed bead-free fibre at PMMA concentration of 6 wt% is in good agreement with the predication using Wnek's semi-

empirical analysis.[195]

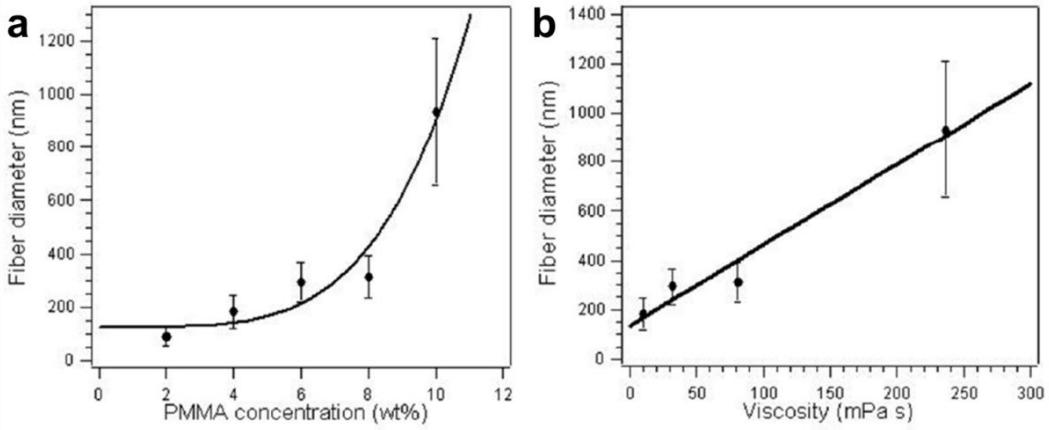

Figure 4.3 (a) The diameter of electrospun fibre as a function of PMMA concentration. (b) The diameter of fibre as a function of solution viscosity. The error bar indicates the FWHM of the distribution function of the fibre diameters.

Figure 4.3a summarises the average diameter of the PMMA fibres as a function of polymer concentration. The measured FWHM of the fibre diameter distribution function is shown as the error bars in Figure 4.3. It is clear that as the concentration increased, both the fibre diameters and their distribution also increased. In particular, a sharp increase of diameter and distribution was found between 8 to 10 wt%. Overall, a power law relationship with an exponent of 4.2 was observed. Similar behaviour has been observed by Gupta et al., although an exponent of 3.1 was reported.[193]

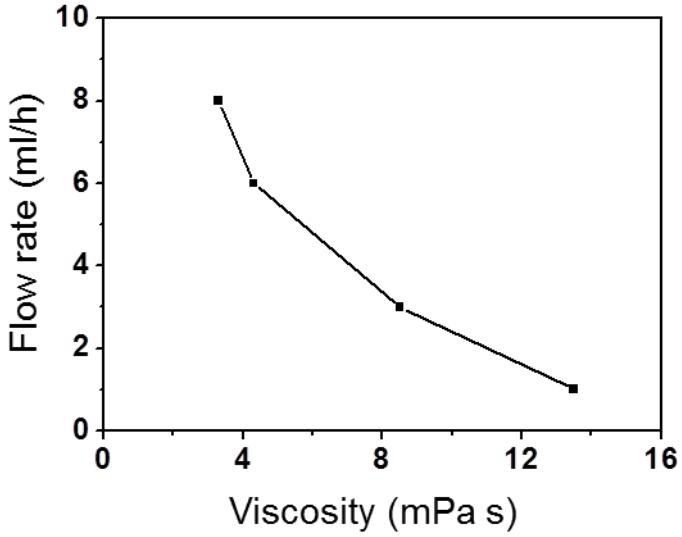

Figure 4.4 A plot of flow rate of the electrospinning as a function of the viscosity.

In order to understand quantitatively effects of solution viscosity, the fibre diameter was plotted against the measured viscosity (Figure 4.3b). A good linear relationship with a slope of 3.24 nm/(mPa s) and a R^2 of 0.983 can be identified, which is slightly different from the power law relationship reported in the literature. Gupta et al.[193] also reported a power relationship with an exponent of 0.72 for a higher molecular weight PMMA solutions. Meanwhile, McKee et al.[191] reported power law dependence with an exponent of 0.8. The small discrepancy between these observations is possibly due to the influence of flow rate. Both Gupta[193] and McKee's[191] measurements were taken with controlled flow rate, while in my measurement; the flow rate is not limited by pumping rate. If the flow rate is determined by the pump rate, it could be significantly less than this pump-free flow rate. This would restrict the natural formation of the Taylor cone, causing an interruption and delay of the electrospinning, during which, the solution concentration could increase due to the evaporation of the solvent to yield fibres with increased diameters. This pump-free process reduces the restriction of the flow control. The measured flow rate is plotted as a function of the viscosity in

Figure 4.4. With an increase of the viscosity, the flow rate of the electrospinning is reduced. This result reflected the nature of the electrospinning with the applied bias, since the electrostatic force is the only power to balance the surface tension of the PMMA solution to spin the fibres. The identified linear relationship in Figure 4.3b implies the significance of the solution viscosity, which reflects the inter-polymer-chain interactions, on the morphology of the polymer fibres.

4.4.3 Effect of the diameter of the pipette orifice

Pipettes with different nozzle diameters were used in order to investigate their effects on the morphology and diameter of the fibres. All other parameters were kept constant; the concentration of the solution was 6 wt%, a bias of 20 kV was applied and the collector was kept at 20 cm away from the end of the pipette. Pipette nozzle diameters of 0.1, 0.3, 0.5, 0.7, 1.0 and 1.2 mm were tested. The results are shown in Figure 4.5. The measured FWHM of the fibre diameter distribution function is shown as the error bars. The results show that it is possible to reduce the diameter of the fibres by reducing the diameter of the pipette orifice. Using a 0.1 mm orifice, uniform fibres with an average diameter of 180 nm were formed. However, using a 1.2 mm pipette orifice, the average fibre diameter was increased to 330 nm with a much wider distribution. The plot shows a sigmoidal dependence of the fibre diameter on the nozzle diameter. The fibre diameters show a steeper increase followed by relatively flat increase as the nozzle diameter increases from 0.1 mm to 0.8 mm. At large nozzle diameter, from 0.8 mm to 1.2 mm, not only does the average fibre diameter increase, but its distribution becomes wider. In such cases, the flow of the solution is no longer restricted by the nozzle diameter.

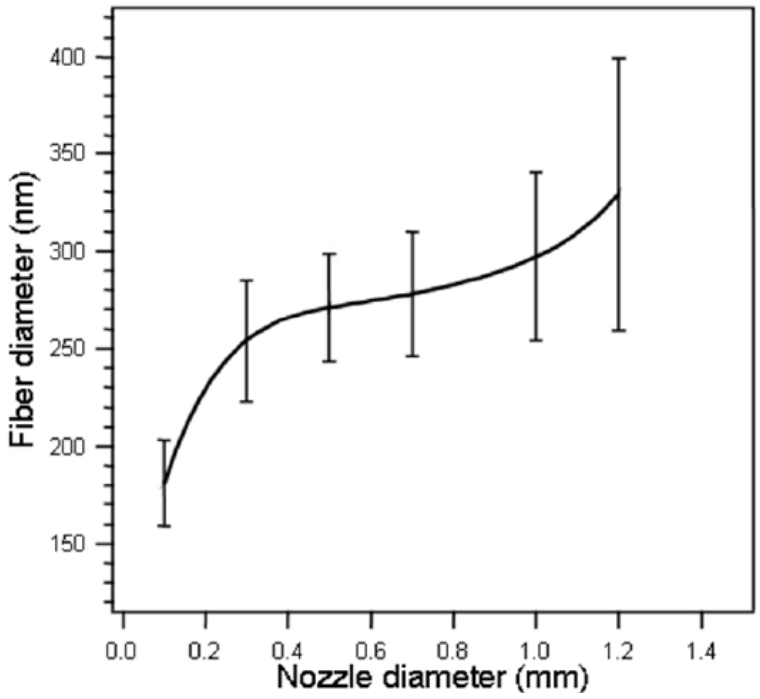

Figure 4.5 The dependence of the measured fibre diameter on the nozzle diameter for electrospinning. The error bars of the fibre diameter are defined as FWHM of the diameter distribution.

My observation is qualitatively in agreement with the measurements taken by Katti et al.,[186] although in their work, only three data points were presented. In contrast, Macossay et al.[187] reported that the nozzle diameter has no influence on the fibre diameter. The reason for such inconsistent results very likely also lies on the effects of flow rate control. When the flow rate is higher than the extraction rate, determined by viscosity, solution charge density and electric field strength, the nozzle size will become irrelevant to the fibre diameter, since much of the solution will accumulate at the end of the nozzle. Equally, when the flow rate is lower than the extraction rate, the flow rate itself will not be able to influence the fibre diameter, which has been observed by Tan et al.[197] The flow rate of our pump-free electrospinning is also presented as a function of the nozzle diameter, as shown in Figure 4.6. The flow rate is highly dependent on the

nozzle size, with a decrease of the nozzle size, the flow rate is decreased. This phenomenon reveals that the volume feed rate is well matched with the extraction rate. Thus a reliable fibre diameter measurement can be achieved quantitatively as a function of the nozzle size. Thus, the size of the Taylor cone is only determined by the orifice diameter of the nozzle, which in turn affects the surface charge density and the diameter of the jet and ultimately the diameter of the fibres. Therefore, the observations of pump-free electrospinning could be more appropriate for theoretical modelling.

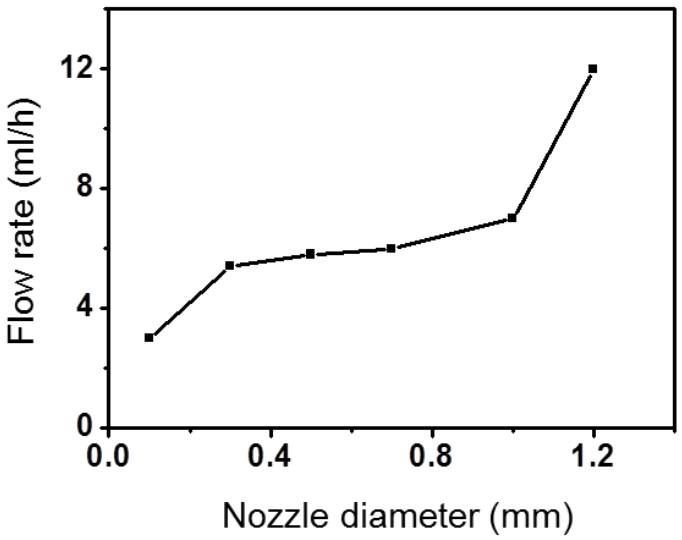

Figure 4.6 A plot of the flow rate as a function of the nozzle diameter for the pump-free electrospinning.

4.4.4 Effect of applied bias

For a PMMA concentration of 6 wt% with a fixed distance between the collector and pipette of 20 cm and a fixed nozzle diameter of 0.4 mm, the voltage dependence of fibre diameter was also studied. Within the voltage range between 10 to 30 kV, good quality polymer fibres were produced. The diameter versus bias is plotted in Figure 4.7.

Increasing the electrospinning voltage caused a small increase in the nanofibre diameter from 290 nm at 10 kV to 308 nm at 30 kV. The observed bias-dependent fibre diameter follows a non-linear relationship, reflecting that, at higher bias, the fibre diameter increases faster. The positive voltage bias drives the charged jet to emerge from the tip through Taylor's cone rapidly when the high electrostatic forces overcome the viscosity. In other words, with fixed diameter and collector position, the higher bias caused faster flow rate or extraction rate and therefore larger fibre diameter.

Although my voltage dependence results are generally in good agreement with the literature, several inconsistent results have also been reported. For instance, Katti et al.[198] reported that an increase in the voltage caused a decrease in the nanofibre diameter initially, and further increasing the voltage caused fluctuation of the nanofibre diameter. More controversially, measurements taken by Gu et al.[188] showed no correlation between fibre diameter and bias voltage. Meanwhile, carefully inspecting the data reported by Nasir et al.[199] and Zhang et al.,[200] the results reveal a sublinear curvature, while my results show a superlinear curvature, and Tan et al.[197] only reported two data points. Such a complex spectra of the voltage dependent results should be thoroughly analysed in order to obtain a comprehensive understanding of the whole picture. It is worth mentioning that, most of these reported results are obtained using flow-control. As the explanation above, flow rate limit on the extraction rate could be the cause for the contradictory results. In my pump-free electrospinning process, the polymer solution is extracted by the electrical field, combining with the solution viscosity and nozzle diameter, it determines the flow rate.

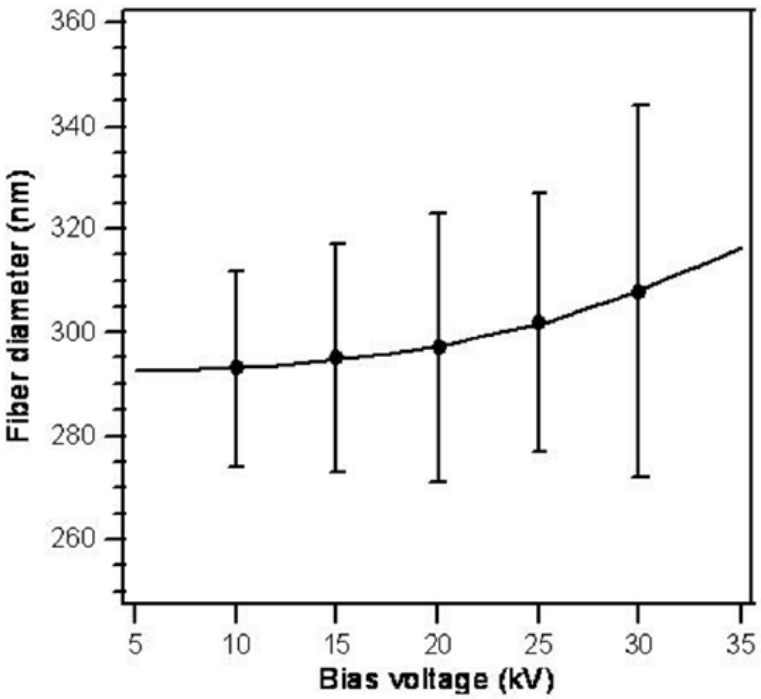

Figure 4.7 The dependence of fibre diameter on the bias voltage applied between the electrospinning nozzle and the collector. The error bars of the fibre diameter are defined as FWHM of the diameter distribution.

With the pump-free electrospinning, at higher voltage bias, the extraction force increases and so does the flow rate. Therefore, the diameter of the nanofibres increases. The increase in the fibre diameter is also accompanied by increasing the fibre diameter distribution, shown as the error bars in Figure 4.5. It is believed that the high ejection rate could cause the splitting and splaying of the polymer fibres, and therefore increase the size distribution. It is also able to observe the increase in the bead production at high electric potential. The formation of beads with fibres has been described in several papers and it was suggested to be affected by the varying the surface tension and the charge density.

4.4.5 Effect of distance between the nozzle to the collector

With a fixed solution concentration (6 wt%), bias voltage (20 kV) and nozzle

diameter (0.4 mm), the fibre diameters were measured as a function the distance between the end of the pipette and the collector, shown in Figure 4.8. While the bias could affect both the charge density and fibre thinning process, the distance between the pipette and collector will only affect the thinning and whipping process. Therefore, it is necessary to distinguish the effects of bias and the effects of distance between the nozzle and the collector. Within the range between 10 cm to 20 cm, high quality uniform and bead-free fibres were formed, while the fibre diameter decreases when the distance increases, following a linear relationship.

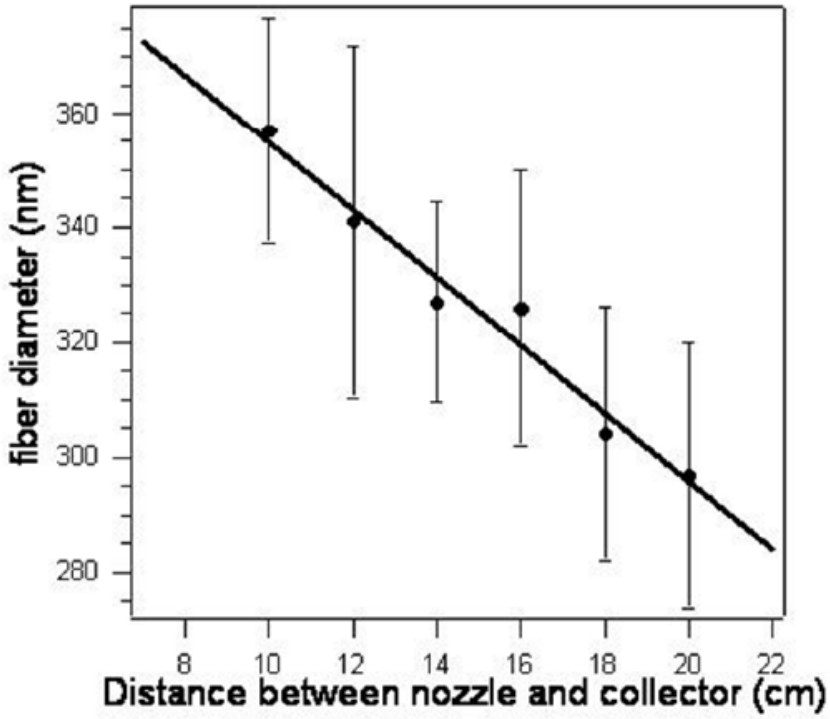

Figure 4.8 The measured fibre diameter as a function of distance between the nozzle and the collector. The error bars of the fibre diameter are defined as FWHM of the diameter distribution.

Similar to the decrease of bias voltage, an increase of the collector distance will reduce the electric field strength. Thus the fibre diameter will be expected to decrease

with an improved fibre quality. Meanwhile, the increase in distance provides more time for the thinning process, arising from the whipping instability, which also results in finer fibres with a narrower diameter distribution. In my experiments, it is difficult to quantitatively distinguish the contribution of electric field strength from the fibre thinning process. Further experiments can be carried out to maintain the strength of the electric field, using a constant ratio of the applied voltages to the nozzle-to-collector, so only the contribution from the thinning time can be measured.

4.5 Conclusions

The effects of the critical processing parameters, including viscosity, concentration, nozzle diameter, voltage bias and nozzle-to-collector distance, on the diameter and morphology of electrospun PMMA fibres have been investigated. Having recognized the significant effects of the flow rate, a pump-free electrospinning process is developed to measure the dependence of finer morphology on processing parameters. This study has shown that, in the absence of mechanical pumping and flow control, the morphology and diameter of nanofibres can be controlled and their formation can be understood at a fundamental level. This technique can be used for further detailed experimental and theoretical study of electrospinning.

The viscosity of the PMMA solution was measured as a function of solution concentration with an excellent agreement with that predicted by the Mark-Houwink-Sakurada relationship. The critical entanglement concentration, c_e = 3.3 wt% is identified. More importantly for the fibre diameter, the viscosity dependence shows a linear relationship. The interference of flow control on the viscosity dependence is also discussed. This method offers an opportunity to understand the natural of the electrospinning with electrostatic power only.

With the fixed concentration, the fibre diameter dependence on the processing

parameters, including nozzle diameter, voltage bias and nozzle to collector distance, has been quantitatively analysed. It was found that decreasing the nozzle diameter can reduce the fibre diameter significantly with improved quality. The bias dependence showed that decreasing the bias will reduce the average diameter and give a narrower distribution. Meanwhile, increasing the distance between the end of the nozzle and the collector, can also reduce the fibre diameter. The flow rate of the electrospinning was further studied as a function of the nozzle size, indicating the fibre diameter measurement is reliable for basic modelling.

The fundamental researches of this work are significant for controlling the morphologies of the metal oxide materials for further applications of harvesting solar energy. The optimised method of fabricating the polymer nanofibres provides a template to generate metal oxide one-dimensional (1D) nanofibres. Moreover, inspired by this study, zero-dimensional (0D) metal oxide hollow hemispheres (HHSs) were synthesised. Both of these nanostructured materials are unique in solar applications, studied in the following chapters.

Chapter 5 Thickness control in electrophoretic deposition of WO_3 nanofibre thin films for solar water splitting

5.1 Abstract

One dimensional (1D) electrospun nanofibres were used for solar water splitting. Electrophoretic deposition (EPD) of ground WO_3 nanofibres was applied to create photoanodes with a controlled morphology for application in photoelectrochemical (PEC) water splitting. The correlations between deposition parameters and film thicknesses were investigated with theoretical models to precisely control the morphology of the nanostructured porous thin film. The photoconversion efficiency was further optimised as a function of film thickness. A maximum photoconversion efficiency of 0.93% from an EPD of electrospun WO_3 nanofibres was achieved at a film thickness of 18 μm.

5.2 Introduction

Direct harvesting of sunlight by photoelectrochemical (PEC) water splitting offers a carbon free and sustainable source of renewable energy. WO_3 has attracted significant interest due to its chemical stability[201] and suitable band gap (E_g = 2.5 – 2.8 eV).[202-204] More importantly, the minority charge (hole) diffusion length of WO_3 (~150 nm)[205] is much longer than that of other semiconductors, such as anatase TiO_2 (~100 nm)[206], ZnO (~125 nm)[207] and α-Fe_2O_3 (~4 nm),[208] offering lower charge recombination rate. Different methods of creating nanostructured WO_3 thin films have been specifically developed for application in PEC water splitting. For instance, anodisation and hydrothermal methods were used to create WO_3 nanostructures.[209-214] Many of these methods, however, are restricted to small substrates with limited control of film

thickness. Electrospinning is an effective way of creating large quantities of metal oxide nanofibres. Unfortunately, the high temperature calcination required to convert precursors into oxides reduces the adhesion and electrical contact of the fibres with the chosen substrates. This is because the as-spun fibres are a few centimetres long with entanglements, reducing the contact points between the fibres and the substrate. In addition, big gaps in between the as-spun fibres are another factor that causes a poor adhesion, which can adversely affect the reliability of the photoanode for PEC water splitting.

Electrophoretic deposition (EPD) is a promising technique for the creation of nanofibrous thin films with a control of the film morphology and thickness. EPD casting with variety ceramic colloidal suspension were extensively studied.[215-217] Recently, Xu et al. created 3D colloidal photonic crystals using the EPD method.[218] Santhanagopalan et al. synthesised aligned MnO_2 nanoforests using a high voltage EPD.[219] EPD is a rapid and cost-effective method to create good quality thin films with reproducible film quality.[220] Using a well dispersed suspension, EPD can result in a highly homogeneous casting with a high mechanical strength and a low surface roughness. The homogeneity of the EPD film is guaranteed, because the particle velocity depends on the strength of the working electrical field, which typically decreases with an increase of the film thickness. It allows precise and quantitative control of the film thickness with excellent adhesion on substrates.[221-223] However, limited work was reported to use high quality EPD metal oxide thin films as photoanodes with their application in PEC water splitting.

Here, a combination of electrospinning and electrophoretic deposition (EPD) is developed as a versatile method to create porous metal oxide nanofibrous photoanodes with controlled film thicknesses and excellent electrical contact. The EPD deposition

parameters were investigated in order to control the thickness of deposited film and its relation to the generated photoconversion efficiency. The photoconversion efficiency of the PEC water splitting from the EPD films was extensively characterised. It is believed that the method for casting nanofibre thin films could be adapted to a wide range of complex metal oxide multilayer nanostructured thin films for high quality photoelectrodes.

5.3 Experimental

WO_3 nanofibres were synthesised through the previously reported pump-free electrospinning procedure.[105] 1.12 g of tungstic acid (H_2WO_4, Fisher Scientific) was dissolved in 10 mL ammonium hydroxide solution (NH_4OH, 35%, Sigma-Aldrich). Separately, 1.20 g of poly(vinyl pyrrolidone) (PVP, MW = 1,300,000, Sigma-Aldrich) was dissolved in 10.0 mL ethanol. The two prepared solutions were then mixed and stirred for 48 hours in order to make the electrospinning precursor. The resulting pale-yellow sol-gel was loaded into a plastic syringe and delivered through a stainless steel needle (inner diameter 0.2mm). A high voltage (20 kV DC) was applied to the needle in order to initiate the electrospinning procedure. PVP/tungsten composite nanofibres were deposited on an earthed aluminium foil collector attached to a rotating drum placed at a distance of 15 cm from the tip of the needle. In order to remove the PVP and convert the tungsten precursor into WO_3, the composite nanofibres were calcined in air at a rate of 2 ℃/min up to 800 ℃, and held for 2 hours before being allowed to cool to room temperature. A Fourier transform infrared spectrometer (FTIR) in attenuated total reflectance (ATR) mode probed the as-prepared nanofibres, as well as at 200 ℃, 300 ℃ and 400 ℃ during the calcination, and a powder X-ray diffractometer (XRD) monitored the crystal formation within the fibres in the calcination at the temperatures of 300 ℃, 400 ℃ 500 ℃ and 800 ℃.

The deposition of WO_3 nanofibres was carried out using the EPD procedure. WO_3 nanofibrous powder was prepared by mechanically grinding the prepared nanofibres. The created powder was then suspended in water at concentrations ranging from 0.5 to 2.5 wt%, concentrations being defined by the ratio between the weight of the ground fibres and the total weight of water and the fibres. A Cu plate and fluorine-doped tin oxide (FTO) glass (Sigma-Aldrich) were cut into 10 mm × 20 mm pieces for the electrophoretic anode and cathode, respectively. The electrodes were immersed in the WO_3 nanofibre solution with a distance of 25 mm. Following this, a voltage bias (ranging from 30 to 70 V) was applied to the electrodes, allowing the deposition of WO_3 nanofibres onto the FTO glass. The as-prepared substrate was further annealed in air at 400 ℃ for an hour to stabilise the film. The thickness of the film was controlled by the applied voltage and the duration of EPD. The EPD current density was monitored by homemade software with the USB data logger (U12, Labjack).

The morphologies of the WO_3 nanofibres and the nanofibrous thin films were studied using a scanning electron microscope (SEM, Joel JSM 820M). The diameters and thicknesses of the nanofibres were measured from the SEM images using the ImageJ analysis software (National Institutes of Health, USA). The crystal structures of the WO_3 samples at different calcination temperatures were identified using a powder XRD (Siemens D500). A FTIR-ATR (Perkin Elmer Spectrum One) was used to study the decomposition of PVP at elevated calcination temperatures.

The PEC water splitting performances were measured using a standard three-electrode system. The cell comprised a KCl saturated Ag/AgCl electrode as the reference electrode (0.1976 V_{RHE} at 25 ℃), a Pt foil as the cathode and the nanofibre electrode as the photoanode. The anodic photoresponses were measured under the illumination of a 300 W Xe arc lamp equipped with an AM 1.5G filter. The full spectral

power density of the light source was adjusted to 100 mW/cm^2, calibrated by an optical power meter (Newport 1830-C with 818-UV). An aqueous solution of 0.5M H_2SO_4 (*pH* 0) was used as electrolyte. The photon-to-electron conversion efficiency under UV and visible light irradiation was studied using optical filters (GG395 and UG11, Schott).

5.4 Results and discussion

5.4.1 Synthesis of WO_3 nanofibres

The electrospinning of metal oxide nanofibres are carried out with a PVP solution mixed with tungsten precursors, which results in composite nanofibres. Typical morphologies of the electrospun composite nanofibres are shown in Figure 5.1A. The composite nanofibres display smooth surfaces, and an average diameter of 450±20 nm. The error in the average diameter is obtained from 200 measurements in different areas of the samples. Figure 5.1B shows the WO_3 nanofibres after calcination at 500 ℃. Crystal facets can be observed on the surface of nanofibre in the inset of Figure 5.1B. This indicates the occurrence of large-scaled crystallisation within the WO_3 nanofibres during calcination. The average diameter of the nanofibres is reduced to 300±20 nm after calcination. The nanofibre diameter shrinkage (>30%) is due to the degradation of PVP and the crystallisation of the amorphous tungsten species. The calcined nanofibre sample shows a pale yellow colour determined by the WO_3 band gap.

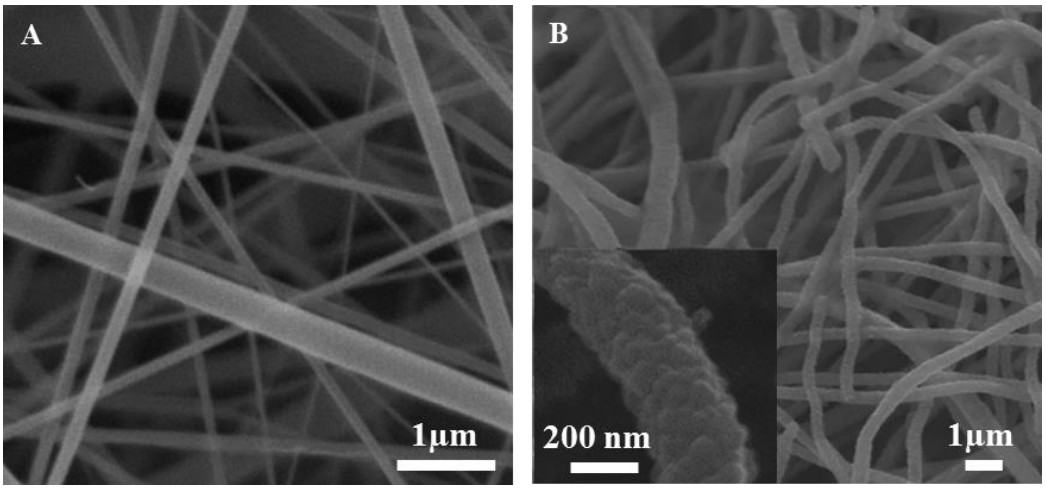

Figure 5.1 SEM images of (A) the as-spun composite nanofibres and (B) the WO_3 nanofibres calcined at 500 ℃. The inset in B shows a magnified image of WO_3 nanofibre.

The thermal degradation of PVP was monitored by temperature dependent FTIR, shown in Figure 5.2. The spectrum from the as-prepared composite nanofibres displays a broad band peak at 3450 cm^{-1} that is assigned to the stretching mode of the hydroxyl functional group (O–H). By increasing the annealing temperature to 200 ℃, all the dominant peaks are still observed without any significant reduction of the peak intensities. Further increase in the annealing temperature to 300 ℃ leads to the reduction of the peak intensity, leaving a broad peak at 1100 cm^{-1}. This peak is assigned to the (C–N) stretch of the tertiary amine group of PVP, and is associated with the degradation of PVP polymer chain. Above 400 ℃, the dominant phonon peak at 650 cm^{-1} of the WO_3 species remains.

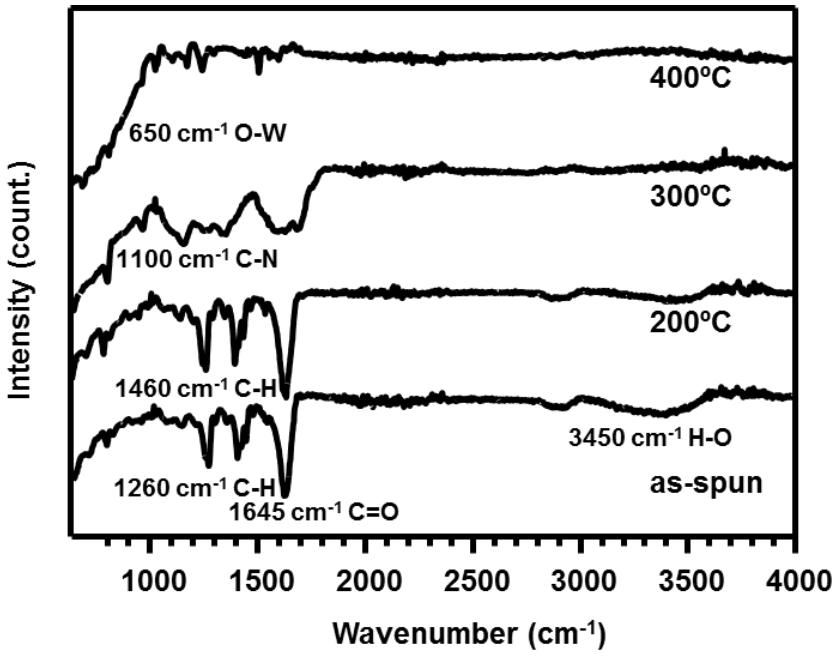

Figure 5.2 ATR-FTIR spectra of composite nanofibres as a function of calcination temperature, showing the gradual decomposition of PVP and the formation of WO_3 phase.

XRD was used to monitor the crystalline phase transitions during the calcination of the as-prepared WO_3 nanofibres, as presented in Figure 5.3. The as-prepared composite nanofibres display broad XRD peaks that are attributed to the ammonium tungstate tetrahydrate species formed between ammonium and tungstic acid in the precursor solution. These peaks disappear above 300 ℃, indicating the decomposition of ammonium tungstate.[224-226] Above 400 ℃, sharp peaks corresponding to the (002), (020), (200), (120), (112), (022), (202), (220) and (122) crystal planes of monoclinic WO_3 were observed (*JCPDS #75-2072*). At 400 ℃, the mean crystal size is about 22 nm, which increases to 37 nm at 500 ℃. Following a further elevation of the calcination temperature to 800 ℃, the XRD peaks became much sharper. This implies that the quality of the monoclinic phase of the WO_3 is improved, and the crystallinity of the monoclinic WO_3 is thermodynamically stable at 800 ℃.

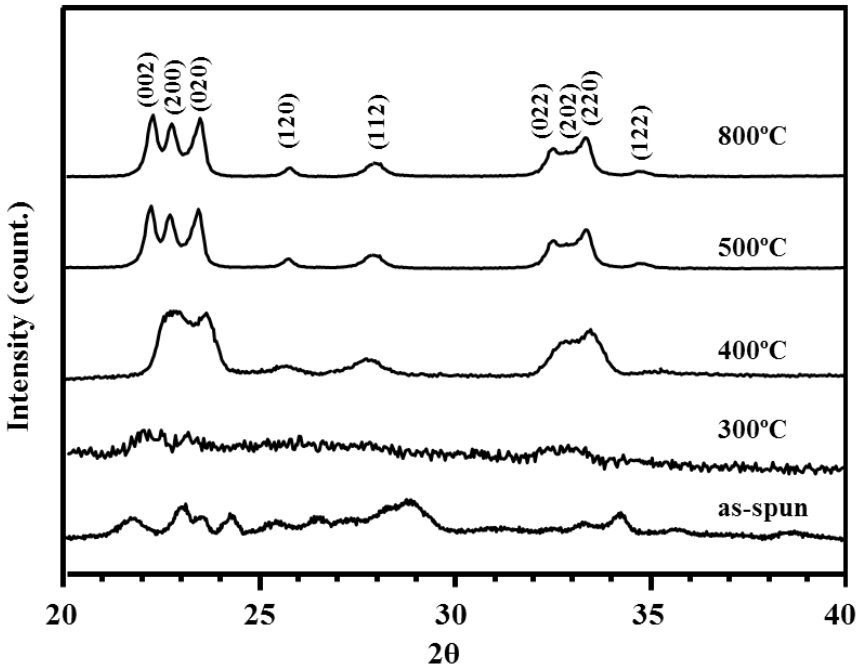

Figure 5.3 XRD spectra of nanofibres as a function of calcination temperature. The as-prepared composite nanofibres display broad XRD peaks that are attributed to the ammonium tungstate tetrahydrate species. Above 400 ℃, monoclinic WO_3 was formed.

5.4.2 Electrophoretic deposition of WO_3 nanofibres

Figure 5.4 shows typical SEM images of an EPD deposited nanofibrous WO_3 thin film on a FTO glass with 40 V bias for 300 s using a 0.7 wt% WO_3 ground nanofibres suspension in water. The top view of the thin film in Figure 5.4A reveals that within the porous film, short fibre morphology is maintained after grinding and EPD deposition. A certain degree of entanglement of the nanofibres can also be observed. The porous structure is important for electrolyte transportation; the entanglement would help the charge transfer within the oxide layer, and enhance the mechanical stability of the thin film. Figure 5.4B shows a cross-sectional view of the film. The thickness of the WO_3 film measured from the SEM image is about 5.0 μm.

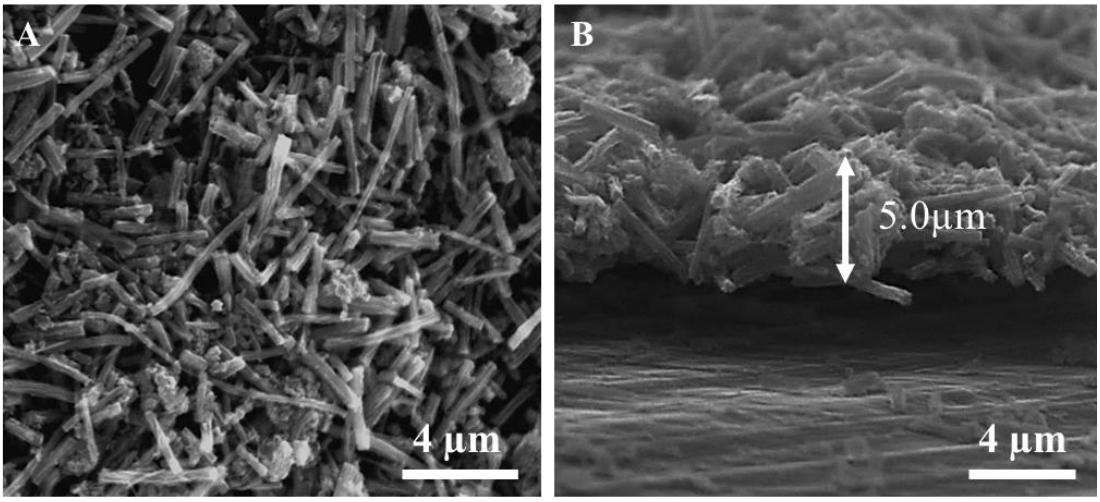

Figure 5.4 SEM images of (A) top and (B) cross-sectional views of EPD deposited WO_3 thin films with 0.7 wt% WO_3 nanofibres aqueous suspension at a bias of 40 V for 300 s.

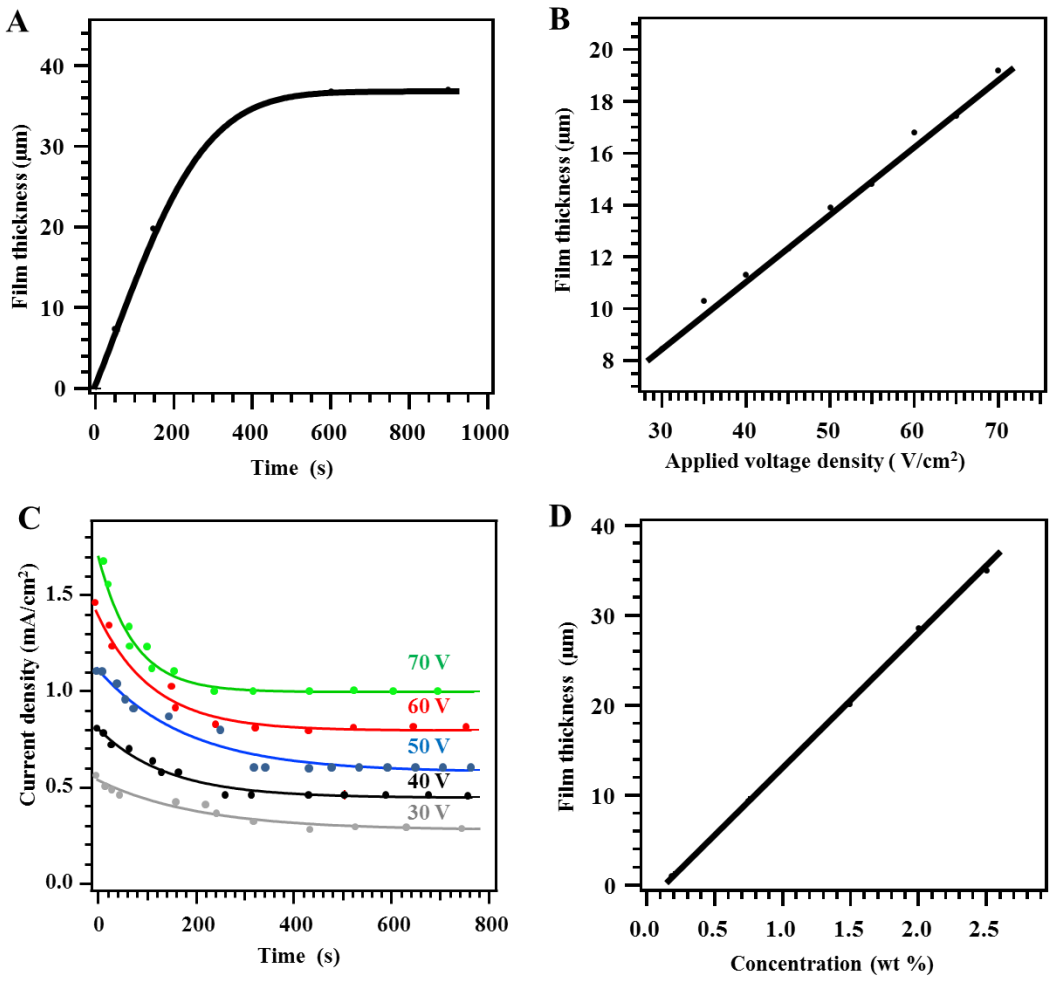

Figure 5.5 Growth profiles during the EPD processes. (A) The film thickness as a function of the deposited time at electrical field strength of 16 V/cm with an initial suspension solution of 2.5 wt%, can be fitted in Equation 5.1. It gradually approaches a maximum thickness due to the consumption of fibres. (B) Film thickness as a function of applied bias measured at 100 s with the suspension concentration of 2.5 wt%. (C) The transient current density curves at bias of 30, 40, 50, 60 and 70 V. (D) Thickness of the EPD films at 40 V, and measured at 600 s as a function of suspension concentration.

Controlling the film thickness is important for optimising photoconversion efficiency of a photoanode. Although a thicker film will benefit from the absorption of light, it usually suffers from a poor charge mobility within the film. The advantage of

using EPD is that the film thickness can be precisely controlled by managing the deposition parameters. Figure 5.5 shows an in-depth study of the variation of the different EPD parameters to the film thickness, which were measured through the cross-sectional view of SEM images, including the voltage bias, transient deposition current density and suspension concentrations. Figure 5.5A shows the relationship between the film thickness and the deposition time, when a bias of 40 V was applied between a Cu plate and a FTO glass substrate, separated by 25 mm, in a 2.5 wt% suspended solution of nanofibres. SEM images corresponding to the deposition time of 200 s and 400 s are shown in Figure 5.6A and 5.6B, respectively. As a function of deposition time, it is clear that the thickness of deposited film increases linearly up to 300 s, after which, the film thickness gradually approaches its maximum of 36 μm. This maximum thickness of the WO_3 film is determined by the voltage bias, the suspension concentration and the electrode surface area, and possibly by the amount of suspended material, which could be affected by the sedimentation of the fibres. The total weight of the nanofibres deposited on the FTO glass was 31 mg. The surface area of the FTO sample is 200 mm^2, while the film thickness is 36.0 μm, so the total volume of the coated film is 7.2 mm^3. This gives the apparent density of the porous film of 4.3 g/cm^3, which is about 60% of the standard WO_3 density. Therefore, the pore volume can be estimated as about 40% of the total film volume.

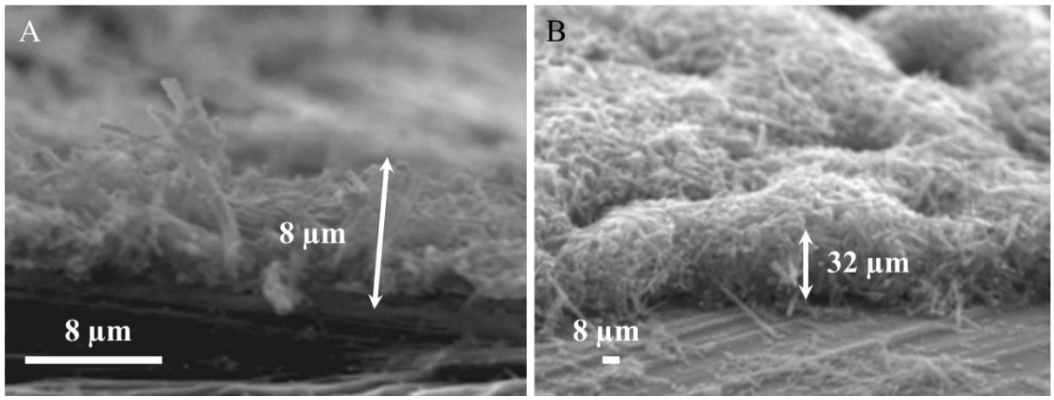

Figure 5.6 The cross-sectional view of the nanofibres thin film obtained at electrical field strength of 16 V/cm with an initial suspension solution of 2.5 wt% in duration of (A) 200 s and (B) 400 s.

With a fixed substrate (FTO) surface area, *S*, and constant specific density of the deposited nanofibres, ρ, the deposited mass of the oxide powder, *m(t)*, can be directly converted to the film thickness, *l(t)*, through the relationship:[227]

$$l(t) = \frac{m(t)}{S\rho} = \frac{M}{S\rho}\left[1 - \left(1 + \frac{r_0}{r_\infty}\left(e^{t/\tau} - 1\right)\right)^{-1}\right] \qquad \text{(Equation 5.1)}$$

where r_0 and r_∞ are the initial and final solution resistivity, respectively. The characteristic time constant, τ, is defined by the total deposited mass, *M*, electrophoretic mobility, u_e, the electrical field strength, *E*, the substrate surface area, *S*, and initial concentration, C_0, as: [227]

$$\tau = M/(u_e E S C_0) \qquad \text{(Equation 5.2)}$$

Equation 5.1 is derived from the resistivity model,[227] which shows that at t = 0,

$l(0) = 0$, while at $t = \infty$, the thickness of the film reaches its maximum, $\frac{M}{S\rho}$, assuming there is no sedimentation. More importantly, for the initial deposition with small variation of the resistivity, r, Equation 5.1 reduces to a linear equation:

$$l(t) = U_e E C_0 t/\rho \qquad \text{(Equation 5.3)}$$

Equation 5.3 suggests that the EPD deposition can achieve a higher rate at a larger field strength, a higher concentration and electrophoretic mobility. This linear relationship is verified in Figure 5.5A. In my experiment, the surface area of the sample, S, is 200 mm^2. The apparent density of the film, ρ, is about 4.3 g/cm^3 while the electrical field strength, E, is 16 V/cm and initial concentration, C_0, is 0.025 g/cm^3. The measured initial linear growth rate is 0.113 μm/s. This gives the electrophoretic mobility, u_e, of 1.21 $\times 10^{-4}$ cm^2/Vs, fitted from Equation 5.3. This value is significantly smaller than that of typical metal oxide nanoparticles, which is around 3 cm^2/Vs.[228] This is possibly due to the large size and elongated shape of the nanofibres. Only with the resistivity model, the whole range of the EPD process can be accurately analysed. By fitting the full spectrum in Figure 5.5A directly with Equation 5.1, the characteristic time constant, τ, and the resistivity ratio, $\frac{r_0}{r_\infty}$, were found to be 92.0 s and 0.30. Therefore, towards the end of the EPD process, the resistivity of the solution increases by a factor of 3.

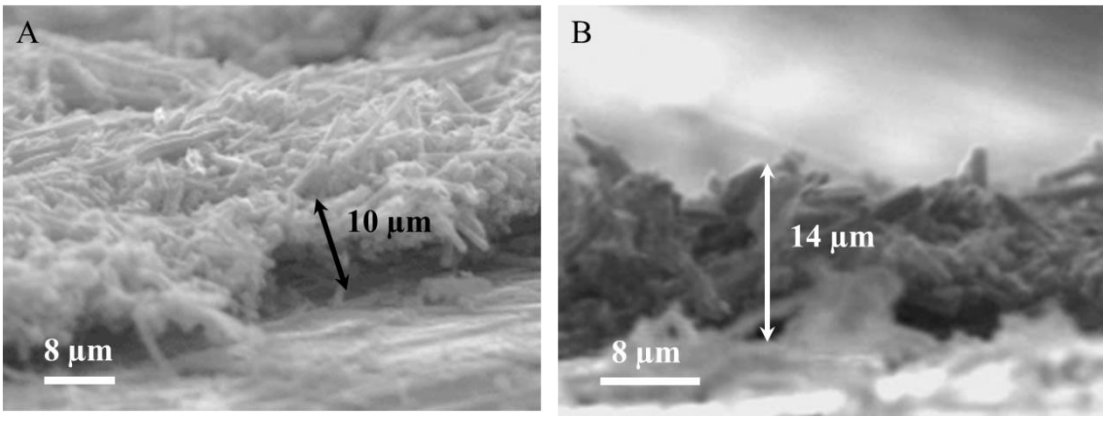

Figure 5.7 The cross-sectional view of the nanofibre thin film obtained at 100 s with the suspension concentration of 2.5 wt%, under applied voltage of (A) 35 V and (B) 50 V.

Figure 5.5B shows the linear relationship between the applied voltage and the deposited thickness at a deposition duration of 100 s, corresponding to the initial deposition process. The measurement was taken from a 2.5 wt% suspended solution of nanofibres, and gives a measured slope of 0.26 µm/V. Figure 5.7A and 5.7B present the cross-sectional view SEM images at applied voltage of 35 V and 50 V, respectively. The distribution of the film thickness corresponding to Figure 5.7 B is plotted in Figure 5.8. The average thickness is around 14 µm, however, the range is widely distributed from 11 to 19 µm. Such wide distribution is probably due to the irregular assembling of the elongated nanofibres. This observation is consistent with the linear Equation 5.3 and gives the derived electrophoretic mobility, u_e, of 1.12×10^{-4} cm^2/Vs , which is similar to the value obtained from the time dependent thickness measurement at fixed bias of 40 V (1.21×10^{-4} cm^2/Vs) in Figure 5A.

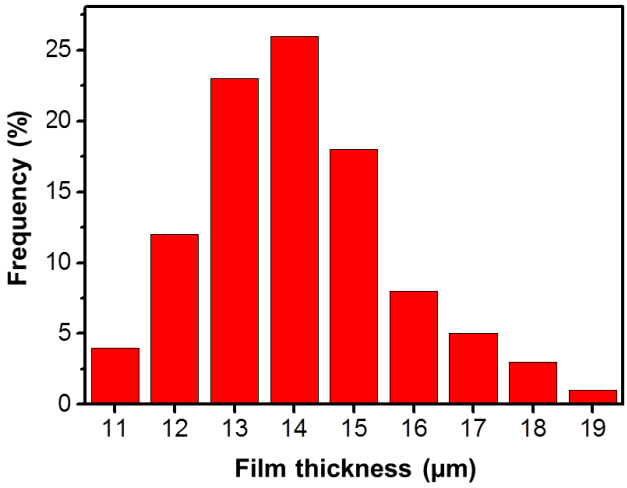

Figure 5.8 The distribution of the WO_3 nanofibre film thickness from Figure 5.7B.

In principle, the EPD current density is proportional to the film growth rate, which can be used for predicting the film thickness. During the EPD deposition process, the current density decreases as the concentration of the suspension decreases, the resistivity increases and the film thickness increases. Figure 5.5C shows the measured current densities, at different biases, as a function of deposition time. The initial rapid decrease in current density is due to the fast depletion of the suspension solution. The rate of decrease of the current density also directly relates to the voltage, as can be seen in Figure 5.5C. A higher bias leads to a faster deposition, thus a sharper decrease in current. The majority of the deposition is finished when a minimum current density is achieved. The residual current density could possibly be due to a contribution from the electrolysis of water under voltage bias, which also depends on bias.

By assuming a negative linear dependence of the suspension resistivity on the suspension concentration, the measured current density was derived as a function of time:

$$I(t) = V\left[e^{-t/\tau}\left(\frac{1}{r_0} - \frac{1}{r_\infty}\right) + \frac{1}{r_\infty}\right] \qquad \text{(Equation 5.4)}$$

Equation 5.4 describes an exponential decay of current as a function of time as demonstrated in Figure 5.5C. It also guarantees that at t = 0 s, the initial current density, $I(0) = V/r_0$, and when t = ∞, $I(\infty) = V/r_\infty$. The exponential decay of current density suggests the EPD is a rapid deposition process, driven by the depletion of the suspension solution. Figure 5.5C shows that both the initial and final electrophoretic currents are proportional to the voltage, which is in agreement with Equation 5.4. Figure 5.5C also demonstrates that at a fixed suspension concentration, the higher EPD field strength results a faster deposition rate with a smaller τ value, which is consistent with Equation 5.2.

The final film thickness could also be affected by the initial suspension concentration. Figure 5.5D presents the influence of the suspension concentration on the deposited thickness measured after 600 s deposition at 40 V. Figure 5.9A and 5.9B show the cross-sectional view SEM images from the suspension of 0.8 wt% and 2.0 wt%, respectively. As the EPD is a rapid process, we would expect most of the nanomaterials are deposited onto the FTO substrate within 600 s, as indicated from Figure 5.5A. The linear relationship suggests that the deposition is complete, and the thickness is determined from Equation 5.1 under the condition of $t \gg \tau$.

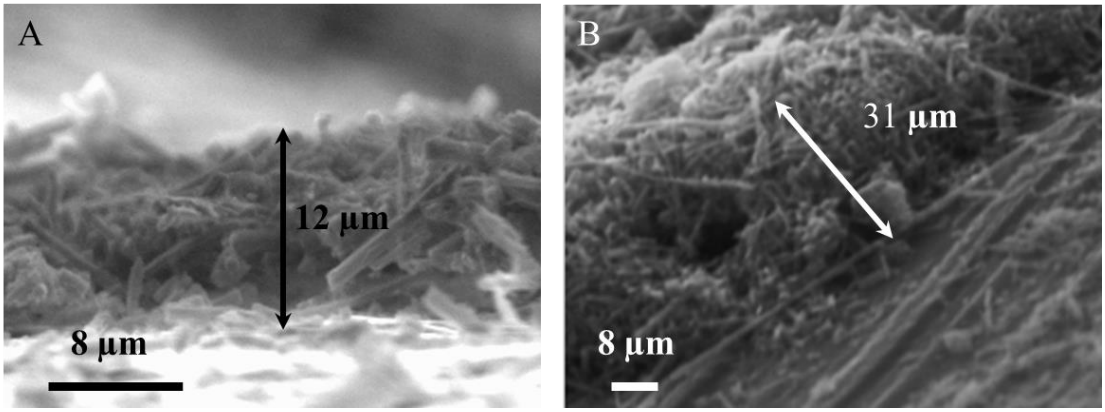

Figure 5.9 The cross-sectional view of the nanofibres thin film obtained deposited at 40 V and measured at 600 s with the concentration of (A) 0.8 wt% and (B) 2.0 wt%.

5.4.3 Photoelectrochemical water splitting using WO_3 electrodes

The EPD method creates a thin film material with a specific nano-morphology, enabling a precise control of the film thickness. The EPD process with a post thermal treatment improves the adhesion of the metal oxide semiconductor to the substrate,[229] which is essential for a stable photoanode in PEC applications. The photocurrents of photocatalytic water splitting using the EPD WO_3 nanofibrous photoanodes in relation to film thickness are shown in Figure 5.10A, together with the dark current (black curve). All the photocurrents gradually increase as the electrochemical potential increases towards the positive bias. At potential of $1.2V_{Ag/AgCl}$, a maximum photocurrent density of 2.3 mA/cm^2 was achieved, with a corresponding film thickness of 18 µm.

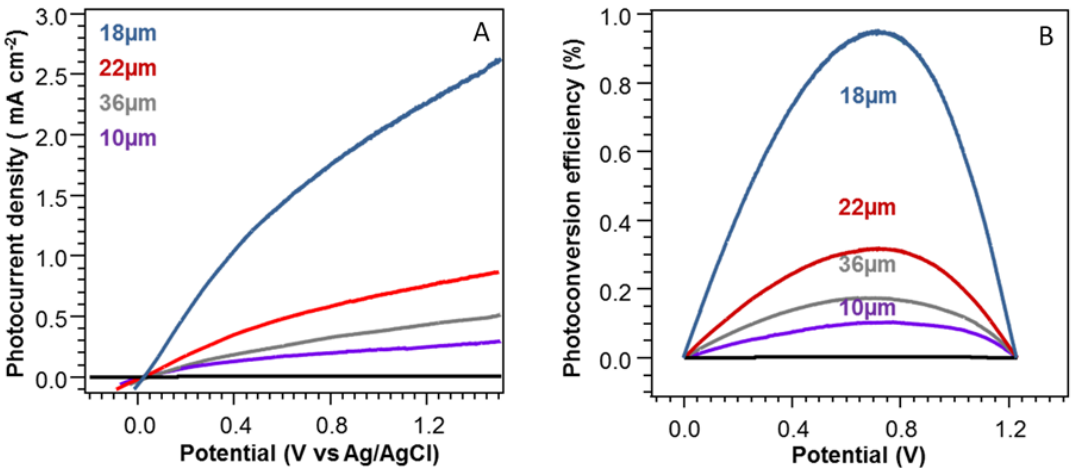

Figure 5.10 (A) The measured photocurrents and (B) calculated photoconversion efficiencies of WO_3 films as a function of film thickness.

The corresponding photoconversion efficiency under AM 1.5G illumination is calculated using Equation 3.14 in section 3.3.1, and the result is shown in Figure 5.9B. This was calculated from the ratio between the electrochemical energy density and the photoenergy density. An optimal photoconversion efficiency of 0.93% was achieved at a film thickness of 18.0 µm. The photoconversion efficiency is lower than that of the PbS modified WO_3 nanoflower (1.3%).[230] When pure WO_3 material is fabricated into a nanostructure as a photoanode, the EPD nanofibre film gives a much higher photoconversion efficiency in comparison with nanocrystalline (0.55%)[231] and sheet-like nanostructured WO_3 (0.3%).[232] This result could be attributed to the large surface area of the porous nanofibre EPD film and the improved direct contact between WO_3 nanofibres and FTO conductive layer. However, combined electrospinning and EPD is a rapid, reliable and cost effective method for fabricating a stable thin film on most of the conductive substrates with restriction on the size and shape. The actual photoconversion efficiency achieved by WO_3 photoelectrodes is much lower than the theoretical maximum photoconversion efficiency (4.8 %), which is based on the nature of the

bandgap, band edges and charge mobility.[233] This can be attributed to the crystallinity of WO_3, the crystal defects acting as recombination centres, resulting in poor photoconversion efficiency.[203]

Table 5.1 The measured UV and visible photoconversion efficiencies for water splitting on EPD deposited WO_3 nanofibrous films as a function of film thickness.

Film thickness (μm)	AM 1.5G efficiency (%)	UV efficiency (%)	Visible efficiency (%)
10	0.116	0.070	0.046
18	0.924	0.545	0.379
22	0.316	0.188	0.126
36	0.175	0.091	0.084

WO_3 has a band gap around 2.5 eV,[234] which can be excited under UV and visible light irradiation. The photocatalytic response from the UV and visible radiation was measured using appropriate optical filters, and the corresponding photoconversion efficiencies are presented in Table 1. While both UV and visible photoconversion efficiencies follow the same trend as a function of film thickness, the UV excitation contributes to around 60% of the AM 1.5G photoconversion efficiency of the WO_3 thin films. This observation is in good agreement with previously reported results.[235]

As the WO_3 nanofibre thin film photoanodes are naturally porous, the electrolyte can penetrate through the film. In a porous structure, the diffusion and oxidation of water by the minority charge carriers are both improved. Therefore, the holes generated in the deeper layers of the films will still be able to undertake local PEC water splitting, which could increase the resulting photocurrent.

The film thickness and its quality can also affect the photoconversion efficiency in

several ways. The light absorption is normally linearly proportional to the film thickness, until all the refracted photons are absorbed. On the other hand, increase of the film thickness can also affect the charge mobility and charge recombination. Photoexcited electrons have to transfer to the base of the conductive layer before recombining with holes. The optimum photoconversion efficiency was observed in my experiment at 18 μm thickness. For films thinner than 18 μm, the increase of the film thickness increases the light absorption. However, when the film is thicker than 18 μm, the charge transporting barrier restricts the collecting of photoelectrons, which increases the charge recombination. This can be accredited to the poor light penetration in the thick WO_3 nanofibrous film with a long and resistive pathway for the electrons travelling to the electrode, which increases the possibility of charge recombination, resulting in a reduced photoconversion efficiency.[236]

5.5 Conclusions

Here, we demonstrated a combination of electrospinning with EPD to deposit WO_3 nanofibres as thin films, with a controlled thickness. The influences of the different experimental factors in controlling the thickness of the EPD thin films were quantitatively studied. The acquired understanding provides a precise control of the film quality. Furthermore, the influence of the film thickness on the photocatalytic water splitting efficiency was also investigated, and peak efficiency of 0.93% was recorded with an optimal film thickness of 18 μm. However, the efficiency is still a long way from the 10 ~ 11% currently state-of-the-art,[237] mainly restricted by inappropriate band edges, indirect band gap and the limited charge mobility. However, different free-standing metal oxides nanofibers can also be deposited with the EPD method, which could potentially improve the PEC water splitting efficiency. Also, further improving

the interconnection of the fibres in the film could facilitate the movements of electron and charge to increase overall performance.

Chapter 6 TiO_2 hollow hemisphere films for enhanced photocatalytic applications

6.1 Abstract

TiO_2 is a promising material for photocatalytic applications. Novel nanostructures and morphology of TiO_2 can effectively enhance photocatalytic efficiency. In this chapter, the electrospray method was used to synthesise three-dimensional (3D) hollow hemisphere (HHS) thin films with a controlled morphology for photoelectrochemical (PEC) water splitting and dye sensitised solar cells (DSSCs). A hydrolysis precipitation phase separation method was developed to preserve the nanostructure of the TiO_2 HHSs thin film, and the nanopores on the surface of the HHSs. The TiO_2 HHS thin film showed higher photoconversion efficiencies than that of commercial Degussa P25 thin film in two different applications. The TiO_2 HHSs film presented the maximum PEC water splitting efficiency of 1.04%, when the thickness is around 24 μm. Within the same thickness, the photovoltaic performance of the dye sensitised solar cell was also measured with the photovoltaic efficiency of 3.26%.

6.2 Introduction

The investigation of TiO_2 electrode for photocatalytic reaction has been carried out for more than four decades, since the first demonstration of photoelectrochemical (PEC) water splitting by Fujishima and Honda.[27] To date, development of TiO_2 as a photocatalyst still attracts intense interest, owing to its stability and chemical resistance. The chemical inertness of the semiconductor metal oxide is one of the crucial factors that affects the working life of a photoanode in operation. There are several reasons for this requirement. One is due to the fact that the water oxidation pathways involve the

formation of hydroxyl radical and hydrogen peroxide (H_2O_2).[43] Thus, the semiconductors are subjected to an oxidative environment during the PEC process. Any elements that are partially oxidised, such as dopants, will not able to maintain their PEC activity.[238, 239] In addition, the electrolyte of PEC water splitting should be adjusted either in extreme alkaline or acidic conditions, so that the water redox potential can be shifted up or down relative to the semiconductor band edges. Many metal oxide semiconductors with small band gap energy, such as CuO, Fe_2O_3 and NiO, are not stable enough in alkaline or acidic electrolyte, while TiO_2 is stable in these conditions.[240] Thus, TiO_2 has a longer working life in the natural environment than many other metal oxides,[241, 242] and is still the most promising candidate for commercial production.

However, the PEC water splitting efficiency of a TiO_2 photoanode still remains low. This is mainly due to two reasons: firstly, a redundant charge-recombination process is inevitable in semiconductor materials during PEC water splitting. Such recombination processes waste the absorbed solar energy. Secondly, the intrinsic band gap of TiO_2 (anatase ~ 3.2 eV and rutile ~ 3.0 eV)[243] determines that it is only active by absorbing the ultraviolet (UV) spectrum, which is only about 10% of the total solar emission.[47] Many investigations have been conducted to overcome these barriers and to enhance the photoconversion efficiency.[244-247] Nanostructured pristine TiO_2 is still one of the important strategies to improve the photoconversion efficiency,[242, 248] since it could fundamentally optimise the electrons mobility[57] and light absorption behaviour.[58]

Nanoparticles always attract tremendous attention. This type of structure offers large surface area with possibility of control the band gap for the photocatalytic applications. However, if the particle size is too small in the nanoscale, the formed film would have a high density, which limits light and electrolyte penetration. There are two

significant factors that need to be taken into account, when applying nanoparticle metal oxide film in photocatalytic applications. Firstly, the channels in the nanoparticle film could maximise the interfacial photoreaction area, decreasing the carrier-mobile distance to reduce the rate of charge recombination. Secondly, the morphology of the nanoparticles should be carefully controlled in order to increase the density of effective reaction centres.

Hollow hemisphere (HHS) is a unique type structure, which provides a high surface area as nanoparticles, so potentially able to improve the photoconversion efficiency. Several synthesis methods were reported towards photocatalytic applications. The templating method uses self-assembled spheres as a template to synthesise the TiO_2 HHSs film.[249-251] However, since this method requires very careful control of the inversion of the sphere structure to form hemispherical structures, it is very difficult to create multi-layered TiO_2 HHS films. Such monolayer film restricts the ability to absorb the incident light. Etching TiO_2 spheres to create voids is another way used to fabricate HHSs thin film, yet the morphology of the TiO_2 HHSs is difficult to control.[252] Recently, TiO_2 HHSs were synthesised with a control of the thermodynamic and kinetic factors of the thioglycolic acid treated Ti precursor. However, the control of the structure and morphology was too complicated to obtain high quality products.[253] Electrospraying is a versatile method to synthesise HHSs.[254] In this method, the structure and the film thickness can be easily controlled with the spraying time. Since electrospray is a solution based method, a broad range of inorganic precursors can be applied.[255] A high voltage encourages the particles to form a stable film; meanwhile it is able to create micro-channels on the HHS surface, which could improve the PEC efficiency with increased reaction centre densities at the heterogeneous interface.

Herein, TiO_2 HHSs thin films are synthesised for PEC water splitting and DSSC

applications. The influences of the electrospray processing parameters to the polymer HHSs are investigated firstly. When 2 wt% rhodamine B is doped in the HHSs, the morphology of the polymer HHSs is also studied using total internal reflection fluorescence microscopy (TIRFM). A hydrolysis precipitation phase separation (HPPS) method is developed to control the morphology of TiO_2 HHS and micro-channels of the film. The maximum conversion efficiency of the PEC water splitting obtained by the TiO_2 HHS film (24 μm) is around 1.04%, which presents a significant enhancement, when compared with the commercial Degussa P25 thin film (maximum efficiency ~ 0.56% with film thickness at 20 μm). This electrospray method is able to create a unique metal oxide HHS structure in a conventional processing. A widely range of the applications can be further considered, such as sensors, solar cells, hybrid devices, lithium ion batteries and supercapacitors.

6.3 Experimental

The poly(methyl methacrylate) (PMMA, Sigma-Aldrich) (MW = 35,000) was dissolved into nitromethane (NM, Sigma-Aldrich) at room temperature. Then titanium isopropoxide (TTIP, Sigma-Aldrich) and acetyl acetone (AA, Sigma-Aldrich) were blended into the prepared polymer solution as the inorganic precursor and stabiliser, respectively. The concentration of PMMA in the solution was fixed at 10 wt% in NM. For creating TiO_2 HHSs, TTIP with the concentrations of 2 to 8 wt% and 1 wt% AA were added into the PMMA solutions. The solutions were stirred at room temperature for 24 hours until the yellowish solution became transplant. For the TIRFM test, rhodamine B was used as the fluorescent dye and 2 wt% of it was mixed into the polymer solution (10 wt% PMMA) before electrospraying into HHS.

The mixture solution was loaded in plastic syringes with the needle inner diameters ranging from 0.603 to 0.159 mm for the electrospraying with a constant flow

rate of 2.5 ml/hr, controlled by a syringe pump. A positive bias (from 15 to 30 KV) was applied at the metallic needle while the collector is grounded. The distance between the end of the needle and the FTO glass was kept at fixed distances (from 4 to 16 cm). The as-prepared HHS with titanium precursor were hydrolysed using steam at 80 ℃ followed by annealing at 800 ℃ overnight with ramping at a rate of 1 ℃/min. The photoanode for photoelectrochemical water splitting is used as the calcined TiO_2 HHS on the FTO substrate.

Degussa TiO_2 P25 particles were used as received, and electrophoretic deposition method was used to fabricate them into a thin film structure on the FTO glass. As-deposited P25 film was sintered at 400 ℃ for an hour by ramping at rate of 5 ℃/min to minimise the cracking of the film. Ditetrabutylammonium cis-bis(isothiocyanato)bis(2,2'-bipyridyl-4,4'-dicarboxylato)ruthenium(II)) (N719, Sigma) was used as the dye to sensitise the TiO_2 film. Both TiO_2 HHSs and P25 film were soaked in 0.3 mM N719 ethanol solution for 24 hours. An ethanol solution of 0.5 mM H_2PtCl_6 (Sigma-Aldrich) was used to form Pt coating on a FTO glass as the cathode. The solution was spin-coated on a FTO glass, followed by calcination at 400 ℃ for 20 minutes. A mixture solution of the electrolyte was prepared by dissolving 0.6 M 1-methyl-3-n-propylimidazolium iodide (PMII, Sigma Aldrich), 0.5 M 4-tert-butylpyridine (TBP, Fisher Scientific), 0.05 M iodine (I_2, Fisher Scientific) and 0.1 M Litium iodidie (LiI, Fisher Scientific) in acetonitrile; the chemical structures are shown in Table 6.1.

Table 6.1 The chemical compounds of dye and electrolyte for fabricating DSSC.

Component in solar cell	Chemical name	Structure
Dye	Ditetrabutylammonium cis-bis(isothiocyanato)bis(2, 2'-bipyridyl-4,4'-dicarboxylato)ruthenium (II)) (N719)	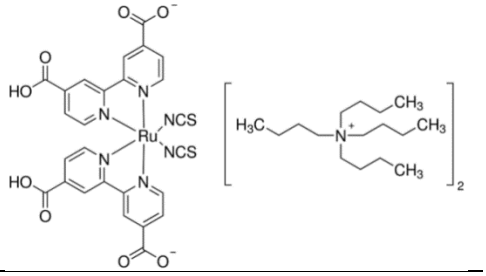
Electrolyte	1-methyl-3-propylimidazolium iodide (PMII)	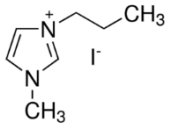
	4-tert-Butylpyridine (TBP)	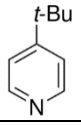
	Lithium iodide	LiI
	Iodine	I_2

The morphologies of the HHSs were studied by scanning electron microscopy (SEM, Joel JSM 820M). The diameters of the HHS were measured by ImageJ (National Institutes of Health, USA). A home-made TIRFM was further used to study the hollow hemisphere morphology. The crystal structures of TiO_2 HHS samples at different calcination temperatures were identified using a powder XRD (Siemens D500). A FTIR (Perkin Elmer, Spectrum One) was used in attenuated total reflectance (ATR) mode to study the decomposition of PMMA at elevating calcination temperatures. A standard 100 mW/cm^2 light source with an AM 1.5G filter was used to test the efficiency of the PEC water splitting and DSSC.

6.4. Results and discussions

6.4.1 Electrospray synthesis of polymer hollow hemispheres

The morphology of the electrospun nanostructures critically depends on the strength of the polymer chain interactions, which is sufficient to balance the surface

tension generated during the extrusion process. The work in Chapter 4 has identified the critical entanglement concentration, 3.3 wt%, for high molecular weight PMMA (MW 996,000 g/mol) in dimethylformamide (DMF), indicating the threshold for the strength of the entanglement. The critical point is indicated by the specific solution viscosity, which was about 5.5 mPa s, below which, beads were formed in the electrospinning process, defined as electrospray. In this work, in order to form HHSs, a low molecular weight PMMA (MW 35,000 g/mol) was used to dissolve in NM. The relatively low molecular weight implies short molecular chains, so that the entanglement at corresponding solution concentration is also reduced. The reduced entanglement encourages the formation of beads instead of fibres, as it is insufficient to balance the surface tension. Meanwhile, the solvent, NM, with a higher vapour pressure was chosen instead of DMF. At room temperature, the vapour pressures are 35 and 3.7 mmHg for NM and DMF, respectively. The fast vaporisation rate of NM solvent is essential for the formation of hollow morphology.[256] During electrospinning, since the entanglement of the solution determines the length of the fibres, it thus also determines the size of the HHS. Therefore, the outer diameter of HHSs is determined by the length of polymer chain and PMMA concentration. The wall thickness is determined by the evaporation rate of the solvent, as well as the PMMA concentration.[256]

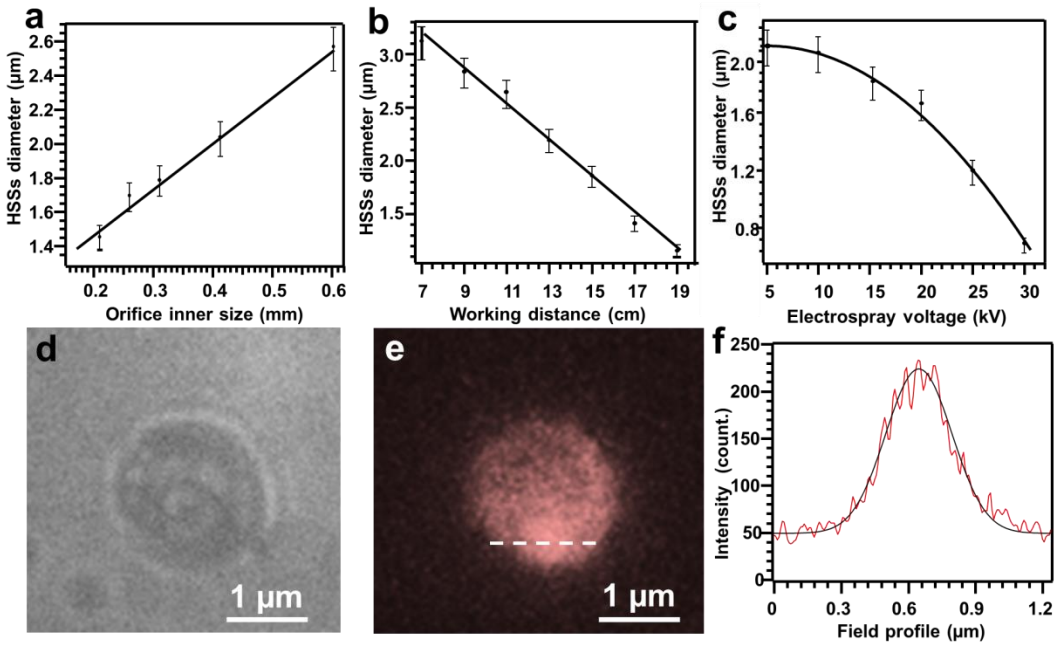

Figure 6.1 Characterisation PMMA hollow hemisphere. The outer diameter of the HHSs as a function of (a) the orifice inner size of spinneret, (b) the distance between the end of the orifice and (c) the collector and the applied voltage. (d) A typical TIRFM image of PMMA HHS doped with rhodamine B. (e) The corresponding fluorescence image under excitation at a wavelength of 523 nm. (f) The linear profile of the light intensity from Figure 6.1e.

The processing parameters, including the orifice size of the spinneret; the distance between the collector and the orifice; and the applied voltage are investigated to control the morphology and structure of HHSs. The average outer diameter of the HHSs as a function of the inner diameter of the needle is shown in Figure 6.1a. A linear relationship can be observed as the increase of needle diameter with the increase of the HHSs size. This observation is qualitatively in an agreement with the previous electrospinning study for nanofibres. Needles with an increased diameter will deliver an increased quantity of the solution jet with larger cross sections, resulting in an enlarged Taylor cone shape, and hence the diameter of the HHS is increased. Figure 6.1b and

6.1c demonstrate the average diameter of the HHSs as a function of the distance between the end of the orifice of the spinneret and the collector and the applied voltage, respectively. Both increases of the working distance and of the electrical potential cause a decrease of the HHS diameter. At an increased voltage bias, the extrusion force at the tip of the needle is increased, which causes the solution jet to become thin, thus forming the HHS with a reduced diameter. On the other hand, by increasing the working distance, the solution jet has an enhanced travelling time. This will increase the probability of breaking down into smaller droplets, as the polymer entanglement is not sufficient to balance the surface tension. This will result in the formation of HHSs with reduced diameter. Similar to the electrospinning nanofibres, with higher applied voltage bias, the diameter of HHS will increase faster giving a non-linear relationship with the applied voltage.

Figure 6.1d shows a typical TIRFM image of a PMMA HHS doped with Rhodamine B. Figure 6.1e is the corresponding fluorescence image under light excitation at the wavelength of 523 nm. The Rhodamine B trapped in the wall of the HHS was excited with emission at a wavelength of 580 nm. The fluorescence brightness is not evenly distributed across the HHS. The linear intensity profile is plotted in Figure 6.1f. The highest emission light intensity can be located at the centre of the HHS cavity. Such images further demonstrate the formation of 3D hollow hemispherical structure through electrospray.

6.4.2 Synthesis of TiO_2 HHSs

TTIP was blended into the polymer solution as the titanium precursor to synthesise TiO_2 HHSs. The electrospray was carried out with a voltage bias of 20 kV, collector distance of 15 cm and a flow rate of 2.5 ml/hr. The concentration of the TTIP in the precursor polymer affects the morphology of the electrosprayed HHS.

Homogeneous HHS structures can be obtained when the concentration of TTIP is 4 wt%, as shown in Figure 6.2a. However, when the concentration of TTIP was increased to 6 wt%, multiple dented droplets were formed instead of HHS structure, shown in Figure 6.2b. This phenomenon is because when the concentration of TTIP is increased, the overall viscosity of the polymer solution is decreased, since TTIP is a liquid at room temperature. Lower viscosity reduces the entanglement in the polymer solution, resulting in the formation of inhomogeneous dented HHSs with a wide range of size. The same phenomenon also happened with a low polymer concentration.

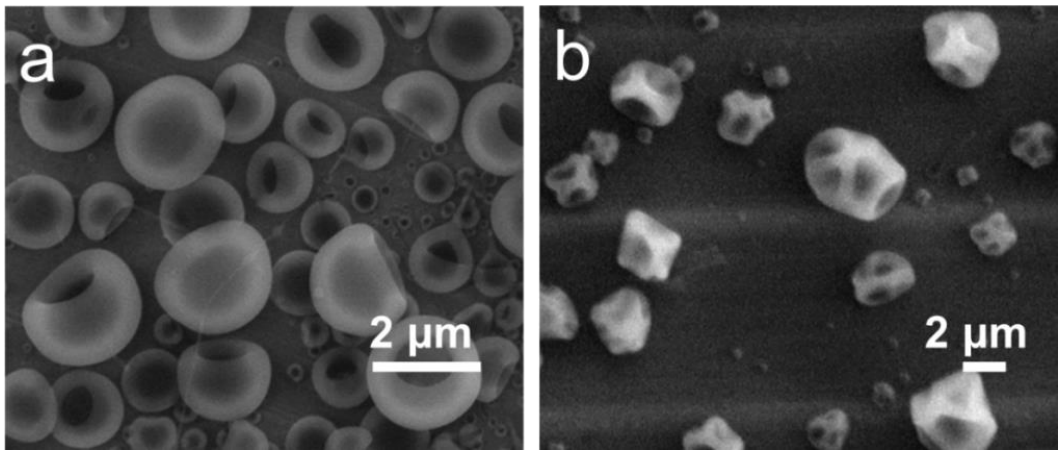

Figure 6.2 The morphology of as-prepared TTIP/HHSs prepared by various TTIP concentrations of (a) 4 wt% and (b) 6 wt%.

The composite HHSs were calcined in a furnace to remove the polymer and to convert TTIP to TiO_2 HHSs. The PMMA thermal decomposition process is studied using ATR-FTIR, shown in Figure 6.3. Initially, the intense peaks appeared at the wavenumber of 1150 cm^{-1} and 1700 cm^{-1}, corresponding to the stretching modes of the C-O and C=O, located on the ester group of PMMA. When the sintering temperature is increased to 200 ℃, all the dominant peaks still can be observed with a reduced intensity. By further increasing the temperature to 300 ℃, only the C-C stretching mode

is observed (1450 cm^{-1} and 1600 cm^{-1}), from the residue of the calcined PMMA. The results indicate that PMMA is decomposed by cleaving the ester group, leaving the carbon to be calcined with elevated temperature in the range of 300~400 ℃.

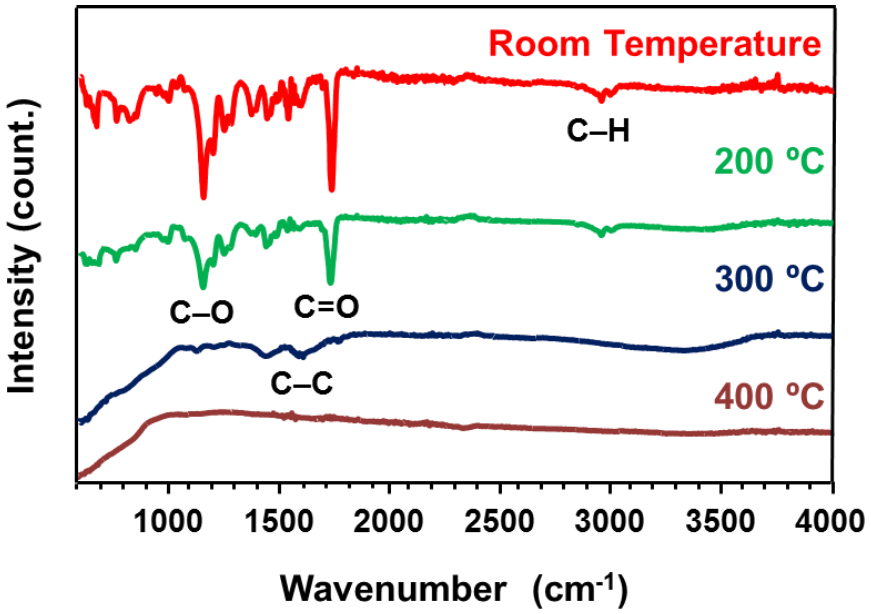

Figure 6.3 The thermal degradation of the PMMA/TTIP HHSs film using FITR-ATR, at room temperature, 200 and 300 and 400 ℃. The thermal degradation of the PMMA/TTIP HHSs film using FITR-ATR, at room temperature, 200 and 300 and 400 ℃. The peaks at 1150 and 1700 cm^{-1} correspond to the stretching modes of the C-O and C=O of ester group. The peaks at 1450 and 1600 cm^{-1} are the C-C stretching modes from the residual of the decomposed PMMA.

Typical SEM images of TiO_2 HHS are shown in Figure 6.4a. The tilted cross-sectional view shows that the HHSs are homogeneously deposited on the substrate. The inset of Figure 6.4a shows the thickness of the HHSs film, collected by 4 hours electrospraying. Figure 6.4b shows a top-view image of the TiO_2 HHS thin film. The inset shows the image of a single HHS. It is noticeable that some crystal facets are

formed on the wall of the TiO_2 HHS, confirming that large-scale crystallisation happened during calcination at 400 ℃.

The crystallinity of the TiO_2 HHSs was monitored by XRD with increased annealing temperatures, as shown in Figure 6.4c. At 400 ℃, pure anatase phase of TiO_2 (*JCPDS#89-4921*) is obtained, showing diffraction peaks located at 2θ = 25.156°, 37.385°, 47.782°, 53.344° and 54.752°, corresponding to (101), (004), (200), (105), (211) and (204) crystal planes. With a further increase of the calcination temperature to 650 ℃, additional diffraction peaks are generated, located at 2θ = 27.259°, 35.769°, 40.900°, 43.750°, 53.895° and 68.460°, corresponding to (110), (101), (111), (210), (211) and (301) crystal planes, attributed to rutile (*JCPDS#21-1276*) phase of TiO_2. The rutile phase is thermodynamically more stable than anatase, thus when temperature is increased to 800 ℃, rutile became the dominant composition. The diameter distribution of the observed nanopores was measured from the high resolution SEM images (inset of Figure 6.4b). The result is displayed in Figure 6.4d with an average pore diameter of 75 nm. This is in contrast with the polymer HHS in Figure 6.2a, in which, the surface is smooth. Such porous texture on the HHS surface could effectively increase the number of active centres for the PEC reaction, although it might also increase possibility of the electron-hole recombination.

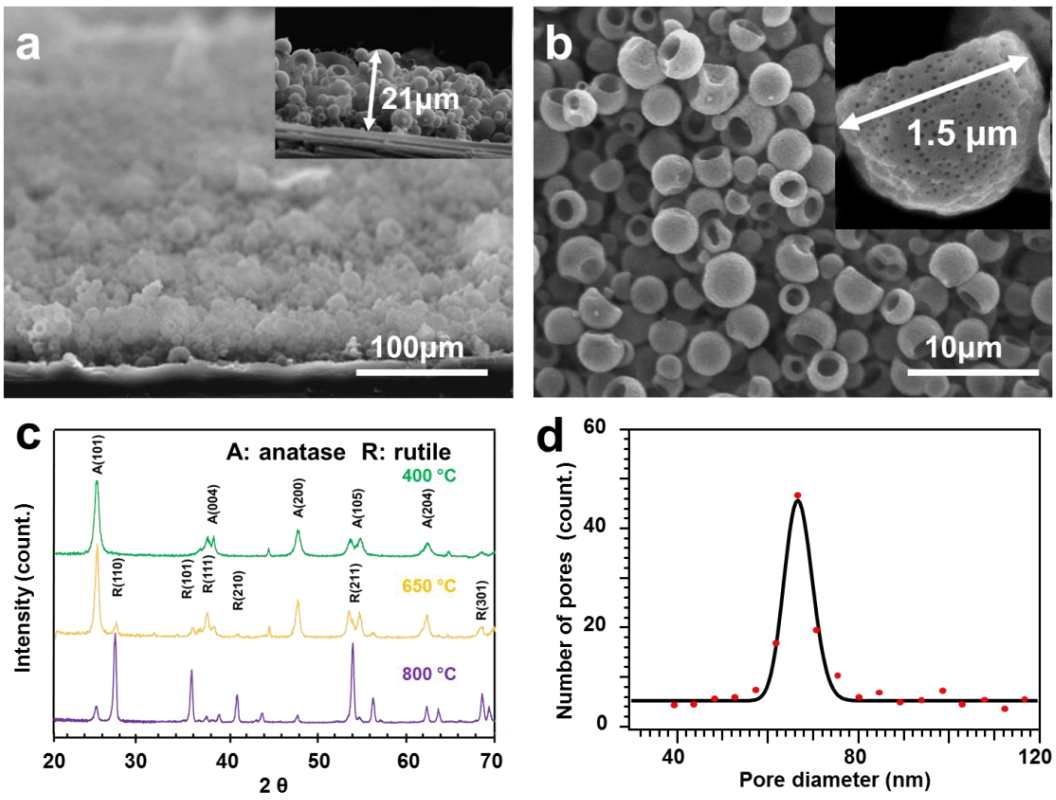

Figure 6.4 Characterisation of the TiO_2 HHSs. (a) A tilted cross-sectional view of the TiO_2 HHSs thin film, the inset presents the thickness of the as-prepared TiO_2 film. (b) A Typical SEM image of the TiO_2 HHSs, the inset is an individual HHS, presenting a typical diameter of the HHS. (c) The XRD patterns of the TiO_2 HHSs under different annealing temperatures. (d) The nanopore distribution on the surface of the HHS.

The morphology of the synthesised TiO_2 HHS is not only dependent on the TTIP concentration, but also sensitive to the thermal treatment of the as-prepared HHS. Due to the high volatility of TTIP (melting point 17 ℃ and boiling point 232 ℃), the morphology of the HHS can be easily distorted, during the calcination process. Thus far, limited methods were reported to overcome such destruction in the thermal treatment.[101] In order to maintain the HHS morphology, an effective HPPS method was developed to encourage the hydrolysis of TTIP. The as-sprayed composite HHSs were treated with steam, which converts the TTIP to $Ti(OH)_4$ by the HPPS. The mechanism is proposed

as the following reaction (Equation 6.1):[257]

$$Ti(OC_3H_7)_4 + 4H_2O \rightarrow Ti(OH)_4 + 4C_3H_7OH \qquad \text{(Equation 6.1)}$$

In this reaction, hydroxide ions are attracted to the Ti^{4+} ions, and replace the isopropoxide ligands, leading to the formation of the relatively stable $Ti(OH)_4$ species. The formed titanium hydroxide is further decomposed into TiO_2 through dehydration during calcination. By converting the TTIP to the titanium hydroxide species, the volatility of the titanium species is significantly reduced, and the morphology of HHS can be preserved at a high calcining temperature.

A typical HPPS process involves the hydrolysis precipitation, in which, a inorganic phase is separated from an organic phase. Once the phases are separated, further thermal removal of the organic phase could create a porous structure in the metal oxide framework. Figure 6.5 shows the SEM images of the sintered TiO_2 HHSs after HPPS at various durations of the as-sprayed HHSs. Without any hydrolysis treatment, almost all the HHSs were evaporated during the calcination process as shown in Figure 6.5a. After 2 hours of hydrolysis treatment, only a small amount of residual TiO_2 was left after calcination, shown in Figure 6.5b. The significant loss of the titanium can be attributed to the low boiling point of TTIP. At this stage, there is almost no HHS structures left on the substrate after calcination.

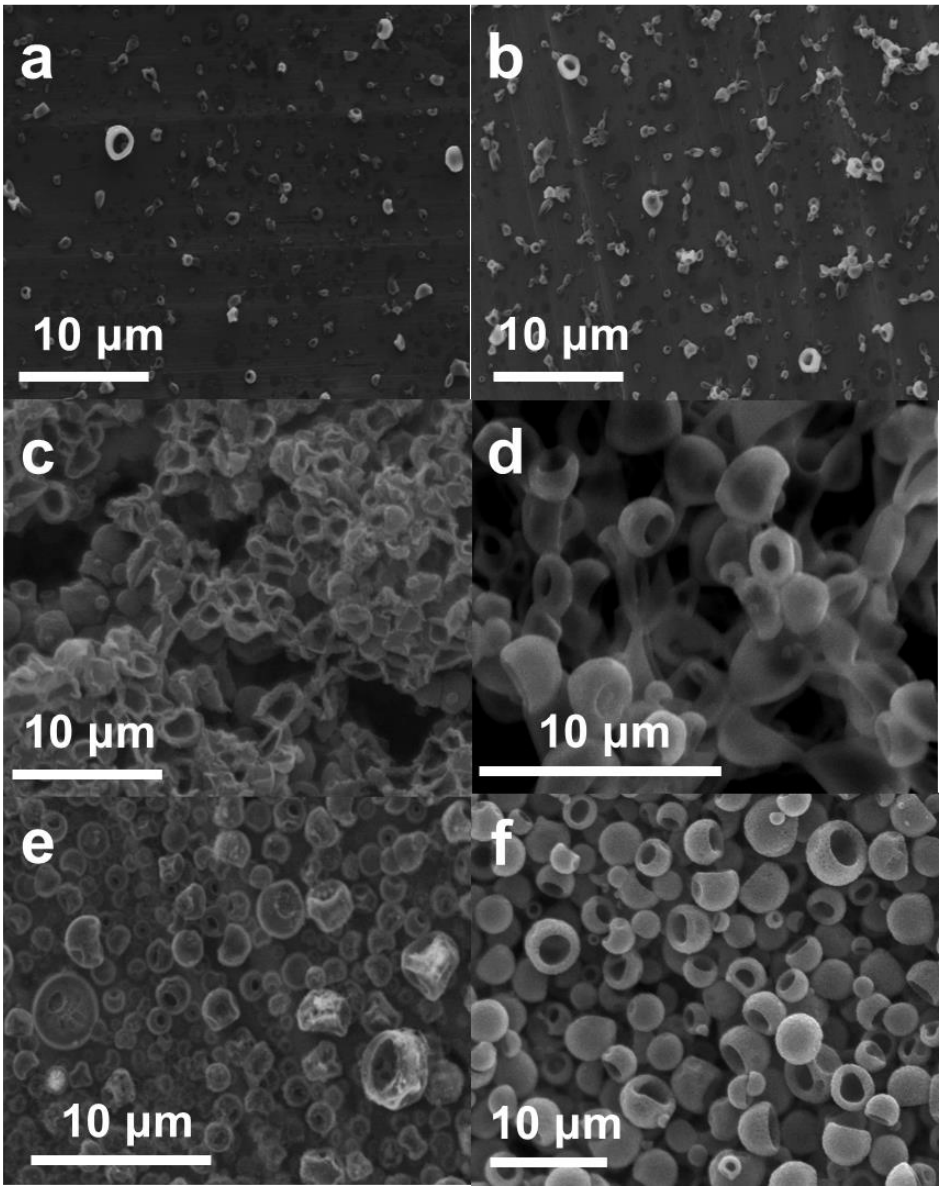

Figure 6.5 Typical SEM images of sintered TiO_2 HHSs after HPPS process with durations of (a) 0 hour, (b) 2 hours, (c) 4 hours, (d) 6 hours, (e) 8 hours and (f) dipping in water followed by an hour of hydrolysis treatment.

As the duration of the hydrolysis treatment increased to 4 hours, Figure 6.5c, the quality of the TiO_2 HHSs improved, which suggests an increased conversion of TTIP to $Ti(OH)_4$. This process stabilised the titanium species, and encouraged the formation of the TiO_2 HHSs. At this stage, the coalescence and coagulation of the HHSs can still be observed, possibly due to the melting of PMMA HHSs, as there is insufficient $Ti(OH)_4$

to support the HHSs morphology. The image also shows that the wall of the hollow structure is much thinner than the HHSs before calcination. Figure 6.5d shows that the aggregation of the HHSs was reduced after 6 hours of hydrolysis treatment. Although the individual HHS can be clearly recognised from the image, some degree of coalescence can still be observed. By extending the hydrolysis treatment duration to 8 hours, the quality of the TiO_2 HHSs is significantly improved, shown in Figure 6.5e, but still with some deformations.

Such time dependent observation demonstrates the importance of the hydrolysis treatment in stabilising to form TiO_2 HHS. Without converting TTIP into $Ti(OH)_4$, the HHSs morphology will lose during calcination. The slow rate of TTIP hydrolysis is due to the limited accessibility of H_2O vapour into the PMMA matrix. Based on such understanding, a much more effective HPPS is developed by dipping the as-sprayed PMMA/TTIP HHSs thin film into deionised water followed by an hour of hydrolysis treatment. The resulting TiO_2 HHS morphology is shown in Figure 6.5f. The temperature of the steam is also important. The softening point of PMMA is about 125 ~ 150 ℃, depending on the wall thickness of the HHS. With the steam temperature at 85 ℃, it is expected that the surface of PMMA is slightly melted to facilitate the phase separation, while overall HHS morphology is maintained.

It is important to note that not only the hemispheric morphology of the HHSs was preserved, nanopores were also formed on the wall of the HHSs structure. The formation of the nanopores is directly caused by the hydrolysis-phase separation process, which is similar to the conventional immersion precipitation method usually used to create porous polymer membranes.[258] It is believed that the size of the pores can be controlled using this HPPS method by control of the TTIP concentration, the duration, and the temperature of HPPS treatment. Furthermore, such a method can be

used to create electrospun porous metal oxide nanofibres or metal oxide thin films, if a metal precursor is initially used with the polymer matrix.

6.4.3 Photocatalytic applications of TiO_2 HHSs

The TiO_2 HHS thin film was applied in PEC water splitting to evaluate photoactivity. The TiO_2 HHS film formed with an average diameter of 1 μm. The thickness of the film is 21 μm, as shown in the inset of Figure 6.4a. For comparison, a P25 thin film was also fabricated through an electrophoretic deposition method, with a film thickness of 20 μm, as presented in the inset of Figure 6.7a. Since the crystallinity of the TiO_2 HHSs film highly relates to the photoreactions, both of the samples were annealed at 650 ºC for an hour. As shown in Figure 6.6b, the annealed TiO_2 HHSs and P25 film have almost identical XRD patterns. The measured photocurrent density as a function of applied electrochemical potential (*J-V*) is plotted in Figure 6.6c. The potential was swept linearly at a scan rate of 10 mV/s between -0.7 and 0.8 $V_{Ag/AgCl}$. Under dark conditions, the measured electrochemical current was negligible, indicating that no electrochemical reaction took place. Under illumination, a steady increase of the current flow is observed as the potential rose. During the photoexcitation process, electron-hole pairs were generated, the electrons occupy the conduction band and the holes stay in the valence band. The holes oxidise water into oxygen gas, while the electrons travel to the counter electrode (Pt) to reduce H^+ ions into hydrogen.

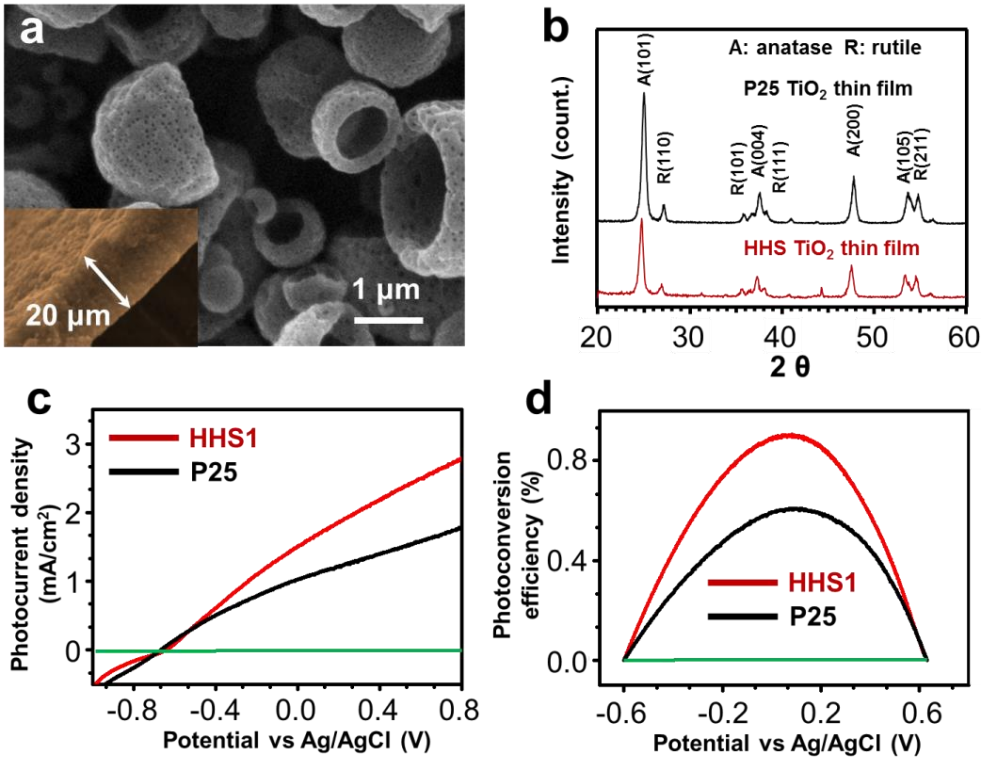

Figure 6.6 PEC water splitting performance of the TiO_2 HHSs and the P25 thin film. (a) The preserved structure of the HHS after 5 hours water splitting experiment, and the inset show the thickness of the P25 thin film for water splitting. (b) The XRD patterns of the TiO_2 HHSs and P25 thin film. (c) The photocurrent densities of the TiO_2 HHSs and P25 photoanodes. (d) The corresponding photoconversion efficiency under AM 1.5G.

The photoconversion efficiency of TiO_2 HHSs and P25 thin film are shown in Figure 6.6d. The calculation of the total output power of the PEC water splitting is following Equation 3.14 in Chapter 3. The plot of the output power as a function of the applied potential of the TiO_2 HHSs thin film (thickness of 21 μm) is shown in Figure 6.6d. The maximum output power under AM 1.5G is 0.9%, while the P25 film (thickness of 20 μm) presented a maximum conversion efficiency of 0.56%. Moreover, the TiO_2 HHSs film presents a good stability, where no significant degradation of the

morphology of the HHSs film after 5 hours PEC reaction is observed, as shown in Figure 6.6a.

The photoconversion efficiency of the TiO_2 HHSs film was also investigated as a function of the annealing temperature, shown in Figure 6.7, at a fixed film thickness of ~24 μm. The results reveal that the maximum efficiency around 1.04% is achieved for that annealed at 650 ºC. A dramatic increase of the photoconversion efficiency can be observed as compared with the HHSs film calcined at 400 ºC (0.31%). For the TiO_2 HHSs film calcined at 800 ºC, the photoconversion efficiency is decreased. This result is due to the TiO_2 phase transition (Figure 6.4c) from anatase to rutile at increased temperature. The rutile phase of TiO_2 has a direct band gap and larger effective mass for electrons and holes. Therefore, the charge recombination rate for rutile phase is expected to be higher than that for anatase phase, resulting a decreased photoconversion efficiency.

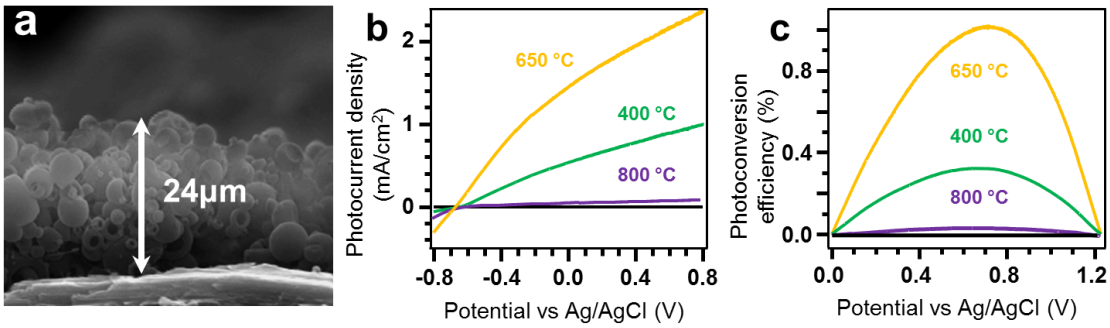

Figure 6.7 (a) The cross-sectional view of the TiO_2 HHSs film for the photoreaction studies. (b) The photocurrent density of the TiO_2 HHSs film with calcination temperatures of 400 650 and 800 ℃ and (c) the corresponding photoconversion efficiency.

The P25 film has a denser porous structure than TiO_2 HHSs film. Therefore, a

further comparison of the photoconversion efficiency between the P25 and TiO_2 HHSs was made, as a function of the film thicknesses, and the results are displayed in Figure 6.8a. It is obvious that the maximum photoconversion efficiency for P25 is only around 0.56% with a film thickness of 20 μm, which is much lower than the optimised photoconversion efficiencies of the TiO_2 HHSs (1.04% with a film thickness of 24 μm).

In order to identify a clear relationship of the porous film structure with the PEC performance, the weight and porosity of the film are also taken in a consideration. The porosity (P) of the film can be obtained through $P = V_p/V_f$, where V_p is the volume for the particle film and V_f is the volume of the solid film. For P25 thin film, 20 μm thick film is deposited on a FTO glass (1 cm×4 cm), which have a weight of 15 mg. Since the density (ρ) of the TiO_2 is 4.23 g/cm^3, the volume of the P25 film is 3.54×10^{-3} cm^3. As the solid film volume (V_{f1}) is 0.008 cm^3, the porosity of P25 film is around 44.3%, indicating that the P25 film formed through the electrophoretic deposition method is quite compact. For HHS, 24 μm thick film deposited on a ITO glass (1 cm×4 cm) is 11 mg, and the volume of HHSs is calculated (2.60×10^{-3} cm^3). The solid film volume (V_{f2}) is given 0.0096 cm^3, so the porosity of HHSs is around 27.1%. Such micron channels with the less packed HHS film play an important role in PEC water splitting and could improve the mass transportation of electrolytes.

Two main reasons are credited for the enhanced PEC water splitting efficiency by using TiO_2 HHSs. Firstly, TiO_2 HHS thin films have micro-channels, and the packing is naturally less dense than P25 thin film. This could improve the mass transportation of electrolytes and ions into and out of the film. Secondly, the HHS is formed with large crystal size than P25 nanoparticles with an average diameter of 21 nm. Although the overall surface in the P25 film is expected to be higher, the nanopores formed during HPPS treatment of the HHS could compensate the surface area with decreased domain

boundaries. Therefore, with the improved charge mobility and liquid-solid contact, the enhanced photoconversion efficiency from the TiO_2 HHS film is not a surprise.

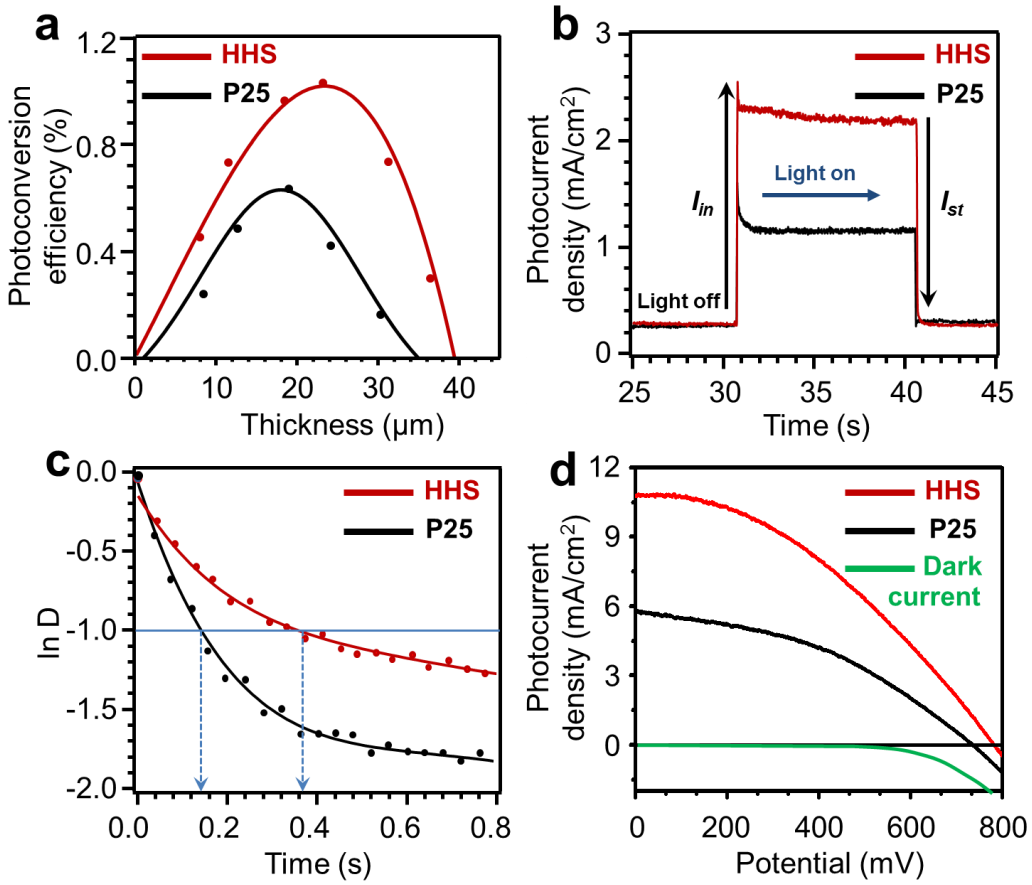

Figure 6.8 (a) The photoconversion output power of the TiO_2 HHSs and P25 film as a function of the film thickness under illumination. (b) Anodic photocurrent dynamics of the photoanodes. (c) The corresponding normalised plots of ln*D* (obtained from Equation 6.2) as a function of the illumination time. (d) The optimised thickness of the TiO_2 HHSs and P25 film are applied as a typical the dye sensitised solar cell.

In a photocatalytic reaction, charge recombination is, to some extent, inevitable. Therefore, the recombination rates were compared between P25 and TiO_2 HHSs thin film. The current spikes formed as transients under illumination are known to be

evidence of accumulation of photoexcited holes at the interface between the semiconductor and electrolyte.[259] Such oversaturation will delay the oxidation process with slower oxygen evolution reaction kinetics. Such hole accumulation at the interface can be estimated by a quantitative analysis of the initial photocurrent spike. Figure 6.8b presents a comparison of the transient moment that light irradiates the TiO_2 HHS and P25 film with optimised thicknesses (24 μm thick film for HHSs and 20 μm thick film for P25) under constant bias of 0.4 V. The corresponding normalised parameter (*D*) is calculated using Equation 6.2 to estimate the recombination rate:

$$D = (I_t - I_{st})/(I_{in} - I_{st}) \qquad \text{(Equation 6.2)}$$

where I_t , I_{in} and I_{st} are the time-dependent, initial and steady state photocurrent responses, respectively. The recombination rate is depicted in Figure 6.8c, which shows ln*D* as a function of time for both of the samples. The transient time constant (τ) is measured as the time when ln*D* = -1, i.e. the 1/e decay. The time constant for P25 is about 0.14s, while for HHSs, it is about 0.38 s. Thus, it confirms that the P25 film has a faster recombination rate in comparison with that of the TiO_2 HHSs film. In Figure 6.8b, it is also possible to notice that the photocurrent of the HHS generally becomes steady around 10s, while the P25 film become steady in 2s, this is possibly due to the light trapping effect from the HHS structure. The multiple light reflections could preserve the exciton in a longer life than that for P25 film.

The 24 μm thick HHS TiO_2 film and 20 μm thick P25 film were also tested as photoanodes for standard DSSCs. Ru dye (N719) and the electrolyte with organic solvent (acetonitrile) were important compositions for DSSCs. N719 facilitates visible light absorption in DSSC to generate photoexcited electrons. It absorbs a wide range of

visible light spectrum up to a wavelength of 750 nm[260] with three major bands at 393, 414 and 533 nm, as shown in Figure 6.9.[261] The band in UV region at 393 nm corresponds to the metal-to-ligand charge transfer (MLCT) transitions, between the negative charged oxygen and the Ru. The bands in the visible region at 414 and 533 nm are more energetic ligand-centred charge transfer (LCCT) between two ligands.[261]

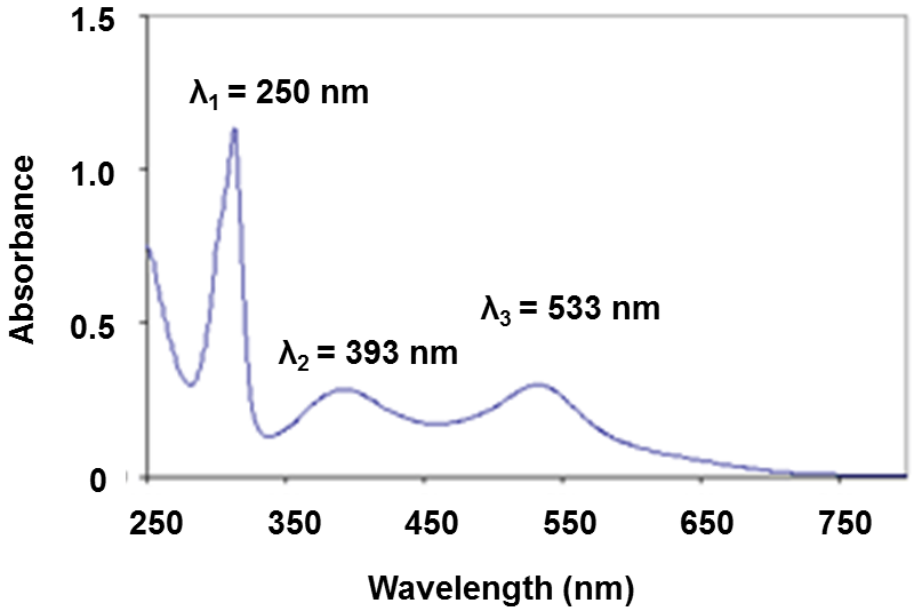

Figure 6.9 Light absorption of the Ru dye (N719), presented three major peaks at 250 nm, 393 nm and 533 nm.[261]

Table 6.2 Photovoltaic properties of DSSC assembled by using TiO_2 HHSs film and Degussa P25 particle film with optimised thickness.

	Thickness (μm)	V_{oc} (mV)	J_{sc} (mA/cm^2)	Fill Factor	Efficiency (%)
TiO_2 HHSs film	25	781	10.76	0.39	3.26
P25 film	18	735	5.71	0.41	1.72

The ionic liquid PMII together with LiI and I_2, was used as the electrolyte, PMII

is non-volatile, non-flammable with an extremely high ionic conductivity.[262] LiI and I_2 were used to form the redox couple (I^-/I_3^-) in PMII as the 'vehicle' for internal electron exchange. TBP was used as a stabiliser to passivate the interface defect on TiO_2. It is chemisorbed onto the Ti atoms surface via the pyridine group, which could effectively reduce the charge recombination probability at the TiO_2/electrolyte interface.

The measured *J-V* plot is shown in Figure 6.8d under solar simulator irradiations. TiO_2 HHS film obviously exhibits a higher photovoltaic efficiency than P25 film, since it gives a higher photocurrent in the full voltage range. The detail of the photovoltaic properties are summarised in Table 6.2. The P25 film solar cell has the open current voltage (V_{oc}) and fill factor (*FF*, defined in section 3.3.2) of 735 mV and 0.41, respectively, which are close to those obtained using HHSs film (V_{os} = 781 mV and *FF* = 0.39). However, the short circuit current (J_{sc}) obtained from the HHSs film is 10.76 mA/cm^2, which is about double of that obtained from P25 film (5.71 mA/cm^2). J_{sc} essentially indicates the quantity of the excited electrons in the CB under light illumination. Such performance can be mainly credited to the unique structure of the TiO_2 film. In the sensitising process, the dye can be loaded into the nanopores and the internal cavity of the HHSs. The large micro gaps between HHSs also improve the transportation of the electrolyte, while the unique hollow morphology may help to trap the scattered light in the HHSs film.

6.5 Conclusions

TiO_2 HHSs thin films were synthesised through an electrospray method as photoanodes for PEC water splitting and DSSC. The morphology and structure of the PMMA HHS were investigated as a function of process parameters. A HPPS method was developed to preserve the TiO_2 HHS structure, and to create nanopores on the

surface of the HHSs. The film thickness was further optimised to generate a photoconversion of 1.04% at the film thickness of 24 μm in the PEC water splitting application. This result represented a significant enhancement in a comparison to the P25 thin film. The charge recombination process was further investigated by analysing the curvatures of the initial spikes in photocurrent. DSSCs were also assembled using the TiO_2 HHS and P25 film within the optimised thickness. The J_{sc} obtained from the HHSs film (10.76 mA/cm^2) was about double that obtained from P25 film (5.71 mA/cm^2), which confirms that the unique morphology of the TiO_2 HHS is responsible for the enhanced photoconversion efficiency in PEC water splitting and photovoltaics. From the results, although TiO_2 is only able to absorb UV light, a relatively good water splitting efficiency is presented. However, in term of the DSSC, despite a broad absorption spectrum, presented a low photoconversion efficiency, which is due to a poor *FF* of the DSSC. The *FF* of this DSSC may due to the connection between the dye and the TiO_2 base, which might be improved by modifying the surface of the TiO_2 or the ligands of the dye.

Chapter 7 Embedded metal nanowire networks in a polymer as tough and flexible electrodes for a transparent triboelectric nanogenerator

7.1 Abstract

Transparent and flexible energy harvesting devices are important for integrated, wearable electronics and smart fabrics. In this work, a transparent triboelectric nanogenerator (TENG) was developed to harvest mechanical energy. One dimensional (1D) metal nanowires percolation networks were developed as flexible and transparent electrodes. Theoretical simulations were carried out to establish the working mechanism of triboelectric devices. The influences of area fraction of the silver nanowire networks in the electrode were investigated to assess the output performance of the triboelectric devices. The fine balance between the output performance and the transparency of the triboelectric device was further optimised. This work forms the foundation to design and to fabricate a hybrid cell by integrating the transparent triboelectric cell with an organic solar cell. Such a hybrid cell could harvest both mechanical and solar energies, as is demonstrated in Chapter 8.

7.2 Introduction

Wireless and wearable electronics require rechargeable energy sources that can be integrated into electronics. The recent emergence of flexible film TENGs attracts great interest as a device to harvest mechanical energy. In comparison with other generators,[74, 263] it has potential advantages, including high conversion efficiency, scalability, robustness, simple design and cost-effective fabrication. It is compatible with a wide range of complex applications, from self-powered electronics,[264, 265] and

sensors[266] to high-density energy production.[267, 268] In addition, a transparent triboelectric device offers the possibility to integrate with a solar cell as a hybrid cell,[72] which is designed to harvest different forms of energy.[269] In such a transparent device, using 1D silver nanowires (AgNWs) as electrodes, the efficiency of a triboelectric device is increased as the density of the AgNWs increases, but the optical transparency will reduce. Therefore, it is necessary to investigate quantitatively the correlation between the triboelectric output performance and the overall transparency of a T-TENG.

Herein, T-TENGs are fabricated using AgNWs percolated network electrodes. The mechanical stability of the electrode is improved by embedding the nanowire networks into a polymer matrix. The optical properties and morphology of the AgNW embedded electrode are carefully studied. The influences of the area fraction (*AF*) of the AgNWs networks in the electrode on the output performance of the triboelectric device were investigated. The fine balance between the output performance and the transparency of the triboelectric device was optimised. This study is essential to design the T-TENG using 1D metal nanowires. This kind of device is developed as a simple and cost-effective transparent thin film power supply. Its light weight and flexibility offer the potential to integrate with flexible solar cell as a hybrid energy system, and with flexible and invisible electronics.

7.3 Experimental

AgNWs were synthesised using a modified polymer-mediated polyol process. In detail, poly(vinyl pyrrolidone) (PVP) (0.26 g, MW = 1,300,000) and $FeCl_3$ (0.15 mg) were dissolved in ethylene glycol (50 ml) under stirring. The solution was pre-heated at 180 ℃ for 30 minutes to remove volatile contaminates, such as water, and cooled to room temperature spontaneously. $AgNO_3$ (0.1168 g) was added to the solution until completely dissolved, then the solution was sealed in a glass bottle and kept at 145 ℃

for 12 h in an oven. Afterwards, the as-prepared AgNWs were washed with acetone and ethanol three times each, and then re-dispersed in ethanol forming a stock of AgNW ink. Here, ethylene glycol is used as the reduction agent, and PVP is used to control the crystal facets, since it energtically prefers to adsorb on (100) faces of the Ag crystal.[270] A small amount of chloride is used as stabiliser for AgNWs, but also used to facilitate the dissolving of Ag nanoclusters during the Oswald growth of AgNWs.

The AgNW percolation network was fabricated through the Mayer-rod method, in which, a glass rod was used to spread the ink on a silicon wafer substrate.[143] In compariosn with a spray method, the Mayer-rod can spread the AgNW ink homogeneously on a substrate even at high concentration. The junctions of the AgNWs networks were welded by annealing the AgNW thin film on a hot-plate at 250 ℃ for 10 minutes. Two polymers, fluorinated polyimide (PI) and poly(methyl methacrylate) (PMMA, AR-P 661.09, Allresist GmbH), were used as the carrier substrates spin-coated on the AgNW networks. The coated PMMA film was dried at 80 ℃ for 10 minutes on a hot-plate. The cured AgNW/PMMA film can be peeled off and used as transparent electrodes. A T-TENG was fabricated through a parallel stack of two transparent electrodes with a 1 cm thick polydimethylsiloxane (PDMS) spacer. Since PDMS is a soft and elastic material, it was expected all of the surface area can be in a true contact between the electrodes.

The morphologies, structures and compositions of the electrodes were characterised by scanning electron microscope (SEM, FEI Navo NanoSEM 450). The roughness of the conductive PI film was measured using atomic force microscope (AFM, SPI 4000, Seiko). The optical transmittance was measured using ultraviolet-visible spectrometer (UV-Vis, Shimadzu UV2550). T-TENGs were driven by a resonator (JZK, Sinocera) to trigger the T-TENG with a frequency of 1.5 Hz, controlled

by a signal generator (YE 1311-D, Sinocera). The output voltages of T-TENGs were measured by a low noise voltage preamplifier (Keithley 6514), while the output current was measured by a low-noise current preamplifier (Stanford Research SR560).

7.4 Results and discussion

7.4.1 Fabrication of a flexible transparent triboelectric device

AgNWs/PMMA and AgNWs/PI films were used to fabricate T-TENGs. For the transparent conductive electrodes, AgNW percolation networks were partially embedded in the polymer surface. This arrangement helps to increase the mechanical flexibility and toughness of the electrodes. The T-TENG was operated with vertical contact-separation, and the structure is shown in Figure 7.1a. The corresponding schematic illustration of a T-TENG is presented in Figure 7.1b. In this operation mode, the mechanical movement (contact and separation) create an electrical potential and current as electric power through the triboelectric effect.

As high molecular weight PMMA has long an linear chains, the formed film has good flexibility. The polymer chains are able to form strongly entangled network in the film, effectively enhancing the pliability and robustness of the film as an electrode substrate. PI film generally possesses an outstanding mechanical stability with a good tensile strength. Therefore, these two polymers are appropriate for fabricating T-TENG. Moreover, both PMMA and PI are biocompatible materials, so they can be integrated with wearable and epidermic electronics for bio-applications.[183, 271]

The output voltage generated from a TENG device is governed by the *V*-*Q*-*X* relationship,[180] shown in Equation 7.1, which was derived in section 3.3.3:

$$V = \left(-\frac{Qd}{\varepsilon_0 \varepsilon_p S_c}\right) + \left(\frac{\sigma}{\varepsilon_0} - \frac{Q}{S_c \varepsilon_0}\right) \cdot X(t) \qquad \text{(Equation 7.1)}$$

where *V* is the output voltage; *Q* is the amount of charge transferred between the active layers; d is the thickness of the triboelectric electrode; ε_p and ε_0 are the dielectric constant of triboelectric polymer active layer (either PMMA or PI) and air, respectively; *X(t)* is the separation between two active layers; S_c is the active triboelectric area; and σ is the static charge density, which is equally distributed on the inner triboelectric surface after contact. In this equation, $-\frac{Qd}{\varepsilon_0\varepsilon_p S_c}$ represents the voltage on the polymer active layer, and $\left(\frac{\sigma}{\varepsilon_0}-\frac{Q}{S_c\varepsilon_0}\right)\cdot X(t)$ is the transient voltage from the air gap which varies with the distance between two electrodes. When two electrodes are compressed to contact, *X(t)* = 0 cm, the transient voltage is given by $-\frac{Qd}{\varepsilon_0\varepsilon_p S_c}$. In my study, the thicknesses (d) of both electrodes was fixed at 50 μm. The dielectric constant of the PMMA, PI and air at 20 ℃ are around 2.6,[272] 2.5[273] and 1.0, respectively. *X(t)* varies between 0 and 1 cm, defined by the thickness of the device spacer. The spacer was separated using a 1 cm thick PDMS film. S_c is based on the morphology of the AgNW in the electrode, and will be precisely addressed in the following section.

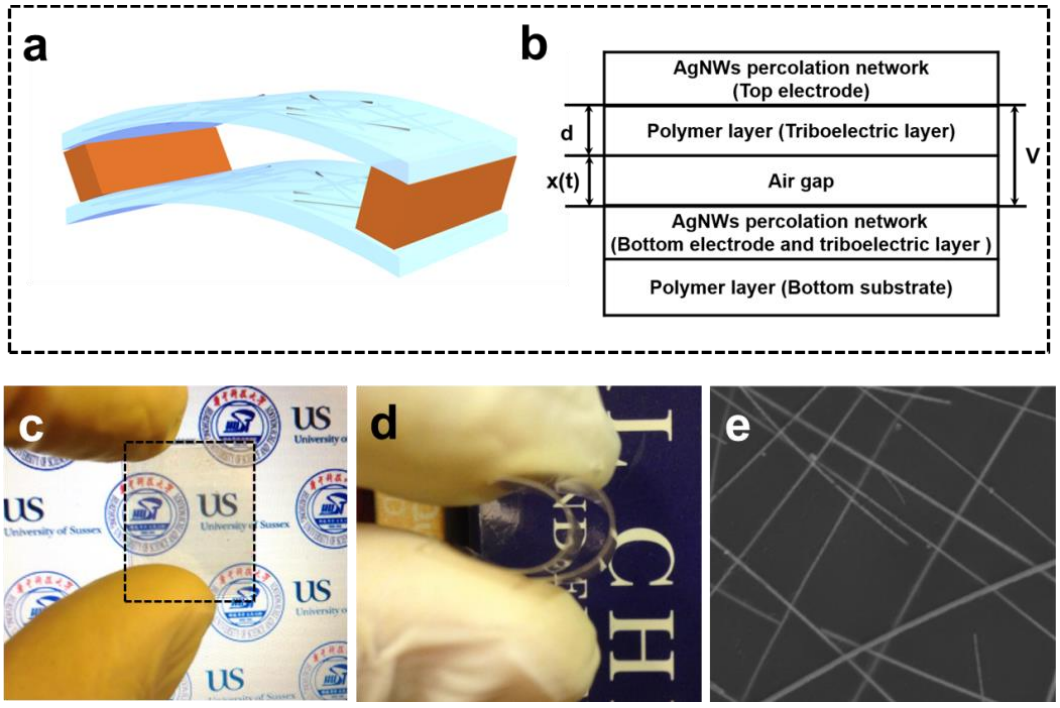

Figure 7.1 Characterisations of the T-TENG. (a) A schematic diagram of the T-TENG. (b) The basic model of the T-TENG and the function of each component. (c) The transparency of a typical two-layer polymer/AgNWs system. (d) The pliability of the system. (Collaborated with Huazhong University of Science and Technology) (e) A typical SEM image of the AgNWs homogeneously embedded in the polymer substrate.

Figure 7.1c shows a photo of the two-layer T-TENG device. The background image is used to demonstrate the transparency of the device. Figure 7.1d shows the pliability of the electrodes. The outstanding flexibility of the electrodes is credited to the use of the one-dimensional AgNW nanowires. When metal wires are extremely thin in nanoscale, the stiffness of the metal is significantly reduced. This property is essential to minimise the fatigue of the nanowires in the bending cycles of the electrodes, improving working life for T-TENG. The SEM image in Figure 7.1e presents the AgNWs in the polymer substrate; the homogeneous distribution of the AgNWs ensures efficient electrical transport.

7.4.2 Optical properties of the polymer embedded AgNWs electrode

The AgNW percolation network is the most important component in this T-TENG system, since it plays four significant roles. Firstly, it is directly used as one of the triboelectric electrodes, which contacts with the top dielectric polymer layer to generate charges through the triboelectric effect. Secondly, it is used as a conductive network to collect charges on both electrodes. Thirdly, it offers the flexibility, which is required by the operation of a TENG. Finally, the embedded AgNW percolation network offers a certain level of light transmittance, which is determined by the density of AgNWs. The morphology of the AgNWs, and the AgNW based electrode are presented in Figure 7.2. Figure 7.2a shows the typical example of AgNWs, which are homogeneously coated on a silicon wafer through the Mayer-rod method. The measured distributions of length and diameter of the AgNWs are shown in Figure 7.2b and 7.2c, respectively. The average length of the AgNWs was 90 ± 63 μm, while the average diameter was 102 ± 20 nm. The results of the average length and diameter are measured from 300 AgNWs in 10 different electrode samples.

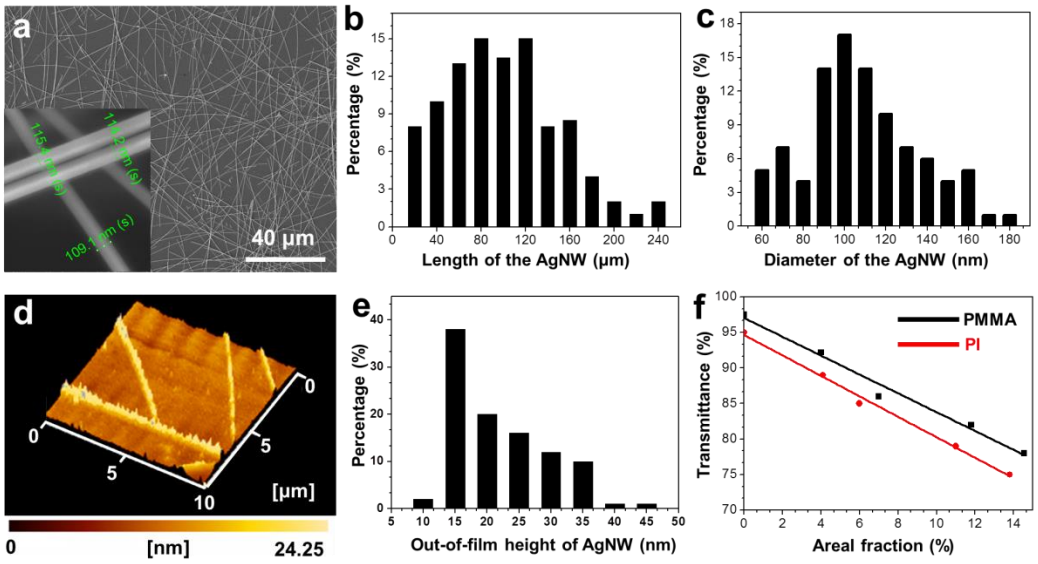

Figure 7.2 Characterisations of the AgNW and the electrode. (a) The SEM image of AgNWs networks coated on a silicon wafer, the inset shows the magnified image of the AgNWs. The analysis of (b) the AgNW length and (c) the AgNW diameter measured from 300 AgNWs in 10 electrode samples. (d) A typical AFM image represents the topography of the electrode. (Collaborated with Huazhong University of Science and Technology) (e) The analysis of the out-of-film height of AgNWs obtained from AFM images. (f) The relationships between the areal fraction and the transmittance using PI and PMMA as the substrate measured at wavelength of 600 nm.

On the basis of Equation 7.1, in this system, because the bottom AgNWs and the top polymer layer act as the active triboelectric surface, so this contact area (S_c) determines the output performances of the T-TENG. Although the hardness of the polymer was not determined, the contacted top polymer layer (PI or PMMA) is assumed to be soft enough. Under this condition, the total out-of-film AgNWs area is in contact with the polymer, and is recognised as the active triboelectric area, shown in Figure 7.3. Figure 7.3a shows that the two electrodes are released, and Figure 7.3b shows the electrodes are compressed to contact. Here the cross section of the AgNW was

simplified as a square shape.

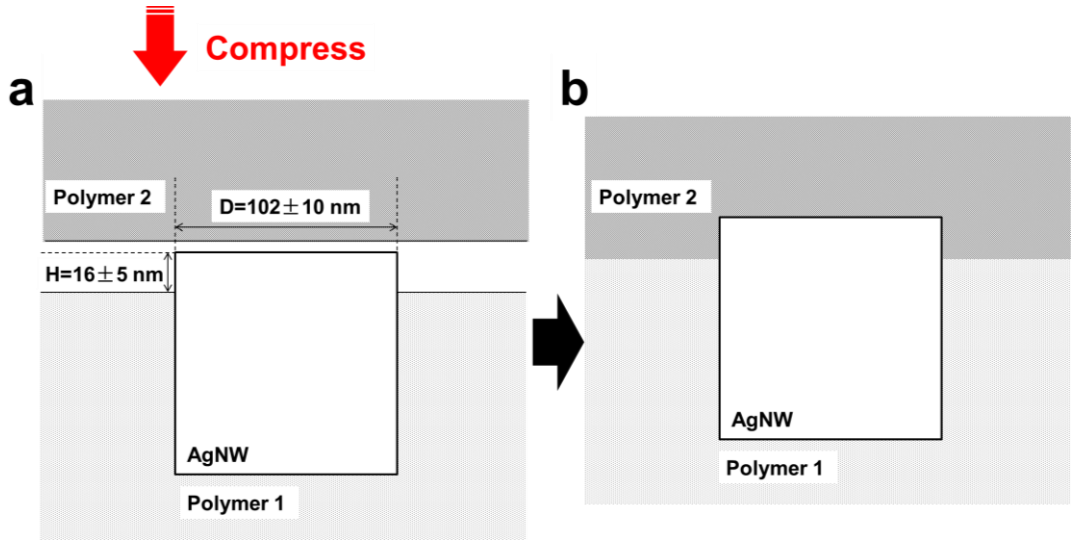

Figure 7.3 The illustration of cross-sectional view of the AgNW, (a) when two electrodes are separated, and (b) when two electrodes are compressed.

The out-of-film area of the AgNWs is naturally affected by the shrinkage of the polymer, which is highly dependent on the concentration of the polymer precursor solutions. In the drying process, the polymer film could shrink in thickness. So, on the surface with embedded AgNWs, once the polymer film is dried, the AgNWs networks will be partially emerging above the flat polymer film. The out-of-film surface area can be calculated by Equation 7.2:

$$S_c = S_s \cdot AF + S_s \cdot AF \cdot \frac{2H}{D} \qquad \text{(Equation 7.2)}$$

where S_s is the surface area of the flat polymer substrate, which is either PMMA or PI. *AF* is the areal fraction of the AgNWs, which represents the percentage of the projected

area of AgNW on the polymer substrate. H is the average value of the out-of-film height of the AgNWs, the measured value is shown in Figure 7.2e (16±5 nm). D is the average diameter of the AgNWs. In Equation 7.2, the term of $S_s \cdot AF$ is the top contact area of the AgNW, and $S_s \cdot AF \cdot \frac{2H}{D}$ expresses the side contact area of the AgNW. The area fraction (*AF*) of the AgNWs embedded in the electrode is determined using Equation 7.3:

$$AF = N_s \cdot L \cdot D \qquad \text{(Equation 7.3)}$$

where N_s is the number of nanowires per unit area, L and D are the average length and diameter of the AgNWs. For my AgNWs, L = 90±63 μm and D = 102±20 nm, then the aspect ratio is given (882). Such a high aspect ratio guarantees a good conductivity with a minimal N_s and surface roughness, leading to a good transmittance of the electrode.[83] Figure 7.2d is a typical AFM image revealing the topography of the electrode. In my experiment, the AgNWs/PMMA film exhibited a very similar topography to the AgNWs/ PI film. The out-of-film portions of the AgNWs can be observed with an average height of 16±5 nm.

AF also correlates to the optical transmittance of the T-TENG. The light blocking of the one-layer electrode has contributions from light reflection from the AgNWs networks and light absorption by the polymer. Since the thicknesses of polymer substrates are fixed at 50 μm, the amount of absorption when light passes through the pristine polymer carrier is a constant value. Figure 7.2f presents the transmittances of the bare PMMA and PI films of 97.5% and 95% at a wavelength of 600 nm, respectively. With embedded AgNWs, the light transmittance (T) can be calculated using Equation 7.4:[274]

$$T\% = 100 - [B_{Ag}AF + (1 - AF)10^{p} - AF_c] \qquad \text{(Equation 7.4)}$$

where B_{Ag} is a fitting parameter, which is determined by the wavelength-dependent optical properties of the nanowires. Variable *p* is the optical absorption properties of the polymer film. AF_c is the crossover area of the AgNWs. In this work, it is relatively small and negligible, since the average diameter of the AgNWs is only 102 nm. The term of $(1 - AF)10^{-p}$ is the light absorption of the polymer film, which is 2.5% for the PMMA and 5% for the PI thin film in this work. Equation 7.5 shows a linear dependence of transmittance on the *AF*. Khanarian et al. reported that when the incident light wavelength is 600 nm, the slope obtained by plotting the transmittance versus *AF* is -1.3 at the average AgNW diameter of 100 nm.[275] My measured results show slopes of -1.33 and -1.44 for the PMMA and PI electrode, respectively, which is in a good agreement with the reported value.

These results further confirm the homogeneity and the quality of the AgNWs. Generally, metal nanowire networks with an increased diameter have larger slope value, indicating that they can block more light. However, if the metal nanowire electrodes are applied for a T-TENG, the larger diameters of the AgNWs in the electrode are able to provide a larger interfacial triboelectric surface, which could enhance the output performance of a T-TENG.

7.4.3 Investigation of the working mechanism

The operation principle of the T-TENG can be described using the coupling of contact triboelectric charging and the electrostatic potential under cyclic compressive forces. The electrostatic potential at the interface between the AgNWs and the polymer layer are simulated using COMSOL Multiphysics Modelling software. (Collaborated with Huazhong University of Science and Technology) The simulated structure of the

T-TENG with the separated and approached situations is presented in Figure 7.4a. The top polymer film acts as the dielectric layer and the circle in the polymer film is the cross-sectional view AgNW in the polymer film. Figure 7.4a depicts the result of the electrical potential distribution caused by the electrostatic induction. In contact, the dielectric layer is negatively charged with the lowest potential of -2.50 V. The AgNW in the bottom polymer is an equivalent positive body at 6.78 V. When the electrodes approach each other, the potential of the dielectric film is around -1.33 V and the potential of the AgNW is around 5.08 V. Thus, the polymer film of the bottom electrode is acting as the carrier substrate. The contacts between the polymer dielectric layer and the metal nanowires in the triboelectric system is the key to generating static charge distribution and electrical potentials, which determines the performance of the T-TENG. Moreover, with the approach of the electrodes, the decreased potential difference indicates the formation of the current.

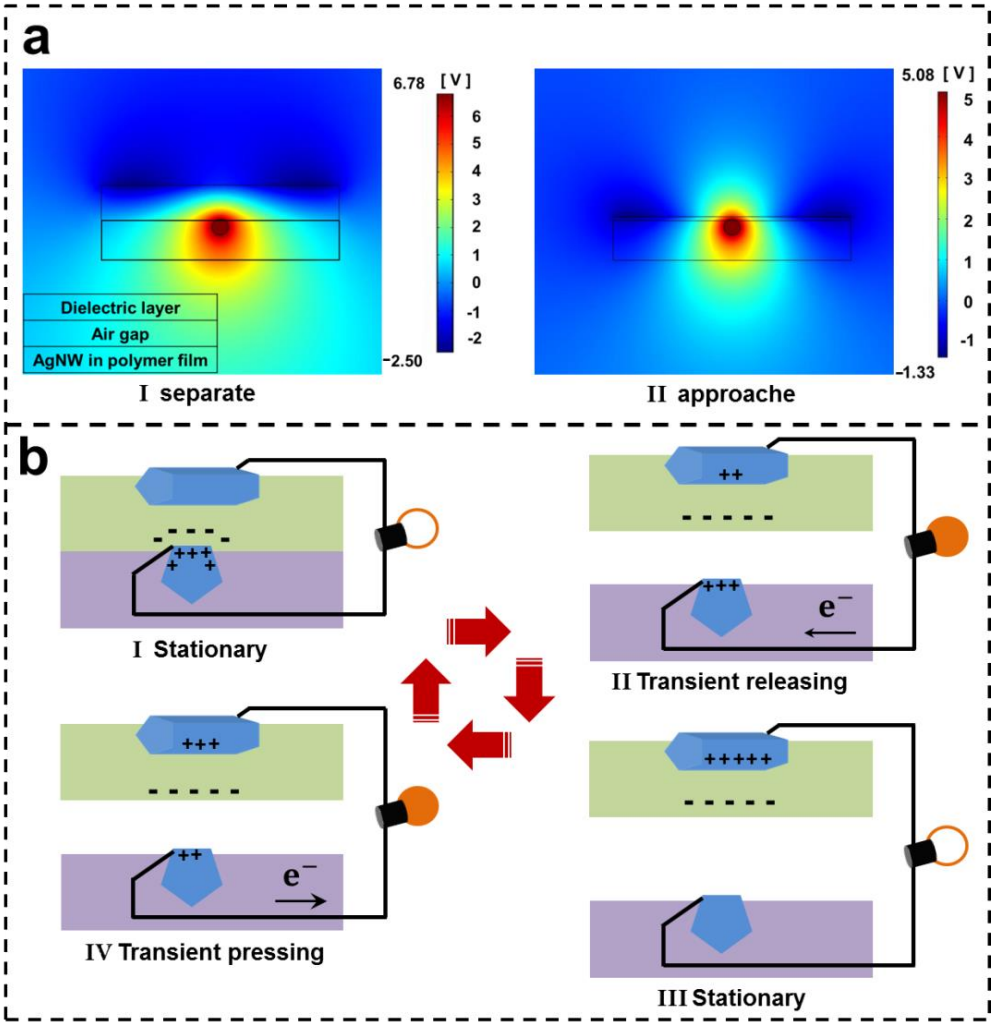

Figure 7.4 The working principle of the metal nanowires based T-TENG.[77, 78] (a) COMSOL simulations of a T-TENG with the separated (I) and approached (II) situation. (Collaborated with Huazhong University of Science and Technology) Four states are used to describe a working cycle of the T-TENG: (b) The stationary state of the T-TENG when two electrodes contacted each other under pressure. (c) A transient state that one electrode is separated from the other one. (d) The stationary state when one electrode is sufficiently far away. (e) A transient state that one electrode is pressed to approach the other one.

The working mechanism of the T-TENG is illustrated in Figure 7.4b.[77, 78] In the original stationary state I, the two electrodes are in contact, the electrostatic potential is

formed at the interface, but no electrical signal can be observed. This is because the electrons are able to transfer from the positive side of the triboelectric material to the negative side, forming an electrical equilibrium. For the AgNW-polymer interface, electrons are transferred from the AgNW to the polymer layer. The injection efficiency, measured from the charge transferred, depends on the nature of the triboelectric interfacial surfaces. When the electrodes start to separate, in state II, the electrons in the bottom electrode possess a higher electric potential than those in the top one, forming an electric potential difference. This difference drives the electrons to move through the external circuit to balance the positive triboelectric charges on the top electrode. When two electrodes are sufficiently separated, all the electrons at the bottom electrode are screened from the top electrode, which forms an equal amount of inductive charge. Once it is pressed, in the state IV, the mechanical force shortens the separation of the electrodes, and such movement generates a potential with a reversed polarity as mentioned above. The electrons are driven in the reversed direction and trapped on the bottom electrode, until the two electrodes contact. These four stages are considered as a complete cycle.

7.4.4 Optimisation of the configuration of the TENG

The influences of the *AF* in the top electrode (AF_{Top}) and bottom electrode (AF_{Bot}) on the performance of the T-TENG were investigated, including the open circuit voltage (V_{oc}), short circuit current (J_{sc}) and the optical transmittance, shown in Figure 7.5. The carrier polymers of the top and bottom electrode are made of PI and PMMA, respectively. The polymer is also optimised in this section later. Figure 7.5a and 7.5b present the V_{oc} and J_{sc}, respectively, as a function of the AF_{Bot} with a fixed AF_{Top} of 3%. When the AF_{Bot} is varied from 3% to 13%, the V_{oc} linearly increases from 0.23 V to 1.28 V, while the J_{sc} linearly rises from 32 nA/cm^2 to 10.9 nA/cm^2. The V_{oc} and J_{sc} presented

in Figure 7.5d and 7.5e were measured as a function of the AF_{Top} with a fixed AF_{Bot} of 3%, respectively. Much smaller responses in V_{oc} and J_{sc} were observed as the AF_{Top} varies. When the AF_{Top} increased from 3% to 13%, the V_{oc} and J_{sc} remain unchanged with around 0.23 V and 3.5 nA/cm^2. This phenomenon can be explained by the introduction of the metal nanowires percolation networks into the electrode. The sparse AgNW network in the bottom electrode acts as a triboelectric layer, directly affecting the injection of the charges. In other words, increasing the effective triboelectric layer, i.e. increasing the AF_{Bot}, is able to increase the charge injection from the metal nanowires to the polymer layer, which is able to improve the output performance of the T-TENG. However, AF_{Top} functions as a conductor to balance the charge and electrostatic potential, so the AF_{Top} has no direct triboelectric contribution to the process.

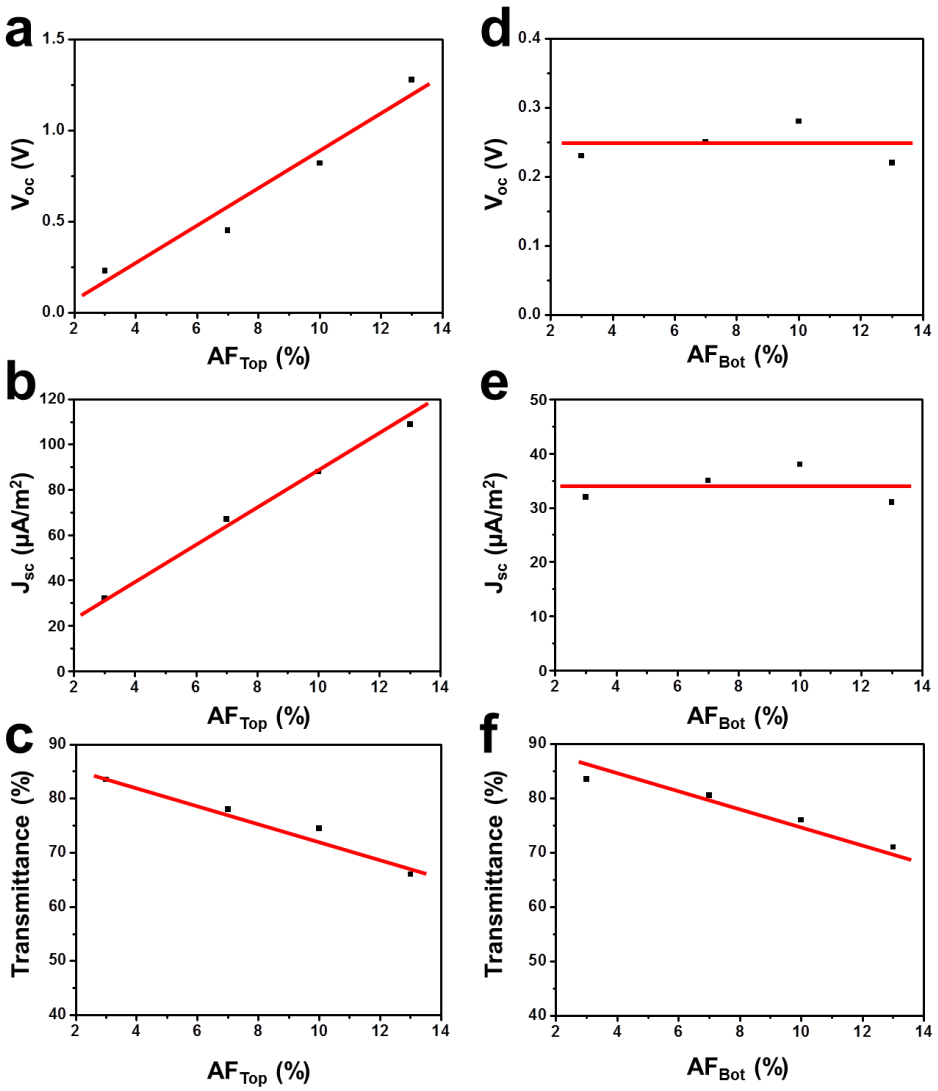

Figure 7.5 The effective regimes of the *AF* in the performances of the T-TENG. The influences of the AF_{Bot} with a fixed AF_{Top} (3%) on (a) the V_{oc} and (b) the J_{sc} and (c) the transmittance of the T-TENG. The influences of the AF_{Top} with a fixed AF_{Bot} (3%) on (d) the V_{oc} and (e) the J_{sc} and (f) the transmittance of the T-TENG. (Collaborated with Huazhong University of Science and Technology)

On the other hand, the trade-off between the *AF* of the AgNW and the transmittance is inevitable. Increasing the output performance of the T-TENG requires the increase of the *AF*, which reduces the optical transmittance of the device. The transmittances of the T-TENG as a function of the *AF*, measured at the wavelength of

600 nm, were also plotted. Figure 7.5c and 7.5f present a linear decrease with the increase of the AF_{Bot} with a slope of -1.68, and AF_{Top} with a slope of -1.26, respectively. These results well followed the linear relationship described in Equation 7.5. Moreover, between two electrodes, the overlap of the AgNWs could also reduce the overall optical loss, which also implies that an optimisation of the AgNWs network pattern is possible to further improve the transparency of the T-TENG.

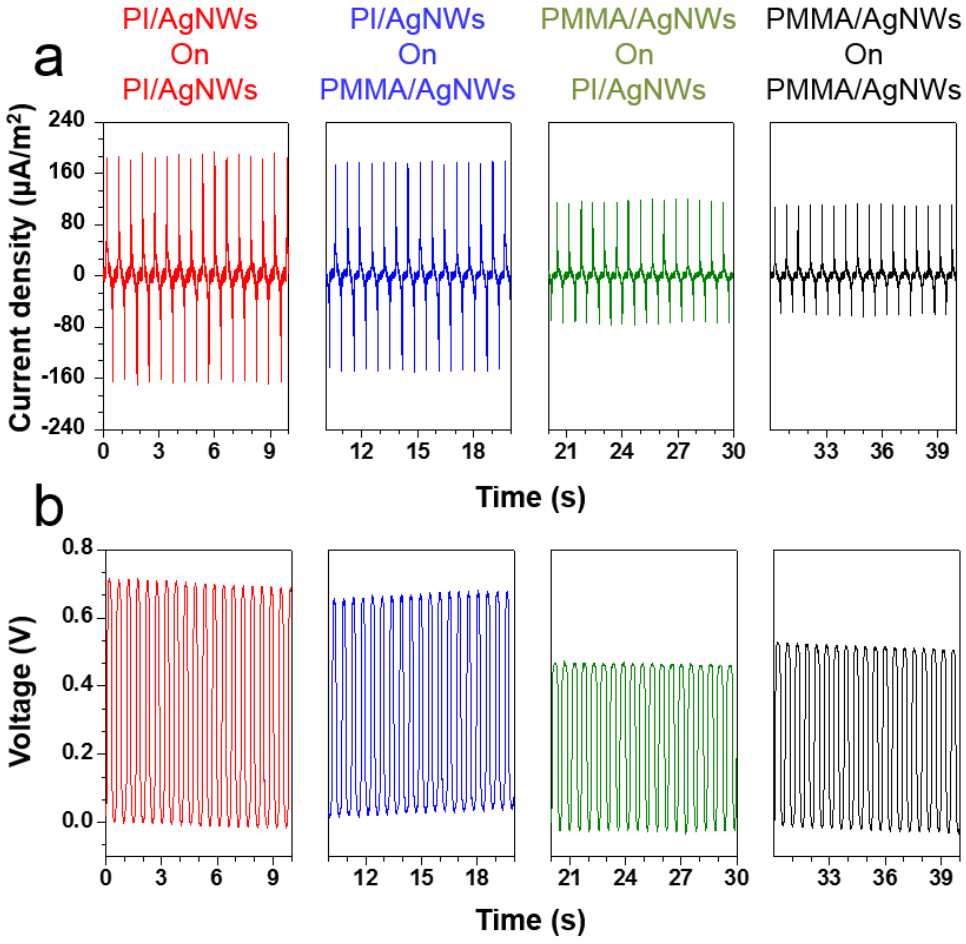

Figure 7.6 The output current density (a) and voltage (b) of the T-TENG using different dielectric polymer layers with 7% AF_{Bot} and 7% AF_{Top}.

The triboelectric property of the polymer substrate is another significant factor directly affecting the output of the T-TENG. In this study, AF_{Top} and AF_{Bot} are fixed in

7%, the J_{sc} (Figure 7.6a) and V_{oc} (Figure 7.6b) were measured using a combination of PI and PMMA as top and bottom electrodes, respectively. The bottom electrode has its AgNWs facing the interface gap, while for the top electrode, the polymer faces the interface. In other words, the triboelectric interface is formed between the AgNWs from the bottom electrode and the polymer layer from the top electrode. The measurements clearly show that both J_{sc} and V_{oc} are not sensitive to the type of the polymer used on the bottom of the electrode. This is consistent with the building concept of the triboelectric device. However, significant differences in the triboelectric performance were observed with different types of polymer in the top electrode. When the PI film is used as the top electrode, the amplitude of the J_{sc} was measured to be about 175 $\mu A/m^2$ with the V_{oc} to be 0.68 V. These values were significantly reduced when the PMMA was used as the top electrode. Only 90 $\mu A/m^2$ and 0.46 V were obtained for J_{sc} and V_{oc}, respectively. In this specific design of TENG, the active triboelectric layer is the carrier substrate of the top electrode, which determines the output efficiency.

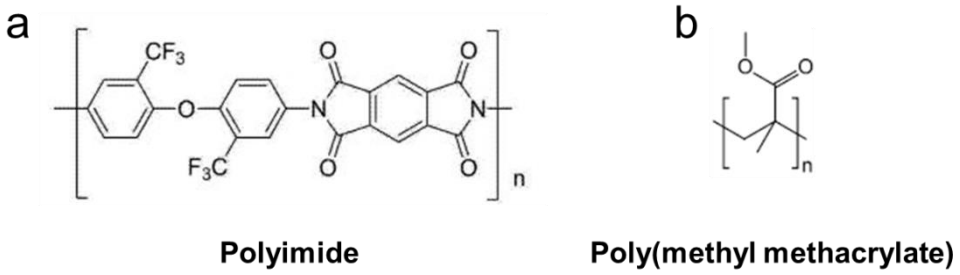

Figure 7.7 The chemical structures of the polymers (a) PI and (b) PMMA.

As listed in Figure 1.13, the PI film surface has a stronger tendency to gain electrons in comparison with the PMMA surface. Therefore, the results are in agreement with the general trend. Additionally, the different performance between PI and PMMA could be related to their polymer structures, as shown in Figure 7.7. PI polymer chain

has a certain degree of conjugation in the system, which can facilitate electron flow. However, PMMA backbones are less conjugated and the electrons are less mobile. Thus, with a PI film, as the AgNW networks were used as the charge collector attached to the back of the PI film, charges can be collected from wider areas than that in the PMMA film. Meanwhile, the imide group is expected to chemically interact with the Ag wire more strongly than the ester group in the PMMA. Therefore, a larger charge shift is expected between PI and Ag nanowires. The asymmetric current curves in Figure 7.6 for the PMMA are probably due to the asymmetric configuration of the AgNWs on PMMA. For a more conductive layer and a better chemical interaction with the Ag, such asymmetric effects become less obvious.

7.4.5 The performance of T-TENG as mechanical energy harvester

The output performance of the T-TENG is further studied in Figure 7.8. Both of the AF_{Top} and AF_{Bot} were used at 7%. The AgNWs/PI and AgNWs/PMMA film were used as top electrode and bottom electrode. Figure 7.8a shows the detail of the output voltage and current density of the T-TENG. The V_{oc} and J_{sc} of this T-TENG are 0.7 V and 170 μA/m^2, respectively. Although, the output power density of this T-TENG is much less than solar cells, the output of T-TENG can be significantly improved with a careful design, which will be discussed in Chapter 8. The V_{oc} and J_{sc} of the T-TENG under different external loadings at a mechanical frequency of 1.5 Hz were also investigated, shown in Figure 7.8b. The current density generally decreases with an increase of the external load resistance from 0 MΩ to 120 MΩ. Meanwhile the output voltage follows the opposite trend, approaching V_{oc}. Accordingly, the instantaneous output power density reaches its maximum value (0.23 mW/m^2) at a corresponding load resistance of 40 MΩ. In this case, the transmittance of the T-TENG is around 78% at the wavelength of 600 nm, shown in Figure 7.8c. In addition, the T-TENG exhibits an

excellent working stability as demonstrated in Figure 7.8d. The output current shows no degradation during a fatigue test of 50,000 cycles. It is believed that permanent damage of the upper polymer will eventually occur and this requires further investigation. However, the work here shows an enhanced working life in comparison to the traditional ITO based T-TENG.

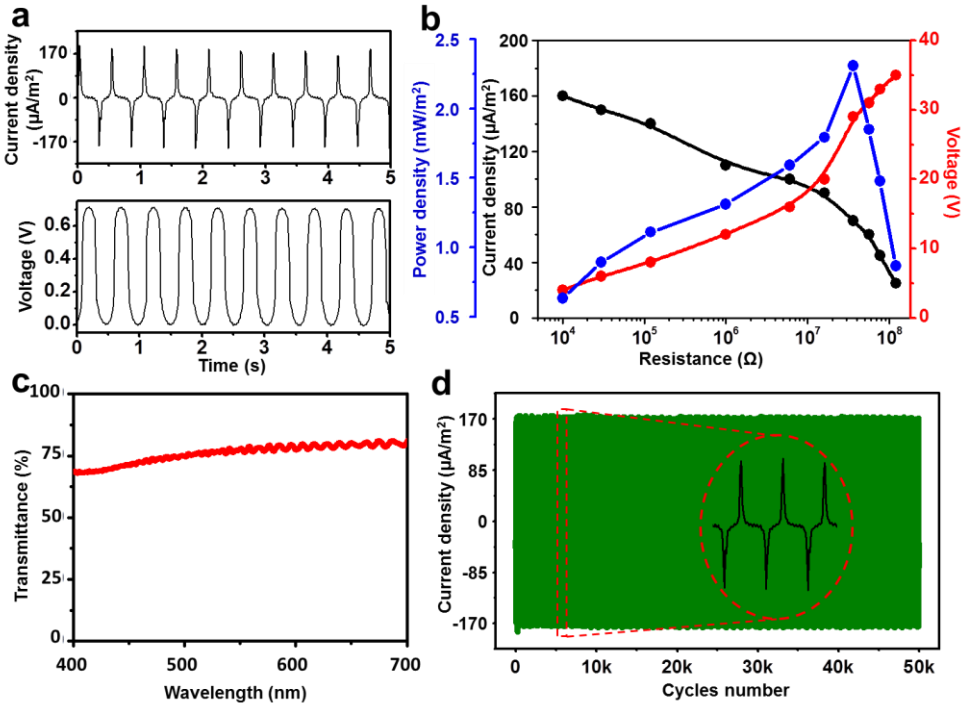

Figure 7.8 The performance of the optimised T-TENG using 7% AF of the AgNWs, PI as the top electrode and 7% *AF* of the AgNWs/PMMA as the bottom electrode. (a) The output current and voltage of the T-TENG. (b) The output efficiency of the T-TENG with different external load resistance. (c) The optical transmittance of the T-TENG. (d) A fatigue test of the T-TENG with 50,000 cycles.

7.5 Conclusions

In conclusion, T-TENGs based on 1D AgNWs percolation network electrodes

were investigated. The transparent electrodes for the triboelectric devices were designed and constructed. The *AF* of the electrodes, and dielectric properties of the polymer carriers were studied as the factors affecting the output performance of T-TENG in this system. The T-TENG was further optimised, with maximum output power of 0.23 mW/m^2 and an optical transmittance of 78% at the wavelength of 600 nm. The working life of the devices was also investigated. The excellent optical transmittance of the TENG encourages us to believe that integrating it with invisible electronics, such as sensors and energy storage devices, is possible, as well as with solar cells as a hybrid power system.

Chapter 8 Solution processed flexible hybrid cell for concurrently scavenging solar and mechanical energies

8.1 Abstract

A flexible device to harvest renewable energy is urgently needed nowadays. A satisfactory device should be able to harvest multi-type energies around the clock without any economic difficulty for mass production. Here a solution processed flexible hybrid cell was reported by integrating an organic solar cell and a triboelectric nanogenerator into a thin film device, which was capable of converting both solar and mechanical energies into electric power independently or simultaneously. The generated energy could be used either to charge an energy storage unit or as a primary energy source for wearable self-powered devices, even under weak light conditions. This work provided a feasible and scalable method to fabricate such a hybrid energy device with a reasonable cost, such a device could be used to overcome the natural restrictions of the single energy harvesting mode.

8.2 Introduction

Autonomous energy harvesting system should be designed to harvest different forms of renewable energy. Such developments will improve its competitiveness in all the end-use categories. The advantages range from wearable consumer electronics,[276] smart building,[277] to grid-level energy production.[84] Solar and mechanical energies are two attractive forms.[278-280] However, most of the commercialised technologies to harvest solar and mechanical energies are based on rigid and heavy bodies, such as single-crystal silicon solar cells and electromagnetic generators. The electromagnetic generator can be as small as millimetre-scale.[281] This kind of generator presented conversion efficiency as high as 86% with a concentrated energy source.[281] But the

concentrated energy source is limited, and the rigid electromagnetic generator is incompatible with most wearable electronics. Meanwhile, the cost to manufacture electromagnetic generators is high with respect to triboelectric devices. Solution processed devices for harvesting renewable energy can be fabricated by directly coating a few functional layers on a polymer substrate. This kind of device is flexible, lightweight and inexpensive, and such properties innovate power generator to minimise negative environmental impacts and economic issues, as well as boost the development of wearable electronic systems. Printable organic solar cells (OSCs) attract attention, since they can be truly flexible, and compatible with triboelectric device.[282] However, OSCs can only work under light irradiation. Also, the output energy would decrease rapidly, when the intensity of irradiation is reduced. Integrating an additional mechanical energy harvesting device with an OSC is a feasible way to compensate this deficiency to a certain extent, overcoming the environmental limitation of single energy harvesting mode. Xu et al. first demonstrated a hybrid cell which is integrated a dye-sensitized solar cell with a piezoelectric nanogenerator.[283] However, these rigid devices are difficult to integrate with flexible OSC.

The emerging polymer-based triboelectric nanogenerator (TENG) offers an opportunity to integrate with an OSC into a flexible energy device. TENG can efficiently convert different ambient renewable mechanical energies, such as irregular wave energy,[263] wind energy[284] and biomechanical energies,[285] into electric power through the triboelectric effect. However, the acceptability of a TENG to integrate with an OSC highly depends on the optical transparency of the TENG. To maximise the transparency could enhance the solar absorption of OSC, leading to an increased output power. Also, the synthesis method of TENG is preferred to be compatible with solution-based processes.

Herein, a solution processed hybrid cell is presented by integrating an OSC with a single-electrode triboelectric nanogenerator (STENG) as a wearable power source. The device is capable of harvesting both solar and mechanical energies individually or simultaneously. Such hybrid device is able to break the environmental restrictions and complementarily utilise available energy around the clock. This kind of device offers a feasible approach for a mass production of inexpensive power source with many potential applications. For example, it can used as a roof-based household electric power supply even on rainy days.[286] It also can upgrade various wearable electronics to get rid of an external power supply, such as epidermal healthcare monitoring.[287]

8.3 Experimental

The conductive and transparent PI/AgNWs electrode was fabricated via in-situ polymerisation following the experimental procedures described in Chapter 7. A STENG was fabricated by bonding a piece of transparent fluorinated ethylene propylene (FEP) film on the bare side of the PI/AgNWs using PI precursor solution, it was annealed at 120 ℃ for 20 mins in air to stabilise the film.

The flexible OSC was constructed on the substrate of the as-prepared STENG device. All the chemical structures of the compositions are listed in Table 8.1. A 40 nm thick layer of modified poly(3,4-ethylenedioxythiophene):poly(styrene sulfonate) (PEDOT:PSS, Clevious P VP A1 4083) was first spun cast on the electrode and annealed at 150 ℃ for 10 min in air. A 2 nm thick layer of poly(ethylene imine) (PEI, Aldrich, MW = 25,000) was spin-coated on the PEDOT:PSS layer at a speed of 5000 rpm for 1 min, and annealed at 100 ℃ for 10 min in air. The PEI solution was prepared by dissolving the branched PEI in 2-methoxyethanol with a concentration of 0.4 wt%. Then, 70 nm of the active layer of poly(3-hexylthiophene) (P3HT, Lumtec):indene-C60 bis-adduct (ICBA, Lumtec) (P3HT:ICBA) (1:1, weight ratio, 24 mg/ml) was spin-

coated upon the PEI layer at a speed of 1000 rpm for 40 seconds in a N_2 filled glovebox followed by annealing at 150 ℃ for 10 min. Another layer of PI/AgNWs was used as the top electrode of the solar cell, which was applied by a transfer lamination technique that has been developed previously.[288] With this technique, the AgNW is first coated on a PDMS film, which is then flipped over to allow the AgNW to contact with the OSC. When the PDMS film is removed, the AgNW is left on the top of the OSC. The hybrid cell was assembled by binding the STENG and OSC using a very thin PI layer to avoid short circuit. The thickness of the PH1000, PEI, P3HT:ICBA and PEDOT:PSS were measured with an AFM. (Collaborated with at Huazhong University of Science and Technology)

Table 8.1 The chemical compounds to synthesise OSC.

Component in solar cell	Chemical name	Structure
Conductor polymer	Poly(3,4-ethylenedioxythiophene): Poly(styrenesulfonate) (PEDOT:PSS)	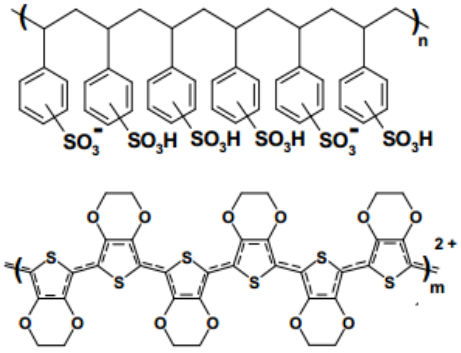
Active polymers	Poly(3-hexylthiophene-2,5-diyl) (P3HT)	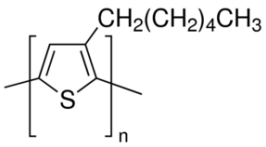
	1',1",4',4"-Tetrahydro-di[1,4methanonaphthaleno[1,2:2',3',56,60:2",3"][5,6]fullerene-C_{60},C_{60} derivative or Indene-C_{60} bisdduct ($IC_{60}BA$)	

The morphologies, structures and compositions of the samples were characterised by scanning electron microscope (SEM, FEI Nova NanoSEM 450). The roughness of the conductive PI film was probed using an atomic force microscope (AFM, SPI 4000, Seiko). The optical transmittance was measured using an ultraviolet-visible spectrometer (UV-Vis, Shimadzu UV2550). Sheet resistance (R_s) was determined using a four-point probe resistivity measurement system. The output current of STENGs were measured by a low noise voltage preamplifier (Keithley 6514), while the output current was measured by a low-noise current preamplifier (Stanford Research SR560). The hybrid cell was fixed on a glass substrate and measured in a glovebox, and the STENG was connected with OSC in parallel. The performances of STENGs in the hybrid cell with different AgNWs density were measured without any irradiation, using a resonator (JZK, Sinocera) covered with a cotton fabric to periodically trigger the STENG with a frequency of 4 Hz controlled by a signal generator (YE 1311-D, Sinocera). The performance of the hybrid cell was measured under a light intensity of 1000 W/m^2 (AM 1.5G) and ~2 W/m^2 (fluorescent light). To simulate the application in wearable electronics, a sparse cotton fabric was placed on the device to shield a portion of the light, one end of the cotton was fixed, and the other end was shaken by hand to trigger the STENG, the output signal was rectified. Simultaneously, the light passed through the cotton fabric can be collected by OSC. The performances of the hybrid cell were measured by a digital sourcemeter (Keithley 2400).

8.4 Results and discussion

8.4.1 Structure of the hybrid cell

A layer-structured flexible and semi-transparency hybrid cell was synthesised through solution processes. The schematic diagram in Figure 8.1a shows an exploded view of the multilayer structure, and the upper inset is the corresponding layout of the

device. The STENG involved a 45 μm thick FEP film bonded with a 55 μm thick AgNWs/PI electrode. Both of them are highly transparent in the visible spectrum and thus have little effect on the photoconversion efficiency of OSC. The OSC was assembled by sandwiching a 80 nm thick semi-transparent active layer (P3HT:ICBA) between a 40 nm thick top electrode (modified PEDOT:PSS, PH1000) and 2 nm thick electron-rich layer (PEI).[289] This assembly was then bonded to the bottom electrode, which was prepared by coating 40 nm thick conductive layer (PEDOT:PSS) on the AgNWs/PI film. In this case, the total thickness of the hybrid cell is about 155 μm, which can be easily adjusted according to requirements, because it mainly depends on the thickness of the PI substrate. The three dominant layers of the device can be clearly seen from the cross-sectional view of the SEM image in lower inset of Figure 8.1a. The relative transparency and the colour appearance of the hybrid device are shown in Figure 8.1b. The flexibility of the hybrid device is also demonstrated in the inset of Figure 8.1b. In comparison with rigid hybrid cells, which are based on inorganic materials,[290] this device exhibits excellent flexibility (bottom inset of Figure 8.1b), which suggests applications as a wearable power source.

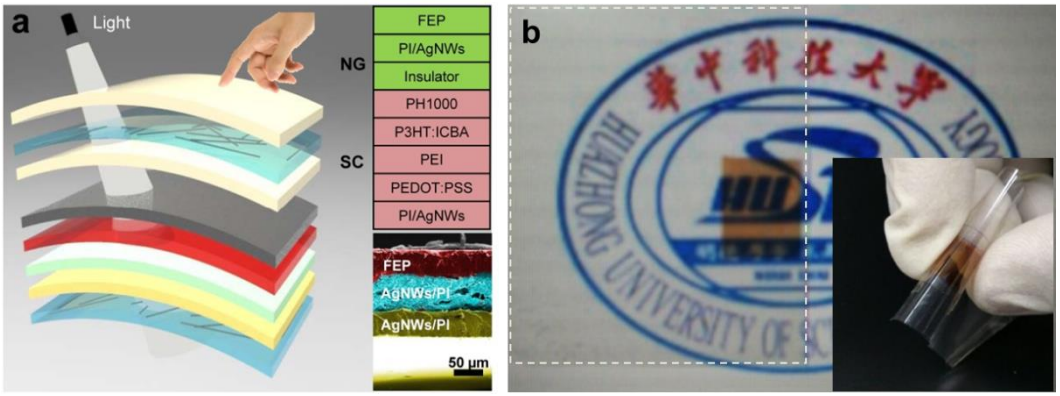

Figure 8.1 The design and layout of the hybrid cell. (a) Exploded view layout of hybrid cell. The upper inset is the schematic illustration of the hybrid cell and the lower inset is the corresponding SEM image of cross-section of the device. (b) The optical transmittance of the hybrid cell. The upper inset shows the reddish semi-transparent hybrid area and highly transparent STENG area, and lower inset presents the flexibility of the hybrid cell. (Collaborated with Huazhong University of Science and Technology)

8.4.2 Metal nanowire based transparent electrode

The electrode acts as a key component of the hybrid cell; it requires good mechanical stability, electrical reliability with excellent optical transparency. In comparison with other transparent conductive electrodes,[291-293] AgNWs network electrode can be simply prepared by a coating of AgNW ink and such electrodes have potential applications in triboelectric devices and solar cells. However, when the AgNWs are only weakly anchored on the substrate by van der Waals force,[294] the AgNW coated electrode is not satisfactory for a triboelectric device, since slip and friction between of the AgNWs may easily break the electrode. Here, AgNWs/PI electrode was developed. In such an electrode, the AgNWs are partially embedded in the PI film to overcome the weaknesses. The AgNWs were first cast on a silicon

substrate, followed by coating a PI film. Once this PI film was detached from the silicon substrate, the AgNWs were partially embedded in the polymer. Thus, the mechanical strength is reinforced by the polymer thin film, while the electrical conductivity is maintained by the semi-naked metallic nanowires. Figure 8.2a shows that the electrode is highly transparent in visible light. The measured resistivity R_s is about 12 Ω/sq, while the optical transmittance is about 92 % at wavelength of 550 nm (Figure 8.2c). This wavelength covers the important optical range for the OSC active absorption, which will be discussed later. Relatively high haze compared to the traditional indium tin oxides (ITO) electrode,[295] can be observed due to light scattering by AgNWs. This might have an additional positive effect on the performance of the OSC, since it increases internal optical reflection. The resistivity is relatively uniform across the electrode with a standard deviation of 1.22 Ω/sq as shown in Figure 8.2b, this is a benefit from the homogenously suspended AgNWs in ethanol. Such well-dispersed ink allows a uniform distribution of AgNWs (Figure 8.2d) on a substrate. This value is acceptable for most optoelectronic devices.[296]

The cast AgNWs/PI thin film was thermally annealed at 250 ℃ for 10 mins to weld the junctions of the AgNWs networks. The tightly welded junctions of AgNWs after annealing (inset in Figure 8.2d) effectively reduce the overall R_s, and the interconnections between the AgNWs enhance the mechanical and electrical stability during mechanical deformation, such as bending. The welding of the AgNWs also significantly enhanced the binding strength between the AgNWs and PI substrate. As seen in Figure 8.2c, R_s can be preserved after a scotch tape test with an applied force of 4.3 N. Such mechanical stability of the electrode is critical for STENG. The tilted SEM image in Figure 8.2e shows that the AgNWs are partially embedded, but not completely immersed in the PI substrate. The surface roughness of the electrode is about 10 nm, as

shown in AFM image (Figure 8.2f). This composite structure ensures the conductivity of the electrode, and also prevents an undesired short circuit with the adjacent electrode of the OSC for an integrated device, since the thickness of PI substrate is 55 μm. Hence, the PI/ AgNWs is an excellent electrode for hybrid cell, and potentially can be used in many other restricted conditions.[297]

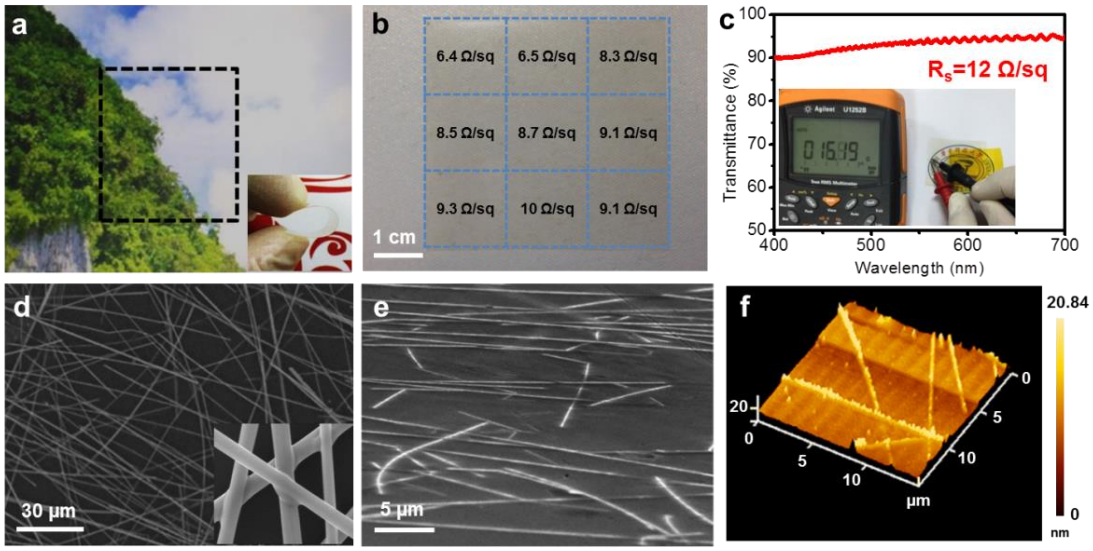

Figure 8.2 Characterisations of the AgNWs/PI electrode. (a) Photographs show the highly transparent and flexible (inset) AgNWs/PI film. (b) Uniform sheet resistance distribution on the AgNWs/PI electrode. (c) Plot of transmittance versus wavelength of AgNWs/PI electrode - the inset is the resistance measurement after scotch tape test. (d) SEM images of as-prepared AgNW networks and the welded junctions (inset). (e) The 45 °titled SEM image of the AgNWs embedded in PI substrate. (f) AFM image of the surface roughness profile of the AgNWs/PI electrode. (Collaborated with Huazhong University of Science and Technology)

8.4.3 Single-electrode transparent triboelectric nanogenerator

The hybrid cell was fabricated by binding the STENG and OSC using

PI/AgNWs composite electrode as described in the experimental section, and each unit can work independently. The fact that hybrid cell works without light irradiation is demonstrated in Figure 8.4. Under such conditions, all the electric power was contributed from the STENG only. To simulate mechanical energy input, STENG was triggered using a cotton fabric, which is fixed on a resonator. The fabric touches the FEP film periodically with a frequency of 4 Hz, (different substances such as fingers, theoretically, even water drops[298] can be used for power generation but the output performance would vary). The working mechanism is illustrated in Figure 8.3, has been studied in previous work, and can be briefly described as follows. The process of generating static charges and electric power can be identified in four stages.[77, 78] Initially, the cotton fabric tightly contacts with the FEP film in Figure 8.3a, since FEP is more triboelectrically negative than cotton, as shown in Figure 1.13. The FEP is able to acquire electrons from the cotton fabric under contact electrification, and the system is in equilibrium, no charge is transferred in the external circuit. After that, the cotton fabric is separated from the FEP film, as shown in Figure 8.3b, and the uncompensated negative charges on the FEP film would electrostatically induce the positive charges in the bottom AgNWs electrode to neutralise the partial negative charges. This process drives free electrons in AgNWs to the ground, inducing current until the cotton fabric is completely removed (Figure 8.3c). Reversely, as shown in Figure 8.3d, the cotton fabric is able to neutralise the negative charges on the FEP film again, resulting in the electrons flowing to the AgNWs electrode from the ground. In this sense, the cycles can be repeated utilising external objects as a pump to drive the electrons up and down.

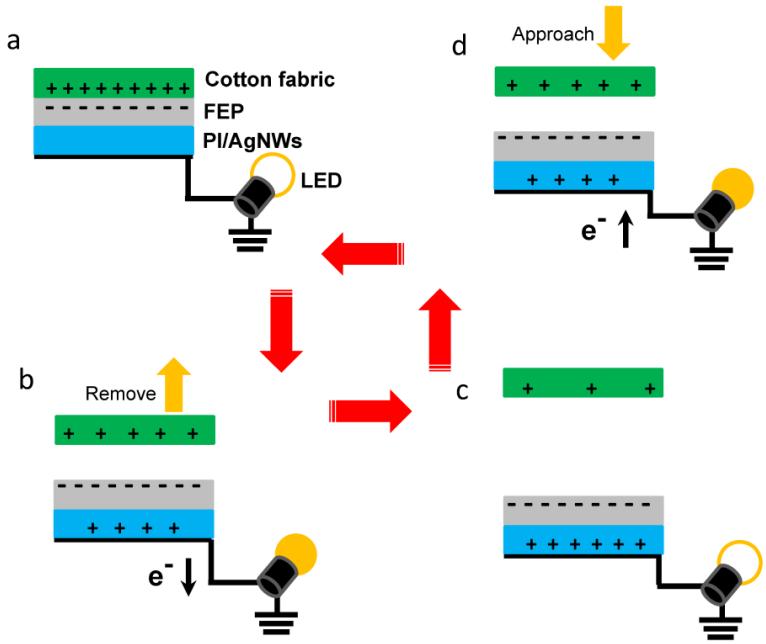

Figure 8.3 The schematic diagram of working mechanism of the STENG.[77] Four states are used to describe a working cycle of the T-TENG: (a) The stationary state of the T-TENG when two electrodes contact each other under pressing. (b) A transient state that one electrode is separated from the other one. (c) The stationary state when one electrode is sufficiently far away. (d) A transient state that one electrode is pressed to approach the other one.

In comparison with previous TENGs, which used sputter-coated metallic film as the electrodes,[299, 300] the transparency of the STENG electrode in this hybrid device has to be maintained, since the STENG is designed as the upper surface of a hybrid cell to collect external mechanical energy. Therefore, it must be transparent enough to ensure the light absorption of the bottom OSC.

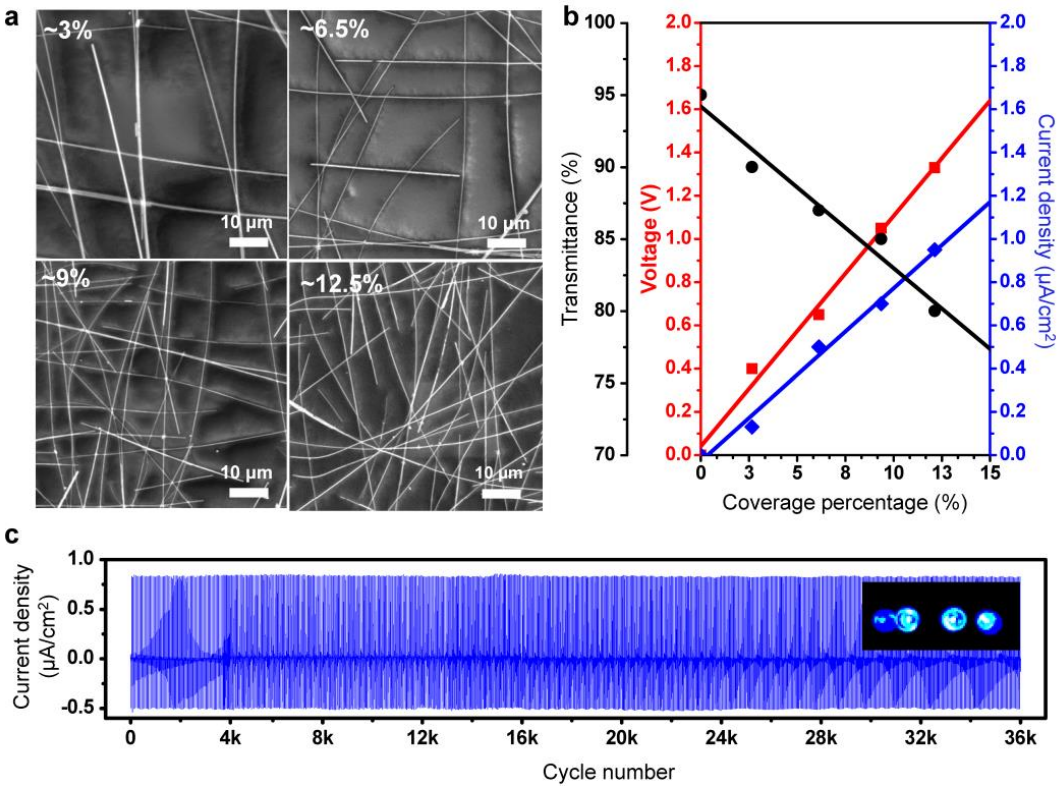

Figure 8.4 The relationship between AgNWs/PI electrode and STENG performance of the hybrid cell without light irradiation. (a) The SEM images of AgNWs/PI electrode with the coverage percentages of AgNWs corresponding to 3%, 6.5%, 9% and 12.5%. (b) The optical transmittance, J_{sc} and V_{oc} of STENG plotted as a function of coverage percentage. (c) The stability of the STENG. The inset shows how 4 commercial LED bulbs can be lit up solely using the STENG that has transmittance of 85%.

The STENG performance significantly depends on the density of the AgNWs in the electrode, as shown in the investigation in section 7.4.4. The density of the AgNWs can be adjusted by controlling the deposition times of the AgNW ink, SEM images in Figure 8.4a clearly show that the density of AgNWs in PI substrate is proportional to the deposition times of AgNW ink. Considering the distribution of the AgNWs is uniform with the average diameter of AgNW around 100 nm, the coverage area can be measured directly from the SEM images. The measured optical transmittance, the

STENG open-circuit voltage (V_{oc}) and short circuit current (J_{sc}) are plotted as a function of the coverage percentage of the AgNWs in Figure 8.4b. The output voltage and current gradually increase with enlarging the coverage area of AgNWs from around 3% to 12.5% with the J_{sc} increases from 0.15 to 0.95 μA/cm^2, while the V_{oc} increases from 0.4 to 1.25 V, respectively. Both follow a good linear relationship with respect to the coverage in this specific range. This is due to the fact that the sparse AgNW networks restrict the density of induced positive charges. Increasing the density of the AgNWs leads to more conductive paths that can acquire more positive charges, thus enhancing output performance. This result is further proved by comparing with the STENG using sputter coating Ag film on the PI substrate as the electrode, the J_{sc} is increased to 3.8 μA/cm^2 in Figure 8.5a, while no signal is observed with a bare PI film in Figure 8.5b. In comparison with the T-TENG described in Chapter 7, a significant enhancement of the output performance (around 45 times) is demonstrated. This is mainly due to the use an excellent triboelectric polymer of FEP. The triboelectric tendency of different polymers is presented in Figure 1.13.

In addition, the STENG exhibits a good working stability as demonstrated in Figure 8.4c. The output has no degradation during a fatigue test of 35,000 cycles indicating the extremely long working life of the STENG, a unit of 4 commercial light-emitting diode (LED) bulbs can be lit up twice in each cycle using STENG only (inset in Figure 8.4c).

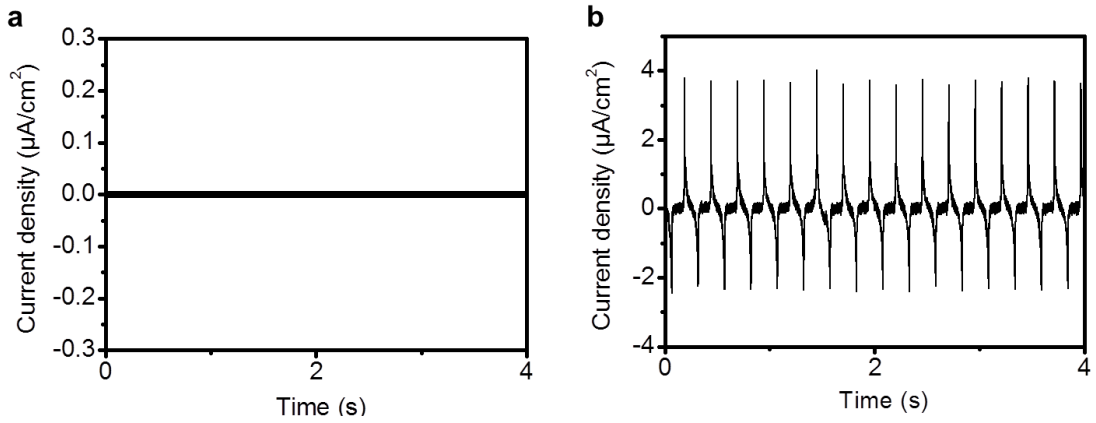

Figure 8.5 Current density of the STENG using (a) bare PI electrode and (b) Ag sputter coated PI film as the electrode.

On the other hand, a decrease of the optical transmittance was observed with the gradual increase of the coverage area of the AgNWs, as shown in Figure 8.4b. This means that the density of AgNWs should be controlled to balance the trade-off between the STENG performance and the optical transmittance. Thus, the STENG has an optical transmittance of 85% was used for the hybrid cell. Therefore, the density of the AgNWs in the hybrid cell was 10%, which gives the output performance of STENG with J_{sc} ~ 0.65 μA/cm^2 and the V_{oc} ~ 1.08 V.

8.4.4 Structure of the organic solar cell

In the OSC, because the electrode must be conductive enough for the collection and transport of electrons, as well as having a high optical transmittance for a broad range of light wavelengths. The typical conductive transparent polymer poly(3,4-ethylenedioxythiophene):poly(styrene sulfonate) (PEDOT:PSS) was used for both top and bottom electrodes, since the material shows superior optical transparency in the visible light range,[301] high electrical conductivity[302] and an intrinsically high work function (4.9 ~ 5.2 eV)[289]. Moreover, it also has good film forming ability by versatile fabrication methods.[303] The detail of the structure is shown in Table 8.1. In the complex

structure, the PEDOT acts as the conductor, since it has an aromatic backbone structure.[304] The PSS is added as a dopant to increase the water solubility. The PSS also acts as the charge balance during the polymerisation of the PEDOT to reduce the possibility of side reactions.[305]

In this research, the modified PEDOT:PSS (PH 1000) was used for the top electrode. The molar ratio of PSS and PEDOT is 2.5 to 1, which gives high conductivity (>850 S/cm). For the bottom electrode, the PEDOT:PSS is used in conjunction with a transparent and conductive PI/AgNWs film. Here, the PEDOT:PSS has a ratio of PSS to PEDOT of about 6:1, which gives a low conductivity (2×10^{-4} S/cm), but better stability. This film homogenises the conductivity between the heterojunction active layer and the highly conductive AgNWs layer.

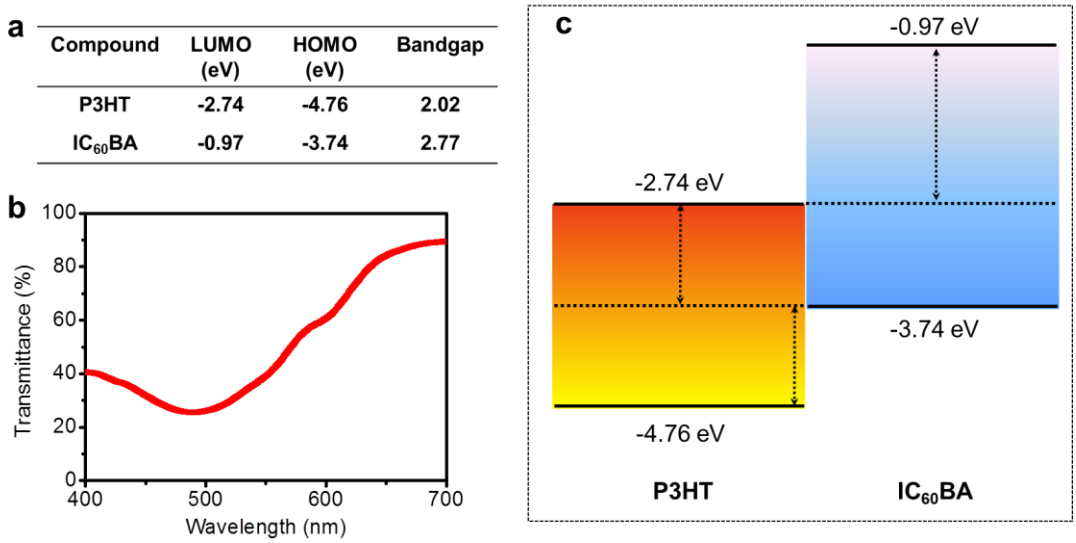

Figure 8.6 (a) The LUMO, HOMO and bandgap of the P3HT and $IC_{60}BA$. (b) The light transmittance and (c) the bandgap of the P3HT and $IC_{60}BA$ bulk heterojunction structure.

The OSC active layer is formed by a bulk heterojunction between Indene-C_{60}

bisdduct ($IC_{60}BA$) and poly(3-hexylthiophene-2,5-diyl) (P3HT), blend in 1 to 1 ratio. The active layer is deposited on a very thin layer (5 nm) of branched poly(ethylene imine) (PEI). The PEI layer helps to reduce the work function of PEDOT:PSS electrode to improve the dissociation of the excitons.[289] The chemical structure of the $IC_{60}BA$ and P3HT are shown in Table 8.1. The electron energy values of the P3HT and $IC_{60}BA$ are shown in Figure 8.6a, and their band gap structure is illustrated in Figure 8.6c. The absorbing band covers the wavelength range from 448 to 614 nm, which corresponds to the band gap of P3HT (2.02 eV) and $IC_{60}BA$ (2.77 eV). Under the AM 1.5G irradiation, the formed excitons are dissociated at the interface between P3HT and $IC_{60}BA$. The separated electrons and holes are further promoted to the LUMO of the P3HT and HOMO of the $IC_{60}BA$ toward to the cathode and anode, respectively. Figure 8.6b shows the transmittance of the OSC. A broad peak is observed around 450 to 600 nm, corresponding to 2.76 to 2.07 eV. These results are in good agreement with the band gaps of $IC_{60}BA$ and P3HT.

8.4.5 Performance of the hybrid device

The synergistic behaviour to harvest the renewable energy by superposing the energy of the outputs from the STENG and the OSC demonstrates the advantages of a hybrid cell, as seen in Figure 8.7. For the applications in wearable electronics, this flexible hybrid cell is demonstrated with covering by a cloth under irradiation, as illustrated in Figure 8.7a. The photons can pass through the clothing fabrics (cotton fabric in our study) and the transparent STENG to reach the active layer of OSC for photovoltaic reaction. Simultaneously, the fabric would touch the STENG irregularly to convert biomechanical motion energy into electric power when the body moves. The typical current density versus voltage (*J*-*V*) curves of the hybrid cell without input of STENG are demonstrated under different light irradiation conditions, as shown in

Figure 8.7b, such as the simulated AM 1.5G irradiation (intensity of 100 mW/cm^2), standard indoor fluorescent lighting (0.2 mW/cm^2) and under the cover of the cotton fabric. The efficiency of OSC only is 2.4% with the J_{sc} of 5.8 mA/cm^2, the V_{oc} of 0.74 V and the fill factor (*FF*) of 55% under the AM 1.5G. This performance can be further improved by increasing the thickness of the active layer, but the total transmittance of the hybrid cell would decrease. In this situation, the output performance of the hybrid device is dominated by the OSC and the output of STENG is negligible. However, the J_{sc} of the OSC dramatically decreases to 0.05 mA/cm^2 under a standard indoor fluorescent light. The J_{sc} is further decreased to 0.015 mA/cm^2, when it was covered with the fabric, as shown in the inset table of Figure 8.7b. However, the measured *FF*, a parameter indicating the device internal efficiency, is significantly improved from 55% (AM 1.5G) to 67% (indoor). This suggests that the charge recombination of the OSC plays an important role for the OSC performance.

The weak performance of the OSC at low light can be compensated by the integrating of the STENG device, when it is used as the power source for wearable electronics. Figure 8.7c demonstrates the output *J*-*V* curve of the hybrid cell with indoor light and the repeated contacts between cotton fabric and STENG. The device exhibits notable enhancement in the output energy with a signature of the superimposed OSC and STENG *J*-*V* curves. In this case, the contribution of the STENG in the hybrid cell is significant, and the performance is comparable to the OSC.

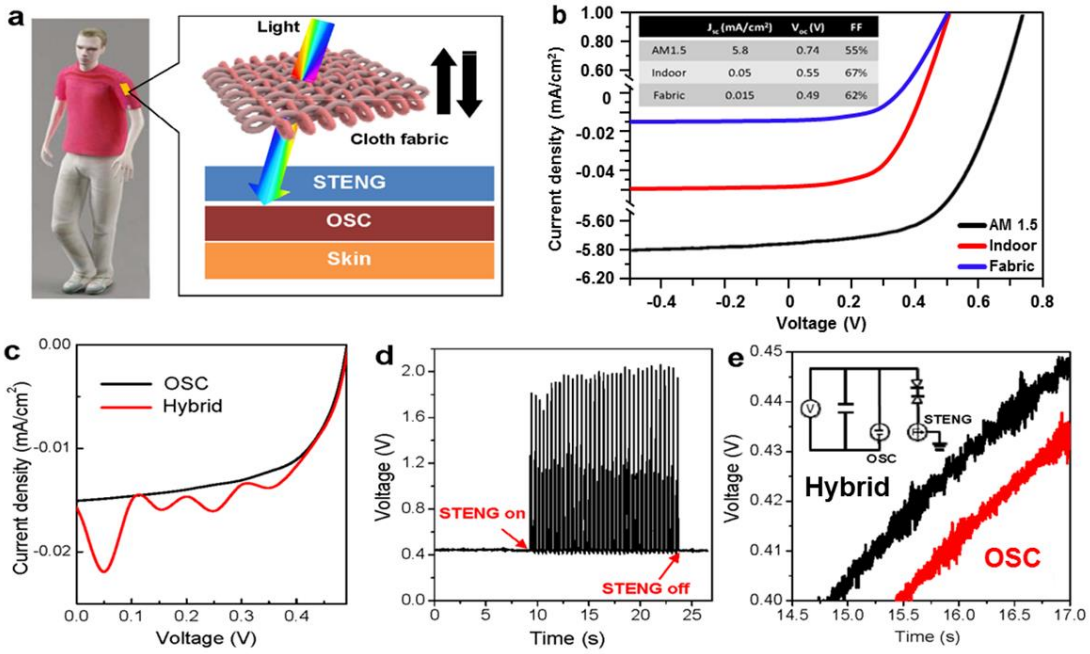

Figure 8.7 The output performances of the hybrid cell. (a) Schematic illustration of the working mechanism of the hybrid cell hidden under the cloth fabric as wearable power source. (b) Comparisons of the *J-V* characterisation of the hybrid cell under simulated AM 1.5G irradiation (intensity of 100 mW/cm^2), standard indoor fluorescent lighting (2 mW/cm^2) with and without cover of cotton fabric. (c) Comparison of the *J-V* curve of the OSC only and the hybrid cell under the indoor lighting, in which the STENG was triggered by shaking the fabric. (d) The output voltage of the OSC and the hybrid cell with and without the STENG. (e) The time spent to charge a 10 μF commercial capacitor using the hybrid cell with and without the STENG input. The inset depicts the equivalent loop circuit to store the electrical energy that produced by the hybrid cell. (Collaborated with Huazhong University of Science and Technology)

The synergetic behaviour of the hybrid cell is further identified through the time-dependent behaviour of output voltage, as shown in Figure 8.7d with the OSC and the STENG units connected. The steady output voltage of the OSC, when it was covered with the fabric, is around 0.45 V under indoor light. When the STENG is triggered by

shaking the fabric, the output voltage of the hybrid cell can reach a peak value up to ~ 1.9 V. This result proves that the units in the hybrid cell can work independently to compensate the deficiency of the one energy harvesting mode, also can enhance the output if both units are available. The practical application of the hybrid cell is demonstrated through the transient study of charging a commercial capacitor (10 μF) using OSC only and fully functional hybrid cell, as shown in Figure 8.7e. The equivalent loop circuit used to charge the capacitor is illustrated as the inset of Figure 8.7e. The time required to charge the capacitor is obviously shorter with the fully functional hybrid cell than the OSC alone. Therefore, the hybrid cell can harvest both solar and mechanical energy, which is a more effective power generator than any single energy unit. It provides a truly feasible energy source to charge other integrated energy storage units, such as batteries and supercapacitors. This semi-transparent energy device can also be applied on glass windows to harvest energies from sunlight and the wind or rain drops, if the devices are weatherproof.

8.5 Conclusions

In summary, an all solution processed hybrid energy harvesting system is presented by integrating a STENG with an OSC. The transparent, conductive and flexible PI/AgNWs electrodes enable the flexibility and mechanical stability of the device. The as-fabricated hybrid cell is capable of converting both solar mechanical energies into electricity independently or simultaneously. The contributions from both OSC and STENG are identified. Under weak light conditions, the contribution from STENG becomes significant and apparent. The practical application of the hybrid cell was demonstrated in a system to charge a capacitor. The output energy (E) is the sum of the output energy from the STENG (E_t) and the OSC (E_o), which can be calculated based on the previous measurements: $E_t = 0.9\ \mu\text{A}cm^{-2} \times 1.3\ \text{V} \times 4\ \text{Hz} =$

4.68 μ$Wcm^{-2}s^{-1}$, and $E_o = 5.8\ \text{mA}cm^{-2} \times 0.74\ \text{V} \times 1\ \text{Hz} = 4.29\ mWcm^{-2}s^{-1}$. In this system, if the surface areas of both devices are 1 cm^2, $E = E_t + E_o = 4.68\ \mu Ws^{-1} + 4.29\ mWs^{-1}$. In this situation, the output energy from triboelectric device is too small. If this device is used to charge a 9V/1.2A rechargeable battery, the time can be calculated (2518 s). Although, it is still not effective enough as a commercialised battery charger, such a synergistic energy harvesting device provides a feasible way to overcome the limitations of a single mode energy device. A similar concept could be developed with other ambient energy harvesting units, such as thin film thermoelectric [306] and piezoelectric energy generator, which can be further integrated into the hybrid cells.

Chapter 9 Conclusion, future work and outlook

9.1 Conclusions

In this thesis, metal and metal oxide nanomaterials with different morphologies and optical and electrical properties were synthesised. The applications of the nanomaterials were developed in harvesting solar energy through the PEC water splitting and the photovoltaic effect, and in collecting mechanical energy using triboelectric effect.

Solar energy is considered as the most important renewable energy, since it is enormously available around the world. Two kinds of devices were investigated to harvest solar energy, including photoelectrochemical (PEC) water splitting and photovoltaics. For PEC water splitting, solar energy is stored in the form of H_2. Such a direction is considered as a significant way to harvest solar energy, because H_2 is zero carbon emission energy storage with a high energy density. Thus, it could significantly reduce our reliance on the carbon economy. In this work (Chapter 5), electrospun WO_3 nanofibres were fabricated into thin films as photoanodes for PEC water splitting. With careful optimisations of the WO_3 film thicknesses through an electrophoretic deposition (EPD) method, the photoanode presented a peak efficiency of 0.93% with a film thickness of 18 μm. In comparison, in Chapter 6, TiO_2 hollow hemisphere (HHS) films were also reported, in synthesising photoanodes for PEC water splitting. Such HHS film presented the maximum efficiency of 1.04% with a film thickness of 24 μm. The band gap of WO_3 (E_g = 2.5 – 2.8 eV) allows it to absorb visible light with wavelength up to 500 nm, while, TiO_2 is only capable of absorbing UV light, as the band gap of TiO_2 is about 3.2 eV. However, the band edges of WO_3, as shown in Figure 1.9, restrict the efficiency of PEC water splitting, so that extra voltage is required to split using a WO_3

photoanode. Also, the HHS structure is considered as a better structure than the nanofibre in PEC water splitting, since the unique HHS presented an improved porous structure. Such a structure could enhance the light absorption and the electrolyte transport. Overall, the photoefficiency of PEC water splitting is still too low to 10 ~ 11% compared to the state-of-the-art. Further developments of metal oxide materials are still necessary to approach the theoretical efficiency.

In additional to the photoconversion efficiency, a number of issues must be addressed. The way of storing and transporting H_2 gas is fairly limited and expensive. When it is mixed with air, H_2 gas can spontaneously ignite and is very explosive. Also, H_2 can dissolve in many metals, so if metal contacts with H_2 gas, it may have adverse effects, such as hydrogen embrittlement, which could lead the metal to crack, and subsequently cause explosions. Moreover, the hydrogen flame is extremely hot and invisible, thus it is fairly easy to cause accidental burns.

Alternatively, solar cells convert solar energy directly in the form of electricity. Third generation solar cells, including dye sensitised solar cells (DSSCs) and organic solar cells (OSCs), were also demonstrated in this research. OSCs were mainly used in the hybrid cell, when it was integrated with a triboelectric device. In Chapter 6, TiO_2 HHS films were applied for DSSC with a photovoltaic efficiency of around 3.26%. Since the Ru dye was used, the extended visible light absorbing wavelength allowed the photovoltaic efficiency to be made much higher than that for PEC water splitting. But this photoefficiency was relatively low compared with reported DSSCs.[59] However, with the same fabrication processes, the P25 nanoparticle film based DSSC presented only about half of the photoefficiency of our HHS film (1.72%). In summary, the main reason for the low photovoltaic efficiency is due to the low fill factor, which is determined by the connection between the dye and the TiO_2 base, hence improvements

of the fabrication process are still required.

Although the fabrication cost of DSSCs is considerably reduced, in comparison with the commercialised Si based solar cells, a number of issues are still needed to be addressed. In terms of efficiency and working life, the DSSCs performed much worse than typical Si based solar cells. To increase their working life, DSSCs require structural improvement to avoid the use of the liquid electrolyte. The component materials, including the electrodes, the electrolyte, the metal oxide base and the dye, all require further developments to increase the efficiency. Overall, solar cells still take priority over the PEC water splitting for commercialisation, due to their higher photoconversion efficiency and conventional output energy.

Mechanical energy is also an important energy source, which is widely harvested through the electromagnetic effect and used as electrical energy. In this work, the triboelectric effect was studied to harvest mechanical energy. The output performance of the triboelectric device is very low with respect to a general electromagnetic system. However, the input energy and applications are quite different. For the high output electromagnetic system, the input energy is required to be high grade energy with a continuous input, which could give a continuous electrical output with a high current density. A Triboelectric nanogenerator (TENG) has a working cycle in a compression and separation, so it requires high frequency, but only low grade energy input, to keep it being compressed and released. In contrast to the electromagnetic system which is normally used to harvest mechanical energy from concentrated sources (wind energy and hydroelectric power), the triboelectric devices are available to harvest low grade mechanical energy from sources such as rain energy, low grade wind energy and bio-mechanical energy. Thus, the applications are fairly different between the electromagnetic system and triboelectric device. Although, the dimensions of the

electromagnetic system can be designed as small as a few millimetres, polymer thin film based triboelectric devices are still advancing in a number of applications. For instance, TENG can be used to create micro-power sources for mobile/wearable electronics and sensor networks. TENG can be directly used as a self-powered sensor. This kind of sensor, based on triboelectric effect, can be designed to detect mechanical triggering, pressure fluctuation and environmental stimulation.[300] Moreover, some other challenging applications can also be considered, including human-machine interfacing, smart skin, robotics, security, biomedical and infrastructure monitoring.[307]

In this research, silver nanowire (AgNW) networks were used to create truly transparent and flexible electrodes for triboelectric applications, described in Chapter 7. In comparison with the traditional transparent conductive oxide electrodes, they presented an enhanced mechanical stability, flexibility and an extended working life. However, the maximum output current density of the transparent triboelectric nanogenerator (T-TENG) was only 170 $\mu A/m^2$ with a transparency around 75%. Such low performance can be further elevated. For instance, in this system, the active surface area is determined by the surface area of the AgNW, which can be modified to increase the triboelectrically active area. More importantly, although, polyimide (PI) and poly (methyl methacrylate) (PMMA) are conventionally used to fabricate into thin film with the embedded AgNW networks, the triboelectric properties of the polymers restrict the output performance. The triboelectric tendencies of the polymers are listed in Figure 1.13, such demonstration could lead to further investigation of the synthetic polymer science for increasing overall output performance of triboelectric devices. As demonstrated in Chapter 8, when a fluorinated ethylene propylene (FEP) film is physically attached to the PI electrode, the output current density is elevated about 45 times. Although the enhanced performance may also due to the design of a single

electrode triboelectric system, it should be considered as the increased triboelectric tendency of the FEP film. This T-TENG was integrated with an OSC to work as a flexible hybrid cell.

Subsequently, this kind of hybrid device can be used to harvest both mechanical and solar energies. As an energy harvesting device, the level of the output performance of the triboelectric device is too low to compare with solar cells, the output current density of a general solar cell is at least ten times to the triboelectric device. However, triboelectric devices present some advanced properties, which makes the concept of the hybrid device viable. A typical output voltage of a triboelectric device is much higher than solar cells, allowing them to compensate each other in some applications, which require both a high current density and high voltage. More importantly, the input source of solar cells limits them only to work under light irradiation, whereas the triboelectric device is based on the availability of mechanical energy. Thus, especially at night, a triboelectric device could take over solar cells to become the majority of the device. This kind of application is especially useful for the wireless electronics, which require a relatively low power supply, but must be maintained to work for 24 hours a day.

In summary, the research of this thesis provides a fundamental understanding of the material science for solar and mechanical energy harvesting devices. Also an energy harvesting system is further investigated to enhance the conversion efficiency and widen the applications. This research could be significant to demonstrate the ideas, which are possible to reduce the reliance on fossil fuels, and subsequently to reduce carbon emissions towards the problem of climate change.

9.2 Future work and outlook

9.2.1 Further control of the electrospinning and electrospray

Electrospinning/electrospray provides a versatile and cost-effective route to

synthesise nanomaterials. Currently, the homogeneous control of the electrospun products still remains a challenge. For future work, an optimisation of the chemical composition of the precursor may improve the control of the diameter distribution of the electrospun nanofibres. Such uniform morphology is critical for their development for optoelectronic applications. The optical and quantum properties of the nanofibres could be significantly affected by the variations of the nanofibre diameters.[308] On the other hand, the high temperature calcination process also highly affects the morphology and the structure of the electrospun product. In order to overcome such problems, a low temperature hydrothermal treatment method may be used for the electrospun nanofibres. In this process, metal precursors will be hydrolysed and crystallised at a relatively low temperature (<200°C) to form stable metal oxide nanomaterials. The carrier polymer will be extracted by solvent. Nanopores may be created in the hydrolysis process and the overall nano-morphology can be maintained.

Recently, electrospun polymer nanomaterials attract interest for bio-applications. Electrospun biocompatible nanomaterials offer promising therapeutic approaches, such as tissue repair and functional restoration. For instance, a template created with electrospun aligned nanofibres could directly grow neurons, and such demonstration has the potential to repair damage to the human neural system in the future.[183] In medicinal fields, electrospun materials could also offer some new application directions. For instance, vitamins can be loaded into the electrospun products, such as nanofibres and nanospheres. The polymer matrix with a control of the loaded vitamin may effectively manage the release kinetics of the vitamin for an enhanced pharmaceutical effect.

9.2.2 Understanding the polyol method of nanomaterials synthesis

A variety of nanomaterials is nowadays synthesised using polyol methods. The advantages of this method are that the products can be controlled in different sizes,

shapes and morphologies, from a few nanometres up to several hundred micrometres.[309] Many applications are motivated by the advantages of polyol product, such as catalysis,[309] photocatalysis,[310] sensors,[198] magnetism,[311] solar cells,[312] high-power batteries,[313] and thin film electronics.[314] But the limitations of polyol method are also obvious. The rapid thermal decomposition, which has the temperature near the boiling point, limits the accessible temperature range of reactions. Also, the rapid re-oxidation of the less-noble metal is a problem. The details of nucleation in the polyol method are unclear. An investigation of the nucleation process may facilitate optimisation of the synthesis conditions. Complex, multi-element nanomaterials could be developed with unique physical and optical properties for wide-ranging applications.

9.2.3 Electrophoretic deposition using non-conductive electrode

EPD is a well-established method, which is widely used in academy and industry, and the mechanism is quite clear. Recently, the demonstration of depositing nanomaterials on a non-conductive substrate opens up a whole new range of applications, such as gas sensors,[315] and thermal barrier coatings.[316] A thin sacrificial conductive carbon layer is used and burned out in the final sintering step. However, it requires further study of the fundamentals of EPD processing onto a conductive carbon film coated substrate. On the other hand, using water to replace organic solvent is also accessible for EPD. Although the applied voltage has limitations, it also presents advantages, because the cost can be further reduced, and environmental concerns associated with the use of organic solvents can be minimised.

9.3 Energy harvesting devices

9.3.1 Dye sensitised solar cell and perovskite solar cell

For harvesting solar energy, solar cells are dominant in research and industry. The

investigation of DSSCs have been ongoing for more than 25 years.[28] The fabrication of the devices is already standardised. The barrier to commercialising DSSC is mainly due to the liquid electrolyte, because liquids can easily leak and evaporate. Reliable encapsulation technology is required to seal the electrolyte. Also, the working life of the inexpensive dye is also critical to commercialise DSSCs.

Perovskite solar cells have recently emerged, as an improved solar cell based on DSSCs. The low cost perovskite materials and the high conversion efficiency of the cell have attracted a lot of attentions. The general perovskite chemical structure is ABX_3, where X can be oxygen, carbon, nitrogen, or halogen. Cation A occupies a cube-octahedral site, and cation B occupies an octahedral site. A typical example is $CH_3NH_3PbI_3$, which has a valance band maximum, a conduction band minimum and a band gap of 5.43 eV, 3.93 eV and 1.5 eV, respectively.[317] Theoretically, the absorption onset wavelength is about 826 nm, which widely covers the visible spectrum. A standard single junction structured cell could have a photoconversion efficiency around 20%.[318] This is mainly due to the superb optoelectronic properties of the organo metal halide perovskite material, which are even better than the single crystal GaAs film. The efficiency can be further improved by nano-engineering the active layers. However, in order to commercialise perovskite solar cell, at least four issues must be addressed. Firstly, the encapsulating technology is critical for excluding moisture, since the perovskite material is readily decomposed by water contact. Secondly, the photo-stability of the perovskite material needs to be explored to extend the working life. For a commercialisation, scaling up the production with a preserved photoconversion efficiency is also necessary.[319] Finally, the environmental issue caused by Pb element in perovskite materials also must be concerned.

9.3.2. Improving photoelectrochemical water splitting efficiencies

Using photoelectrochemical (PEC) water splitting to harvest solar energy has been known for a long time, but the conversion efficiency is still quite low. Developing a stable and highly efficient photocatalyst material still remains a challenge. Essentially, the material should have a good visible light absorption and appropriate band edges.

Also, control of the morphology and porosity is able to increase the water splitting efficiency dramatically. Such control could facilitate improvement of the charge transfer between the semiconductors and the counter electrode with a reduced charge recombination probability. Three strategies were mainly taken into account to reduce the photorecombination effect and enhance the overall photoconversion efficiency: (1) the plasmonic effect; (2) Z-scheme photoelectrocatalyst; and (3) surface passivation deposition.[320]

In summary, the semiconductor should be selected with three key issues as follows: (1) expanding light absorbing with full visible spectrum; (2) developing inexpensive materials with a potential to improve charge transportation; and (3) designing multicomponent heterojunctions of the semiconductors to reduce the electron-hole recombination probability.

9.3.3. Improving the efficiencies of the triboelectric devices and hybrid devices

TENGs are recently emerging due to the high conversion efficiency, which is at least 5 times of that of a traditional piezoelectric nanogenerator.[300] The flexibility and long working life offers the possibility of harvesting conventional mechanical/kinetic energy in daily life. On basis of the fundamental understanding, many candidate materials can be introduced for this purpose, such as 2D nanomaterials including graphene and Bi_2Te_3 thin film. They can be fabricated into a highly conductive electrode with a high transparency. The electronic confinement of the 2D thin films may reduce the energy loss in the working cycle and increase the output.

In this work, the hybrid device has been demonstrated to harvest both mechanical and solar energies. To my knowledge, this is the first flexible and semi-transparent device, which is capable of harvesting both solar and mechanical energies. However, the output power of the triboelectric device is too low for some portable electronics. The concept of a flexible hybrid device can be further developed to harvest multiple energy sources. For instance, an OSC can be integrated with a thermoelectric device.[321] The temperature difference between the ambient environment and the human skin can be used to generate electrical energy. The device can also be integrated with an energy storage device, such as a film battery,[322] with storage of the collected energy for a further use.

9. References

1. T. Hargreaves, M. Nye and J. Burgess, *Energy pol.*, 2010, **38**, 6111-6119.
2. E. Brutschin and A. Fleig, *Energy Pol.*, 2016, **97**, 27-38.
3. A. Gupta and S. Arora, *IUP J. International Relat.*, 2015, **9**, 52-65.
4. C. Liu, P.-C. Hsu, H.-W. Lee, M. Ye, G. Zheng, N. Liu, W. Li and Y. Cui, *Nat. Commun.*, 2015, **6**, 6205.
5. S. Solomon, G. K. Plattner, R. Knutti and P. Friedlingstein, *Proc. Natl Acad. Sci. U. S. A*, 2009, **106**, 1704-1709.
6. J. Hansen, R. Ruedy, M. Sato and K. Lo, *Rev. Geophys.*, 2010, **48**, RG4004.
7. W. Knorr, *Geophys. Res. Lett.*, 2009, **36**, L21710.
8. A. Brunnengräber and M. Schreurs, *Nuclear energy and nuclear waste governance perspectives after the fukushima nuclear disaster*, Springer, 2015.
9. J. G. Koomey, *Environ. Res. Lett.*, 2008, **3**, 034008.
10. B. V. Mathiesen, H. Lund and K. Karlsson, *Appl. Energ.*, 2011, **88**, 488-501.
11. I. McConnell, G. Li and G. W. Brudvig, *Chem. Biol*, 2010, **17**, 434-447.
12. I. Angelidaki and D. J. Batstone, *Solid Waste Technology & Management*, Wiley, 2010.
13. K. Kaygusuz, *Energ. Explor. Exploit.*, 2001, **19**, 603-626.
14. C. C. Chan, K. S. Kuan and S. H. Hsieh, *J. Chinese Institute Engineer.*, 2010, **33**, 863-875.
15. G. Boyle, *Renewable energy*, OXFORD university press, 2004.
16. R. Everett, G. Boyle, S. Peake and J. Ramage, *Energy systems and sustainability: power for a sustainable future*, Oxford Univerity Press, 2012.
17. B. Boxer, *The China Quarterly*, 1988, **113**, 94-108.
18. T. Takagahara and K. Takeda, *Phy. Rev. B*, 1992, **46**, 15578.
19. A. Usami, *Sol. Energy Mater. Sol. Cells*, 2000, **64**, 73-83.
20. T. Schwartz, G. Bartal, S. Fishman and M. Segev, *Nature*, 2007, **446**, 52-55.
21. H. Hosono, H. Ohta, M. Orita, K. Ueda and M. Hirano, *Vacuum*, 2002, **66**, 419-425.
22. X. Zhu-you, X. Qi-ming, Z. Peng and T. Xiao-zhen, *J. Xi'an Univer. Architect. Technol.*, 2004, **1**, 026.
23. R. Bergmann, C. Berge, T. Rinke, J. Schmidt and J. Werner, *Sol. energ. mater.*

sol. cells, 2002, **74**, 213-218.

24. S. G. Kumar and K. S. R. K. Rao, *Ener. Environ. Sci.*, 2014, **7**, 45-102.
25. S. Wang, Y. Ding, S. Xu, Y. Zhang, G. Li, L. Hu and S. Dai, *Chem. Eur. J.*, 2014, **20**, 4916-4920.
26. S.-E. Park, S. Kim, D.-Y. Lee, E. Kim and J. Hwang, *J. Mater. Chem. A*, 2013, **1**, 14286-14293.
27. A. Fujishima and K. Honda, *Nature*, 1972, **238**, 37-38.
28. B. O'regan and M. Grätzel, *Nature*, 1991, **353**, 737-740.
29. J. Burschka, N. Pellet, S.-J. Moon, R. Humphry-Baker, P. Gao, M. K. Nazeeruddin and M. Gratzel, *Nature*, 2013, **499**, 316-319.
30. J. Liu, Y. Liu, N. Liu, Y. Han, X. Zhang, H. Huang, Y. Lifshitz, S.-T. Lee, J. Zhong and Z. Kang, *Science*, 2015, **347**, 970-974.
31. W. Zeng, Y. Cao, Y. Bai, Y. Wang, Y. Shi, M. Zhang, F. Wang, C. Pan and P. Wang, *Chem. Mater.*, 2010, **22**, 1915-1925.
32. Y. Wu, M. Marszalek, S. M. Zakeeruddin, Q. Zhang, H. Tian, M. Gratzel and W. Zhu, *Energ. Environ. Sci.*, 2012, **5**, 8261-8272.
33. D. Joly, L. Pellejà, S. Narbey, F. Oswald, J. Chiron, J. N. Clifford, E. Palomares and R. Demadrille, *Sci. Rep.*, 2014, **4**, 4033.
34. A. K. Ghosh and T. Feng, *J. Appl. Phys.*, 1973, **44**, 2781-2788.
35. C. W. Tang, *Appl. Phys. Lett.*, 1986, **48**, 183-185.
36. F. Diederich, R. Ettl, Y. Rubin, R. L. Whetten, R. Beck, M. Alvarez, S. Anz, D. Sensharma, F. Wudl and K. C. Khemani, *Science*, 1991, **252**, 548-551.
37. T. Aernouts, P. Vanlaeke, W. Geens, J. Poortmans, P. Heremans, S. Borghs, R. Mertens, R. Andriessen and L. Leenders, *Thin solid films*, 2004, **451**, 22-25.
38. Y. Liu, J. Zhao, Z. Li, C. Mu, W. Ma, H. Hu, K. Jiang, H. Lin, H. Ade and H. Yan, *Nat. Commun.*, 2014, **5**, 5293.
39. G. Grancini, M. Maiuri, D. Fazzi, A. Petrozza, H. Egelhaaf, D. Brida, G. Cerullo and G. Lanzani, *Nat. Mater.* , 2013, **12**, 29-33.
40. G. Li, V. Shrotriya, J. Huang, Y. Yao, T. Moriarty, K. Emery and Y. Yang, *Nat. Mater.*, 2005, **4**, 864-868.
41. J. K. van Duren, X. Yang, J. Loos, C. W. Bulle-Lieuwma, A. B. Sieval, J. C. Hummelen and R. A. Janssen, *Adv. Funct. Mater.*, 2004, **14**, 425-434.
42. L. Barreto, A. Makihira and K. Riahi, *Int. J. Hydrogen Energy*, 2003, **28**, 267-284.

43. Y. Ando and T. Tanaka, *Int. J. Hydrogen Energy*, 2004, **29**, 1349-1354.
44. M. Marszewski, S. Cao, J. Yu and M. Jaroniec, *Mater. Horiz.*, 2015, **2**, 261-278.
45. M. G. Walter, E. L. Warren, J. R. McKone, S. W. Boettcher, Q. Mi, E. A. Santori and N. S. Lewis, *Chem. Rev.*, 2010, **110**, 6446-6473.
46. R. van de Krol, Y. Liang and J. Schoonman, *J. Mater. Chem.*, 2008, **18**, 2311-2320.
47. S. Chandrasekhar, *Radiative transfer*, Courier Corporation, 2013.
48. S. D. Tilley, M. Cornuz, K. Sivula and M. Grätzel, *Angew. Chem.*, 2010, **122**, 6549-6552.
49. B. Cole, B. Marsen, E. Miller, Y. Yan, B. To, K. Jones and M. Al-Jassim, *J. Phys. Chem. C*, 2008, **112**, 5213-5220.
50. Z. Zhang, R. Dua, L. Zhang, H. Zhu, H. Zhang and P. Wang, *ACS Nano*, 2013, **7**, 1709-1717.
51. Z. Zhang and P. Wang, *J. Mater. Chem.*, 2012, **22**, 2456-2464.
52. R. B. Setlow, *Proc. Natl Acad. Sci. U. S. A*, 1974, **71**, 3363-3366.
53. R. Janisch, P. Gopal and N. A. Spaldin, *J. Phys.: Condens. Matter*, 2005, **17**, R657.
54. X. Hong, Z. Wang, W. Cai, F. Lu, J. Zhang, Y. Yang, N. Ma and Y. Liu, *Chem. Mater.*, 2005, **17**, 1548-1552.
55. X. Yang, A. Wolcott, G. Wang, A. Sobo, R. C. Fitzmorris, F. Qian, J. Z. Zhang and Y. Li, *Nano Lett.*, 2009, **9**, 2331-2336.
56. J. H. Park, O. O. Park and S. Kim, *Appl. Phys. Lett.*, 2006, **89**, 163106.
57. A. M. Mohamed, A. S. Aljaber, S. Y. AlQaradawi and N. K. Allam, *Chem. Commun.*, 2015, **51**, 12617-12620.
58. H. Lin, C. Huang, W. Li, C. Ni, S. I. Shah and Y.-H. Tseng, *Appl. Cata. B Environ.*, 2006, **68**, 1-11.
59. M. A. Green, K. Emery, Y. Hishikawa, W. Warta and E. D. Dunlop, *Prog. Photov. Res. Appl.*, 2015, **23**, 1-9.
60. Z. Liu, C. Pan, L. Lin and H. Lai, *Sensor. Actuat. A-Phys.*, 2013, **193**, 13-24.
61. X. Shi, H. Jeong, S. J. Oh, M. Ma, K. Zhang, J. Kwon, I. T. Choi, I. Y. Choi, H. K. Kim and J. K. Kim, *Nat. Commun.*, 2016, **7**, 11943.
62. R. G. Ehl and A. J. Ihde, *J. Chem. Educ.*, 1954, **31**, 226.
63. B. C. Chan, *Proc. IEEE*, 2007, **95**, 704-718.
64. M. Chinchilla, S. Arnaltes and J. C. Burgos, *IEEE Trans. Energ. Conver.*, 2006,

21, 130-135.

65. P. P. Tsai, H. Schreuder-Gibson and P. Gibson, *J. Electrostat.*, 2002, **54**, 333-341.
66. M.-H. Zhao, Z.-L. Wang and S. X. Mao, *Nano Lett.*, 2004, **4**, 587-590.
67. K. Herbert, *Weather*, 1997, **52**, 286-290.
68. S. Katzir, *Archive for history of exact sciences*, 2003, **57**, 61-91.
69. G. Schitter and A. Stemmer, *IEEE Trans. Contol Syst. Technol.*, 2004, **12**, 449-454.
70. M. Niskanen, M. Kuisma, O. Cramariuc, V. Golovanov, T. I. Hukka, N. Tkachenko and T. T. Rantala, *Phys. Chem. Chem. Phys.*, 2013, **15**, 17408-17418.
71. Z. L. Wang and J. Song, *Science*, 2006, **312**, 242-246.
72. Y. Fang, J. Tong, Q. Zhong, Q. Chen, J. Zhou, Q. Luo, Y. Zhou, Z. Wang and B. Hu, *Nano Energy*, 2015, **16**, 301-309.
73. J. Avela, H. Kyröläinen and P. V. Komi, *J. Appl. Physiology*, 1999, **86**, 1283-1291.
74. X. Wang, *Nano Energy*, 2012, **1**, 13-24.
75. J. Henniker, *Nature*, 1962, **196**, 474.
76. D. Davies, *J. Phys. D Appl. Phys.*, 1969, **2**, 1533.
77. Z. L. Wang, *ACS Nano*, 2013, **7**, 9533-9557.
78. F.-R. Fan, L. Lin, G. Zhu, W. Wu, R. Zhang and Z. L. Wang, *Nano Lett.*, 2012, **12**, 3109-3114.
79. L. Gao, Y. Zhang, H. Zhang, S. Doshay, X. Xie, H. Luo, D. Shah, Y. Shi, S. Xu and H. Fang, *ACS Nano*, 2015, **9**, 5968-5975.
80. J. Zhong, H. Zhu, Q. Zhong, J. Dai, W. Li, S.-H. Jang, Y. Yao, D. Henderson, Q. Hu and L. Hu, *ACS Nano*, 2015, **9**, 7399-7406.
81. B.-U. Hwang, J.-H. Lee, T. Q. Trung, E. Roh, D.-I. Kim, S.-W. Kim and N.-E. Lee, *ACS Nano*, 2015, **9**, 8801-8810.
82. B. Zhang, Z. M. Xiang, S. W. Zhu, Q. Y. Hu, Y. Z. Cao, J. W. Zhong, Q. Z. Zhong, B. Wang, Y. S. Fang, B. Hu, J. Zhou and Z. L. Wang, *Nano Res.*, 2014, **7**, 1488-1496.
83. D. S. Ghosh, T. L. Chen, V. Mkhitaryan and V. Pruneri, *ACS Appl. Mater. Interfaces*, 2014, **6**, 20943-20948.
84. J. Chen, J. Yang, Z. Li, X. Fan, Y. Zi, Q. Jing, H. Guo, Z. Wen, K. C. Pradel and

S. Niu, *ACS Nano*, 2015, **9**, 3324-3331.

85. A. Weeber and H. Bakker, *Physica B Condens. Matter.*, 1988, **153**, 93-135.
86. J. Arbiol, B. Kalache, P. R. i Cabarrocas, J. R. Morante and A. F. i Morral, *Nanotechnology*, 2007, **18**, 305606.
87. G. Shen, Y. Bando and D. Golberg, *J. Nanosci. Nanotechnol.*, 2009, **9**, 572-576.
88. A. L. Pan, L. Yao, Y. Qin, Y. Yang, D. S. Kim, R. Yu, B. Zou, P. Werner, M. Zacharias and U. Gösele, *Nano Lett.*, 2008, **8**, 3413-3417.
89. W. I. Park, D. Kim, S.-W. Jung and G.-C. Yi, *Appl. Phys. Lett.*, 2002, **80**, 4232-4234.
90. M. Macias-Montero, A. Borras, Z. Saghi, J. P. Espinos, A. Barranco, J. Cotrino and A. Gonzalez-Elipe, *Nanotechnology*, 2012, **23**, 255303.
91. Y. Hao, M. Bharathi, L. Wang, Y. Liu, H. Chen, S. Nie, X. Wang, H. Chou, C. Tan and B. Fallahazad, *Science*, 2013, **342**, 720-723.
92. Q. Dumont and R. B. Cole, *Mass Spectrom. Rev.*, 2014, **33**, 418-423.
93. N. Tucker, J. J. Stanger, M. P. Staiger, H. Razzaq and K. Hofman, *J. Eng. Fabr. Fiber.*, 2012, **7**, 63-73.
94. F. Iskandar, *Adv. Powder Technol.*, 2009, **20**, 283-292.
95. I.-D. Kim, J.-M. Hong, B. H. Lee, D. Y. Kim, E.-K. Jeon, D.-K. Choi and D.-J. Yang, *Appl. Phys. Lett.*, 2007, **91**, 163109.
96. X. Lu, X. Liu, W. Zhang, C. Wang and Y. Wei, *J. Colloid Interface Sci.*, 2006, **298**, 996-999.
97. A. Kumar, R. Jose, K. Fujihara, J. Wang and S. Ramakrishna, *Chem. Mater.*, 2007, **19**, 6536-6542.
98. Z. Li, H. Zhang, W. Zheng, W. Wang, H. Huang, C. Wang, A. G. MacDiarmid and Y. Wei, *J. Am. Chem. Soc.*, 2008, **130**, 5036-5037.
99. C. Niu, J. Meng, X. Wang, C. Han, M. Yan, K. Zhao, X. Xu, W. Ren, Y. Zhao and L. Xu, *Nat. commun.*, 2015, **6**, 7402.
100. B. Song, C. Wu and J. Chang, *Acta Biomater.*, 2012, **8**, 1901-1907.
101. S. Park, J. B. Kim, S. Lee, J. H. Bang and Y. S. Kim, *Mater. Lett.*, 2012, **69**, 34-36.
102. A. S. Nair, Y. Shengyuan, Z. Peining and S. Ramakrishna, *Chem. Commun.*, 2010, **46**, 7421-7423.
103. K.-H. Roh, D. C. Martin and J. Lahann, *Nat. Mater.* , 2005, **4**, 759-763.
104. Y. Xin, Z. Huang, J. Chen, C. Wang, Y. Tong and S. Liu, *Mater. Lett.*, 2008, **62**,

991-993.

105. J. S. Bedi, D. W. Lester, Y. X. Fang, J. F. C. Turner, J. Zhou, S. M. Alfadul, C. Perry and Q. Chen, *J. Polym. Eng.*, 2013, **33**, 453-461.
106. Z.-M. Huang, Y.-Z. Zhang, M. Kotaki and S. Ramakrishna, *Compos. Sci. Technol.*, 2003, **63**, 2223-2253.
107. J. Varabhas, G. Chase and D. Reneker, *Polymer*, 2008, **49**, 4226-4229.
108. H.-J. Jin, S. V. Fridrikh, G. C. Rutledge and D. L. Kaplan, *Biomacromolecules*, 2002, **3**, 1233-1239.
109. T. J. Sill and H. A. von Recum, *Biomaterials*, 2008, **29**, 1989-2006.
110. K. Onozuka, B. Ding, Y. Tsuge, T. Naka, M. Yamazaki, S. Sugi, S. Ohno, M. Yoshikawa and S. Shiratori, *Nanotechnology*, 2006, **17**, 1026.
111. X. Lu, Q. Zhao, X. Liu, D. Wang, W. Zhang, C. Wang and Y. Wei, *Macromol. Rapid Commun.*, 2006, **27**, 430-434.
112. G. T. Wang, A. A. Talin, D. J. Werder, J. R. Creighton, E. Lai, R. J. Anderson and I. Arslan, *Nanotechnology*, 2006, **17**, 5773.
113. J. Chang, M. Dommer, C. Chang and L. Lin, *Nano Energy*, 2012, **1**, 356-371.
114. Y. T. Kim and C. K. Baek, *J. Polym. Sci., Part B: Polym. Phys.*, 2003, **41**, 1572-1577.
115. C. Chang, V. H. Tran, J. Wang, Y.-K. Fuh and L. Lin, *Nano Lett.*, 2010, **10**, 726-731.
116. Y. Gu, D. Chen and X. Jiao, *J. Phys. Chem. B*, 2005, **109**, 17901-17906.
117. A. D. Lueking, L. Pan, D. L. Narayanan and C. E. Clifford, *J. Phys. Chem. B*, 2005, **109**, 12710-12717.
118. P.-C. Yu, R.-J. Yang, Y.-Y. Tsai, W. Sigmund and F.-S. Yen, *J. Eur. Ceram. Soc.*, 2011, **31**, 723-731.
119. Y. Sun and Y. Xia, *Science*, 2002, **298**, 2176-2179.
120. B. Cao and W. Cai, *J. Phys. Chem. C*, 2008, **112**, 680-685.
121. S. Sōmiya and R. Roy, *Bull. Mater. Sci.*, 2000, **23**, 453-460.
122. H. Amano, N. Sawaki, I. Akasaki and Y. Toyoda, *Appl. Phys. Lett.*, 1986, **48**, 353-355.
123. D. E. Perea, E. R. Hemesath, E. J. Schwalbach, J. L. Lensch-Falk, P. W. Voorhees and L. J. Lauhon, *Nat. Nanotechn.*, 2009, **4**, 315-319.
124. R. Ortega-Borges and D. Lincot, *J. Electrochem. Soc.*, 1993, **140**, 3464-3473.
125. G. Bruckman, *Kolloid Z*, 2014, **65**, 1-11.

126. P. Nair, M. Nair, V. Garcıa, O. Arenas, Y. Pena, A. Castillo, I. Ayala, O. Gomezdaza, A. Sanchez and J. Campos, *Sol. Energy Mater. Sol. Cells*, 1998, **52**, 313-344.
127. L. Vayssieres, *Adv. Mater.*, 2003, **15**, 464-466.
128. M. Law, L. E. Greene, J. C. Johnson, R. Saykally and P. Yang, *Nat. Mater.* , 2005, **4**, 455-459.
129. C. Badre, T. Pauporté, M. Turmine and D. Lincot, *Nanotechnology*, 2007, **18**, 365705.
130. S. Xu, C. Lao, B. Weintraub and Z. L. Wang, *J. Mater. Res.*, 2008, **23**, 2072-2077.
131. S. Baruah and J. Dutta, *J. Sol-Gel Sci. Technol.*, 2009, **50**, 456-464.
132. F. Fievet, J. Lagier, B. Blin, B. Beaudoin and M. Figlarz, *Solid State Ion.*, 1989, **32**, 198-205.
133. Y. Xia, Y. Xiong, B. Lim and S. E. Skrabalak, *Angew. Chem. Int. Ed.*, 2009, **48**, 60-103.
134. D. Larcher and R. Patrice, *J. Solid State Chem.*, 2000, **154**, 405-411.
135. B. Pietrobon and V. Kitaev, *Chem. Mater.*, 2008, **20**, 5186-5190.
136. M. R. Langille, J. Zhang, M. L. Personick, S. Li and C. A. Mirkin, *Science*, 2012, **337**, 954-957.
137. D. Li, Y. Wang and Y. Xia, *Nano Lett.*, 2003, **3**, 1167-1171.
138. C. Feldmann, *Solid State Sci.*, 2005, **7**, 868-873.
139. J. Livage, *Mater. Sci. Forum*, 1994, **152**, 43-54.
140. B. Feng, H. Wang, D. Wang, H. Yu, Y. Chu and H.-T. Fang, *Nanoscale*, 2014, **6**, 14371-14379.
141. P.-G. Su and S.-L. Peng, *Talanta*, 2015, **132**, 398-405.
142. T. Itoh, T. Uchida, I. Matsubara, N. Izu, W. Shin, H. Miyazaki, H. Tanjo and K. Kanda, *Ceram. Int.*, 2015, **41**, 3631-3638.
143. J.-S. Lee, G. S. Park, H. I. Lee, S. T. Kim, R. Cao, M. Liu and J. Cho, *Nano Lett.*, 2011, **11**, 5362-5366.
144. Y.-Z. Zheng, H. Ding, E. Uchaker, X. Tao, J.-F. Chen, Q. Zhang and G. Cao, *J. Mater. Chem. A*, 2015, **3**, 1979-1985.
145. N. V. Long, Y. Yang, M. Yuasa, C. M. Thi, Y. Cao, T. Nann and M. Nogami, *RSC Adv.*, 2014, **4**, 8250-8255.
146. W. Chen, L. Li, Q. Peng and Y. Li, *Nano Res.*, 2012, **5**, 320-326.

147. J. Ungelenk, M. Speldrich, R. Dronskowski and C. Feldmann, *Solid State Sci.*, 2014, **31**, 62-69.
148. H. Dong, Y.-C. Chen and C. Feldmann, *Green Chem.*, 2015, **17**, 4107-4132.
149. P. Schmitt, N. Brem, S. Schunk and C. Feldmann, *Adv. Funct. Mater.*, 2011, **21**, 3037-3046.
150. J. Ungelenk and C. Feldmann, *Appl. Cata. B Environ.*, 2012, **127**, 11-17.
151. L. Besra and M. Liu, *Prog. Mater Sci.*, 2007, **52**, 1-61.
152. B. Ferrari and R. Moreno, *Mater. Lett.*, 1996, **28**, 353-355.
153. C.-Y. Chen, S.-Y. Chen and D.-M. Liu, *Acta Mater.*, 1999, **47**, 2717-2726.
154. A. Bhattacharya and A. Milchev, *Phys. Rev. E*, 2002, **66**, 041806.
155. N. Mavrogiannis, M. Desmond and Z. R. Gagnon, *Electrophresis*, 2015, **36**, 1386-1395.
156. K. Hasegawa, S. Kunugi, M. Tatsumisago and T. Minami, *J. Sol-Gel Sci. Technol.*, 1999, **15**, 243-249.
157. P. S. Nicholson, P. Sarkar and X. Haung, *J. Mater. Sci.*, 1993, **28**, 6274-6278.
158. D. Grujicic and B. Pesic, *Electrochim. Acta*, 2002, **47**, 2901-2912.
159. E. Kumacheva, R. K. Golding, M. Allard and E. H. Sargent, *Adv. Mater.*, 2002, **14**, 221.
160. T. Hosomi, M. Matsuda and M. Miyake, *J. Eur. Ceram. Soc.*, 2007, **27**, 173-178.
161. T. Ishihara, K. Shimose, T. Kudo, H. Nishiguchi, T. Akbay and Y. Takita, *J. Am. Ceram. Soc.*, 2000, **83**, 1921-1927.
162. A. Demirbas, *Green energy and technology*, Springer, London., 2009.
163. D. B. Holt and D. C. Joy, *SEM microcharacterization of semiconductors*, Academic Press, 2013.
164. H. Kuhn, H.-D. Försterling and D. H. Waldeck, *Principles of physical chemistry*, John Wiley & Sons, 2009.
165. K. Thamaphat, P. Limsuwan and B. Ngotawornchai, *Kasetsart J. Nat. Sci.*, 2008, **42**, 357-361.
166. G. I. Waterhouse and M. R. Waterland, *Polyhedron*, 2007, **26**, 356-368.
167. J. I. Langford and A. Wilson, *J. Appl. Crystallogr.*, 1978, **11**, 102-113.
168. D. Calloway, *J. Chem. Educ.*, 1997, **74**, 744.
169. H. Kaneko, S. Nishimoto, K. Miyake and N. Suedomi, *J. Appl. Phys.*, 1986, **59**, 2526-2534.
170. S. John, C. Soukoulis, M. H. Cohen and E. Economou, *Phys. Rev. Lett.*, 1986,

57, 1777.

171. S. Ilican, *J. Alloys Compd.*, 2013, **553**, 225-232.
172. H.-J. Butt, B. Cappella and M. Kappl, *Surf. Sci. Rep.*, 2005, **59**, 1-152.
173. G. Binnig, C. F. Quate and C. Gerber, *Phys. Rev. Lett.*, 1986, **56**, 930-933.
174. A. M. Fajardo and N. S. Lewis, *Science*, 1996, **274**, 969-972.
175. J. C. Hill and K.-S. Choi, *J. Mater. Chem. A*, 2013, **1**, 5006-5014.
176. A. Luque and A. Mart ί, *Phy. Rev. Lett.*, 1997, **78**, 5014.
177. G. Araujo and E. Sanchez, *Sol. Cells*, 1982, **5**, 377-386.
178. R. A. Pala, J. White, E. Barnard, J. Liu and M. L. Brongersma, *Adv. Mater.*, 2009, **21**, 3504-3509.
179. I. Schnitzer, E. Yablonovitch, C. Caneau, T. Gmitter and A. Scherer, *Appl. Phy. Lett.*, 1993, **63**, 2174-2176.
180. S. Niu, S. Wang, L. Lin, Y. Liu, Y. S. Zhou, Y. Hu and Z. L. Wang, *Energ. Environ. Sci.*, 2013, **6**, 3576-3583.
181. C. Kim, K. S. Yang, M. Kojima, K. Yoshida, Y. J. Kim, Y. A. Kim and M. Endo, *Adv. Funct. Mater.*, 2006, **16**, 2393-2397.
182. X. H. Qin and S. Y. Wang, *J. Appl. Polym. Sci.*, 2006, **102**, 1285-1290.
183. H. Xia, Q. Chen, Y. Fang, D. Liu, D. Zhong, H. Wu, Y. Xia, Y. Yan, W. Tang and X. Sun, *Brain Res.*, 2014, **1565**, 18-27.
184. K. Fujihara, A. Kumar, R. Jose, S. Ramakrishna and S. Uchida, *Nanotechnology*, 2007, **18**, 365709.
185. Z. Liu, D. D. Sun, P. Guo and J. O. Leckie, *Nano Lett.*, 2007, **7**, 1081-1085.
186. D. S. Katti, K. W. Robinson, F. K. Ko and C. T. Laurencin, *J Biomed. Mater. Res. Part B: Appl. Biomater.*, 2004, **70**, 286-296.
187. J. Macossay, A. Marruffo, R. Rincon, T. Eubanks and A. Kuang, *Polym. Adv.Technol.*, 2007, **18**, 180-183.
188. S. Gu, J. Ren and G. Vancso, *Eur. Polym. J.*, 2005, **41**, 2559-2568.
189. A. Jaworek, *Powder Technol.*, 2007, **176**, 18-35.
190. Z. Dobkowski, *Eur. Polym. J.*, 1984, **20**, 399-403.
191. M. G. McKee, G. L. Wilkes, R. H. Colby and T. E. Long, *Macromolecules*, 2004, **37**, 1760-1767.
192. R. H. Colby, L. J. Fetters, W. G. Funk and W. W. Graessley, *Macromolecules*, 1991, **24**, 3873-3882.
193. P. Gupta, C. Elkins, T. E. Long and G. L. Wilkes, *Polymer*, 2005, **46**, 4799-

4810.

194. M. Alger, *Polymer science dictionary*, Springer Science & Business Media, 1996.
195. S. L. Shenoy, W. D. Bates, H. L. Frisch and G. E. Wnek, *Polymer*, 2005, **46**, 3372-3384.
196. J. E. Mark, *Physical properties of polymers handbook*, Springer, 2007.
197. S. Tan, R. Inai, M. Kotaki and S. Ramakrishna, *Polymer*, 2005, **46**, 6128-6134.
198. C. Kittel, *Introduction to solid state physics*, Wiley, 2005.
199. M. Nasir, H. Matsumoto, T. Danno, M. Minagawa, T. Irisawa, M. Shioya and A. Tanioka, *J. Polym. Sci., Part B: Polym. Phys.*, 2006, **44**, 779-786.
200. C. Zhang, X. Yuan, L. Wu, Y. Han and J. Sheng, *Eur. Polym. J.*, 2005, **41**, 423-432.
201. K. S. Ahn, S. H. Lee, A. C. Dillon, C. E. Tracy and R. Pitts, *J. Appl. Phys.*, 2007, **101**, 093524.
202. Q. Liu, Q. P. Chen, J. Bai, J. Y. Li, J. H. Li and B. X. Zhou, *J. Solid State Electr.*, 2014, **18**, 157-161.
203. X. Liu, F. Wang and Q. Wang, *Phys. Chem. Chem. Phys.*, 2012, **14**, 7894-7911.
204. G. R. Bamwenda, K. Sayama and H. Arakawa, *J. Photochem. Photobiol. Chem*, 1999, **122**, 175-183.
205. S. S. Kalanur, Y. J. Hwang, S. Y. Chae and O. S. Joo, *J. Mater. Chem. A*, 2013, **1**, 3479-3488.
206. P. Salvador, *J. Appl. Phys.*, 1984, **55**, 2977-2985.
207. Y. Fang, W. C. Lee, G. E. Canciani, T. C. Draper, Z. F. Al-Bawi, J. S. Bedi, C. C. Perry and Q. Chen, *Mater. Sci. Engineer. B*, 2015, **202**, 39-45.
208. K. Sivula, F. Le Formal and M. Gratzel, *Chem. Mater.*, 2009, **21**, 2862-2867.
209. K. N. Chappanda, Y. R. Smith, L. W. Rieth, P. Tathireddy, M. Misra and S. K. Mohanty, *J. Electrochem. Soc.*, 2014, **161**, H431-H437.
210. N. Mukherjee, M. Paulose, O. K. Varghese, G. K. Mor and C. A. Grimes, *J. Mater. Res.*, 2003, **18**, 2296-2299.
211. V. Cristino, S. Caramori, R. Argazzi, L. Meda, G. L. Marra and C. A. Bignozzi, *Langmuir*, 2011, **27**, 7276-7284.
212. N. De Tacconi, C. Chenthamarakshan, G. Yogeeswaran, A. Watcharenwong, R. De Zoysa, N. Basit and K. Rajeshwar, *J. Phys. Chem. B*, 2006, **110**, 25347-25355.

213. M. Yagi, S. Maruyama, K. Sone, K. Nagai and T. Norimatsu, *J. Solid State Chem.*, 2008, **181**, 175-182.

214. D. D. Qin, C. L. Tao, S. A. Friesen, T. H. Wang, O. K. Varghese, N. Z. Bao, Z. Y. Yang, T. E. Mallouk and C. A. Grimes, *Chem. Commun.*, 2012, **48**, 729-731.

215. A. R. Boccaccini, U. Schindler and H. G. Kruger, *Mater. Lett.*, 2001, **51**, 225-230.

216. I. Zhitomirsky, *J. Eur. Ceram. Soc.*, 1998, **18**, 849-856.

217. A. R. Boccaccini and P. A. Trusty, *J. Mater. Sci.*, 1998, **33**, 933-938.

218. Y. Xu, X. Zhu, Y. Dan, J. H. Moon, V. W. Chen, A. T. Johnson, J. W. Perry and S. Yang, *Chem. Mater.*, 2008, **20**, 1816-1823.

219. S. Santhanagopalan, A. Balram and D. D. Meng, *ACS Nano*, 2013, **7**, 2114-2125.

220. G. Injeti and B. Leo, *Sci. Technol. Adv. Mater.*, 2008, **9**, 043001.

221. G. Girishkumar, K. Vinodgopal and P. V. Kamat, *J. Phys. Chem. B*, 2004, **108**, 19960-19966.

222. Y. C. Wang, I. C. Leu and M. H. Hon, *J. Am. Ceram. Soc.*, 2004, **87**, 84-88.

223. E. Khoo, P. S. Lee and J. Ma, *J. Eur. Ceram. Soc.*, 2010, **30**, 1139-1144.

224. G. J. French and F. R. Sale, *J. Mater. Sci.*, 1981, **16**, 3427-3436.

225. J. Zeng, C. Francia, C. Gerbaldi, V. Baglio, S. Specchia, A. S. Arico and P. Spinelli, *Electrochim. Acta*, 2013, **94**, 80-91.

226. S. J. Choi, C. Choi, S.-J. Kim, H.-J. Cho, M. Hakim, S. Jeon and I. D. Kim, *Sci. Rep.*, 2015, **5**, 8067.

227. B. Ferrari, R. Moreno and J. A. Cuesta, *Electrophoretic Deposition: Fundamentals and Applications VI*, 2006, **314**, 175-180.

228. J. J. Sene, W. A. Zeltner and M. A. Anderson, *J. Phys. Chem. B*, 2003, **107**, 1597-1603.

229. M. F. De Riccardis, *Ceramic Coatings Obtained by Electrophoretic Deposition: Fundamentals, Models, Post-Deposition Processes and Applications*, INTECH Open Access Publisher, 2012.

230. B. Hu, W. Chen and J. Zhou, *Sen. Actuators B-Chem.*, 2013, **176**, 522-533.

231. C. Santato, M. Ulmann and J. Augustynski, *Adv. Mater.*, 2001, **13**, 511-514.

232. Z. Jiao, J. Wang, L. Ke, X. W. Sun and H. V. Demir, *ACS Appl. Mater. Interfaces*, 2011, **3**, 229-236.

233. Z. Li, W. Luo, M. Zhang, J. Feng and Z. Zou, *Energ. Environ. Sci.*, 2013, **6**,

347-370.

234. P. P. Gonzalez-Borrero, F. Sato, A. N. Medina, M. L. Baesso, A. C. Bento, G. Baldissera, C. Persson, G. A. Niklasson, C. G. Granqvist and A. F. da Silva, *Appl. Phys. Lett.*, 2010, **96**, 061909.
235. G. Hodes, D. Cahen and J. Manassen, *Nature*, 1976, **260**, 312-313.
236. S.-H. A. Lee, Y. Zhao, E. A. Hernandez-Pagan, L. Blasdel, W. J. Youngblood and T. E. Mallouk, *Faraday Discuss.*, 2012, **155**, 165-176.
237. L. J. Minggu, W. R. W. Daud and M. B. Kassim, *Int. J. Hydrogen Energy*, 2010, **35**, 5233-5244.
238. L. Liao, Q. Zhang, Z. Su, Z. Zhao, Y. Wang, Y. Li, X. Lu, D. Wei, G. Feng and Q. Yu, *Nat. Nanotechnol.*, 2014, **9**, 69-73.
239. J. Kondo, *Chem. Commun.*, 1998, 357-358.
240. S. Hu, M. R. Shaner, J. A. Beardslee, M. Lichterman, B. S. Brunschwig and N. S. Lewis, *Science*, 2014, **344**, 1005-1009.
241. P. Charvin, S. Abanades, G. Flamant and F. Lemort, *Energy*, 2007, **32**, 1124-1133.
242. W. C. Lee, Y. X. Fang, R. Kler, G. E. Canciani, T. C. Draper, Z. T. Y. Al-Abdullah, S. M. Alfadul, C. C. Perry, H. Y. He and Q. Chen, *Mater. Chem. Phys.*, 2015, **149-150**, 12-16.
243. S.-D. Mo and W. Ching, *Phys. Rev. B*, 1995, **51**, 13023.
244. Y. H. Hu, *Angew. Chem. Int. Ed. Engl.*, 2012, **51**, 12410-12412.
245. J. H. Park, O. O. Park and S. Kim, *Appl. Phys. Lett.*, 2006, **89**, 163106.
246. D.-J. Yang, S.-C. Yang, J.-M. Hong, H. Lee and I.-D. Kim, *J. electroceram.*, 2010, **24**, 200-204.
247. A. Wolcott, W. A. Smith, T. R. Kuykendall, Y. Zhao and J. Z. Zhang, *Small*, 2009, **5**, 104-111.
248. X. Lai, J. E. Halpert and D. Wang, *Energ. Environ. Sci.*, 2012, **5**, 5604-5618.
249. H. G. Moon, Y.-S. Shim, H. W. Jang, J.-S. Kim, K. J. Choi, C.-Y. Kang, J.-W. Choi, H.-H. Park and S.-J. Yoon, *Sens. Actuator B-Chem.*, 2010, **149**, 116-121.
250. H. G. Moon, H. W. Jang, J.-S. Kim, H.-H. Park and S.-J. Yoon, *Electro. Mater. Lett.*, 2010, **6**, 135-139.
251. S.-C. Yang, D.-J. Yang, J. Kim, J.-M. Hong, H.-G. Kim, I.-D. Kim and H. Lee, *Adv. Mater.*, 2008, **20**, 1059.
252. J. Lu, P. Zhang, A. Li, F. Su, T. Wang, Y. Liu and J. Gong, *Chem. Commun.*,

2013, **49**, 5817-5819.

253. C. Jia, P. Yang, H.-S. Chen and J. Wang, *CrystEngComm*, 2015, **17**, 2940-2948.
254. J. S. Bedi, D. W. Lester, Y. X. Fang, J. F. C. Turner, J. Zhou, S. M. Alfadul, C. Perry and Q. Chen, *J. Polym. Engineer.*, 2013, **33**, 453-461.
255. S. Park, J. B. Kim, S. Lee, J. H. Bang and Y. S. Kim, *Mater. Lett.*, 2012, **69**, 34-36.
256. J. Liu, A. Rasheed, H. Dong, W. W. Carr, M. D. Dadmun and S. Kumar, *Macromol. Chem. Phys.*, 2008, **209**, 2390-2398.
257. H. Sakai, H. Kawahara, M. Shimazaki and M. Abe, *Langmuir*, 1998, **14**, 2208-2212.
258. N. A. Hashim, F. Liu, M. M. Abed and K. Li, *J. Memb. Sci.*, 2012, **415**, 399-411.
259. Z. D. Li, C. H. Yao, Y. H. Yu, Z. Y. Cai and X. D. Wang, *Adv. Mater.*, 2014, **26**, 2262-2267.
260. J. Lin, Y.-U. Heo, A. Nattestad, M. Shahabuddin, Y. Yamauchi and J. H. Kim, *Phys. Chem. Chem. Phys.*, 2015, **17**, 7208-7213.
261. N. Hirata, J.-J. Lagref, E. J. Palomares, J. R. Durrant, M. K. Nazeeruddin, M. Gratzel and D. Di Censo, *Chem. Eur. J.*, 2004, **10**, 595-602.
262. R. Kawano, H. Matsui, C. Matsuyama, A. Sato, M. A. B. H. Susan, N. Tanabe and M. Watanabe, *J. Photochem. Photobio. Chem.*, 2004, **164**, 87-92.
263. G. Zhu, Y. Su, P. Bai, J. Chen, Q. Jing, W. Yang and Z. L. Wang, *ACS Nano*, 2014, **8**, 6031-6037.
264. M. Ha, J. Park, Y. Lee and H. Ko, *ACS Nano*, 2015, **9**, 3421-3427.
265. W. Tang, J. Tian, Q. Zheng, L. Yan, J. Wang, Z. Li and Z. L. Wang, *ACS Nano*, 2015, **9**, 7867-7873.
266. Q. Jing, Y. Xie, G. Zhu, R. P. Han and Z. L. Wang, *Nat. commun.*, 2015, **6**, 8031.
267. W. Tang, B. Meng and H. Zhang, *Nano Energy*, 2013, **2**, 1164-1171.
268. C. K. Jeong, K. M. Baek, S. Niu, T. W. Nam, Y. H. Hur, D. Y. Park, G.-T. Hwang, M. Byun, Z. L. Wang and Y. S. Jung, *Nano Lett.*, 2014, **14**, 7031-7038.
269. Q. Liang, X. Yan, Y. Gu, K. Zhang, M. Liang, S. Lu, X. Zheng and Y. Zhang, *Sci. Rep.*, 2015, **5**, 9080.
270. Y. Sun and Y. Xia, *Nature*, 1991, **353**, 737.
271. R. Richardson, J. Miller and W. Reichert, *Biomaterials*, 1993, **14**, 627-635.

272. H. Tsung-Syun, S. Yan-Kuin and W. Po-Cheng, *Jpn. J. Appl. Phys*, 2008, **47**, 3185.

273. G. Maier, *Prog. Polym. Sci.*, 2001, **26**, 3-65.

274. R. M. Mutiso, M. C. Sherrott, A. R. Rathmell, B. J. Wiley and K. I. Winey, *ACS Nano*, 2013, **7**, 7654-7663.

275. G. Khanarian, J. Joo, X.-Q. Liu, P. Eastman, D. Werner, K. O'Connell and P. Trefonas, *J. Appl. Phys.*, 2013, **114**, 024302.

276. K. Nomura, H. Ohta, A. Takagi, T. Kamiya, M. Hirano and H. Hosono, *Nature*, 2004, **432**, 488-492.

277. C. G. Granqvist, *Sol. Energy Mater. Sol. Cells*, 2007, **91**, 1529-1598.

278. C.-C. Chen, L. Dou, R. Zhu, C.-H. Chung, T.-B. Song, Y. B. Zheng, S. Hawks, G. Li, P. S. Weiss and Y. Yang, *ACS Nano*, 2012, **6**, 7185-7190.

279. G. J. Snyder and E. S. Toberer, *Nat. Mater.* , 2008, **7**, 105-114.

280. Q. Zhong, J. Zhong, B. Hu, Q. Hu, J. Zhou and Z. L. Wang, *Energ. Environ. Sci.*, 2013, **6**, 1779-1784.

281. A. Khaligh, P. Zeng and C. Zheng, *IEEE Transac. Industrial. Electron.*, 2010, **57**, 850-860.

282. J. Luo, J.-H. Im, M. T. Mayer, M. Schreier, M. K. Nazeeruddin, N.-G. Park, S. D. Tilley, H. J. Fan and M. Grätzel, *Science*, 2014, **345**, 1593-1596.

283. C. Xu, X. Wang and Z. L. Wang, *J. Am. Chem. Soc.*, 2009, **131**, 5866-5872.

284. J. Bae, J. Lee, S. Kim, J. Ha, B.-S. Lee, Y. Park, C. Choong, J.-B. Kim, Z. L. Wang and H.-Y. Kim, *Nat. Commun.*, 2014, **5**, 4929.

285. Y. Yang, H. Zhang, Z.-H. Lin, Y. S. Zhou, Q. Jing, Y. Su, J. Yang, J. Chen, C. Hu and Z. L. Wang, *ACS Nano*, 2013, **7**, 9213-9222.

286. L. Zheng, Z.-H. Lin, G. Cheng, W. Wu, X. Wen, S. Lee and Z. L. Wang, *Nano Energy*, 2014, **9**, 291-300.

287. J. Zhong, Y. Zhang, Q. Zhong, Q. Hu, B. Hu, Z. L. Wang and J. Zhou, *ACS Nano*, 2014, **8**, 6273-6280.

288. Y. Zhou, T. M. Khan, J. W. Shim, A. Dindar, C. Fuentes-Hernandez and B. Kippelen, *J. Mater. Chem. A*, 2014, **2**, 3492-3497.

289. Y. Zhou, C. Fuentes-Hernandez, J. Shim, J. Meyer, A. J. Giordano, H. Li, P. Winget, T. Papadopoulos, H. Cheun and J. Kim, *Science*, 2012, **336**, 327-332.

290. Y. Yang, H. Zhang, Z.-H. Lin, Y. Liu, J. Chen, Z. Lin, Y. S. Zhou, C. P. Wong and Z. L. Wang, *Energ. Environ. Sci.*, 2013, **6**, 2429-2434.

291. K. Ando, S. Watanabe, S. Mooser, E. Saitoh and H. Sirringhaus, *Nat. Mater.*, 2013, **12**, 622-627.
292. S. Hong and S. Myung, *Nat. Nanotechnol.*, 2007, **2**, 207-208.
293. H. Kang, S. Jung, S. Jeong, G. Kim and K. Lee, *Nat. Commun.*, 2015, **6**, 6503.
294. H. Wu, D. Kong, Z. Ruan, P.-C. Hsu, S. Wang, Z. Yu, T. J. Carney, L. Hu, S. Fan and Y. Cui, *Nat. Nanotechnol.*, 2013, **8**, 421-425.
295. Z. Fang, H. Zhu, Y. Yuan, D. Ha, S. Zhu, C. Preston, Q. Chen, Y. Li, X. Han and S. Lee, *Nano Lett.*, 2014, **14**, 765-773.
296. Y. Zhao, D. Nothern, A. Yadav, K.-h. An, K. P. Pipe and M. Shtein, *Org. Electron.*, 2014, **15**, 3529-3537.
297. M. Kaltenbrunner, T. Sekitani, J. Reeder, T. Yokota, K. Kuribara, T. Tokuhara, M. Drack, R. Schwödiauer, I. Graz and S. Bauer-Gogonea, *Nature*, 2013, **499**, 458-463.
298. Z. H. Lin, G. Cheng, S. Lee, K. C. Pradel and Z. L. Wang, *Adv. Mater.*, 2014, **26**, 4690-4696.
299. G. Zhu, Y. S. Zhou, P. Bai, X. S. Meng, Q. Jing, J. Chen and Z. L. Wang, *Adv. Mater.*, 2014, **26**, 3788-3796.
300. F.-R. Fan, Z.-Q. Tian and Z. L. Wang, *Nano Energy*, 2012, **1**, 328-334.
301. I. Winter, C. Reese, J. Hormes, G. Heywang and F. Jonas, *Chem. Phys.*, 1995, **194**, 207-213.
302. K. Sun, S. Zhang, P. Li, Y. Xia, X. Zhang, D. Du, F. H. Isikgor and J. Ouyang, *J. Mater. Sci. Mater. Electron.*, 2015, **26**, 4438-4462.
303. D. Alemu, H.-Y. Wei, K.-C. Ho and C.-W. Chu, *Energ. Environ. Sci.*, 2012, **5**, 9662-9671.
304. L. Groenendaal, F. Jonas, D. Freitag, H. Pielartzik and J. R. Reynolds, *Adv. Mater.*, 2000, **12**, 481-494.
305. S. Kirchmeyer and K. Reuter, *J. Mater. Chem.*, 2005, **15**, 2077-2088.
306. S. J. Kim, J. H. We and B. J. Cho, *Energ. Environ. Sci.*, 2014, **7**, 1959-1965.
307. Z. L. Wang and X. Wang, *Nano Energy*, 2015, **14**, 1-2.
308. J.-H. Chai and Q.-S. Wu, *Beilstein J. Nanotechnol.*, 2013, **4**, 189-197.
309. X. Li, W.-X. Chen, J. Zhao, W. Xing and Z.-D. Xu, *Carbon*, 2005, **43**, 2168-2174.
310. F. Amano, D. Li and B. Ohtani, *Fullerenes, Nanotubes, and Carbon Nanostructures - 217th Ecs Meeting*, 2010, **28**, 127-133.

311. L. Besra, C. Compson and M. Liu, *J. Power Sources*, 2007, **173**, 130-136.
312. H. Grisaru, O. Palchik, A. Gedanken, V. Palchik, M. A. Slifkin and A. M. Weiss, *Inorg. Chem.*, 2003, **42**, 7148-7155.
313. A. V. Murugan, T. Muraliganth and A. Manthiram, *Electrochem. Commun.*, 2008, **10**, 903-906.
314. C. Feldmann and H. O. Jungk, *Angew. Chem. Int. Ed. Engl.*, 2001, **40**, 359-362.
315. T. Seike, M. Matsuda and M. Miyake, *J. Mater. Chem.*, 2002, **12**, 366-368.
316. O. Van der Biest, E. Joos, J. Vleugels and B. Baufeld, *J. Mater. Sci.*, 2006, **41**, 8086-8092.
317. P. Umari, E. Mosconi and F. De Angelis, *Sci. Rep.*, 2014, **4**, 4467.
318. N. J. Jeon, J. H. Noh, Y. C. Kim, W. S. Yang, S. Ryu and S. I. Seok, *Nat. Mater.*, 2014, **13**, 897-903.
319. W. Nie, H. Tsai, R. Asadpour, J.-C. Blancon, A. J. Neukirch, G. Gupta, J. J. Crochet, M. Chhowalla, S. Tretiak and M. A. Alam, *Science*, 2015, **347**, 522-525.
320. Y. Qu and X. Duan, *Chem. Soc. Rev.*, 2013, **42**, 2568-2580.
321. R. Venkatasubramanian, E. Siivola, T. Colpitts and B. O'quinn, *Nature*, 2001, **413**, 597-602.
322. L. Yuan, X. Xiao, T. Ding, J. Zhong, X. Zhang, Y. Shen, B. Hu, Y. Huang, J. Zhou and Z. L. Wang, *Angew. Chem. Int. Ed. Engl.*, 2012, **124**, 5018-5022.